SIMULATION OF A MAGNETRON USING DISCRETE MODULATED CURRENT SOURCES

by

Sulmer A. Fernández Gutierrez

A dissertation

submitted in partial fulfillment

of the requirements for the degree of

Doctor of Philosophy in Electrical and Computer Engineering

Boise State University

May 2014

BOISE STATE UNIVERSITY GRADUATE COLLEGE

DEFENSE COMMITTEE AND FINAL READING APPROVALS

of the dissertation submitted by

Sulmer A. Fernández Gutierrez

Dissertation Title: Simulation of a Magnetron Using Discrete Modulated Current Sources

Date of Final Oral Examination: 12 March 2014

The following individuals read and discussed the dissertation submitted by student Sulmer A. Fernández Gutierrez, and they evaluated her presentation and response to questions during the final oral examination. They found that the student passed the final oral examination.

Jim Browning, Ph.D.	Chair, Supervisory Committee
Kris Campbell, Ph.D.	Member, Supervisory Committee
Wan Kuang, Ph.D.	Member, Supervisory Committee
Mark Gilmore, Ph.D.	External Examiner

The final reading approval of the dissertation was granted by Jim Browning, Ph.D., Chair of the Supervisory Committee. The dissertation was approved for the Graduate College by John R. Pelton, Ph.D., Dean of the Graduate College.

DEDICATION

I dedicate this dissertation to my parents, Sulmer and Juan, for their unconditional love, endless support, and encouragement throughout my studies and life. They taught me that even the largest task can be accomplished if it is done one step at a time. I also dedicate this dissertation to my little sister, Cindy, for her love and friendship during my studies and throughout the years.

ACKNOWLEDGEMENTS

I would like to thank Dr. Jim Browning for serving as my major professor and guide through my Ph.D. program. It was a pleasure to be his first Ph.D. student; I truly appreciate all the time and advice he gave me throughout my time at Boise State University. The enthusiasm he has for his research was motivational and encouraging for me, even during tough times in the Ph.D. pursuit. Thanks for all the valuable insights and support, which were a major contribution to complete this dissertation. I would also like to thank Dr. Kris Campbell, Dr. Wan Kuang, and Dr. Mark Gilmore for being willing to serve as members of my committee. I would also like to acknowledge all the faculty and staff that I worked with at Boise State University, took classes from, and met throughout my graduate studies. They were wonderful people and a real pleasure to know. I also acknowledge the funding sources that made my Ph.D. work possible. The first year this research was funded by the Air Force Office of Scientific Research (ASFOR) under Contract No. FA9550-09-C-0141. The remaining time to completion was funded by the Electrical and Computer Engineering (ECE) Department at Boise State University.

I would like to thank Dr. Jack Watrous for his help, expertise, advice, and useful discussions about magnetrons. I would also like to acknowledge Tech-X Corporation, especially Dr. David Smithe, Dr. Ming-Chieh Lin, and Dr. Peter Stoltz for their support and advice and for setting up the original magnetron model in VORPAL; their help was

instrumental in this dissertation. Dr. David Smithe, thank you for the professional advice, time you took speaking with me, and overall friendliness.

Thank you to my MVEDs research group: Peter, Marcus, and Tyler, you were always open for discussion, helping me find errors, and checking my work. I appreciate your assistance and friendship. Although, we worked in different projects, we were always able to collaborate with each other.

Finally, I would like to thank my family and friends (too many to list here but you know who you are!) for providing support and friendship that I needed during my studies, and also during my study breaks. For anyone else, whom I forgot to mention here, many thanks.

ABSTRACT

Magnetrons are microwave oscillators and are extensively used for commercial and military applications requiring power levels from the kilowatt to the megawatt range. It has been proposed that the use of gated field emitters with a faceted cathode in place of the conventional thermionic cathode could be used to control the current injection in a magnetron, both temporally and spatially. In this research, this concept is studied using the 2-D particle trajectory simulation Lorentz2E and the 3-D particle-in-cell (PIC) code VORPAL. The magnetron studied is a ten cavity, rising sun magnetron, which can be modeled easily using a 2-D simulation. The 2-D particle trajectory code is used to model the electron injection from gated field emitters in a slit type structure, which is used to protect the gated field emitters. VORPAL is used to study the magnetron performance for a cylindrical, a five-sided, and a ten-sided cathode. Finally, VORPAL is used to simulate a modulated, addressable, ten-sided cathode. The aspects of magnetron performance for which improvements are desired include mode control, efficiency, start oscillation time, and phase control. The simulation results show that the modulated, addressable cathode reduces startup time from 100 ns to 35 ns, increases the power density, controls the RF phase, and allows active phase control during oscillation.

TABLE OF CONTENTS

LIST OF TABLES

LIST OF FIGURES

CHAPTER ONE: INTRODUCTION

1.1 Overview and Introduction

Radio frequency (RF) radiation has improved the way people live in a variety of ways. Microwave ovens, cell phones, satellite communications, radar, global positioning systems, and air traffic are among the many applications. RF radiation is generated using solid-state and vacuum devices. Microwave devices are capable of high output power (GW-class) with applications over a wide range of frequencies [1-5]. Figure 1 shows a graph of power versus frequency performance [6] of various Microwave Vacuum Electron Devices (MVEDs). This graph shows the range of output power that can be achieved with various devices depending on their frequency of operation. The magnetron was the first practical microwave device, and it allowed the development of microwave radar during World War II [1, 7-10]. Since then, many microwave devices have been developed for the generation and amplification of microwave radiation.

One type of MVED, the crossed-field device, is also called the M-type tube after the French TPOM (*tubes à propagation des ondes à champs magnétique*: tubes for propagation of waves in a magnetic field) [5]; this name derives from the concept that the DC electric field and the DC magnetic field are perpendicular to each other. This dissertation is concerned with the magnetron, which is one type of crossed-field device. Magnetrons are oscillators that can be designed to operate over a wide frequency range, to have high efficiency, and to operate at high power levels. The magnetrons can be

continuous-wave (CW) or pulsed. Pulsed magnetrons can generate very high powers (MW) [2, 6, 11]

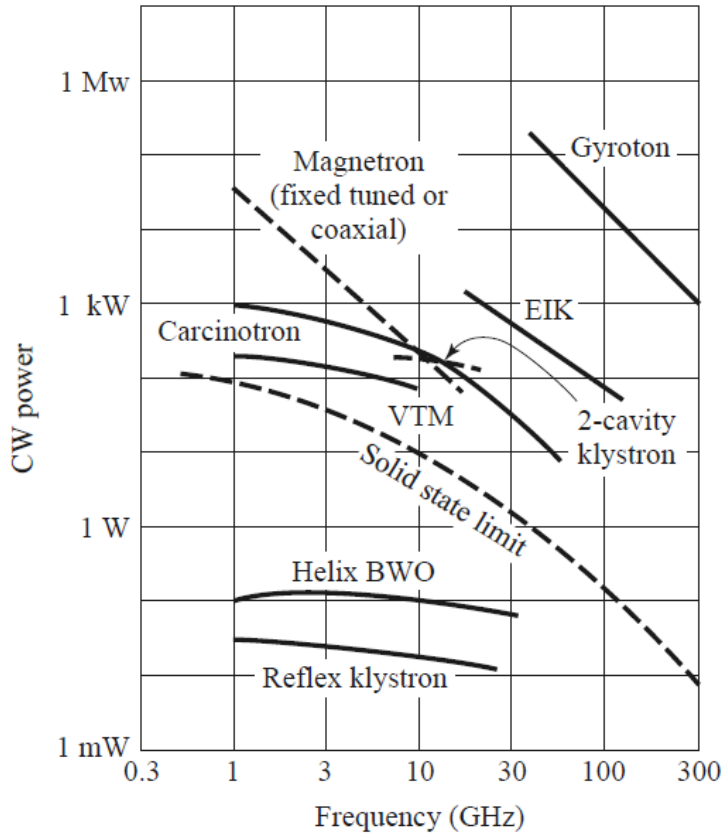

Figure 1: Power versus frequency performance of various microwave oscillator tubes, including backward wave oscillators (BWO) and voltage tunable magnetrons (VTM) [6].

Magnetrons have the advantage of being able to generate high power (from kilowatts to megawatts) at high efficiency (40 to 70%) [5]. Magnetrons are used in numerous applications such as: communications, radar, warfare, medical X-ray sources, and microwave ovens. Figure 2 shows the magnetron as used in a microwave oven. As is shown in the figure, the microwave oven system consists of a microwave source, a

waveguide feed, and an oven cavity. The microwave source is a magnetron tube operating at 2.45 GHz. Power output is usually in the range of 500-1500 W [6].

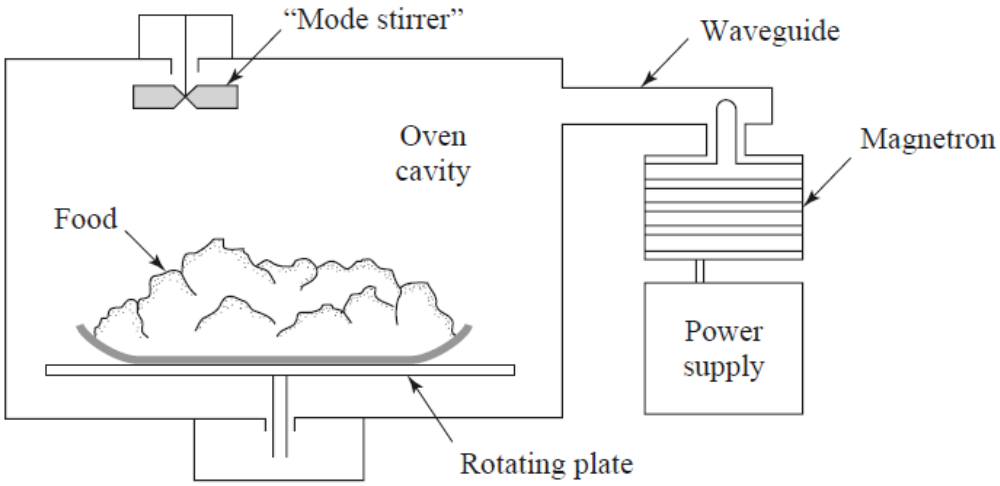

Figure 2: Microwave oven [6].

Figure 3 shows the use of the magnetron in a radar system. As is shown in the figure, the radar system transmits the microwaves towards moving objects that are to be tracked. After the signal is transmitted, the radiation reflects off the object and is later detected by some type of receiver [6]. These objects are as diverse as airplanes, ships, and water vapor in weather systems.

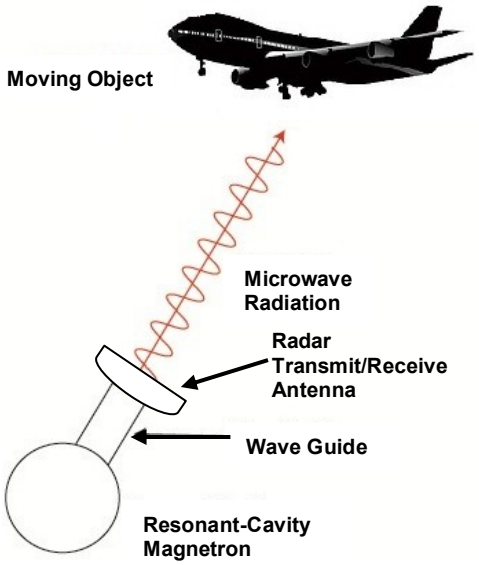

Figure 3: Microwave radar transmission [6].

Magnetrons have been important in the military, commercial, and the plasma physics research communities since the 1940s. There has been a continuing interest in improving performance such as efficiency, power density, start up times, phase locking, and high frequency operation [12-17]. One technique that can help improve these aspects is being developed in this dissertation research. This dissertation involves the simulation of a 2-D model of a ten-cavity rising sun magnetron device using the particle-in-cell (PIC) code VORPAL [18]. The use of gated vacuum field emitters [19, 20] (referred to as discrete current sources in this work) was proposed in a prior work [12] to replace conventional thermionic cathodes used in magnetrons today. This approach would allow control of the electron current injection. The final goal of this dissertation is to perform a temporal and spatial modulation study of the discrete electron sources of the faceted magnetron and to demonstrate phase control of the device.

1.2 Motivation and Contributions

This dissertation consists only of simulation work. An overview of the characteristics of magnetron modeling, the problems presented with simulation analysis, and the contributions of this dissertation to the state of magnetron research are discussed in this section.

Magnetrons are difficult to model. They usually require 3-D rather than 2-D modeling. This dissertation presents a 2-D model of a ten-cavity rising sun magnetron using the electron trajectory code Lorentz2E [21] and the particle-in-cell code (PIC) VORPAL [22]. The rising sun geometry can be easily modeled in 2D, which greatly reduces computation time, and it does not require a complex magnetron model such as the strapped magnetron (see Chapter 2), which can only be modeled in 3-D simulations. Although a 2-D simulation is not the most accurate representation of the device, it is accurate enough [23, 24] to study the device operation, mode separation, and other variables of magnetron performance. There are several different particle-in-cell (PIC) codes available for this type of study; these simulations will be covered in more detail in Chapter 5.

The objective of this research is to demonstrate, via simulation, phase control of the magnetron by implementing a modulated, addressable current source to control the current injection of the device, in place of the traditional thermionic cathodes. This design offers a number of possible advantages: (1) the discrete current sources (emitters) provide a distributed cathode, (2) the electron source can be turned ON and OFF rapidly (<1 ns), and (3) the sources provide the means to spatially and temporally control the current injection. The use of gated field emitters [12] allows temporal modulation of the

electrons, which can be used to control the startup time of the device and to phase control the magnetron. The work presented in this dissertation does not cover phase control of multiple, coupled magnetrons [25-28]; it is focused on the phase control of one magnetron device.

The following contributions were achieved as part of this research:

1) Lorentz2E [21] analysis of electron injection and sensitivity of the injection to operating voltage and electrode location.

2) Development of a faceted cathode model with discrete current sources. This model includes the development of a stable simulation using the particle-in-cell (PIC) code VORPAL [22].

3) Development of a model that controls the device oscillations: temporal and spatial modulation with phase control. This is the major contribution to magnetron research. This model demonstrates phase control of the magnetron oscillations and, moreover, the control of performance of the device. It includes a detailed analysis of magnetron performance under these conditions and analysis of the model stability and possible causes of erratic behavior.

1.3 Dissertation Organization

The remainder of this dissertation is organized into seven additional chapters:

- Chapter 2 gives an introduction to the operating principles of magnetron devices. It provides a background and history of the device and describes the circuit model and basics of magnetron operation.
- Chapter 3 describes in detail the Lorentz2E software and the simulation setup.

- Chapter 4 presents the simulation results obtained with Lorentz2E. It describes the electron trajectory analysis and the sensitivity analysis.
- Chapter 5 gives an introduction to PIC codes. It describes the Finite-Difference Time-Domain (FDTD) method, numerical stability, boundary conditions, and techniques implemented in VORPAL. This chapter introduces the 2-D model of the rising sun magnetron and the simulation setup.
- Chapter 6 and Chapter 7 present extensive simulation work, analysis, and results obtained with VORPAL. The results are divided in two models: the continuous current source, or reference model, and the modulated, addressable, current source model. The continuous current source model is presented in Chapter 6. The temporal modulation and phase control are presented in Chapter 7.
- Chapter 8 includes the summary, conclusions, and proposed future work.

CHAPTER TWO: BACKGROUND

2.1 Magnetron Operating Characteristics

Magnetrons are crossed-field microwave sources that are capable of achieving an output of hundreds of megawatts [29, 30]. They have a rich history beginning in the 1920s with the work by Hull, who investigated the behavior of electrons in a cylindrical diode in the presence of a magnetic field parallel to its axis [1, 8, 10, 13, 30-37]. Figure 4 shows Hull's original diode.

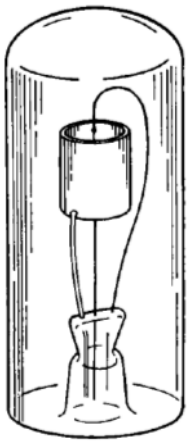

Figure 4: Early type of magnetron: Hull original diode [1].

A cylindrical anode surrounds the cathode (thermionic), which is heated to provide a source of electrons. A uniform magnetic field parallel to the axis of the tube is produced by a solenoid or external magnet not shown in the diagram. In the crossed electric and magnetic field, which exists between the cathode and anode, an electron that is emitted by the cathode moves under the influence of the Lorentz force:

$$\mathbf{F} = q\mathbf{E} + q(\boldsymbol{v} \times \boldsymbol{B}) \tag{2.1}$$

where E is the electric field, $\boldsymbol{B}$ the magnetic field, $\boldsymbol{v}$ the velocity of the electron, and q is its charge [1, 5]. Figure 5 shows the electron motion in a crossed electric and magnetic field. The circular orbit, which turns around at the cathode, is referred to as a "cycloidal orbit."

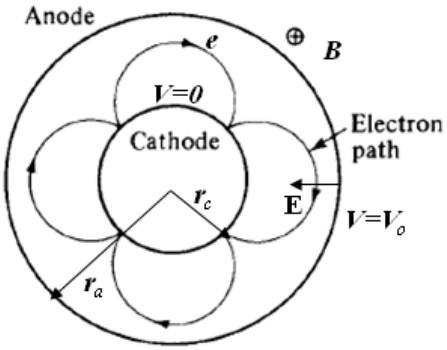

Figure 5: Electron motion in a crossed electric and magnetic field diode configuration [5] showing a cycloidal orbit.

The solution of the resulting equations of motion, which neglect space-charge effects, shows that the path of the electron is a quasi-cycloidal orbit with a frequency given approximately by

$$f_t = \frac{e}{m} B \tag{2.2}$$

where m is the particle mass and e is the electron charge.

A condition of "cutoff" is said to be present when the trajectory of this orbit touches the anode; therefore, the following equation can be written as:

$$\frac{V_o}{B^2} = \frac{e}{8m} r_a^2 \left[1 - \left(\frac{r_c}{r_a} \right)^2 \right]^2 \tag{2.3}$$

where V_o is cathode-anode voltage, and r_a and r_c are the anode and cathode radii [1, 5], respectively (See Figure 5). This equation implies that for V_o/B^2 less than the right hand side of the equation there is no current flowing, and therefore, the electrons will not reach the anode. On the other hand, if V_o/B^2 increases to the condition of cutoff, an increase in the current is observed. Equation 2.3 is also called the *Hull cutoff voltage equation* [5]. The Hull magnetron was not a very successful device. The device had low efficiency, low power, and erratic behavior. The Hull magnetrons were not fabricated in great quantities, although they were used for research purposes by Zarek, Yagi, and Cleeton [1].

After the Hull magnetron, in 1935, K. Posthumous [38] studied a different anode structure for the magnetron with the idea of improving the device efficiency. He discovered that by using high magnetic fields, the RF power was generated with relatively high efficiency. After various experiments, an efficiency of 50% was found in a magnetron operating at a wavelength of 50 cm (600 MHz) [30, 33, 34]. These types of magnetrons were called traveling-wave oscillators. Continuing Posthumous work, A. L. Samuel [39] performed experiments with a magnetron using an anode structure called the hole-and-slot resonator, which provided high frequencies. In 1938, the structure was again modified by scientists Aleksereff and Malearoff [40]. The magnetron was built with a copper anode and hole-slot resonators. This device generated a power of about 100 W at a wavelength of 100 cm [30, 33, 34]. Following this, the magnetron became very important world-wide with the work by Randall and Boot at the University of Birmingham (UK) [7-9, 41-47] in 1939; their work with the magnetron device became

useful in radar applications during World War II. Randall and Boot built a magnetron with an anode containing six resonant cavities, and they called this device the cavity magnetron (see Figure 6) [7, 46, 48]. These cavities generate an RF wave that travels at a phase velocity much less than the speed of light in order to allow for good synchronization with the electrons. This type of anode structure is called a slow wave circuit. In early 1940, an experimental radar system containing a cavity magnetron was in operation. Since then, many microwave devices have been developed for the generation and amplification of microwave radiation [34].

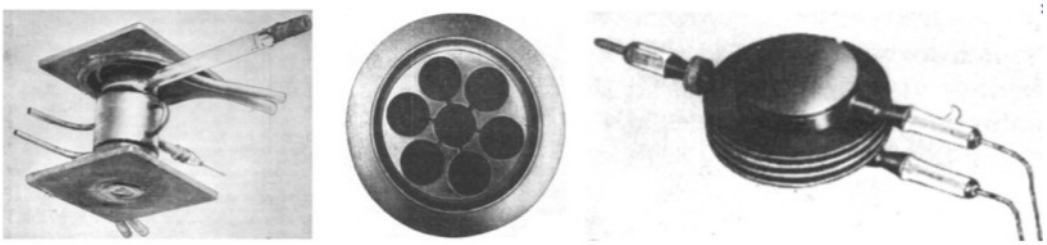

Figure 6: First 10-cm cavity magnetron [1]. The slow wave circuit consists of 6 cavities.

Currently, a typical magnetron is comprised of a coaxial structure with an electron-supplying cathode at the center and a slow-wave structure on the outside [12, 49]. The slow-wave structure in a magnetron usually consists of N resonators spaced around a cylindrical cavity, or as it is also known, a reentrant cavity. A simple example of such a six-cavity magnetron is shown in Figure 7.

Conventional magnetrons typically use thermionic cathodes [50] in which electrons are emitted from a high temperature cathode material in either a space charge or temperature limited regime. Field emission cathodes [51] are also used in high power magnetrons, but these emitters are un-gated. Magnetrons can be either pulsed or CW

(continuous wave). In pulsed magnetrons, a pulse forming network is used to ramp a large DC voltage (100's of kV) to supply the DC electric field [14, 16, 17, 29, 30, 52-56]. The magnetron turns on during the DC voltage pulse. Availability of a cathode that could be modulated could eliminate the need for the high voltage pulse requirement. Therefore, this research is currently exploring the use of gated field emission cathodes as the electron source [12].

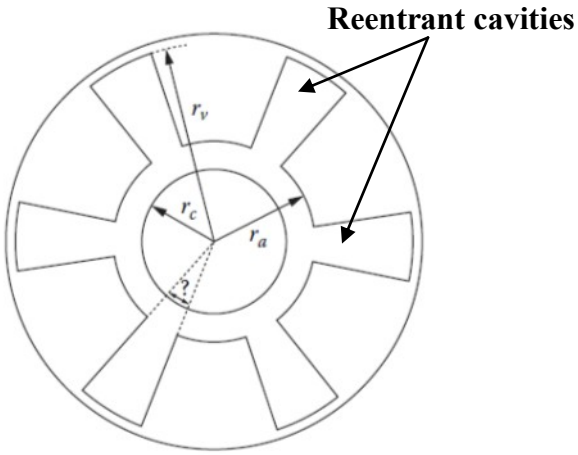

Figure 7: Cross section of a magnetron showing reentrant cavities, with r_c and r_a the cathode and anode radii, and r_v the vane radius [11].

2.2 Cylindrical Magnetron

The anode of a magnetron is usually fabricated out of a cylindrical copper block. A typical cathode might consist of a spiral wound wire filament structure at the center of the device supported by the filament leads (Figure 8). The resonant cavities in combination with the anode-cathode gap determine the various possible modes for the output frequency. The open space between the anode and the cathode is called the interaction space. In this space, the electric and magnetic field interact to exert force upon the electrons. The form of the cavities varies in shape and structure as shown in Figure 9

[57]. In Figure 9, four different cavity types are shown ranging from simple slots to the hole and slot type. The output port is usually a probe or loop extending into one of the cavities and coupled into a waveguide or coaxial line (see output from Figure 8) [57].

The cylindrical magnetron is also known as the conventional magnetron. Figure 8 shows a schematic diagram of a cylindrical magnetron oscillator. In this device, several reentrant cavities (see Figure 7) are connected to the gaps. The DC voltage, $V_{o,}$ is applied between the cathode and the anode. For most magnetrons, the cathode is actually biased at a negative voltage while the anode (slow wave circuit) is held at ground potential. The magnetic flux density, $B_{,}$ is in the positive z direction as shown in Figure 5. When the DC voltage and the magnetic flux are adjusted properly, the electrons will follow cycloidal paths (see Figure 5) in the cathode-anode space under the combined force of both the electric and magnetic fields [5].

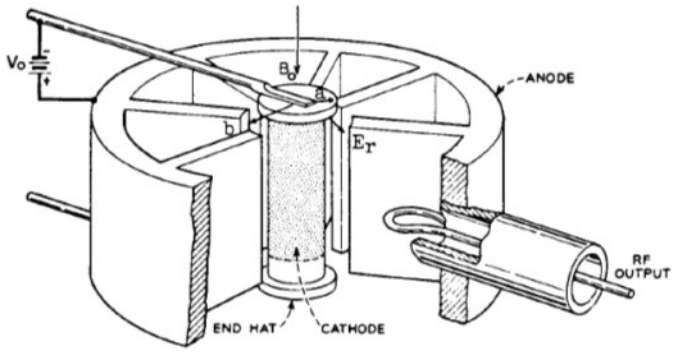

Figure 8: Schematic diagram of a cylindrical magnetron [5].

The magnetron is comprised of a resonant system; therefore the magnetron can operate at a different number of resonant frequencies. In order to guarantee the stable operation of the magnetron, it is important to find the right frequency of operation. In the

process of finding this frequency, changes in the operation modes will be observed [58]. These aspects will be discussed in Section 2.3.

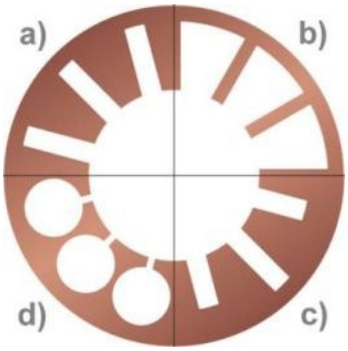

Figure 9: Various forms of the anode block in a magnetron: (a) Slot type, (b) Vane type, (c) Rising sun, and (d) Hole-and-Slot type [57].

2.3 Magnetron Resonant Circuit and Modes of Operation

The magnetron is comprised of resonant cavities, and these cavities can be modeled as resonant circuits. An equivalent circuit for one of the cavity resonators could be designed as a simple parallel circuit. Figure 10 shows an example of an eight-cavity magnetron with the oscillating circuit. *L* and *C* are inductance and capacitance, respectively, representing a single cavity. *C* is the capacitance between the individual anode segment and the cathode. The coupling from one cavity to another in the end spaces is represented by *M* in the circuit [1, 58].

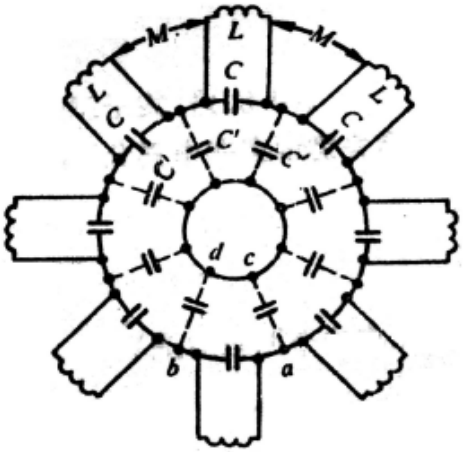

Figure 10: Equivalent circuit of an eight-cavity magnetron [1].

The oscillation frequency corresponding to one individual resonator is:

$$\omega_o = \frac{1}{\sqrt{LC}} \tag{2.4}$$

where ω_o is the oscillation frequency, and L and C are the inductance and capacitance of the individual resonator.

Since the eight cavities have a symmetric distribution, the phase differences (labeled as φ) between adjacent cavities are the same. The voltage between the anode vanes in each cavity can be represented as [1]:

$$V_1 = V_m \sin(\omega_o t) \tag{2.5}$$

$$V_2 = V_m \sin(\omega_o t - \varphi) \tag{2.6}$$

$$V_3 = V_m \sin(\omega_o t - 2\varphi) \tag{2.7}$$

…

$$V_8 = V_m \sin(\omega_o t - 7\varphi) \tag{2.8}$$

$$V_9 = V_m \sin(\omega_o t - 8\varphi) \tag{2.9}$$

where V_m is the amplitude of the RF voltage.

When the system is oscillating, V_9 should be equal to V_1. Therefore, 8φ = 2πn (n = 0,1,2…). The total number of cavities is N, and in order for oscillations to occur the phase condition is given by

$$N\varphi = 2\pi n; \tag{2.10}$$

therefore, the phase shift between two adjacent cavities can be expressed as:

$$\varphi_n = \frac{2\pi n}{N} \tag{2.11}$$

where n is an integer indicating the nth mode of oscillation. In order for oscillations to be produced in the device, the cathode DC voltage and the applied magnetic field must be tuned so that the average rotational velocity of the electrons corresponds to the phase velocity of the field on the slow-wave structure [1, 5, 58]. Magnetrons usually operate in the π mode, that is $\varphi_n = \pi$. Figure 11 shows the lines of force in the π-mode of an eight-cavity magnetron. It can be observed that in the π-mode, the fields are higher in the cavities, and they have opposite phase as they go from cavity to cavity. The pattern of the fields going from high to low in the cavities can also be recognized as a wave following the path of the slow-wave structure [5].

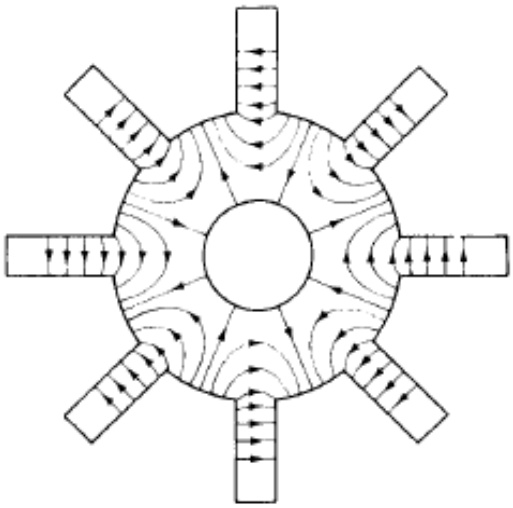

Figure 11: Lines of Force in π-mode of Eight-Cavity Magnetron [5].

2.4 The Hartree and Hull Cutoff Condition

There are specific conditions between the applied anode voltage and the static magnetic field that must be satisfied for a magnetron to operate correctly. In the cylindrical magnetron, in order for an electron to reach the anode, the condition, known as "cutoff", is

$$V_h = \frac{e}{8m} B^2 r_a^{\,2} \left(1 - \frac{r_c^{\,2}}{r_a^{\,2}}\right)^2 \tag{2.12}$$

where V_h is the cutoff cathode-anode voltage, r_c is the cathode radius, r_a is the anode radius, and B is the cutoff static magnetic field.

When the RF field is not present and there is a given magnetic field and the cathode-anode voltage is smaller than V_h, the electrons will not touch the anode. This voltage, V_h, is known as the Hull cutoff voltage [5, 58]. If the magnetron operates below the Hull cutoff voltage, an electron cloud, or hub, will be formed between the cathode

and the anode. To start oscillations in the magnetron, it is necessary that the electrons rotate synchronously with the RF field; thus,

$$\omega_e = \frac{\omega}{n} \tag{2.13}$$

where ω_e is the angular frequency of electron, ω is the angular frequency of the RF field, ω / n the rotating frequency of the corresponding traveling wave, and n is the mode number of the traveling wave.

Applying this synchronous condition to the equations of electron motion:

$$\frac{d^2 r}{dt^2} - r\left(\frac{d\varphi}{dt}\right)^2 = \frac{e}{m} E_r - \frac{e}{m} r B_z \frac{d\varphi}{dt} \tag{2.14}$$

$$\frac{1}{r}\frac{d}{dt}\left(r^2 \frac{d\varphi}{dt}\right) = \frac{e}{m} B_z \frac{dr}{dt} \tag{2.15}$$

which govern the electron movement in a cylindrical coordinate system with φ = angle in cylindrical coordinates; the threshold voltage for oscillation to start in a magnetron can be obtained [58]:

$$V_t = \frac{r_a^2}{2}\left(1 - \frac{r_c^2}{r_a^2}\right)\frac{\omega}{n} B_z - \frac{r_a^2}{2}\frac{m}{e}\left(\frac{\omega}{n}\right)^2 \tag{2.16}$$

The threshold voltage is also known as the Hartree voltage. This voltage is the condition at which oscillations should start, where *B* is sufficiently large so that the undistorted space charge does not extend to the anode. Figure 12 shows the Hartree Threshold Voltage curve for an eight-cavity magnetron. When the anode voltage is slightly above the Hartree voltage curve, the magnetron starts to oscillate. In general, the cathode-anode voltage of a magnetron is always set below the π-1 mode line (n = 3 in Figure 12) to avoid mode competition.

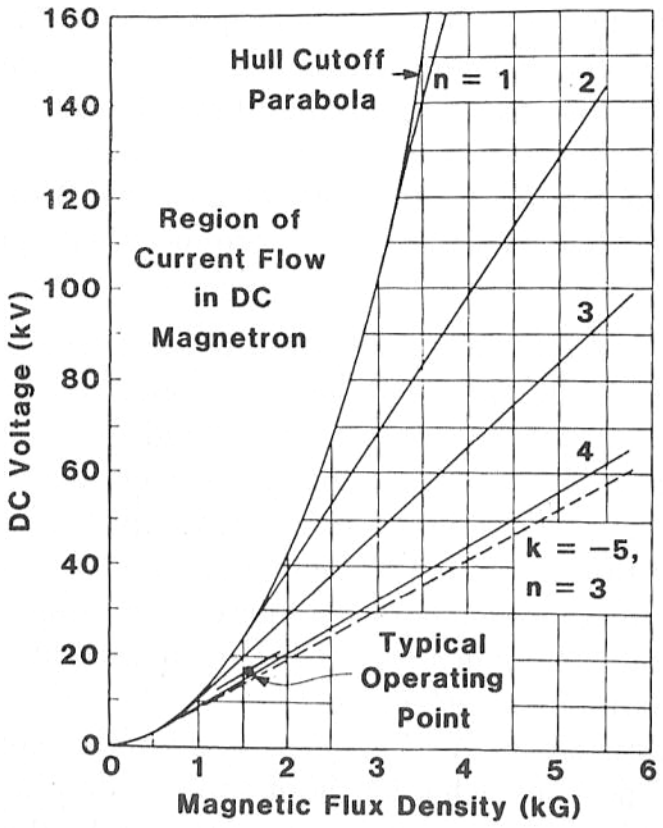

Figure 12: Hartree threshold voltage diagram for an eight-cavity magnetron © 1976 IEEE [48].

2.5 The Diocotron Instability

The diocotron instability is a perturbation that generally occurs in magnetron operation. In a magnetron, electrons leave the cathode and are accelerated toward the anode, due to the DC field established by the voltage source. The magnetic field applied between the cathode and anode produces a force on each electron that is perpendicular to the electric field and the electron velocity vectors; this effect causes the electron trajectories to bend and travel away from the cathode in a cycloidal pattern (see Step 1 in Figure 13). Following this behavior, the electrons eventually form a rotating cloud around the cathode, which is also known as the hub (see Step 2 in Figure 13). The hub will

continue to rotate around the cathode, and a perturbation, such as the diocotron instability, will cause the distortion of the electron hub. The rotating perturbation, or bump, results in a time varying electric and magnetic field from the moving charge. This field interacts with the slow wave circuit resulting in a circuit field with a rotational phase velocity that is synchronous with the motion of the electrons. This field causes further bunching of the electron perturbation or electron bump. In the case of a ten-cavity magnetron operating in the π-mode, 5 bumps will be formed. As these perturbations generate time varying electric and magnetic fields, the fields will grow until spokes form and full oscillation occurs. In Figure 13, this phenomenon can be observed; Step 4 shows the complete spokes. The formation of these spokes is also an indicator that the device started oscillating.

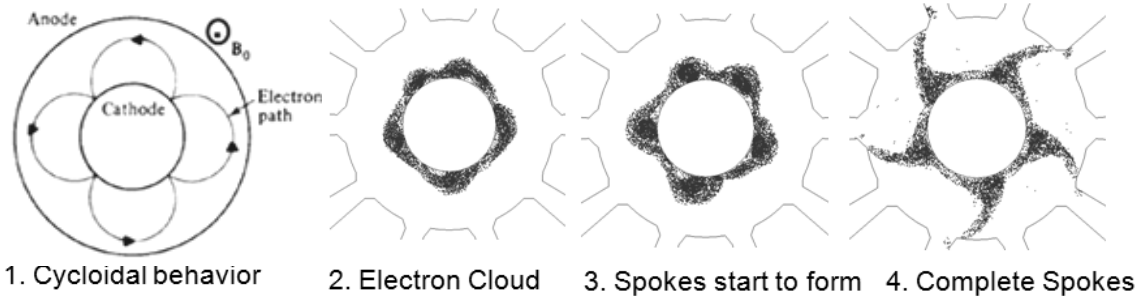

Figure 13: Formation of the spoke-like electron cloud in a ten-cavity rising sun magnetron from VORPAL simulation.

The diocotron instability was one of the first instabilities to be studied since the beginning of magnetron design [2, 59, 60]. Also, it has been considered the main factor responsible for noise generation in crossed-field devices. Figure 14 shows a conceptual example of the diocotron instability [2]. In this example, there are three steps that

describe this mechanism. Figure 14a shows the electron sheet; Figure 14b shows the sinusoidal perturbation applied to the system; and points A and C represent electrons that are moved upward by the electrostatic force of the adjacent electrons. The electrons located at points B and D are moved downward. In Figure 14c, it can be observed that charge bunching is generated by the movement of electrons in A and C to the left and B and D to the right due to the $\boldsymbol{F} \times \boldsymbol{B}$ force (Figure 14b). This charge bunching will increase the growth of the perturbation leading to an $\boldsymbol{E} \times \boldsymbol{B}$ drift [2].

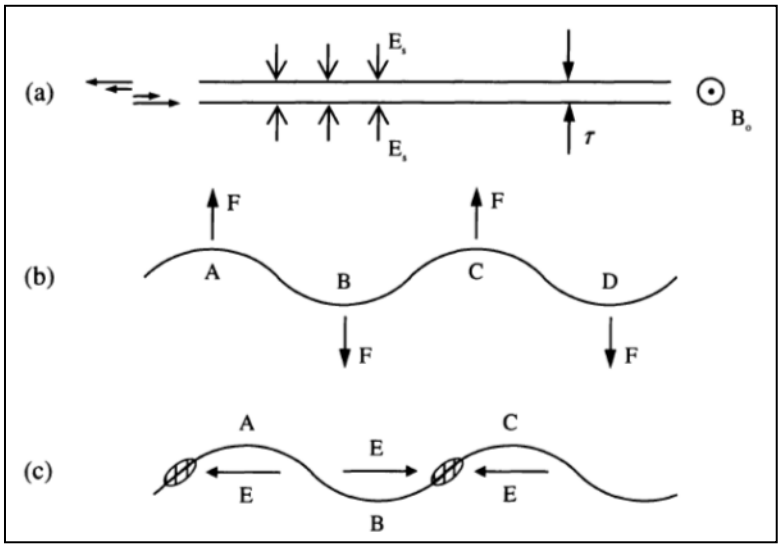

Figure 14: Physical mechanism of the diocotron instability.

(a) Velocity shear generated by the self-electric field of the electron sheet, (b) Initial sinusoidal perturbation of the electron sheet, and (c) growth of the electron-bunching and instability development [2].

2.6 Stability and Mode Separation

Magnetrons may have several modes of oscillation. Usually the desired operating mode in a magnetron is the π mode because it gives better stability and higher output power. In this section, different techniques for mode separation will be described.

Frequency and Mode Competition

Magnetrons are comprised of many resonators coupled together. For this reason, mode competition is a common problem in magnetrons [2, 6, 58]. The mode number is defined as 'n', and it describes the number of times the RF field pattern is repeated going around the anode once. N is defined as the number of cavities, where the maximum number for n is N/2, for π-mode operation. When this occurs, this mode is called the π-mode [34]. A magnetron operating in the π-mode has greater power output and is the most commonly used. For this reason, mode separation became very important for making magnetron oscillators reliable and efficient.

One of the most common problems in the design of magnetrons is to ensure that the operation remains in only one of the many possible resonant frequencies. It has been found that this can be achieved if the circuit is designed so that the operating resonant frequency is well separated from all other resonant frequencies of the structure [61]. Two techniques, the use of straps and the rising sun structure, are used to achieve mode separation. These techniques will be described in the following sections.

Strapping

This technique consists of having alternate anode segments connected at the same RF potential, as shown in Figure 15. These alternate anode segments are connected by a wire or a strap in which the ends are at the same potential. The use of straps adds extra

capacitance to the resonator circuit of each cavity, and therefore it could also add some undesired modes. However, the strapping technique is designed to separate and isolate the π-mode frequency; therefore, other frequencies that could be generated are not significant in comparison to the π-mode. This way the device will not operate in other modes. Strapping was one of the first techniques used in magnetron design and was first implemented by Randall and Boot in 1941 in the cavity magnetron [7]. Figure 16 shows a picture of a strapped magnetron. The wire straps are visible in the image.

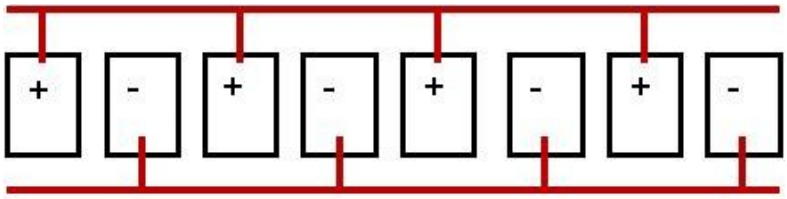

Figure 15: Strapping technique. Alternate anode segments at same potential.

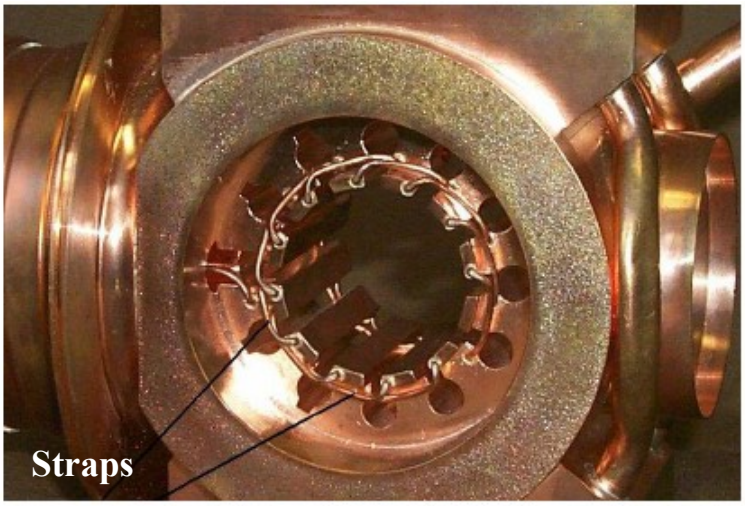

Figure 16: Wire strapping system of an S band cavity magnetron [58].

Rising Sun Geometry

The magnetron design for this work is the rising sun magnetron [61-63]. This design was developed in the search for a stable magnetron operation at wave-lengths close to 1 cm. This design can also achieve stability and can operate in the π-mode without strapping [1, 61-63].

The rising sun anode structure was developed by Millman and Nordsieck [61] in 1944. This design utilizes two different resonator sizes arranged symmetrically around the cathode-anode space, with resonators alternately larger and smaller (See Figure 17). The rising structure has a design that allows mode separation. By examining the field patterns that are associated with different modes, it can be observed that modes that range in the low frequencies are control by the larger cavities. On the other hand, modes associated with higher frequencies are control by the shorter cavities. Hence, the π-mode frequency range can be found in between the resonant frequencies of the two cavities [34, 61]. Figure 17 shows a comparison of the strapped structure versus the rising sun structure.

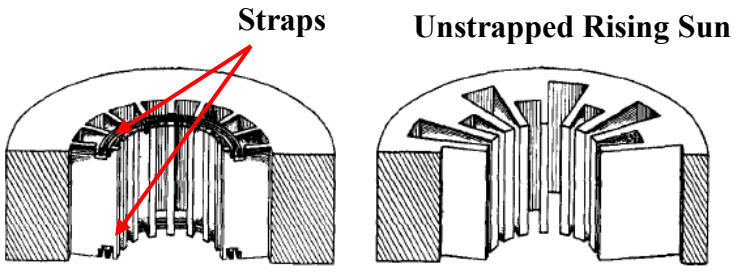

Figure 17: Techniques for achieving mode separation [61].

The rising sun magnetron is an easier geometry to handle in terms of modeling and calculations, since the technique of strapping requires a more complex model, and the calculations that could be done in two-dimension modeling are very limited. The rising sun geometry allows modeling of the magnetron in two dimensions and, therefore, greatly reduces computation time. Figure 18 shows a picture of a sixteen-cavity rising sun magnetron.

Figure 18: Sixteen-cavity rising sun magnetron from Ostron Technologies [64].

2.7 Phase Locking of Magnetrons

Phase locking of magnetrons is a technique used to control the magnetron oscillation and is also used to take advantage of magnetrons that operate at lower powers. These magnetrons can be synchronized together and can be 'phase locked' to a desired phase with the objective of getting a higher power output. Phase locking is used in many applications [26-28, 47, 65] ranging from radar systems to materials processing. The idea is to minimize cost, to take advantage of lower power devices, and to achieve high efficiency. If a group of 100 kW commercial magnetrons could generate power

equivalent to that of a single relativistic magnetron, which is an expensive device, then phase locking could be used to substitute for this expensive device [25]. Phase locking has been studied since World War II with the works of Adler [66] and David [67]. They developed theories applied to phase locking of magnetrons driven by an external source, which was performed by power injection at levels significantly below the magnetron's output power [25]. The condition for locking is known as Adler's condition and is written as [66]

$$\sqrt{\frac{P_D}{P_O}} \geq 2Q\left|\frac{\omega_D - \omega_o}{\omega_o}\right| \tag{2.17}$$

where P_D is the magnitude of injected power, P_O is the oscillator's output power, ω_D is the frequency of the injected signal, ω_o is the free running oscillators output frequency, and Q is the quality factor of the oscillator. The work presented in this dissertation will not cover phase control of multiple magnetrons, which is a technique broadly covered in the literature [2, 25-28, 47, 65, 68]; it will focus on the phase control of oscillations of one magnetron device by using modulated, addressable, controlled electron sources.

2.8 State of the Art and New Magnetron Concept

Ongoing research has been studying different methods to improve magnetron performance. A group at the University of Michigan has completed extensive research to improve startup time of oscillations by using two techniques: cathode priming [63] and magnetic priming [69, 70]. Cathode priming consists of using discrete regions of electron emission periodically arranged azimuthally along the cathode surface. Emission from these regions resulted in faster formation of electron bunches. The magnetic priming used

an azimuthally modulated magnetic field, which led to modulation of the electrons over the solid cathode surface. The group is currently studying two new magnetron concepts: the inverted magnetron and the recirculating planar magnetron [3, 14, 15]. The inverted magnetron [15], as its name implies, consists of having the cathode on the outside and the anode on the inside. The main characteristics of this device are its larger cathode area, the reduction of electron end loss, and a faster startup in comparison with the conventional magnetron. These characteristics are also incorporated in the recirculating planar magnetron. The recirculating planar magnetron [14] is considered a new class of crossed-field device that features both large area cathode and anode, meaning high current and improved thermal management. This device was designed with 12 cavities, 2 planar oscillators with 6 cavities each, operating at a frequency of 1 GHz. Mode control is still under study with this device; using the PIC code MAGIC, they have simulated phase locking, achieving an increase in mode separation and a reduction in the startup time of oscillations.

The University of New Mexico developed the transparent cathode technique [16, 17, 71]. This concept also resulted in faster startup times by combining different priming mechanisms: cathode priming, magnetic priming, and electric priming. The emitters act as discrete emission centers azimuthally about the cathode. The number and position of the emitters with respect to the anode cavities may be selected in order to provide the cathode priming in the desired operating mode [16]. PIC simulations with the transparent cathode have shown improvements in the output characteristics such as: higher output power, higher efficiency, and better stability of oscillations. One of the disadvantages of this technique is that the electron sources cannot be controlled once the device is in

operation, since it does not allow a rapid turn ON/OFF time of the current source. Therefore, it would not allow the temporal modulation of the current sources.

The Air Force Research Lab (AFRL) developed a method to replace thermionic cathodes with explosive field-emission cathodes [51, 72]. The explosive field emission cathodes are lightweight; they deliver high currents and do not require heat for their operation. Three different types of cathodes were tested, each of them with slightly different geometries. Although, these cathodes are not as developed as thermionic cathodes, the results demonstrated that this technique provided a lower turn-on DC electric field and a uniform emission. Moreover, the use of gated field emitters has also been implemented to replace the conventional thermionic cathode. One of the few applications of gated field emitters in MVEDs has been implemented in traveling wave tubes (TWTs) [73, 74]. This project successfully demonstrated the use of modulated gated emitters in TWTs. The emitters cathode pulse time was reduced from the scale of seconds (thermionic cathode) to the scale of nanoseconds (gated emitters). It was demonstrated that the use of gated emitters has the potential to improve TWTs performance that is not achievable with conventional thermionic cathodes.

The proposed magnetron concept for this research is based on using gated field emitters placed in a shielded structure housed within the cathode to prevent ion bombardment to the emitters and to keep the emitters protected from the high electric field environment of the magnetron [12]. Because the emitters must be fabricated on flat surfaces, the cathode is comprised of facet plates with slits [12]. This device concept is shown in Figure 19. The design here shows a ten-cavity rising sun magnetron with a pentagon shaped cathode with five facet plates. Each facet has slits for electron injection.

The front of each facet is a conductor, which forms the sole electrode. Here, the sole electrode indicates a non-emitting cathode structure. While this image shows a few large slits, the actual device concept would have hundreds of slits per facet plate with many thousands of gated emitters placed below the facet. The idea behind this concept is that the gated field emitters could be used to control the electron injection into the interaction space of the magnetron by varying the emission current both spatially and temporally. Hence, the cathode can be modulated to control the beam wave interaction and the device phase. This modulated, addressable-cathode based magnetron is actually an amplifier but is based on the cavity magnetron structure. Such a device can reduce start up times and allow phase locking with other similar devices for increased power output [26, 28, 47].

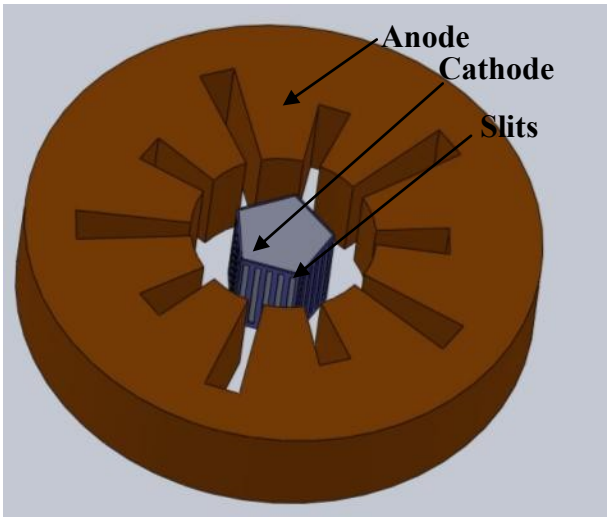

Figure 19: Proposed ten-cavity rising sun magnetron with a five-sided faceted cathode. Each plate would have hundreds of slits with gated emitters beneath.

CHAPTER THREE: LORENTZ2E SIMULATION

3.1 Overview

This chapter describes the simulation setup, procedures, and techniques implemented in the simulation with Lorentz2E. In this research, Lorentz2E is used to study the electron trajectories in the rising sun magnetron model as well as to determine the sensitivity of the electron injection into the device from changes in the operating parameters and geometry.

3.2 Software

The Lorentz2E simulation used in this research is a 2-D serial (it uses one processor core) particle trajectory simulation code developed by Integrated Software [21]. The simulation can include both space-charge and surface-charge effects. The simulation solves for the electric fields using the Boundary Element Method (BEM) [21] and uses a 4^{th} order Runge-Kutta technique [21] for the electron trajectory tracking. The Boundary Element Method (BEM) solves field problems by solving an equivalent source problem. In the case of electric fields, it solves for equivalent charge; while in the case of magnetic fields, it solves for equivalent currents. BEM also uses an integral formulation of Maxwell's Equations, which allows for very accurate field calculations [21].

In Lorentz2E, the simulation can be set to inject a fixed current with a user-determined number of electron rays containing a proportional fraction of that current. The sensitivity analysis studied in this research is performed using the parametric analysis

tool in Lorentz2E, which allows the user to change parameters such as dimensions and materials. The objective of the parametric study is to find the adequate set of parameters that will provide the optimal performance of the device: in other words, to find the optimal conditions regarding geometry and operating parameters that will guarantee the maximum number of electron rays exit the slits in the cathode plate.

3.3 Simulation Setup and Procedures

To model the electron trajectories in the magnetron, the simulation was set to inject a total emission current of 16.3 A, with a resulting current required per slit of 6.5 mA, and a user-determined number of electron rays (200 rays total, 100 rays per side). These parameters were taken from previous work completed by Browning and Watrous [12]. Figure 20 and Figure 21 show the slit structure in more detail. It can be observed in Figure 20 that the emitter arrays are placed on either side of a slit but back from the exit opening of the slit to prevent ion back bombardment. The emitters are lateral devices that emit along the surface of the substrate. The device configuration shows lateral tips with symmetric gates. These emitters can be stacked with multiple layers to provide multiple emission sites. The emission sites comprise an area defined by both the length of the slit (axial direction) and the vertical distance of the emitter stack in order to provide the maximum number of emission sites. The lateral emission of electrons along the surface allows the entire emitter to be placed back from the slit exit opening. Hundreds of slits could be fabricated on a single facet by using standard microfabrication techniques [12]. Figure 21 shows the Lorentz2E model of the shielded cathode slit structure.

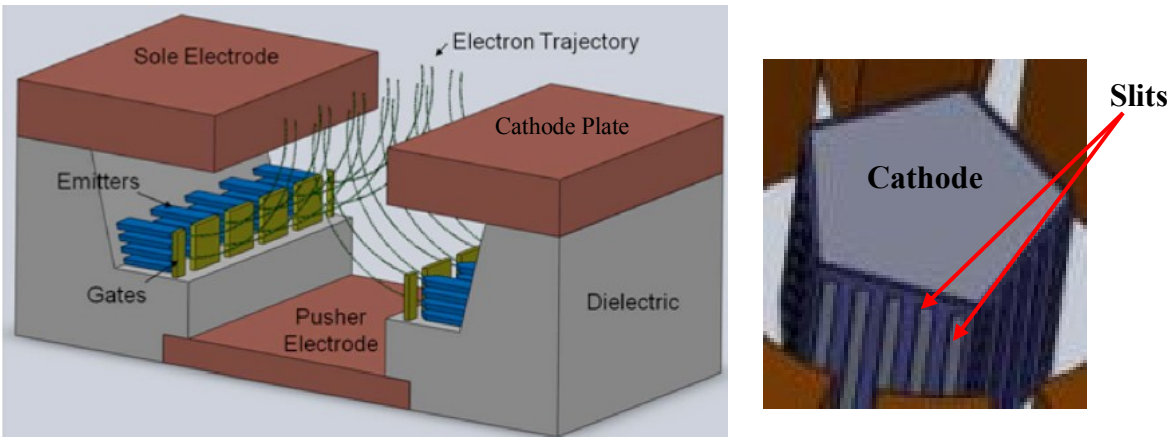

Figure 20: **(a) Shielded cathode slit. Showing the stacked lateral field emission tips on each side of the slit, a pusher electrode, the sole electrode (cathode plate), and the electron trajectories. (b) Faceted cathode showing slits [12].**

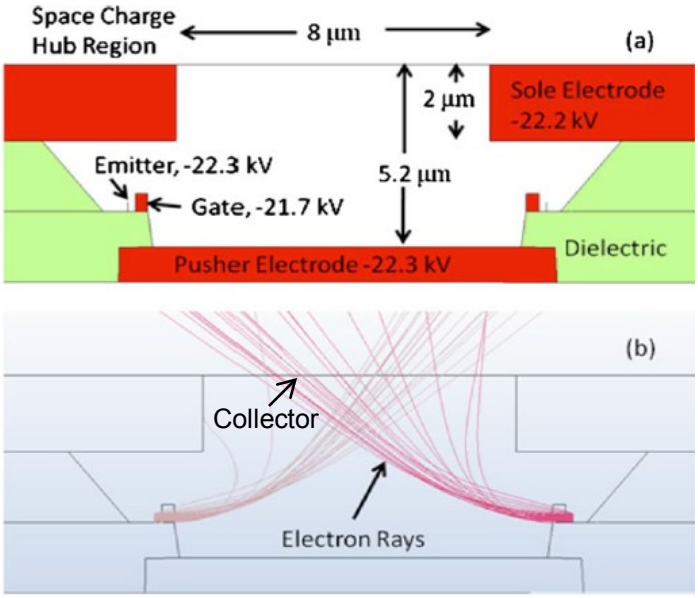

Figure 21: **Lorentz2E model of the shielded cathode slit structure. (a) The emitters on each side, a field emission gate transparent to electrons, a pusher electrode, the sole electrode, the electrode voltages, and the dimensions; and, (b) the electron ray trajectories[12].**

The structure is comprised of the following.

Field emitters: They are the source of electron rays. They were modeled as a line with a fixed injection current. The field emitters are on each side of the slit.

Gate: The gate was modeled as a block that allows electron transit. The gate is biased positive with respect to the emitters to create a large electric field capable of generating field emission.

Sole electrode: Sets the interaction space electric field in the magnetron. This sole electrode is biased negative relative to the anode.

Pusher electrode: The pusher electrode is placed below the level of the field emitter. As the rays move into the slit region, the field from the pusher electrode directs the electrons up through the slit. In order to do this, the pusher electrode is biased negative relative to the sole electrode.

Collectors: Boundaries that collect particles upon collision. In the simulation, a collector is used to estimate the amount of rays that exit the slit.

Figure 22 shows the Lorentz2E complete five-sided faceted cathode with a smooth anode. It shows the ray trajectories at a single slit exit. For the actual device, there would be more than 100 slits per facet. The cathode has a 1 cm radius at the facet corner, while the anode has a 2.24 cm radius. Each facet is 1.18 cm wide. There is a second inner circle in the figure representing a region of volume space charge. A volume space charge was set up in the simulation to represent an electron hub. The hub extends from a radius of 1-1.5 cm. A total volume charge of -1.5×10^{-8} C was used in the simulation to represent the charge hub [12].

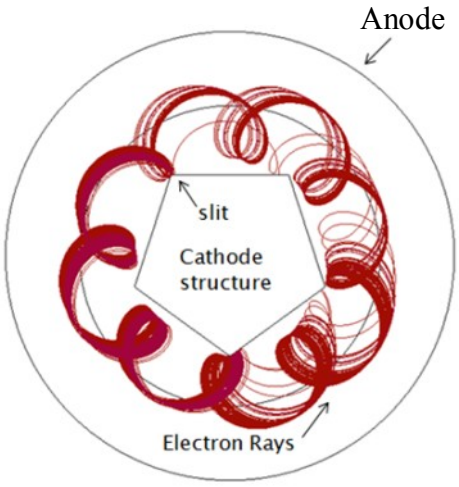

Figure 22: Magnetron model used in Lorentz2E. Five-sided cathode with a smooth dummy anode showing electron ray traces from a single shielded slit structure on the left hand side of the top facet.

The sole electrode (see Figure 21) is set to -22.2 kV, and there is an axial magnetic field of 900 G. The gate was modeled as a block that allows electron transit. All other electrodes were defined as collectors. The slit exit is 8 µm across; the sole electrode is 2 µm thick. Also shown in Figure 21 are the voltages for the electrodes and the emitters with the sole electrode biased at -22.2 kV, the emitters biased at -22.3 kV, the pusher at -22.3 kV, and the gate at -21.7 kV. These values are obtained from this simulation for the best extraction of the electrons out of the slit [12].

3.4 Electron Trajectory Analysis

One concern for the proper operation (best extraction of the electrons out of the slit) of the magnetron is the effect of the initial electron energy distribution given the slit structure and facets. To study this effect, the electron energy distribution was determined from the simulation by developing histogram plots. The values were taken at the exit of the slit where a "collector" was placed in the simulation (see Figure 21). This analysis

included variation in the number of rays to check consistency. The simulations were divided into three cases: 50 rays (25 rays each side), 100 rays (50 rays each side), and 200 rays (100 rays each side). The energy is divided into transverse (parallel to the slit opening) and vertical (perpendicular to the slit opening). The most significant results from these simulations can be found in Chapter 4.

The electron velocity spreads were also extracted from the simulation. They were taken at the slit exits; the velocity was extracted from the simulation in terms of a scatter plot. The results of the electron velocity were taken in the 'x' (horizontal) and 'y' (vertical) direction versus position. These plots were generated for 200 rays (100 rays each side). There results can also be found in Chapter 4.

3.5 Sensitivity Simulations

One of the simulation efforts involved studying the sensitivity of the electron injection into the device with the variation in the operating voltages of the emitter and pusher electrodes as well as the location of the pusher electrode below the emitter. This study was performed to find the best conditions that would guarantee the maximum number of rays exit the slit. These tests are important for design considerations. It is useful to know the sensitivity of the field emitters in terms of voltage and location parameters. Since all of the field emitters will not operate at the same voltage, this technique is used to study a range of voltages (ΔV) that still guarantees adequate operation. Similarly, this range can also be studied by changing the location of the pusher electrode.

In these simulations, the number of rays that reached the "collector" at the slit exit were counted, and the ratio of the collected rays to the total number of emitted rays

was calculated. All of the simulations were completed for a total of 200 rays (100 rays each side).

In order to analyze the sensitivity of the device, a number of tests were simulated: (a) varying pusher electrode voltage, (b) varying emitter voltage, and (c) varying the geometry of the pusher electrode. The simulations were then performed by varying one major parameter while holding others constant, then changing a second parameter while varying the first. For example, the pusher electrode voltage is fixed while the emitter voltage is varied; then the pusher voltage is changed, and the emitter voltage is again varied over the same range as before. This variation can be performed within Lorentz2E using the "parametric function." Example results of this set of simulations are presented in Chapter 4.

Table **3.1** summarizes the sensitivity simulation varied parameters.

Table 3.1: Lorentz2E Magnetron Model Sensitivity Simulations.

Major Parameter	Value of Major Parameter	Varied Parameter	Values of Varied Parameter
Pusher Voltage	-22.20 kV to -22.37 kV	Emitter Voltage	-22.20 kV to -25.0 kV
Emitter Voltage	-22.20 kV to -22.37 kV	Pusher Voltage	-22.20 kV to -25.0 kV
Pusher Geometry	1.70 um thick	Emitter Voltage	-22.20 kV to -25.0 kV
Pusher Voltage	-22.20 kV to -22.37 kV		
Pusher Geometry	1.70 um thick	Pusher Voltage	-22.20 kV to -25.0 kV
Emitter Voltage	-22.20 kV to -22.37 kV		
Pusher Geometry	0.4475 um thick	Emitter Voltage	-22.20 kV to -25.0 kV
Pusher Voltage	-22.20 kV to -22.37 kV		
Pusher Geometry	0.4475 um thick	Pusher Voltage	-22.20 kV to -25.0 kV
Emitter Voltage	-22.20 kV to -22.37 kV		

CHAPTER FOUR: LORENTZ2E SIMULATION RESULTS

4.1 Overview

This chapter presents the simulation results completed with the particle trajectory simulation code Lorentz2E. These simulations include energy distribution analysis, electron velocity analysis, and the sensitivity analysis. This study was completed to use as a reference for future work in the fabrication of the actual magnetron device with gated vacuum field emitter arrays placed in a shielded structure (slits). As was discussed in the previous chapter, the slits are used to protect the emitters from the harsh environment of the magnetron interaction space including ion back bombardment.

4.2 Energy Distribution Analysis

The energy distribution analysis was completed by developing histogram plots of the energy in the transverse direction (parallel to the slit opening) and the vertical direction (perpendicular to the slit opening). The sole electrode (see Figure 21) was set to -22.2 kV, the emitters at -22.3 kV, the pusher electrode at -22.3 kV, and the gate at -21.7 kV, with a magnetic field of 900 G. The current was fixed to 6.5mA per slit with a number of electron rays varying from 50 rays to 200 rays in total. A collector was placed at the exit of the slit to appropriately measure the corresponding values. The simulation with 200 rays total showed the best consistency. Figure 23 shows the transverse energy distribution for 200 electron rays. Figure 24 shows the vertical energy distribution for 200 electron rays (100 rays per side of the slit). The spread is nearly 50% at the exit, and the

use of 200 rays appears to be needed to get a well-defined distribution. The distribution energy plots were studied to find the best consistency and to see how many electron rays were needed to form a well-defined electron hub around the cathode. As shown in the results, 200 rays provided a consistent distribution.

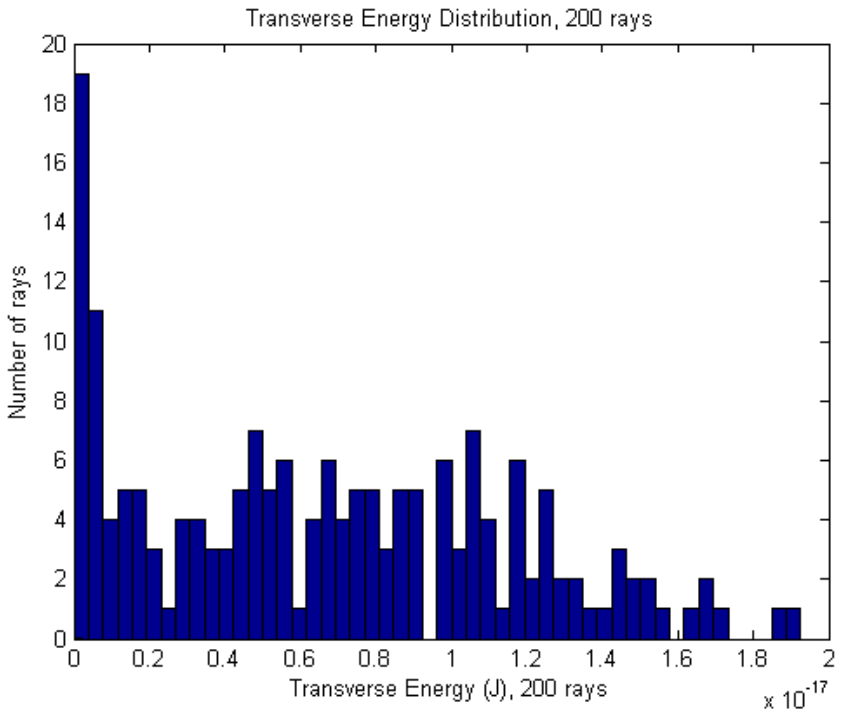

Figure 23: Transverse energy distribution from Lorentz2E for 200 electron rays.

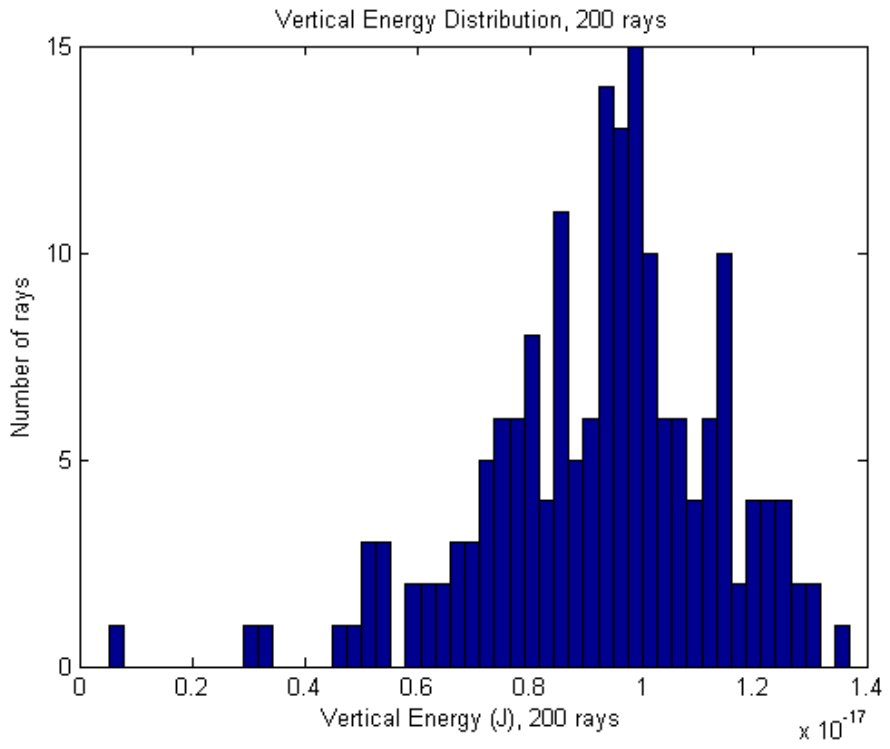

Figure 24: Vertical energy distribution from Lorentz2E for 200 electron rays.

4.3 Electron Velocity

In order to look at the velocity spread at the slit exits, the velocity was also extracted from the simulation in terms of a scatter plot. The previous simulation parameters were also used for this case. Figure 25 and Figure 26 show the results of the electron velocity in the 'x' (horizontal) and 'y' (vertical) direction versus position. These plots were generated for 200 rays (100 rays each side). Note the symmetry in Figure 25 as the rays come out of the slit (velocity in 'x' direction). This plot is showing the velocity from both sides of the slit (100 rays each side). Figure 26 (velocity in 'y' direction) shows the velocity versus position as the rays exit the slit and hit the collector plate. Both results are consistent with the electron trajectories observed in the simulation.

Such velocity plots could be used in future magnetron simulations for studying the effects of velocity spread on the device performance.

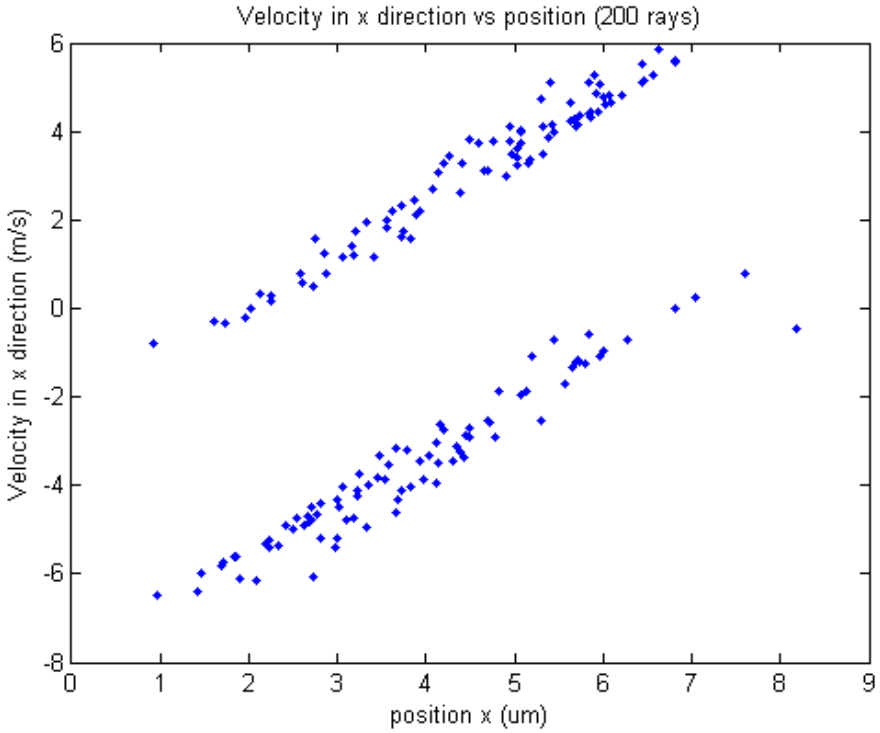

Figure 25: Velocity in the x-direction versus position for 200 electron rays.

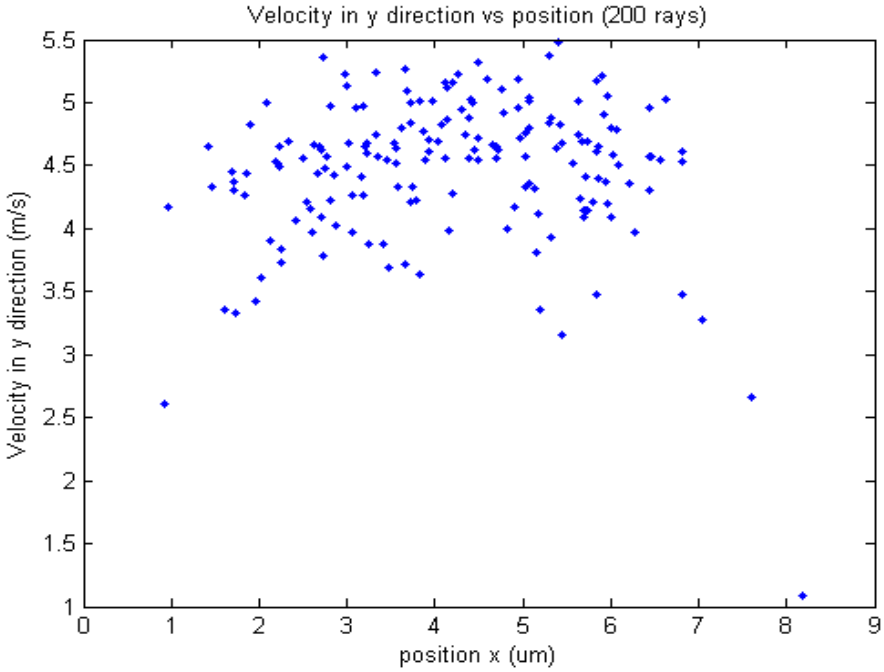

Figure 26: Velocity in the y-direction versus position for 200 electron rays.

4.4 Sensitivity Simulations

All the results shown in this section are for simulations using a total of 200 electron rays (100 rays per side). The Lorentz2E simulation can be run to include the space-charge effects of the individual rays on adjacent rays; however, the simulation will not allow both the ray charge and the simulated space-charge hub at the same time. Therefore, the results shown here do not include ray space charge simultaneously with the hub charge. However, simulations with the ray space charge and no hub charge have been run in previous work [12] and do not show significant effects on the ray trajectories at the slit exits at the current densities simulated. The electron density in the magnetron was found from previous work [12] simulations to have a peak value of $6x10^{10}$ cm^{-3}. The total charge in the volume was estimated to be $-1.35x10^{-8}$ C. To be conservative, a total volume charge of $-1.5x10^{-8}$ C was then used in the simulation to represent the charge hub [12]. The sensitivity simulations are summarized in Table 3.1 from Chapter 3. The results are summarized in three parts: (a) variation of the pusher electrode voltage, (b) variation of the emitter voltage, and (c) variation of the geometry (dimensions) of the pusher electrode.

(a) Varying Pusher Electrode Voltage

The pusher electrode voltage was set as the major parameter and held constant for each simulation. The emitter voltage was then varied using the parametric feature. The pusher voltage was varied from -22.20 kV to -22.37 kV for six cases, including the standard case [12]. The emitter voltage range was varied from -22.20 kV to -25.0 kV using 20 steps. These ranges were chosen to study the total number of rays that exit the slit. Figure 27 shows four examples of the ray trajectories for different emitter voltages.

As can be seen, the rays begin to strike the sole electrode walls and be lost or are turned back to the cathode depending upon the voltage. The simulations were repeated for four additional pusher electrode voltages. These results are presented in Appendix A.

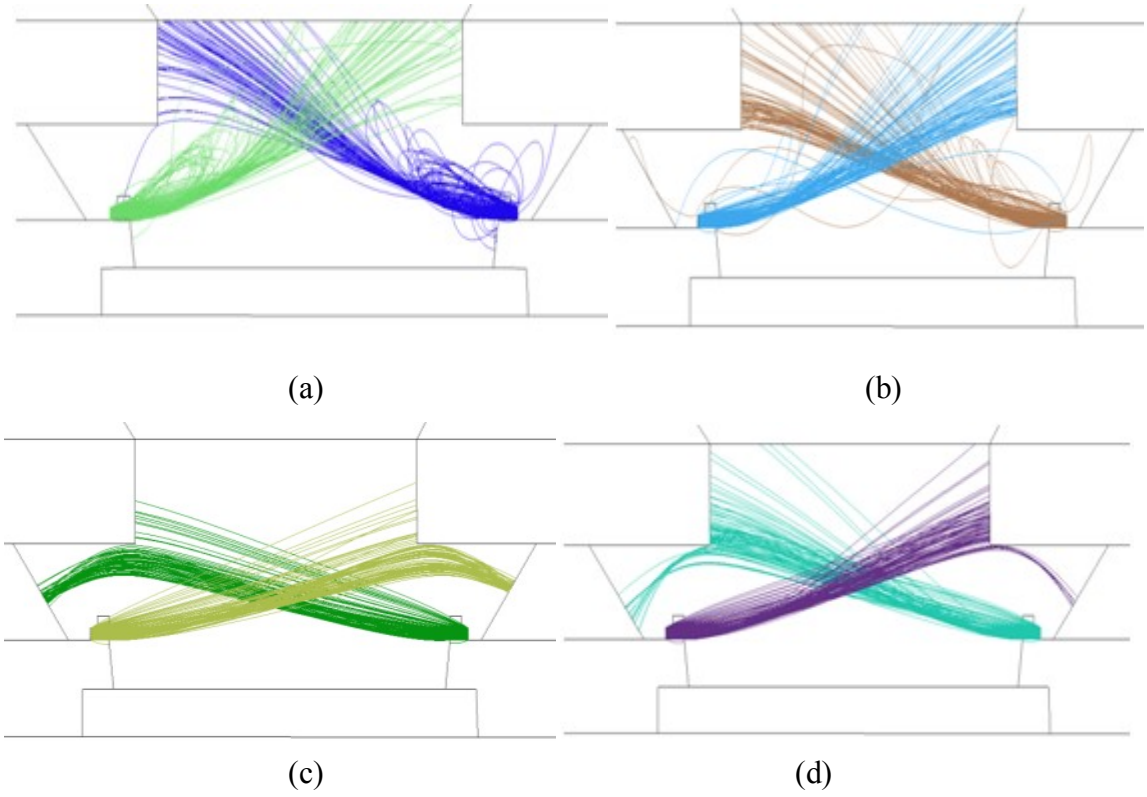

Figure 27: Pusher Electrode Voltage at -22.20 kV. Emitter Voltage at (a) -22.20kV, (b) -22.26 kV, (c) -22.34 kV, and (d) -22.5 kV.

Collector Current Analysis

A diagnostic was placed at the collector to measure the current (number of rays) that exit the slit and strike the collector. In Figure 28, a plot of the ratio of I_{out}/I_{in} vs. emitter voltage is graphed for the five pusher electrode cases. I_{out} and I_{in} are the collector current and emitter current, respectively. The threshold for the maximum current out was set equal or greater to 90% (this threshold was taken into account for the following cases). The threshold value was determined considering that there are a small percentage of rays that never exit the slit. This number of rays was calculated to be approximately

between 10-20 rays in total. This amount of emitter current loss (injected emitter current) was calculated and subtracted from the original injected emitter current. The voltage sensitivity (ΔV) was calculated for this threshold value. These results are shown in Table 4.1. This means that the resulting ΔV calculated for each pusher electrode value shows the sensitivity of the emitters to the change in parameters. A large ΔV indicates low sensitivity to voltage variation, which is desirable for device operation. In this set of simulations, the best case indicates a pusher electrode of -22.37 kV with a ΔV of 189.5 V.

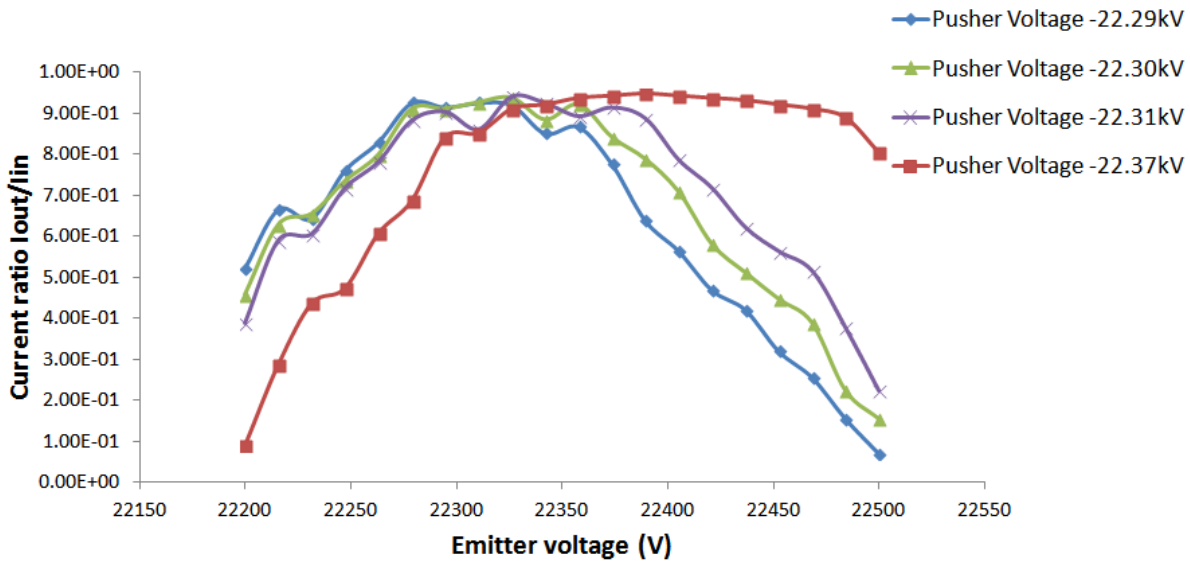

Figure 28: Emitter voltage versus current ratio.

Table 4.1: Voltage sensitivity analysis results for variations in the pusher electrode voltage.

Pusher electrode voltage (kV)	Maximum current out (%)	ΔV (V)
-22.29	97.2%	78.95
-22.30	98.3%	110.5
-22.31	98.3%	102.3
-22.37	98.3%	189.5

(b) Varying Emitter Voltage

The emitter voltage was set as a major parameter with the pusher electrode voltage varied by the parametric function. The emitter voltage was varied from -22.20 kV to -22.37 kV in six cases, including the standard case [12]. The pusher electrode voltage was varied from -22.20 kV to -25.0 kV using 20 steps. Figure 29 show the results of the ray trajectories at different pusher electrode voltages with a fixed emitter voltage of -22.20 kV. As seen in Figure 29, as the pusher voltage increases (pusher voltage > -22.34 kV), the electron trajectories are turned back, and they never hit the collector plate. Therefore, no rays will exit the slit.

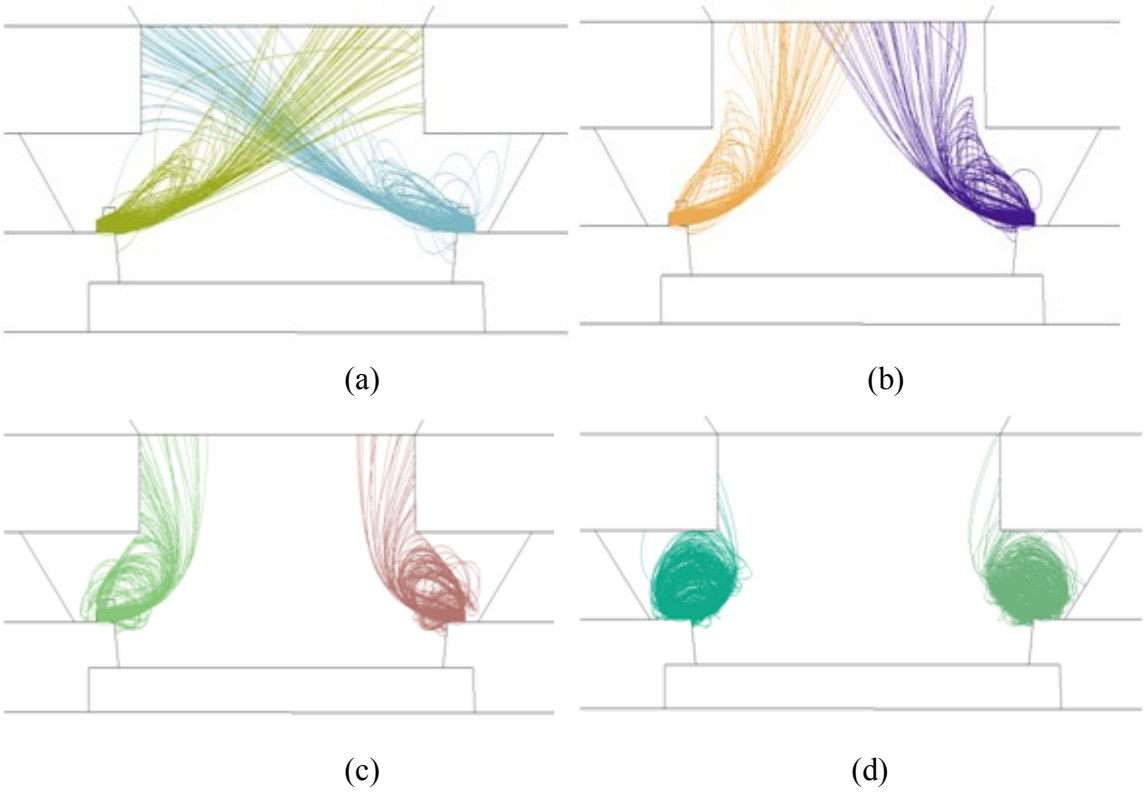

Figure 29: Emitter Voltage at -22.20 kV. Pusher Electrode Voltage at (a) -22.20 kV, (b) -22.26 kV, (c) -22.34 kV, and (d) -22.5 kV.

Collector Current Analysis

A diagnostic was placed at the collector to measure the number of rays that will hit the collector. In Figure 30, a plot of the pusher electrode voltage vs. the rate of I_{out}/I_{in} at different emitter voltages is presented. The voltage sensitivity (ΔV) was calculated and the best case results are presented in Table 4.2. In this case, the best case corresponds to the emitter voltage of -22.37 kV with a ΔV = 157.9. This case also guarantees 98% of the rays exit the slit.

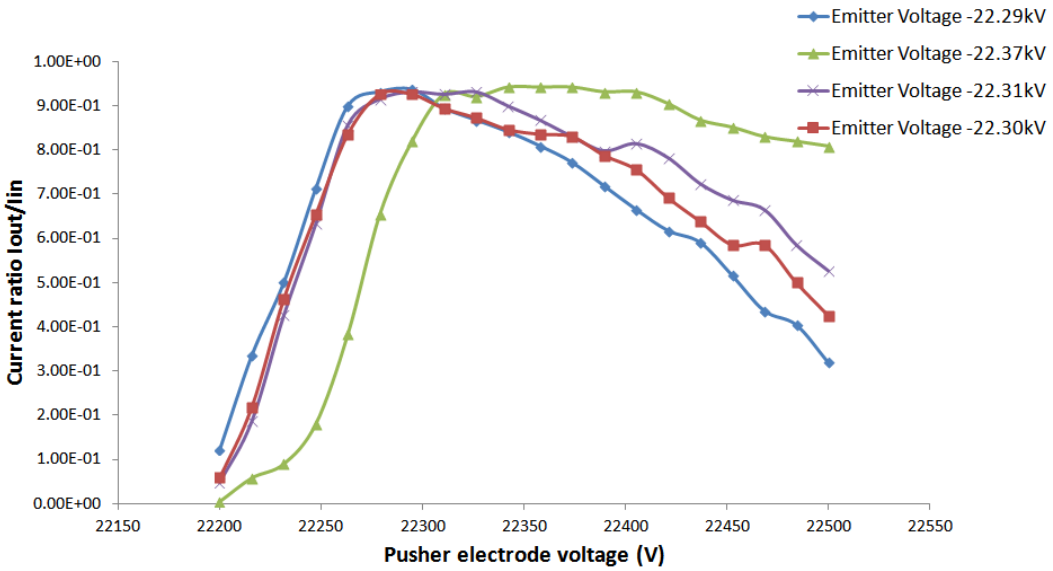

Figure 30: Pusher electrode voltage vs. current ratio.

Table 4.2: Voltage sensitivity analysis results for variations in the emitter voltage.

Emitter voltage (kV)	Maximum current out (%)	ΔV (V)
-22.26	91.1%	63.15
-22.29	97.2%	78.95
-22.30	97.8%	94.74
-22.31	97.2%	126.3
-22.37	98.3%	157.9

(c) Varying the Geometry

In this section, the simulation results are from the variation of the geometry of the pusher electrode; the simulations shown in Section (a) and (b) were repeated for each geometry. The pusher electrode has a thickness of 0.9795 μm from the reference model studied in [12]. This thickness was modified to its maximum and minimum to study the device sensitivity due to changing the geometry/dimensions. The simulations are performed for two different pusher electrode thicknesses: geometry (1) corresponds to a thickness of 1.70 μm and geometry (2) corresponds to a thickness of 0.4475 μm. Some examples of these results are presented in this section. The rest of the results are presented in Appendix A. Figure 31 and Figure 33 correspond to results using a pusher electrode thickness of 1.70 μm with a fixed pusher electrode voltage and a fixed emitter voltage, respectively. Figure 35 and Figure 37 correspond to the results of using a pusher electrode thickness of 0.4475 μm with a fixed pusher electrode voltage and a fixed emitter voltage, respectively. For each case, the extracted current ratio is plotted in Figure 32, Figure 34, Figure 36, and Figure 38. The sensitivity tables are also shown in Table 4.3, Table 4.4, Table 4.5, and Table 4.6. These results clearly show an improvement in the extracted current by moving the pusher electrode closer (vertically) to the emitter.

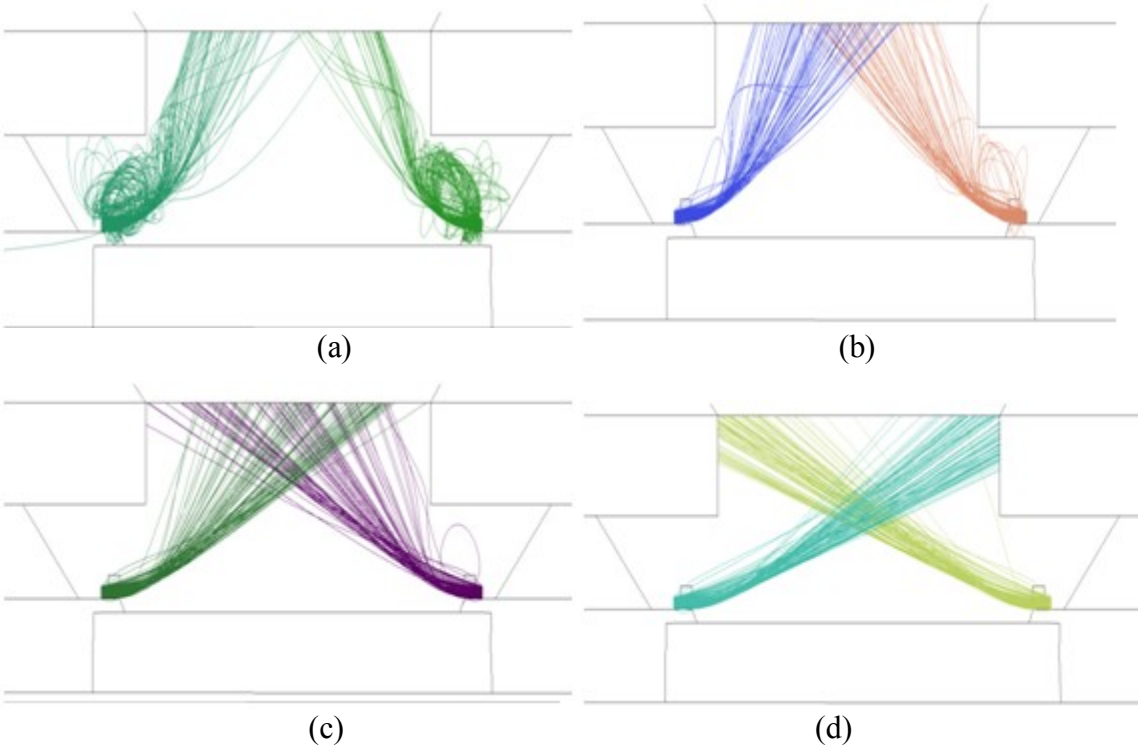

Figure 31: Pusher Electrode Voltage at -22.20 kV. Emitter Voltage at (a) -22.20 kV, (b) -22.26 kV, (c) -22.34 kV, and (d) -22.5 kV. Pusher Electrode Thickness of 1.70 µm.

Collector Current Analysis with Pusher Electrode Voltage Constant and Varying Emitter Voltage for Pusher Electrode Thickness of 1.70 µm

Results are shown in Table 4.3. Comparing these results with the standard case from [12] discussed in Chapter 3, it can be observed that by moving the pusher electrode higher (increasing thickness), the exit current increases.

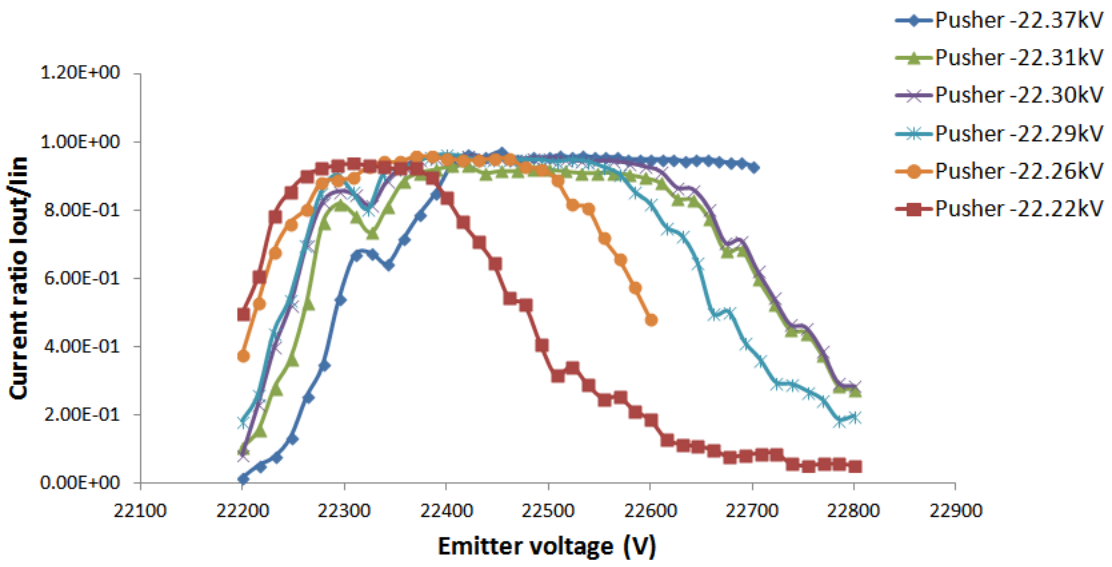

Figure 32: **Emitter voltage vs. current ratio at different pusher electrode voltages.**

Table 4.3: **Voltage sensitivity analysis results for variations in the pusher electrode voltage with a pusher electrode thickness of 1.70 µm.**

Pusher electrode voltage (kV)	Maximum current out (%)	ΔV (V)
-22.20	95.3%	79
-22.26	96.3%	126
-22.29	96.8%	189
-22.30	96.8%	222
-22.31	97.4%	173
-22.37	95.7%	190

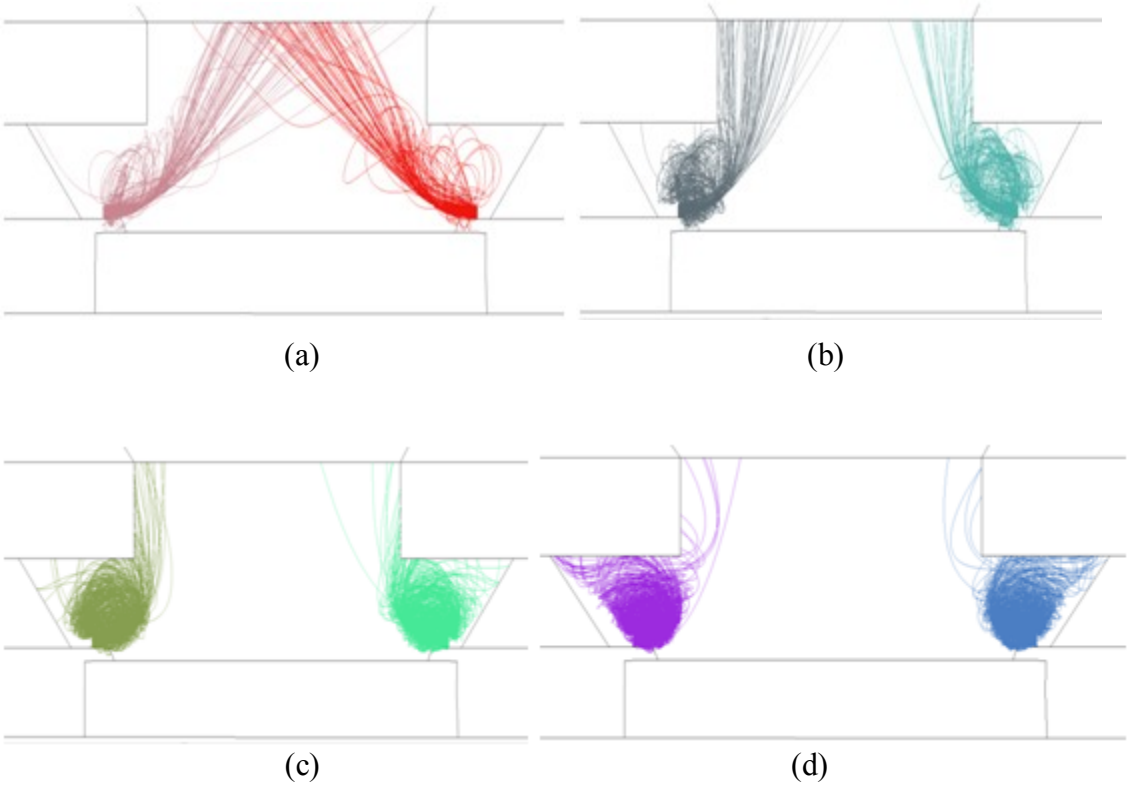

Figure 33: Emitter Voltage at -22.20 kV. Pusher Electrode Voltage at (a) -22.20 kV, (b) -22.26 kV, (c) -22.34 kV, and (d) -22.5 kV. Pusher Electrode Thickness of 1.70 µm.

Collector Current Analysis with Emitter Voltage Constant and Varying Pusher Electrode Voltage for a Pusher Electrode Thickness of 1.70 µm

Results are shown in Table 4.4. Comparing these results with the standard case from [12] discussed in Chapter 3, it can be observed that by moving the pusher electrode higher (increasing thickness), the exit current is increased. As observed in previous results, for pusher electrode voltages greater than -22.34 kV, the rays will not exit the slit.

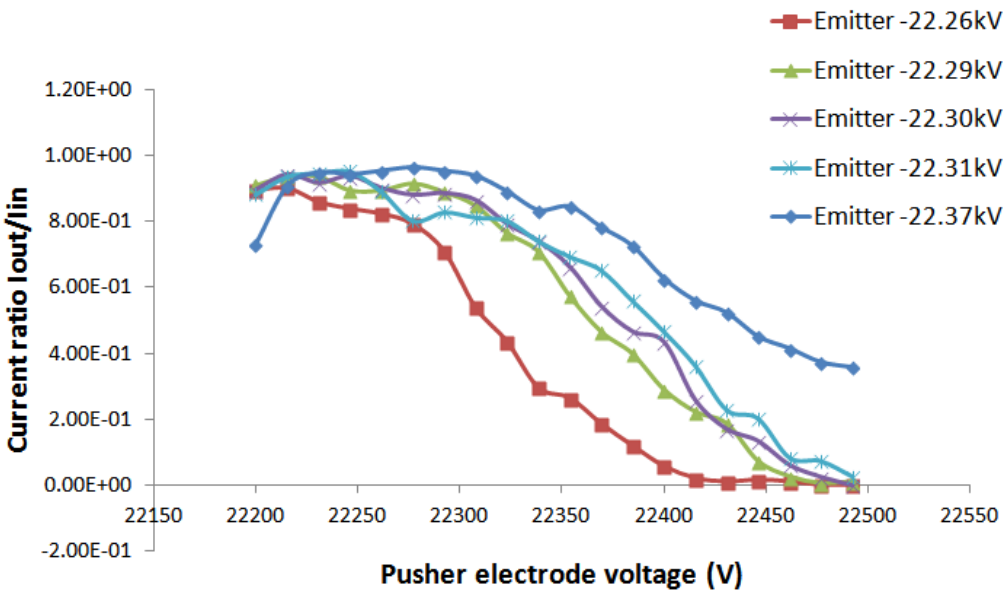

Figure 34: **Pusher electrode voltage vs. current ratio at different emitter voltages.**

Table 4.4: **Voltage sensitivity analysis results for variations in the emitter voltage with a pusher electrode thickness of 1.7 µm.**

Emitter voltage (kV)	Maximum current out (%)	ΔV (V)
-22.26	92.1%	113
-22.29	95.3%	90
-22.30	95.8%	90
-22.31	96.3%	90
-22.37	96.3%	110.5

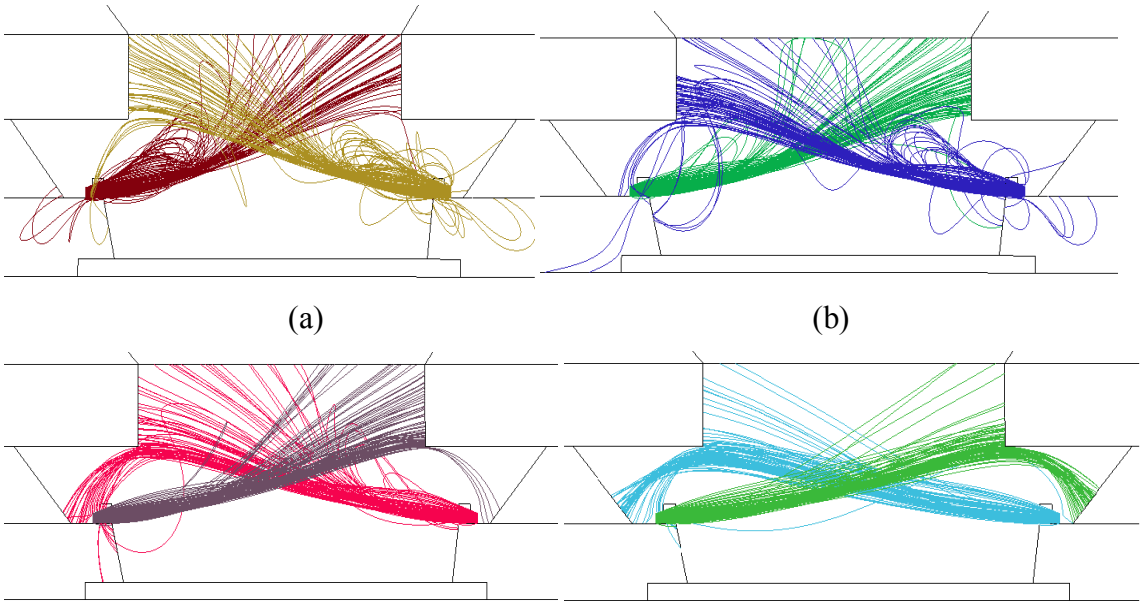

Figure 35: Pusher Electrode Voltage at -22.20 kV. Emitter Voltage at (a) -22.20 kV, (b) -22.26 kV, (c) -22.34 kV, and (d) -22.5 kV.

Collector Current Analysis with Pusher Electrode Voltage Constant and Varying Emitter Voltage for a Pusher Electrode Thickness of 0.4475 µm

The results for ΔV are presented in Table 4.5. Comparing these results with the standard case from [12] discussed in Chapter 3, it can be observed that by lowering (decreasing thickness) the pusher electrode, the amount of current out is improved just for few cases. Therefore, this change is not the most effective.

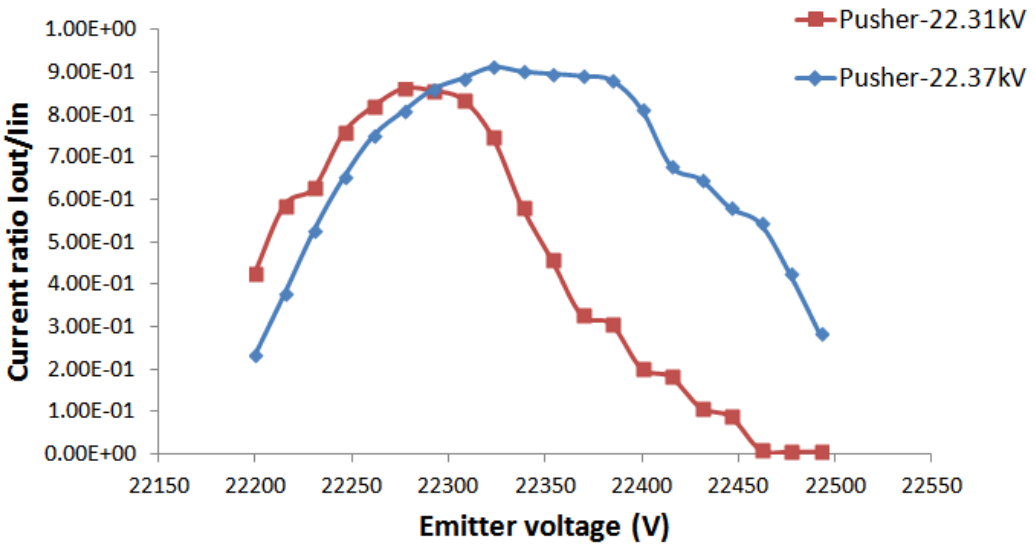

Figure 36: **Emitter voltage vs. current ratio at different pusher electrode voltages.**

Table 4.5: **Voltage sensitivity analysis results for variations in the pusher electrode voltage with a pusher electrode thickness of 0.4475 µm.**

Pusher electrode voltage (kV)	Maximum current out (%)	ΔV (V)
-22.31	92.2%	80
-22.37	98.9%	95

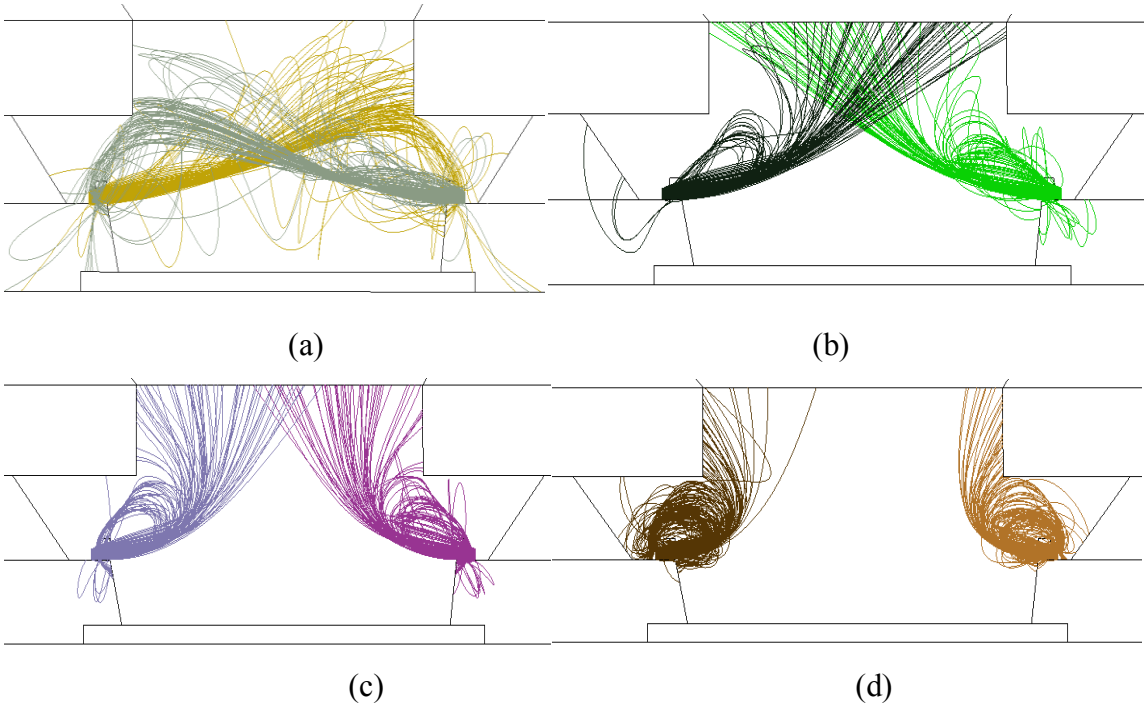

Figure 37: Emitter Voltage at -22.20 kV. Pusher Electrode Voltage at (a) -22.20 kV, (b) -22.26 kV, (c) -22.34 kV, and (d) -22.5 kV.

Collector Current Analysis with Emitter Voltage Constant and Varying Pusher Electrode Voltage for a Pusher Electrode Thickness of 0.4475 μm

The results for ΔV are presented in Table 4.6. The same results are observed as previous case. It can be observed that by lowering (decreasing thickness) the pusher electrode, the amount of current out is improved just for few cases. Therefore, this approach is also not the most effective.

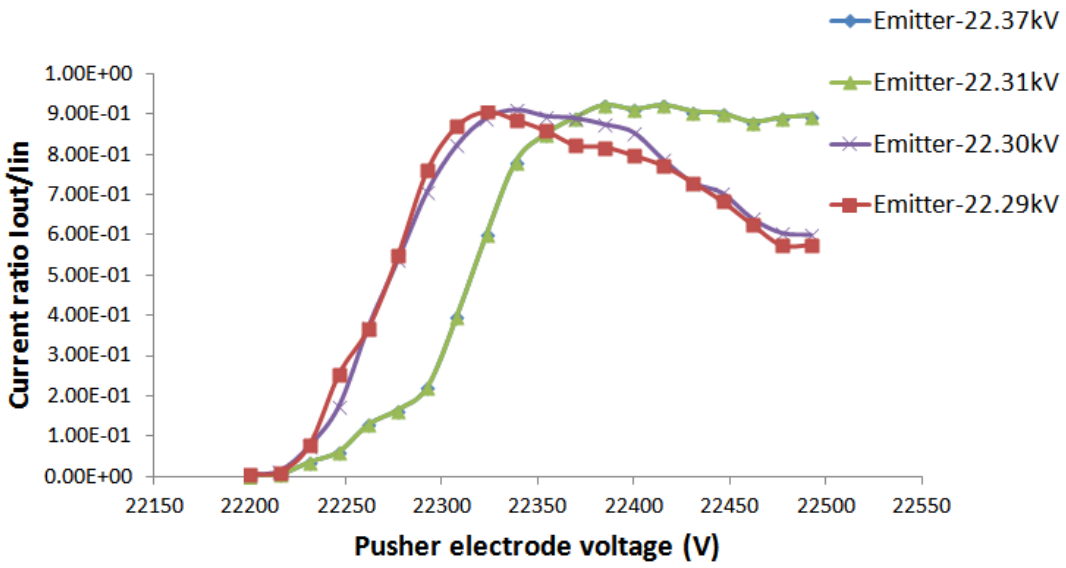

Figure 38: **Pusher electrode voltage vs. current ratio at different emitter voltages.**

Table 4.6: **Voltage sensitivity analysis results for variations in the emitter voltage with a pusher electrode thickness of 0.4475 µm.**

Emitter voltage (kV)	Maximum current out (%)	ΔV (V)
-22.29	97.2%	95
-22.30	97.8%	110.5
-22.31	96.1%	130
-22.37	98.9%	200

4.5 Summary of Results

The tests presented in this chapter are important for design considerations. It is useful to know the sensitivity of the field emitters in terms of voltage and location parameters. Since some of the field emitters will not operate at the same voltage, this technique is used to study a range of voltages (ΔV) that still guarantees adequate operation. Similarly, this range can also be studied by changing the location of the pusher electrode. From the sensitivity analysis, it was found that the maximum current out was

obtained by setting the pusher electrode and the emitter electrode to -22.37 kV, and the thickness of the pusher electrode remained the same at 0.85 μm (reference case [12]). The maximum current (maximum number of rays exit the slit) obtained was of 98.3% with a ΔV range of 160 to190 V. At the beginning of this research, these results were going to be used as input parameters for the VORPAL simulations; however, this was not completed, and the VORPAL model was developed based on previous work completed in ICEPIC [12]. Therefore, the results presented were left as a future activity for device modeling and fabrication.

CHAPTER FIVE: VORPAL SIMULATION SETUP

5.1 Overview

The primary research activity of this dissertation has been in the simulation of the new magnetron device using the modulated, addressable cathode concept. This chapter will give an overview of the particle-in-cell (PIC) code VORPAL used in this research; in addition, a discussion of the basic simulation aspects including the finite difference time domain (FDTD) technique, boundary conditions, the Dey-Mittra cut-cell algorithm, and the simulation setup will be discussed. Finally, the modeling procedures for the 2-D, ten-cavity, rising sun magnetron will be presented.

5.2 Software

Computational techniques are a critical component of the research and design process, which is important for electromagnetic engineering systems where solutions to Maxwell's equations in complex geometries are difficult to solve. Simulation provides many benefits such as numerous diagnostic capabilities and a controlled environment [75]. This work studies the performance of the rising sun magnetron with the faceted-shaped cathode using the particle-in-cell (PIC) code VORPAL 5.2 [22, 76, 77]. Other PIC codes have been used before to study magnetrons including QUICKSILVER [78], MAGIC [13, 24, 26, 29, 31, 35, 37, 47, 58, 79, 80], ICEPIC [12, 71], and others [24, 36, 41-44, 81]. This work dedicates a section of the study to compare results using two PIC

codes: ICEPIC (prior work) [12] and VORPAL. The rest of the simulation work has been carried out using only the PIC code VORPAL.

VORPAL is a particle-in-cell (PIC) code developed by Tech-X Corporation [22, 76] that can model complex electromagnetic structures and is capable of simulating one, two, or three dimensions. VORPAL is designed to run as both a serial code for single-processor workstations and as a parallel code for systems that support Message Passing Interface (MPI). Most of the simulations in this research were run using a single core processor workstation. Although the simulations completed in this research are in 2D, the concepts explained for the numerical methods used in VORPAL are described for general 3D models.

5.3 Finite Difference Time Domain (FDTD) Technique

VORPAL offers a unique combination of physical models to cover the entire range of plasma simulation problems. VORPAL uses the finite difference-time domain (FDTD) method to solve Maxwell's equations and includes an advanced technique known as cut-cell boundaries to allow accurate representation of curved geometries within a Cartesian grid: the Dey-Mittra algorithm [18, 82, 83].

The electromagnetic fields are solved by using the FDTD method constructed by Yee [84]. The FDTD method solves the curl equations 5.1 and 5.2, supposing divergence free initial conditions for the field strengths [85].

$$\nabla \times \mathbf{E} = -\mu_o \frac{\partial \mathbf{H}}{\partial t} \tag{5.1}$$

$$\nabla \times \mathbf{H} = \varepsilon_o \frac{\partial \mathbf{E}}{\partial t} + \mathbf{J} \tag{5.2}$$

where **E** and **H** are the electric and magnetic field vectors, μ_o and ε_o are the permeability and permittivity of free space, and **J** is the current density and is set to:

$$\mathbf{J} = \sigma \mathbf{E} \tag{5.3}$$

where σ is the conductivity.

Under the Cartesian coordinate system, these can be further expanded as:

$$\frac{\partial H_x}{\partial t} = -\frac{1}{\mu_o}\left(\frac{\partial E_z}{\partial y} - \frac{\partial E_y}{\partial z}\right) \tag{5.4}$$

$$\frac{\partial H_y}{\partial t} = -\frac{1}{\mu_o}\left(\frac{\partial E_x}{\partial z} - \frac{\partial E_z}{\partial x}\right) \tag{5.5}$$

$$\frac{\partial H_z}{\partial t} = -\frac{1}{\mu_o}\left(\frac{\partial E_y}{\partial x} - \frac{\partial E_x}{\partial y}\right) \tag{5.6}$$

$$\frac{\partial E_x}{\partial t} = \frac{1}{\varepsilon_o}\left(\frac{\partial H_z}{\partial y} - \frac{\partial H_y}{\partial z} - \sigma E_x\right) \tag{5.7}$$

$$\frac{\partial E_y}{\partial t} = \frac{1}{\varepsilon_o}\left(\frac{\partial H_x}{\partial z} - \frac{\partial H_z}{\partial x} - \sigma E_y\right) \tag{5.8}$$

$$\frac{\partial E_z}{\partial t} = \frac{1}{\varepsilon_o}\left(\frac{\partial H_y}{\partial x} - \frac{\partial H_x}{\partial y} - \sigma E_z\right) \tag{5.9}$$

In Yee's scheme [84], the model is first divided into many small cubes. For simplicity, the cubes are assumed to be the same size. The edges of each cube will form the three-dimensional space grid. Introducing the notation:

$$E^n_{x(i,j,k)} = E_x\left(i\Delta x, j\Delta y, k\Delta z, n\Delta t\right) \tag{5.10}$$

and so on for E_y, E_z, H_x, H_y, and H_z components, where Δt is the time increment and Δx, Δy, and Δz are the spatial discretization. Reducing 5.10 to a 2D grid model:

$$E^n_{x(i,j)} = E_x\left(i\Delta x, j\Delta y, n\Delta t\right) \tag{5.11}$$

and so on for E_y, and H_z components, where Δt is the time increment and Δx, and Δy are the spatial discretization, respectively.

The method starts with the definition of a generally rectangular mesh for the electric field and another staggered grid for the magnetic field in the computational domain. The building blocks of this mesh are the Yee-cells. The basic setup of the Yee electromagnetic field is illustrated in Figure 39. In this setup, electric fields are located on the edges of grid cells, and magnetic fields are located on the faces of the cell surfaces.

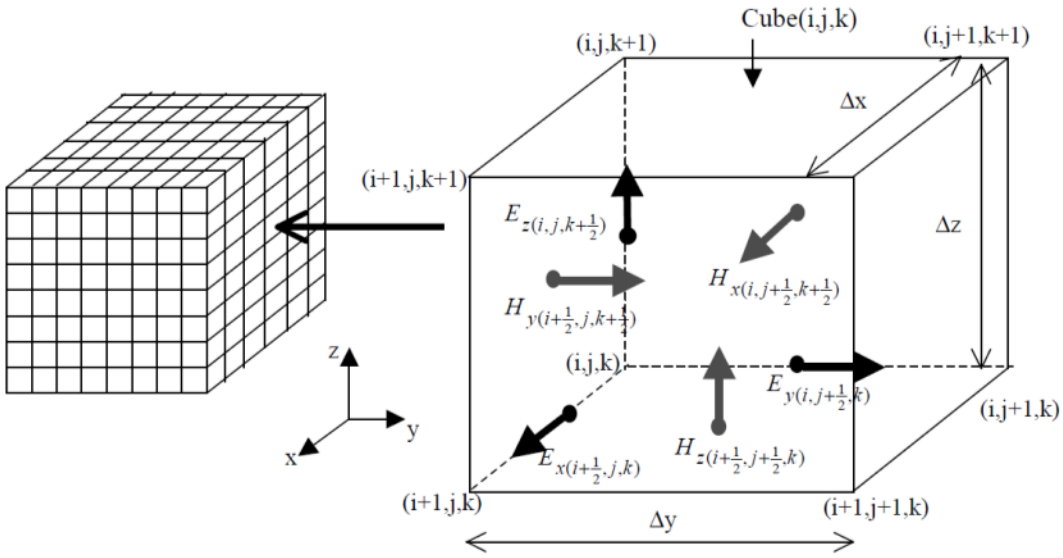

Figure 39: Yee model for placing fields on the grid [86].

Figure 40 illustrates the basic flow of implementing Yee's FDTD scheme on a computer, following these steps: (1) the electric field and magnetic field components are initialized to zero as well as all the sources, (2) the new electric field component values are computed at interior cells, followed by computing the electric field component values at the boundary, (3) the new magnetic field component values are computed, (4) if the

maximum number of time-steps is reached, the algorithm will stop; otherwise, it will restart the process.

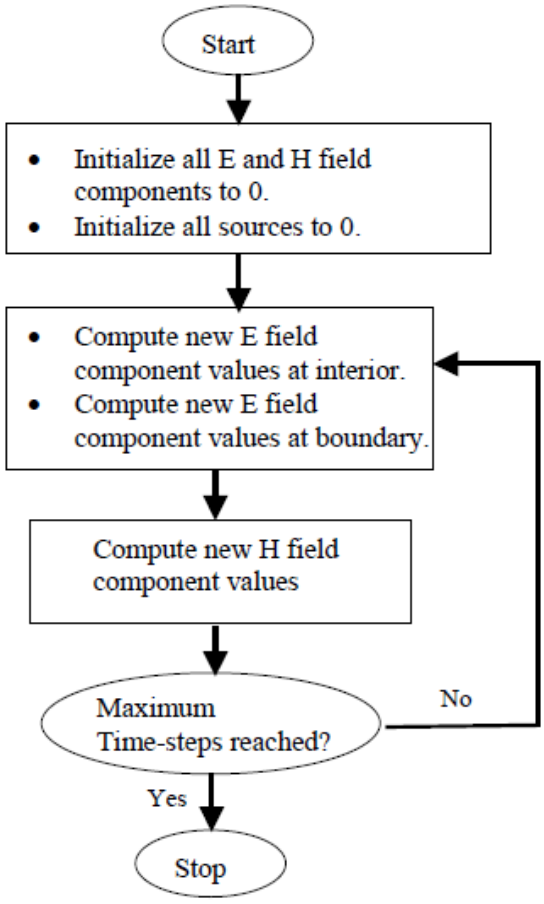

Figure 40: Basic flow for implementation of Yee FDTD scheme without including particle injection [86].

5.4 Numerical Stability

The numerical algorithm for Maxwell's curl equations requires that the time increment, Δt, have a specific bound relative to the spatial discretization Δx, Δy, and Δz. In an electromagnetic simulation, the duration of the time step must not be longer than the time required for light to cross a cell. To ensure this, the time increment has to obey the Courant-Freidrichs-Lewy (CFL) stability criterion [87].

$$\Delta t < \frac{1}{c\sqrt{\frac{1}{\Delta x^2}+\frac{1}{\Delta y^2}+\frac{1}{\Delta z^2}}} \tag{5.12}$$

where c is:

$$c = \frac{1}{\sqrt{\mu_o \varepsilon_o}} \tag{5.13}$$

In 2D the CFL stability criterion is reduced to:

$$\Delta t < \frac{1}{c\sqrt{\frac{1}{\Delta x^2}+\frac{1}{\Delta y^2}}} \tag{5.14}$$

If the Courant condition is not followed, the simulation will not be stable [18, 75].

VORPAL uses a fraction of the Courant time step for which the simulation will be stable when using the Dey-Mittra boundary algorithm with the Yee method. For example, if this fraction is equal to 0.25, then the time step for the simulation must be 25% of the Courant time step [18]. Note that for this research the electron source is modulated temporally at the operating frequency of the magnetron. To ensure that this modulation is consistent over time steps, the time step size was set to an integer fraction of the magnetron RF period while still satisfying the stability condition.

5.5 Boundary Conditions

In a typical simulation, boundary conditions are set at selected surfaces, and they may be set throughout a volume. In VORPAL, they can be specified as [18]:

Wave launcher to specify the characteristics of a wave.

Conductor to specify a perfectly conducting metal wall. Perfect conductors in VORPAL are imagined to have an infinite supply of electrons to cancel any charge buildup.

If an electromagnetic boundary condition is not specified explicitly, the default value is a conductor boundary condition. Simulations can deal with curved boundaries; for this, VORPAL implements either the stair-step approximation of the curved surface or the Dey-Mittra cut cell method.

5.6 Dey-Mittra Cut Cell Algorithm

Curved boundaries are often modeled with stair-step boundaries, which are known to be first order accurate [88]. To overcome this limitation, VORPAL implements the Dey-Mittra [89] cut-cell boundary algorithm, which is known to be second order accurate [82, 83].

The Dey-Mittra algorithm uses a loop integral along the edges of each cell face by using the Faraday update of the magnetic field on the standard Yee mesh. The loop integral is limited to the edges that are completely or partially inside the boundary if the cell is cut by the boundary. If the edges are not completely inside the boundary, their lengths are reduced by the suitable amount. The area used in the integral is also reduced by the area inside the boundary [83]. The time step must obey the Courant condition for the smallest cut cell on the boundary to maintain stability. To keep the time step at a reasonable value, VORPAL introduces an input parameter, which gives the fraction of the Courant step that is allowed. Then, the code checks all the cut cells to see if they would be stable for the first time step. If the cut cells are not stable, they will be discarded [83].

VORPAL also implements area borrowing techniques, which give second order accuracy while allowing the full Courant time step. This borrowing is achieved by adding contributions from neighboring cells for the field update. In effect, area is borrowed from neighboring cells to maintain stability. There are different 'area borrowing' methods, and they vary depending on the cut cells receiving or donating this area [83]. The area borrowing algorithm implemented in VORPAL is the Zagorodnov [90] method, which borrows area from neighboring cells if the cell is cut by more than half [83]. Figure 41 shows an example of the Zagorodnov area borrowing method. As shown in the image, only the area in white will be considered for the calculation. Since in some cells only a part of it is inside the boundary (white area), this portion of the area is 'borrowed' and then added to the calculation for the field update. Therefore, only the area inside the boundary is considered. For example, the highlighted portions in the image are fractions of area borrowed by the cells that are cut by more than half. The arrows indicate the fraction of area borrowed by the adjacent cell. The parameters l_a, l_b, l_c, and l_d are the lengths corresponding to the sides of the area fractions.

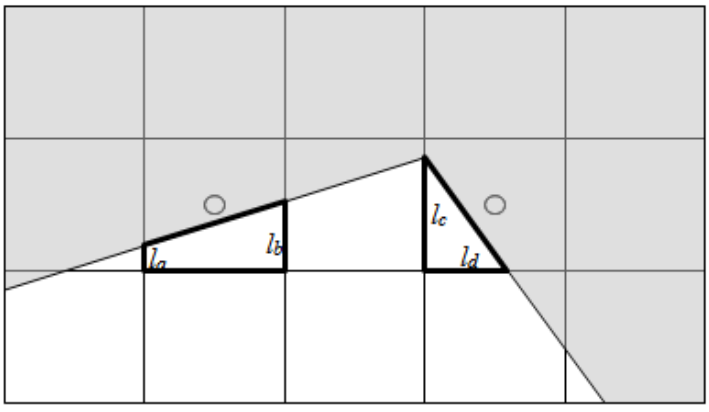

Figure 41: Area fractions borrowed by cut cells in the Zagorodnov boundary algorithm[82].

5.7 Integration of the Equations of Motion

Particles in VORPAL follow the Boris-Push Lorentz force equation [18]:

$$\frac{\partial \gamma m v}{\partial t} = q\left(\mathbf{E} + v \times \mathbf{B}\right) \tag{5.15}$$

where m, q, and v are the mass, charge, and velocity of electron, respectively. γ is the relativistic factor,

$$\gamma = \frac{1}{\sqrt{1 - \frac{v^2}{c^2}}} \tag{5.16}$$

where c is the speed of light and v is the electron velocity.

The particles are represented by species [22]. A species is a collection of macro-particles (each macro-particle is comprised of a number of physical particles) that allows VORPAL to represent a group of physical particles with a given charge, velocity, and spatial distribution. Even though physical particles are modeled as macro-particles using species, their charge is evenly distributed [18]. For example, a macro-particle can be represented as a cloud of physical particles; charge is distributed evenly through this cloud. By default, VORPAL initializes particles with zero velocity. For variably-weighted particles, VORPAL tracks the weight as an additional internal variable [18].

The particle boundary conditions also use either cut-cell or the stair-step method. No charge is built up at the boundary [18].

5.8 Modeling of a 2-D Ten Cavity Rising Sun Magnetron

In this research, VORPAL is used to model a ten-cavity rising sun magnetron [12] in 2-D. The geometry shown in Figure 42 and Figure 43 is that of a two dimensional

rising sun magnetron with two cathode geometries: cylindrical and faceted. As seen in Figure 42 and Table 5.1, the radius of the cylindrical cathode is 1.0 cm, and the inner radius of the anode is 2.24 cm. Long cavities have an outer radius of 10.0 cm and opening angle of 10°. Short cavities have an outer radius of 6.0 cm and opening angle of 10°. The faceted cathode with five facets has a facet width of 1.18 cm and a vertex angle orientation of $3\pi/2$ radians. The vertex angle (see Figure 43) is a parameter that can be varied in the simulation, allowing cathode rotation. The ten-sided cathode has a facet width of 0.618 cm. These geometrical properties control the spectrum and, thus, the operating frequency of the cavity, which is 960 MHz for the cylindrical cathode and 957 MHz for the faceted cathodes.

One long cavity is loaded with a damping parameter, used in VORPAL, with a value of Nu_loading = 200.0 x 10^6 /s to model a coupler to the magnetron. The cavity is loaded as if its volume were resistive (e.g., there is effectively an ohmic current $J=\sigma E$, where σ is tuned to give the desired quality factor Q). This loading parameter may be used to tune the quality factor, Q, of the magnetron, which is proportional to 1/ Nu_loading.

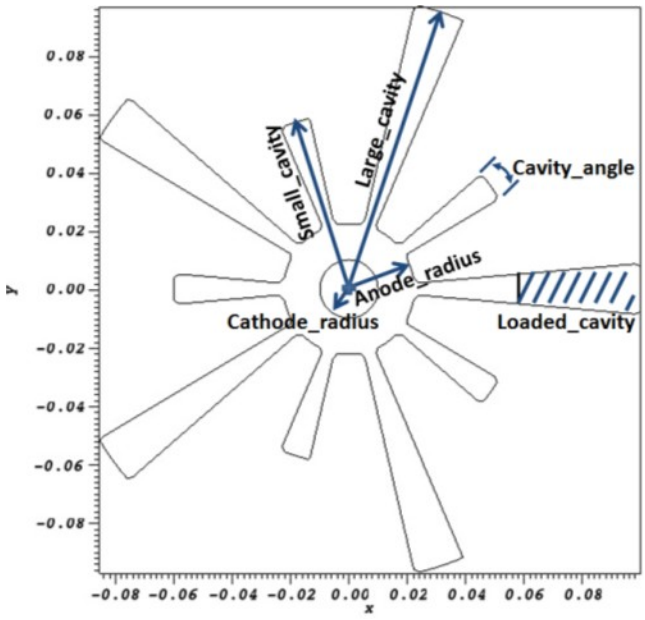

Figure 42: Cylindrical cathode used in VORPAL simulations.

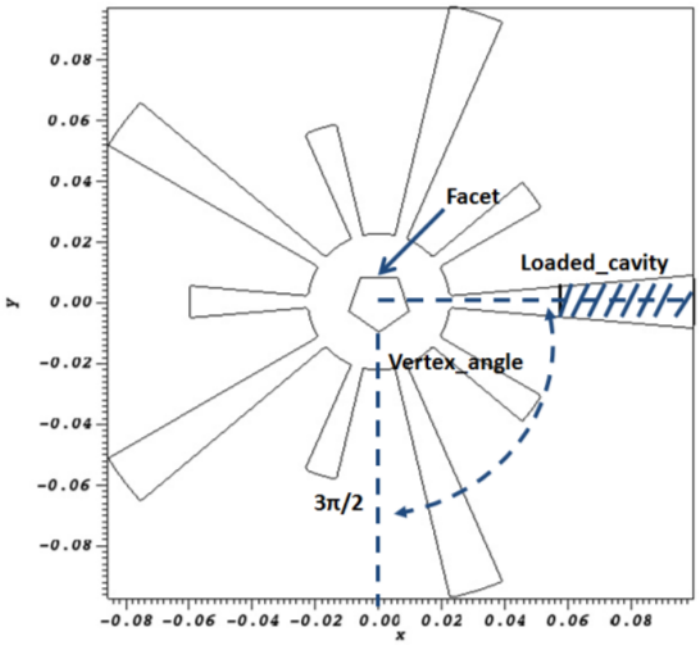

Figure 43: Five-sided faceted cathode used in VORPAL simulations.

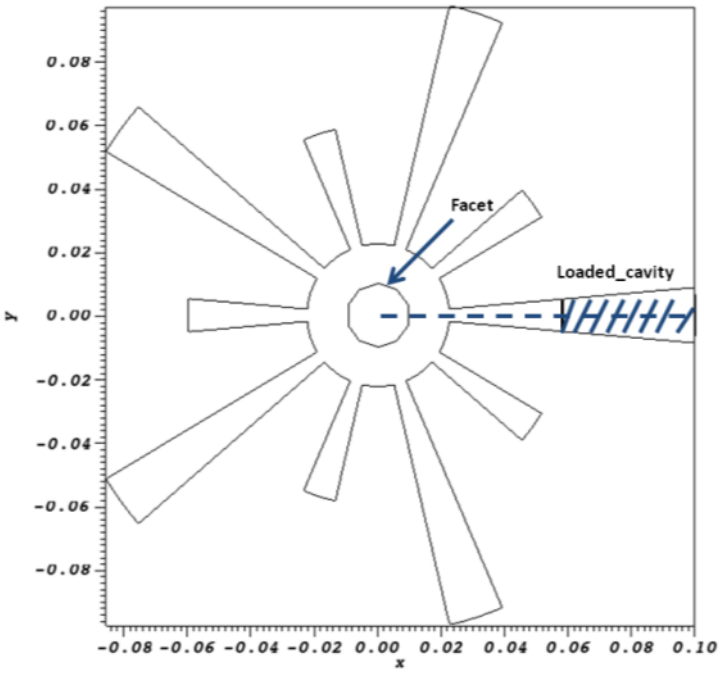

Figure 44: Ten-sided faceted cathode used in VORPAL simulations.

Table 5.1: Rising sun magnetron dimensions for cylindrical, five and ten-sided faceted cathodes.

Cathode radius (cm)	Anode radius (cm)	Facet width (cm)		Small cavity outer radius (cm)	Large cavity outer radius (cm)	Cavity angle (degrees)
		Pentagon	Decagon			
1.0	2.24	1.18	0.618	6.0	10.0	10

5.9 Simulation Setup and Procedures

For this research, a typical VORPAL simulation is set up with a grid of 102x102 cells with a length of 20.4 cm in the x-direction and 20.4 cm in the y-direction. However, for the 10-sided case, the grid must be increased to 202x202 to account for the needed spatial resolution of the finer facets and the emitter sections. The time step size is typically 2.3e-12 s, and the simulation total run time is 600 ns. For the modulated current

case, the simulation run time is shorter, typically 150 ns, and the time step size is an integer fraction of the RF period. So for the 957 MHz operating frequency, the time step is set to an integer fraction of the RF period, τ_{rf}/N, where τ_{rf} is the RF period and N is the number of emitters turned ON per RF period. The particles are controlled by the number of macroparticles per cell per step; this variable is set to 10 macroparticles per cell per step for all simulations, where 1 macroparticle is 10^6 particles.

The important simulation diagnostics used in this research are as follows:

Startup time: the time when oscillations start to take place (spoke formation). This parameter helps to confirm when the magnetron starts oscillating. The startup time can be observed by plotting the frequency of the cavity voltage versus time. The spoke formation is also used in conjunction with this plot to estimate the startup of the magnetron. For example, Figure 45 shows the start up time for a typical magnetron run in VORPAL. In this case, the frequency shows what modes were dominant during startup and after. It is clear from the figure that there is a 650 MHz mode dominant during startup, until it switches to the π-mode at the frequency of operation of 960 MHz, where the stabilization of the oscillations can be observed.

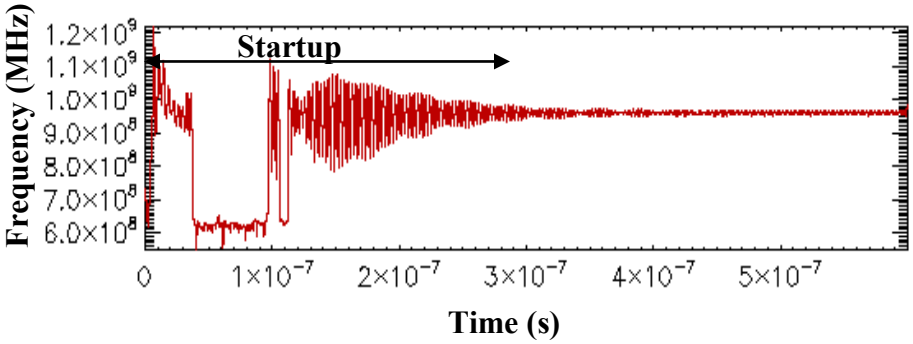

Figure 45: Startup time of a typical magnetron simulation in VORPAL for the cylindrical cathode (V_{ca} = -26.0 kV, B = 0.12 T, and J_a = 500 A/m). Stable oscillation is observed around 300 ns.

Total Emitted Current: This diagnostic measures the total emitted average current of the device. Because this is a 2-D simulation, a linear current density (A/m) is used for this purpose. In this simulation model, the anode structure is set as a collector; the magnetic field is set to zero; and the simulation is run for the total run period, typically 600 ns for the reference case and 150 ns for the current modulated case. Particles are collected on the anode, and then the average emitted current is determined. This diagnostic is used to look for timing errors in the modulation simulations and to make certain that the average emitted current is correct. Figure 46 shows an example of the average linear current density versus time for the cylindrical cathode geometry. This is a typical VORPAL simulation with an emitted linear current density of 500 A/m and a total simulation run of 600 ns.

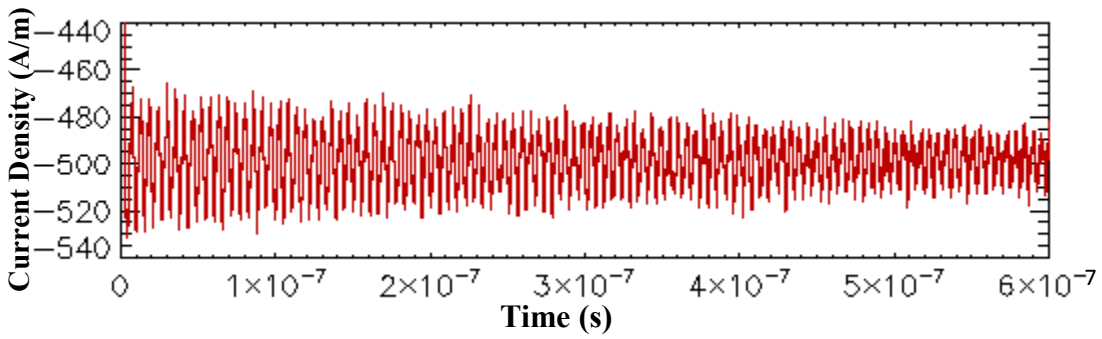

Figure 46: Linear current density vs. time for the cylindrical cathode, typical VORPAL simulation with B field = 0.

Anode Current: This diagnostic measures the total average anode current while the device is in operation. It is used to determine startup of oscillation and to look for stability issues in the oscillations. Note that the anode current density does not become completely stable until after 350 ns. It is also useful for calculating the input power density of the device. For example, Figure 47 shows a typical VORPAL simulation result of the anode linear current density for the cylindrical cathode during operation; this value

averages to approximately 150 A/m. The cathode-anode voltage for this example is 26 kV, which gives an input power of 3.2 MW/m for this case.

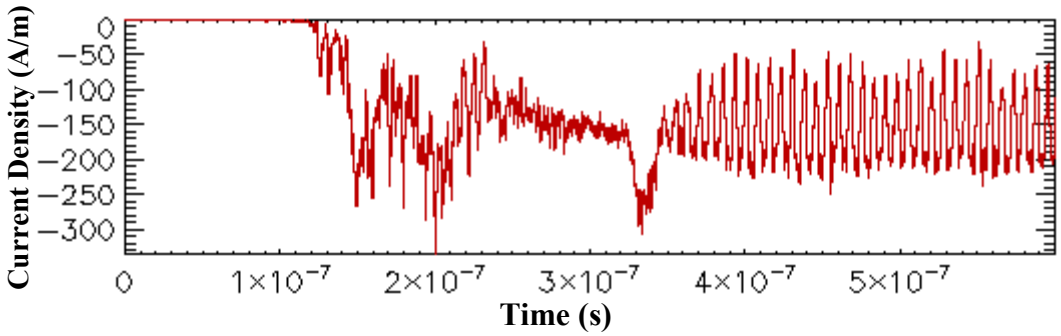

Figure 47: Anode linear current density vs. time during device operation for the cylindrical cathode, typical VORPAL simulation.

Cavity Power: This diagnostic is used to estimate the power at the loaded cavity. There is an absorber in the cavity to measure the loaded cavity power. Figure 48 shows the rising sun magnetron geometry highlighting the loaded cavity. There is no internal loss associated with the structure. There is a loading parameter, refer to as Nu_loading, that is used to tune the quality factor, Q, of the magnetron. Since this simulation is 2D, this power at the loaded cavity is not a true output power from an output port. A meaningful calculation of the device output is not feasible for the 2D simulations. However, it was used to estimate the efficiency of the magnetron. Therefore, this cavity power is only used for reference and to give an estimation of the power absorbed by the dummy load. For example, for the case shown in the previous section, the linear power density at the loaded cavity was calculated to be 3.9 MW/m, and with an input power density of 3.2 MW/m gives an efficiency of 82%.

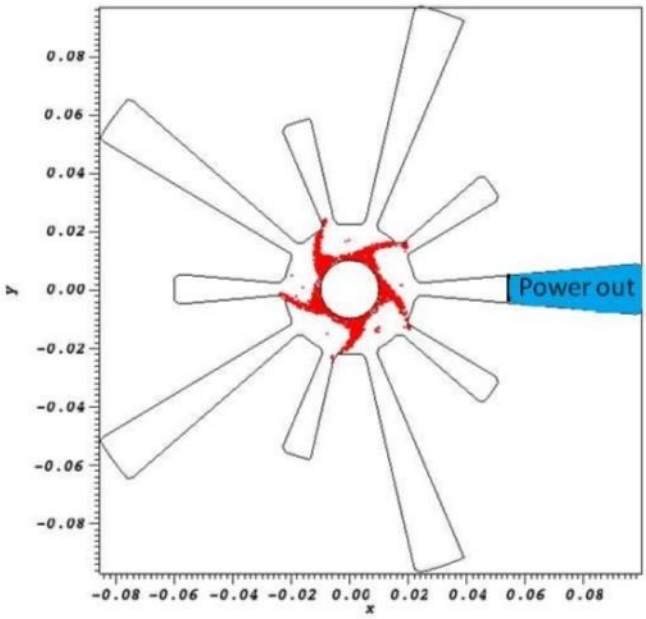

Figure 48: Rising sun magnetron cavity power diagnostic location.

Phase: This diagnostic will help to determine at what relative phase the magnetron is oscillating. Visually, it can be determined by the spoke locations, and the corresponding time step can be found in the simulation. Figure 49 shows an example of the magnetron oscillations (spoke formation) with a selected reference cavity. Measurement of the phase will also be performed by using a correlation between a reference case and the phase changed case to calculate the phase difference from the RF B_z field.

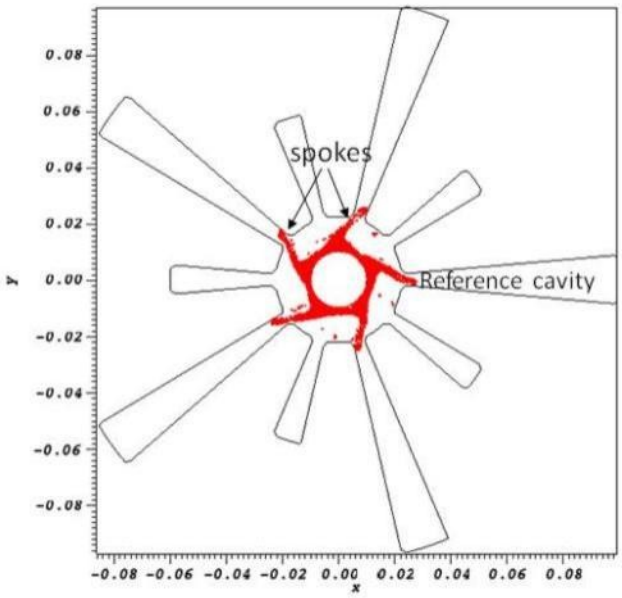

Figure 49: Rising sun magnetron spoke formation.

The VORPAL modeling for this work consists of two parts. The first part of the modeling studies the magnetron performance with the cylindrical and faceted cathodes (five and ten-sided) using a continuous current source. The cylindrical cathode model is used as the reference case. These results (for all three cathode geometries) are used to compare with previous work completed by Browning et al. in the particle-in-cell (PIC) code ICEPIC [12]. The second part of the modeling focuses on the faceted cathodes and the effects on the magnetron performance using discrete (addressable), modulated current sources. A key part of the research is to make incremental changes in the model while ensuring the model is still operating correctly. After creating stable models, the discrete sources are modulated temporally in an attempt to control the oscillations, including start up time and phase. It is important to note that the model studied in this work and the ICEPIC model used for comparison does not require external RF excitation to start oscillation as it is sometimes needed in strapped magnetron simulations.

5.10 Rising Sun Magnetron Model with a Continuous Current Source

There are four run types developed for the cathode geometries. These runs are completed to study the device operation. They consist of (a) the mode spectrum: to study the possible frequencies where the device will have oscillating modes; (b) calibration of the π-mode and the quality factor: the simulation can be tuned to the desired frequency of operation and a plot of the RF B field can be obtained to check for the π mode; (c) calibrating the DC voltage: this run is used to determine the voltage parameter that will support the desired operating mode; and (d) the run with particles: after the model is completely calibrated, a complete run with particles is performed, and then all the diagnostics can be checked. These four simulation runs are discussed in more detail as follows:

The Mode Spectrum:

This simulation is used to predict the magnetron operating frequency. The Fast Fourier Transform (FFT) of the voltage at one of the cavities is analyzed to find the frequency of operation. Figure 50 shows the mode spectrum for a typical run in VORPAL. The Fast Fourier Transform (FFT) of the voltage across the cavity is plotted versus frequency (in Hz). This result indicates that the magnetron is expected to have oscillating modes near 650 MHz and 960 MHz.

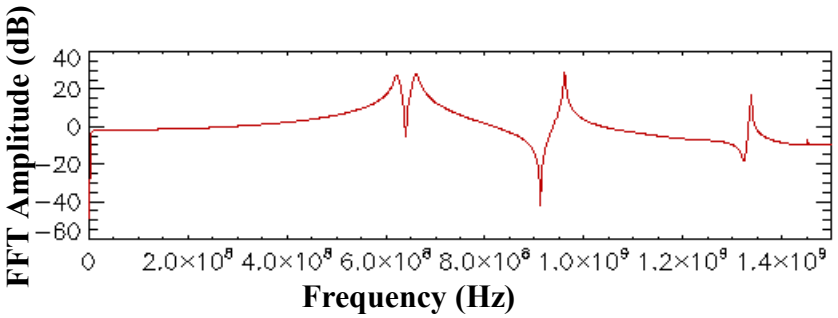

Figure 50: Fast Fourier Transform (FFT) of the cavity voltage versus frequency.

Calibration of the π-mode and the Quality Factor:

In this run, the magnetron geometry can be modified to obtain the desired operating frequency. This simulation can also be used to tune the load and to choose the desirable quality factor. The quality factor is the ratio of energy stored to the energy lost by dissipation. In resonant cavities, high quality factors are usually desired.

Figure 51 shows an example for a typical run. The Fast Fourier Transform (FFT) of the voltage across the cavity is plotted versus frequency. It is observed that after tuning the device, the 960 MHz mode is more pronounced (π mode) than in the previous run, but the 650 MHz mode remains. If another operating frequency is desired, the geometry of the magnetron can be changed to iteratively tune this spectrum.

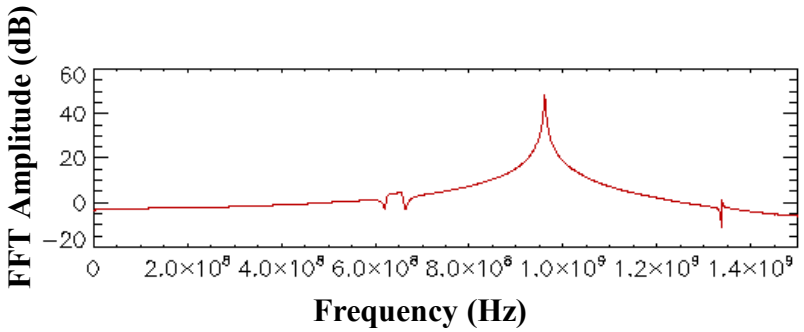

Figure 51: Fast Fourier Transform (FFT) of the cavity voltage versus frequency.

Another parameter that may be tuned is the magnetron quality factor, Q. It is expected that 1/Q will vary as Nu_loading (loading cavity factor), but it is also possible to determine the Q using VORPAL. Using a short no-particle run, the decay of the cavity voltage signal (Figure 52a) and its amplitude (Figure52b) can be used to determine Q by using the following equation [91, 92]:

$$V(t) = V(t_O)e^{-\frac{\omega t}{2Q}} \tag{5.17}$$

where *V(t)* is the cavity voltage, and ω is the angular resonant frequency ($\omega=2\pi f$). Therefore, Q can be expressed as:

$$Q = \frac{\frac{1}{2}\omega\Delta t}{\ln\left[\frac{V(t_1)}{V(t_2)}\right]} \tag{5.18}$$

where $\Delta t = t_2 - t_1$

For example, from Figure 53(b) $t_1 = 0$ ns and $t_2 = 20$ ns, $V(t_1) = 2610$ V and $V(t_2) = 2250$ V; Q is then calculated as

$$Q = (\pi)(0.96e9)(20e\text{-}9)\ln^{-1}(2610/2250) = 406.$$

This Q is the same for all of the simulation work presented in this research.

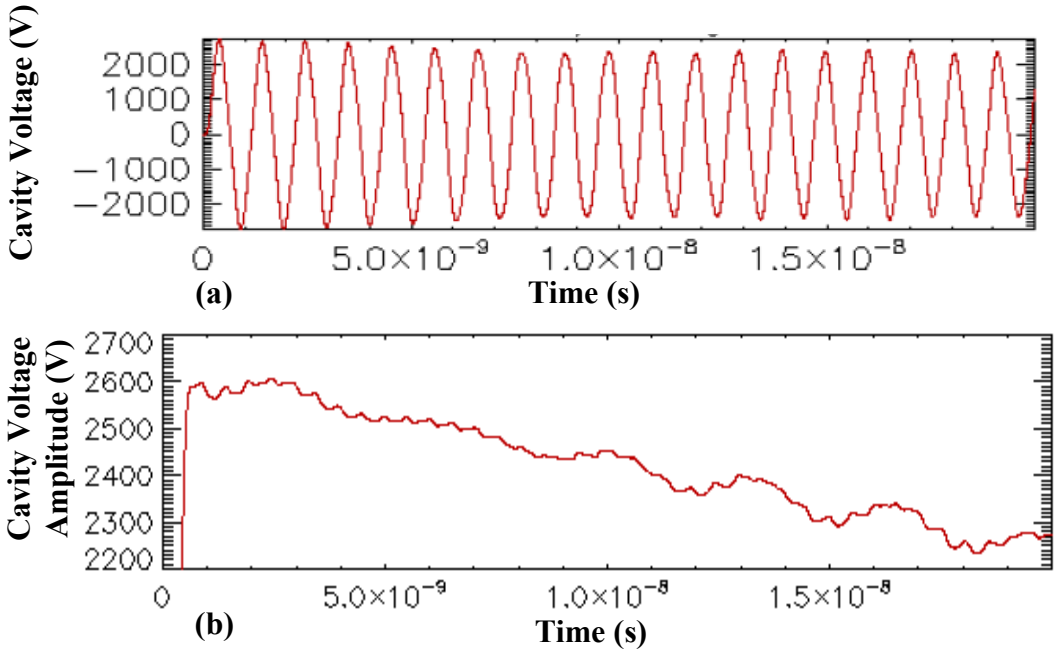

Figure 52: Example showing calculation of the quality factor Q. (a) Cavity voltage versus time, (b) Cavity voltage amplitude versus time from VORPAL, for the cylindrical cathode V_{ca} = -26.0 kV, B = 0.12 T, and J'_e = 500 A/m.

Calibrating the DC Voltage:

For the magnetron to operate at a given operating mode, a DC voltage between the anode and the cathode has to be chosen. In this run type, an electrostatic field generated between the cathode and anode is tuned using a combined source with feedback and drain. This electrostatic field is generated using the approximation of a cylindrical capacitor model, such as:

$$C = \frac{2\pi\varepsilon_o}{\log\left(\frac{r_a}{r_c}\right)} \tag{5.19}$$

$$I_{DC} = C\left(\frac{V_{DC}}{\tau}\right) \tag{5.20}$$

where C is the approximate capacitance, ε_o is the permittivity of free space, r_a is the anode radius, r_c is the cathode radius, I_{DC} is the current, V_{DC} is the cathode-anode voltage, and τ is the rise time. In this model, after the voltage is measured, the amount of the charge current is calculated. Since this adjustment is time dependent, the voltage can overshoot due to a time delay; a drain mechanism is implemented to prevent the overcharging; therefore, a constant drain current is added. This circuit model provides a stable time-dependant voltage by balancing between the charging and drain current [93]. In Figure 53, the resulting voltage between the anode and cathode is plotted versus time. This model was developed by TechX for VORPAL.

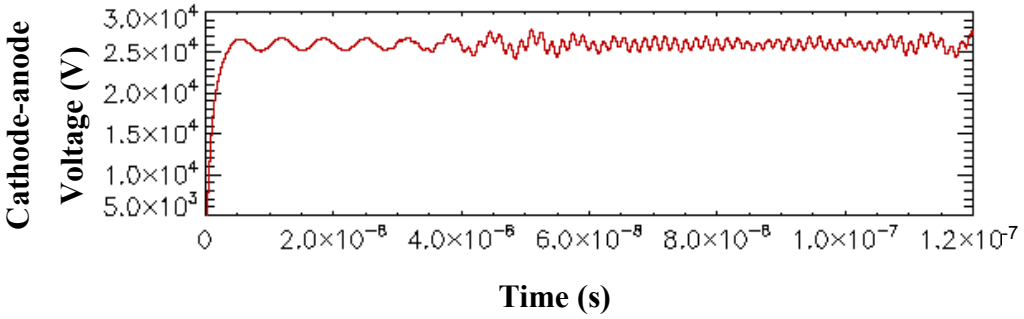

Figure 53: Cathode-anode voltage versus time for the cylindrical cathode model from VORPAL.

Run with particles

Finally, electrons are emitted into the magnetron from the cathode. The previous runs can be iterated to ensure that the electrons show the desired mode. When electrons are emitted from the cathode and the correct V_o and B are chosen, five spokes are eventually formed; Figure 54 shows the stable state of the model. The five spokes

indicate the π-mode where the RF field alternates in phase by 180° for each adjacent cavity.

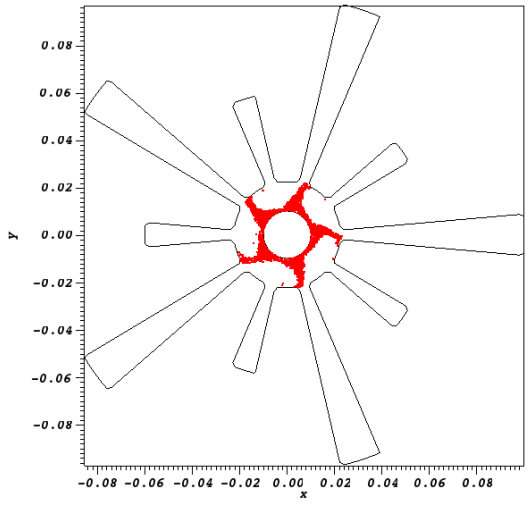

Figure 54: Rising sun magnetron simulation with particles after oscillations start and spokes form.

After calibrating the model, the cylindrical cathode geometry was set up as follows: the cathode-anode voltage (V_{ca}) at -26.0 kV, applied magnetic field (B) at 0.12 T, and a continuous linear current density (J'_e) of 500 A/m (total emitted current). These conditions were set as the reference case for the simulations because the magnetron achieved stable oscillation. Different sets of simulations were completed to study the magnetron performance and check calibrated parameters. The results were compared to the reference case. This set of simulations was completed as follows: (a) varying the cathode-anode voltage, (b) varying the B-field, and (c) varying the total emitted current density. They were performed by varying one parameter at a time while keeping others constant, then changing a second parameter while varying the first. For example, the B-field and the current density are fixed while the cathode-anode voltage is varied; then, the

B-field is changed while the voltage and the current density are fixed. Table 5.2 summarizes the completed simulations. These simulations were performed for model calibration. Only the best results (most stable model) will be presented. The total emitted current was varied from 125A/m to 1000 A/m, keeping the cathode-anode voltage constant (reference case). The startup time for each current value was measured and compared with the reference case.

In the case of the faceted cathodes, a similar procedure was followed. The set of simulations for the five-sided cathode was completed as follows: (a) varying the cathode-anode voltage, (b) varying the B-field, and (c) varying the anode current. From these results, it was found that for this model a V_{ca} = -22.2 kV, B = 0.09 T, and J'_e = 326 A/m were the parameters that gave the most stable model for the faceted cathodes. These simulations were used for model calibration and are shown in Table 5.2 and Table 5.3. For the ten-sided cathode, these simulations were not all completed because this model had better stability, and after investigating some of the parameters, it was easier to determine that the most stable case was for V_{ca} = -22.2 kV, B = 0.09 T, and J'_e = 326 A/m. The total emitted current density was also varied for the faceted geometries from 81.5 A/m to 652 A/m, keeping the cathode-anode voltage constant (reference case). The startup time for each current value was measured and compared with the reference case. These results are presented in Chapter 6.

Table 5.2: Rising sun magnetron: cylindrical cathode VORPAL simulations.

Major Parameter	Value of Major Parameter	Varied Parameter	Values of Varied Parameter
B-field	0.09 T	Cathode-anode Voltage	-21.0 kV to -23.0 kV
Linear Current Density	326 A/m		
B-field	0.12 T	Cathode-anode Voltage	-25.0 kV to -27.0 kV
Linear Current Density	500 A/m		
Cathode-anode Voltage	-26.0 kV	B-field	0.08 T to 0.16 T
Linear Current Density	500 A/m		

Table 5.3: Rising sun magnetron: faceted cathode VORPAL simulations.

Major Parameter	Value of Major Parameter	Varied Parameter	Values of Varied Parameter
B-field	0.09 T	Cathode-anode Voltage	-21.0 kV to -23.0 kV
Linear Current Density	326 A/m		
B-field	0.12 T	Cathode-anode Voltage	-25.0 kV to -27.0 kV
Linear Current Density	500 A/m		
Cathode-anode Voltage	-22.2 kV	B-field	0.08 T to 0.16 T
Linear Current Density	326 A/m		

The final step of this part of the study is to compare the results obtained in VORPAL with previous work completed in ICEPIC. The parameters used from ICEPIC

were: V_{ca} = -22.2 kV, B = 0.09 T, and J'_e = 326 A/m. The cylindrical and faceted cathodes were simulated with these parameters and compared with ICEPIC results. These results are presented in Chapter 6.

5.11 Rising Sun Magnetron Model with Modulated, Addressable, Current Sources

The second part of the modeling focuses on the faceted cathode geometry. For this set of simulations, all the runs were performed using the reference case parameters for this geometry: V_{ca} = -22.2 kV, B = 0.09 T, and J'_e = 326 A/m.

For the first tests, this configuration simulated discrete current sources along each facet but did not include individual temporal and spatial control of the sources. This was achieved by creating a function that allowed emission from one or more current sources. The first step was to vary the number of current sources (emitters) while they were evenly distributed along the facet. This number was varied between 1 and 5 emitters per facet (1 facet = 1 RF period) for the five-sided cathode and 3 emitters per facet (2 facets = 1 RF period) for the ten-sided cathode. Tests included emission from one facet only as well as from all five or ten facets.

The next step was to have individual control over each current source. The model was modified in order to simulate each current source independently. Therefore, each current source can be temporally and spatially modulated. This model allows turning ON and OFF emitters at a specific time and also allows controlling the current injection location. The modulated current sources were modeled individually. In VORPAL, many particle sources can be used in a simulation. For this simulation, each emitter or current

source was modeled as a particle source in which a time of ON and OFF can be specified as well as the location on the facet. The current sources were placed evenly distributed on the facet with small gaps in between them. Figure 55 shows an example (concept) of the application of this technique on the five-sided cathode. For simulation purposes, this case shows the five-sided faceted cathode with 5 emitter elements per facet (25 emitter elements total) (see Figure 55(a)). This particular example helps illustrate the application of the current model. The current injection starts by first turning ON one emitter per facet at a specific time while the others are turned OFF (emitters are represented by arrows as indicated in Figure 55(a)). The emitters are turned ON in a sequence following the electron spoke rotation direction, which is clockwise in this figure. The emitters are turned ON and OFF in sequence and at the device oscillating frequency in order to control the formation and location of the spokes versus time. Figure 55(a) shows how the emitters are turned ON in a sequence. Figure 55(b) shows this behavior in more detail for one of the facets, indicating the number of emitters that are turned ON and the number of emitters turned OFF. This simulation was also repeated with a ten-sided faceted cathode to compare the performance of the device due to a change in cathode geometries.

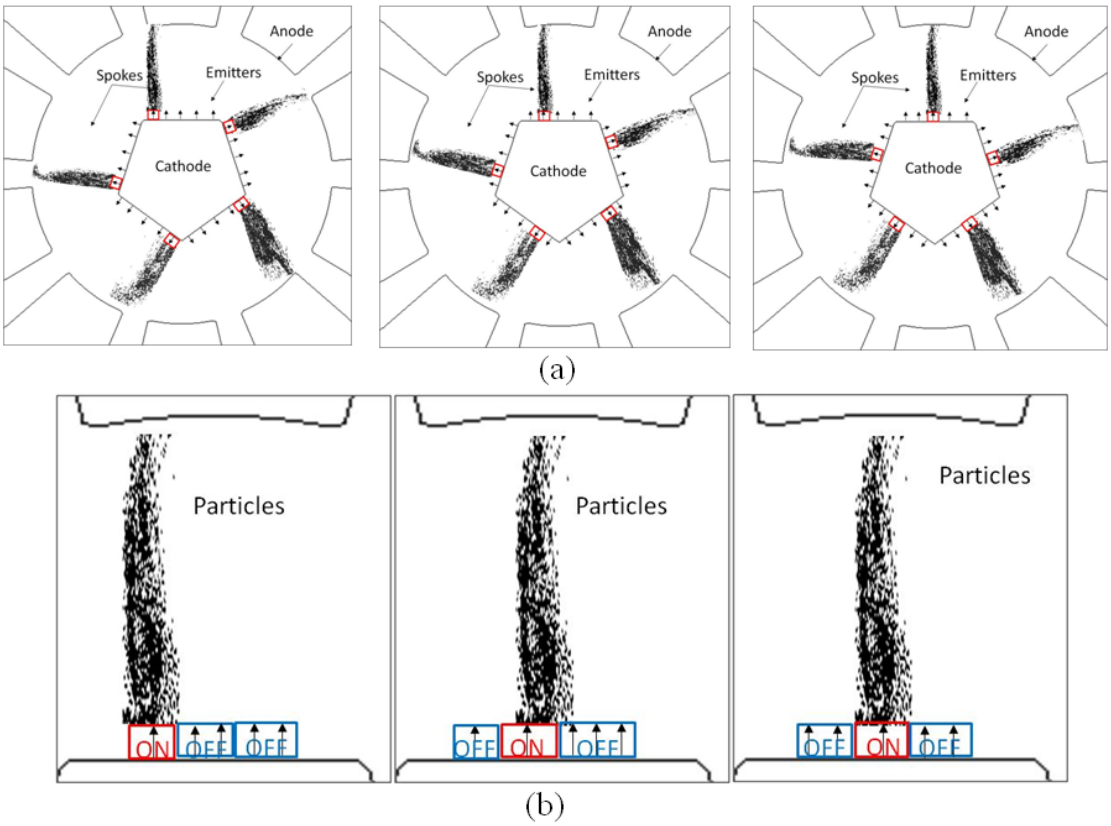

Figure 55: (a) Temporal and spatial modulation concept of the current injection, showing electrons being injected in phase with spokes. (b) Detailed view of one of the facets showing the ON and OFF emitters.

The last step of this work is to demonstrate phase control. As described before, the current sources can be turned ON and OFF in sequence to start oscillation. The sequence can be changed versus time to change the spoke formation during oscillation. Therefore, in the phase control simulation, the emitters can be turned ON and OFF at different times.

After the additional simulation tests, it was found that the ten-sided faceted cathode was more stable. Therefore, this geometry was used for the rest of the simulations and for demonstrating the phase control technique. A dynamic phase shift of 180° was demonstrated. The phase shift was initiated at 88.40 ns, and then oscillations

later in time were compared to a reference point in time before the shift, which was considered as phase 0°. The RF B_z field and spoke locations were used to analyze these results. The signal was partitioned in two parts: the reference with no phase shift and the phase shifted portion. The two curves were compared for different RF periods after the phase shift to check how fast/slow the phase changed in time and achieved a steady state at 180°. These results are presented in Chapter 7.

5.12 Additional Simulation Setups

During the research, various issues were encountered with the five-faceted cathode and the modulation technique. The spokes did not completely form, and gaps or blank spaces in the spokes were observed as well as instabilities in the anode current density. In order to study these issues and improve performance and stability of the magnetron, other simulation concepts were considered.

(a) The modulated, addressable current source model concept shown in Figure 55 was repeated, replacing the five-sided faceted cathode by a ten-sided faceted cathode. In this case, each facet plate contained 3 emitters that can be addressed spatially and modulated temporally. The ten-cavity magnetron has 5 spokes in π-mode; therefore, for the ten-sided cathode, a single spoke rotates past 2 cathode facet plates (6 emitters) every RF period. These results were compared to the five-sided faceted cathode and are presented in Chapter 7.

(b) The modulated, addressable, current source with a DC hub: The same concept as shown in Figure 55 was implemented, with the addition of a "DC hub" to improve the formation of spokes (improve stability), to cover the space gaps, and to achieve desired spoke thickness. The DC hub consisted of a continuous current source that was turned

ON together with the modulated current sources during the simulation. However, only a fraction of the total emitted current density is DC while the rest is modulated. These current fractions were varied, and the most stable case was used. The DC hub was turned ON at the start of the simulation, and the duration of the ON time was varied between 5 ns and continuous ON for the total simulation run time. The total current of the DC hub was varied from 5% to 10% of the total emitted current. The best results from this technique are shown in Chapter 7.

(c) The modulated, addressable, current source with time overlap: This simulation was completed to improve stability of the device oscillations and to also cover the gaps in the electron bunches. The timing diagram for this concept is shown in Figure 56. The example in the figure corresponds to a 25% of current overlap and shows the sequence for the first RF period. This concept consists of overlapping the ON time of the emitters by a $\Delta\tau_o$ (overlap time). It corresponds to one facet of the cathode with a total of five emitters. Since this case is a 25% overlap and since there are 5 emitters per facet, $\Delta\tau_o$ = 0.25*1/5 τ_{RF}, where τ_{RF} = 1.04 ns corresponding to a frequency of operation of 957 MHz. As observed in the figure, the first emitter is turned ON from 0 to 2.6e-10 s, the second emitter follows from 2.08e-10 to 4.68e-10 s, and so on. The results for this particular case are shown in Chapter 7.

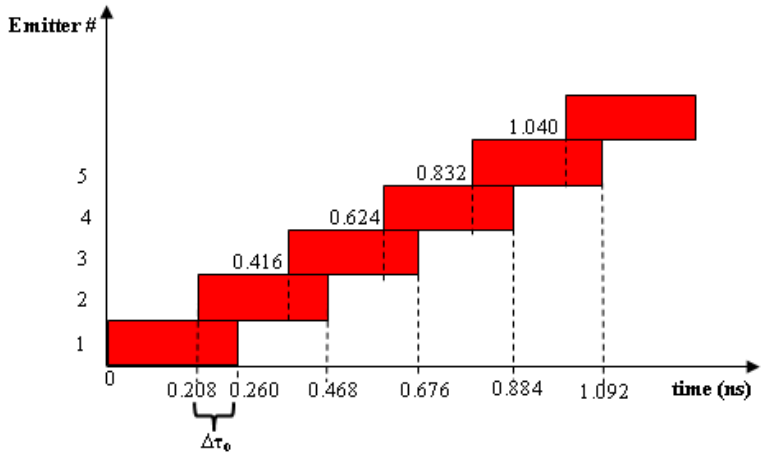

Figure 56: Modulated current overlap time diagram for the five-sided faceted cathode. This diagram shows an example with 5 emitters in 1 facet (1 RF period).

(d) The modulated, addressable, current source with time overlap and a DC hub: The same concept shown in Figure 56 was implemented with the addition of both a DC hub and time overlap to help the formation of spokes (improve stability, cover gaps) and to achieve desired spoke thickness. For this case, the DC hub was kept turned ON for the entire simulation run time. The total emitted current was varied between 5% J'_e from hub, 95% J'_e from the modulated beam, up to 60% J'_e from hub, and 40% J'_e from the modulated beam. The best results from this technique are shown in Chapter 7. Table 5.4 shows a summary of the additional simulations previously discussed along with a list of the diagnostics used for the analysis.

Table 5.4: Five-Sided Faceted Cathode Additional Simulation Tests with Modulated, Addressable Current Sources.

Simulation Test	Diagnostic	% DC Hub Current	% Overlap Time
Modulated Beam	• Spoke Formation. • Spoke Stability. • Anode Current. • Total Emitted Current. • Frequency. • Power.	0	0
Modulated Beam with DC hub	• Spoke Formation. • Spoke Stability. • Anode Current. • Total Emitted Current. • Frequency. • Power.	5%, 10%	0
Modulated Beam with Time Overlap	• Spoke Formation. • Spoke Stability. • Anode Current. • Total Emitted Current. • Frequency. • Power.	0	10%, 25%, 50%
Modulated Beam with Time Overlap with DC hub	• Spoke Formation. • Spoke Stability. • Anode Current. • Total Emitted Current. • Frequency. • Power.	5%, 10%, 20%, 30% 40%, 50%, 60%	10%, 25%, 40%, 50%

CHAPTER SIX: VORPAL SIMULATION RESULTS FOR THE CONTINUOUS CURRENT SOURCE CATHODE MODEL

6.1 Overview

This chapter covers the simulation results of the continuous current source model with the cylindrical and faceted cathodes in VORPAL. This model was tuned and tested to develop a reference case for both geometries. The results obtained from both models are compared with previous work [12] completed in ICEPIC.

6.2 Continuous Current Source Model: Cylindrical Cathode

The cylindrical cathode model was simulated in VORPAL; after tuning the operating parameters, it was found that the most stable case for this configuration was at a cathode-anode voltage (V_{ca}) of -26.0 kV, applied magnetic field (B) of 0.12 T, and a continuous linear current density (J'_e) of 500 A/m (total emitted current). These parameters gave an operating frequency of 960 MHz. Figure 57-60 show the RF B_z field for the rising sun magnetron with the cylindrical cathode, the mode switching during start up, and the FFT of the cavity voltage, respectively from VORPAL. The plot of the RF B_z field changes phase by 180° at adjacent cavities, indicating the π-mode operation.

Figure 59 shows a startup time of approximately 300 ns for oscillation. The linear power density at the loaded cavity was calculated to be 3.9 MW/m for this configuration. Figure 60 shows the results of this 2-D model (V_{ca}=-26 kV, B=0.12 T, J'_e=500 A/m)

presenting (a) the electron hub at 0.012 ns, before oscillation occurs and (b) the spokes that have formed showing oscillation at a time of 276 ns. Figure 61 shows the total emitted linear current density (B field is turned off in the simulation) to check the actual injected current. Oscillatory behavior of the current is also observed in this plot. This can be attributed to the numerical resolution in the PIC code. Since these macroparticles are being collected on the anode, they are not emitted exactly the same for every time step; therefore, this variation results in oscillations that will eventually average to the total current injected. This diagnostic was designed for analysis, and its results should only be used to determine the average value of the injected current. Figure 62 shows the anode linear current density during the device normal operation, and the oscillation startup after 300 ns can be seen. The cylindrical cathode geometry was also simulated at V_{ca} = -22.2 kV, B = 0.09 T, J'_e = 326 A/m for comparison with the faceted cathode models. The anode linear current density for this case can be observed in Figure 63.

An analysis of the startup current was also studied. The total emitted linear current density was varied from $0.25J'_e$ to $2J'_e$. Figure 64 shows a graph of startup time versus the total emitter linear current density of the device for the cylindrical cathode and other cathode geometries (five-sided and ten-sided cathode). This result illustrates the variation in the startup time of the device for the different cathode geometries. From the curve, it is observed that the magnetron starts at 310 ns for the cylindrical cathode at V_{ca}=-26 kV, B=0.12 T, J'_e=500 A/m. Even though these parameters do not give the fastest startup for this device, it does give the most stable model, showing clean spokes and stable oscillations for the cylindrical cathode geometry. Note also that the startup time levels off for J'_e > 700 A/m but increases almost linearly below 700 A/m.

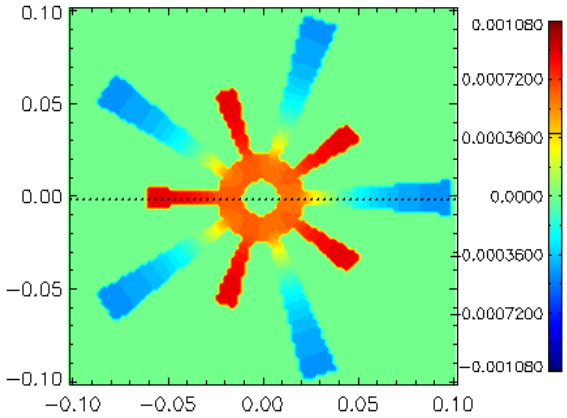

Figure 57: **Cylindrical cathode model from VORPAL simulation showing the RF B-field and π-mode. This result corresponds to V_{ca} = -26.0 kV, B = 0.12 T, and J'_e = 500 A/m.**

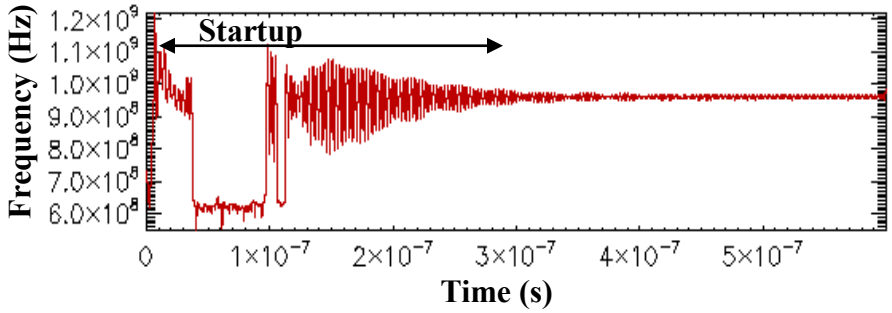

Figure 58: **Cylindrical cathode cavity voltage frequency versus time with moving window, showing the startup time of the device at 300 ns, and the mode switching from 650 MHz to the Operating Frequency (π-mode) 960 MHz from VORPAL.**

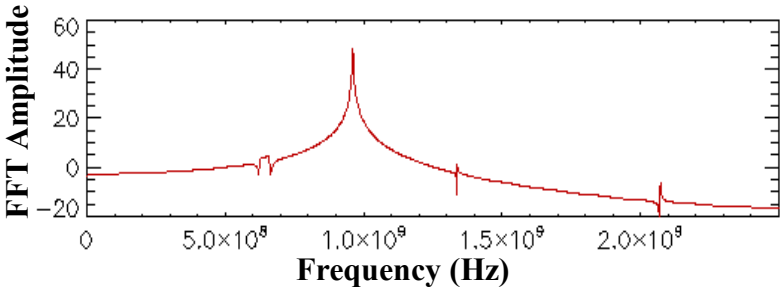

Figure 59: **Cylindrical cathode Fast Fourier Transform (FFT), over entire simulation time, of the loaded cavity voltage from VORPAL simulation. This plot clearly indicates that the π-mode is dominant at the frequency of operation of 960 MHz.**

(a) (b)

Figure 60: **Cylindrical cathode VORPAL simulation results for V_c = -26.0 kV, B = 0.12 T, and J'_e = 500 A/m. The red dots indicate electron macroparticles. Figure 61(a) is at 0.012 ns, before oscillation, and Figure 61(b) is at 276 ns, after oscillation starts and the model is stable.**

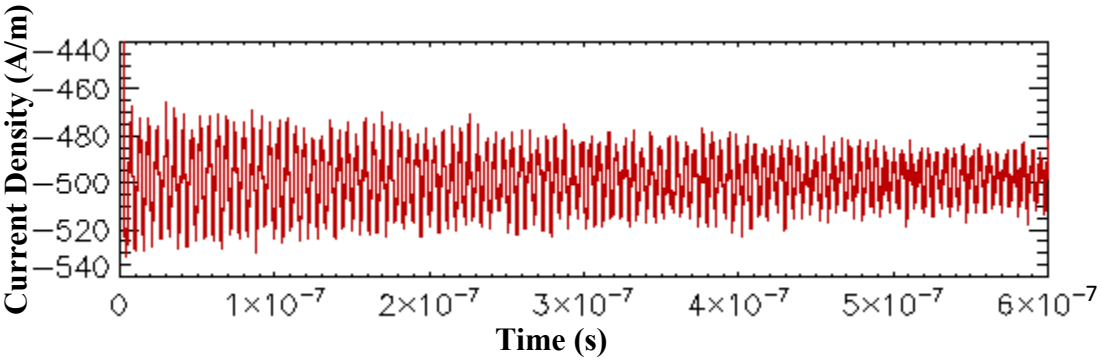

Figure 61: **Cylindrical cathode continuous total emitted linear current density versus time with no applied magnetic field (B=0).**

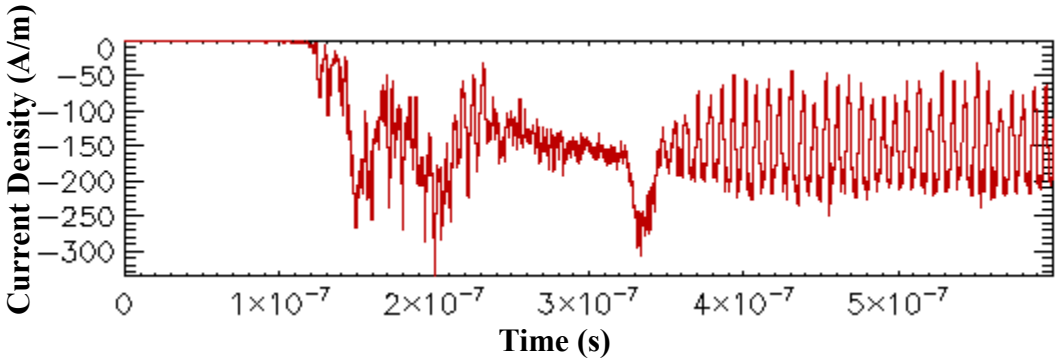

Figure 62: **Cylindrical cathode continuous anode linear current density during device operation versus time.**

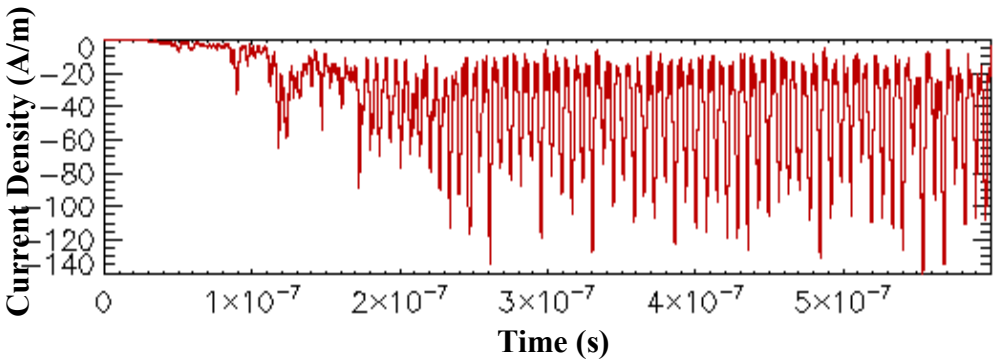

Figure 63: **Cylindrical cathode (V_{ca} = -22.2 kV, B = 0.09 T, J'_e = 326 A/m) continuous anode linear current density during device operation versus time.**

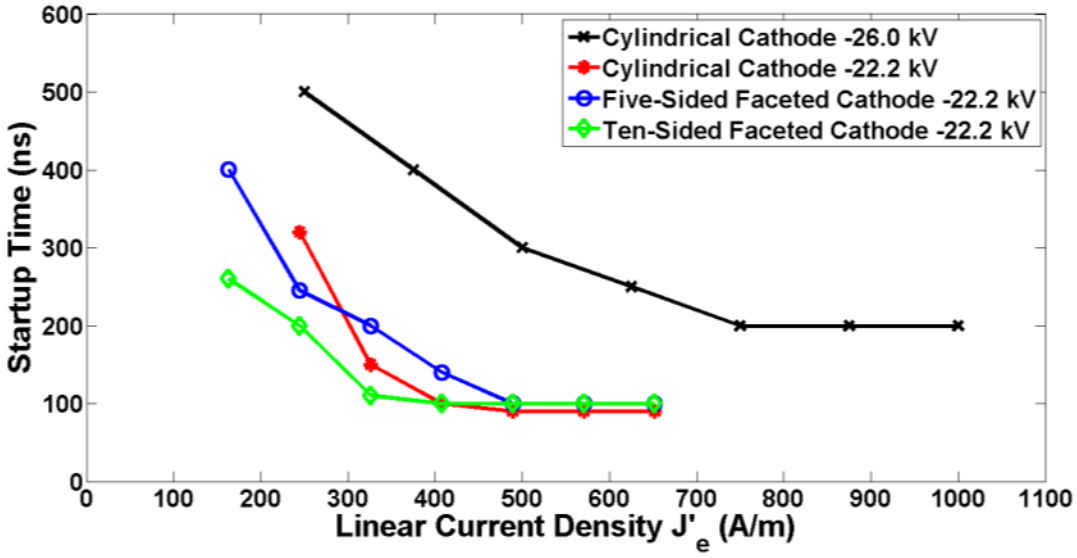

Figure 64: **Startup time versus continuous total emitted linear current density for different cathode geometries: cylindrical and faceted.**

6.3 Continuous Current Source Model: Five-Sided Faceted Cathode

A five-sided faceted cathode with a vertex angle of 3π/2 was then simulated as a replacement for the cylindrical cathode with all other parameters in the calculation unchanged. It was found that the reference parameters: V_{ca} = -26.0 kV, B = 0.12 T, and a J'_e = 500 A/m were not the optimum for this configuration. The spokes were unstable and

a clean oscillation was not observed. Using the results from a previous model [12] developed in ICEPIC, these parameters were changed to V_{ca} = -22.2 kV, B = 0.09 T, and a J'_e = 326 A/m. It was found that the model developed in ICEPIC and the VORPAL models were comparable. With these parameters the five-sided faceted cathode was able to oscillate at a frequency of 957 MHz. The cylindrical cathode model was also simulated using these same parameters for comparison purposes. Figure 65 shows the RF B_z field, indicating the π-mode operation for the five-sided faceted cathode. Figure 66 shows the mode switching during start up. Initially there is a 650 MHz mode before stable operation. Figure 67 shows the FFT of the cavity voltage, with a clear peak at 957 MHz. The linear power density at the loaded cavity was calculated to be 1.2 MW/m.

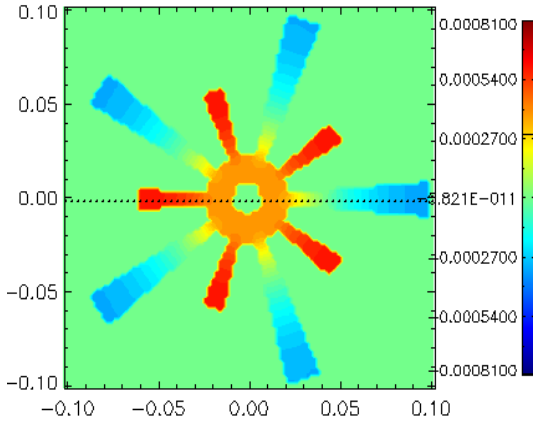

Figure 65: Five-sided faceted cathode model from VORPAL simulation showing the RF B-field and π-mode. This result corresponds to V_{ca} = -22.2 kV, B = 0.09 T, and J'_e = 326 A/m.

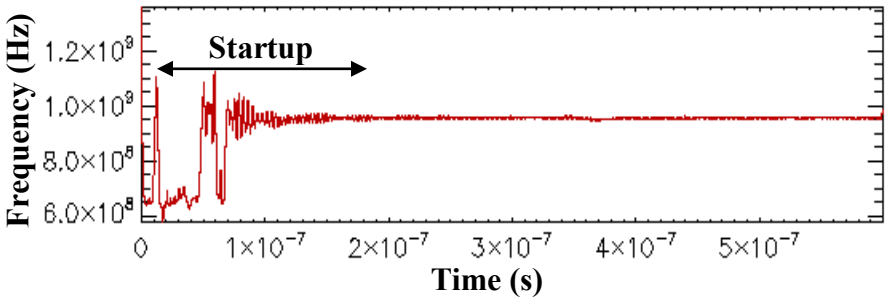

Figure 66: **Five-sided faceted cathode cavity voltage frequency versus time with moving window, showing the startup time of the device at 200 ns, and the mode switching from 650 MHz to the operating frequency (π-mode) 957 MHz from VORPAL.**

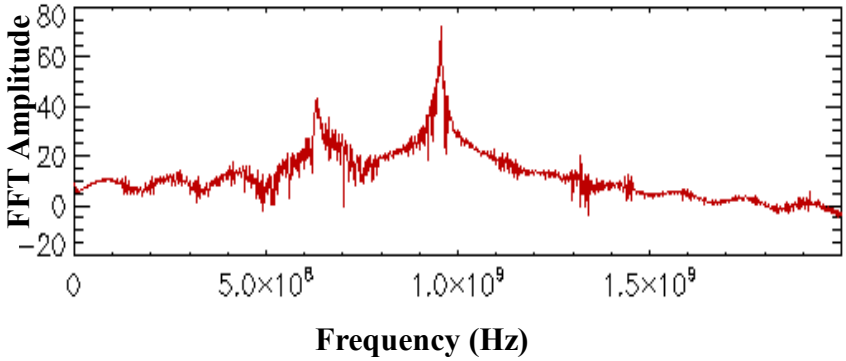

Figure 67: **Five-sided faceted cathode Fast Fourier Transform (FFT), over entire simulation time, of the loaded cavity voltage from VORPAL simulation. This plot indicates that the π-mode is dominant at the frequency of operation of 957 MHz.**

The spoke formation results are shown in Figure 68. Figure 68(a) shows the pre-oscillation state (t= 0.012 ns). Figure 68(b) shows the spokes forming after oscillation at t= 317 ns. These VORPAL results, both cylindrical and faceted cathodes, were compared with a 2-D simulation previously performed in ICEPIC [12]. It was found that the cylindrical cathode at V_{ca} = -26.0 kV, B = 0.12 T, and a J'_e = 500 A/m modeled in VORPAL was a more stable simulation with very clean spokes compared to the simulation parameters used in ICEPIC (-22.2 kV, 0.09 T, 326 A/m). However, the

cylindrical cathode was simulated at the ICEPIC parameters for comparative purposes. On the other hand, the ICEPIC parameters for the faceted cathodes were the most stable choice for both cases (five-sided and ten-sided). In addition, the startup time for the -22.2 kV, 0.09 T, 326 A/m is shorter for the cylindrical cathode. Figure 69 shows the comparison among the three models. It is observed that the VORPAL 2D model is closer to the 3D ICEPIC model, in terms of spoke formation. The spokes are much clearer in the 2D VORPAL model than in the 2D ICEPIC model. An analysis of the startup current was also performed. The total emitted linear current density was varied from $0.25J'_e$ to $2J'_e$ as shown in Figure 64. A graph of the startup time of the device versus the total emitter linear current density is presented. From the curve, it is observed that the five-sided faceted cathode magnetron starts up at 200 ns for the reference parameters (-22.2 kV, 0.09 T, 326 A/m), while the cylindrical cathode at the V_{ca} = -22.2 kV, B = 0.09 T, and a J'_e = 326 A/m parameters shows a startup time of 150 ns (see Figure 64). Even though it starts up faster, it is not the most stable model. The startup time levels off above 400 A/m. The startup time increases dramatically below 400 A/m and will not start below 250 A/m.

(a) **(b)**

Figure 68: Five-sided faceted cathode VORPAL simulation results for V_c = -22.2 kV, B = 0.09 T, and J'_e = 326 A/m. The red dots indicate electron macroparticles. Figure 68(a) is at 0.08 ns, before oscillation, and Figure 68(b) is at 317 ns, after oscillation starts and the model is stable.

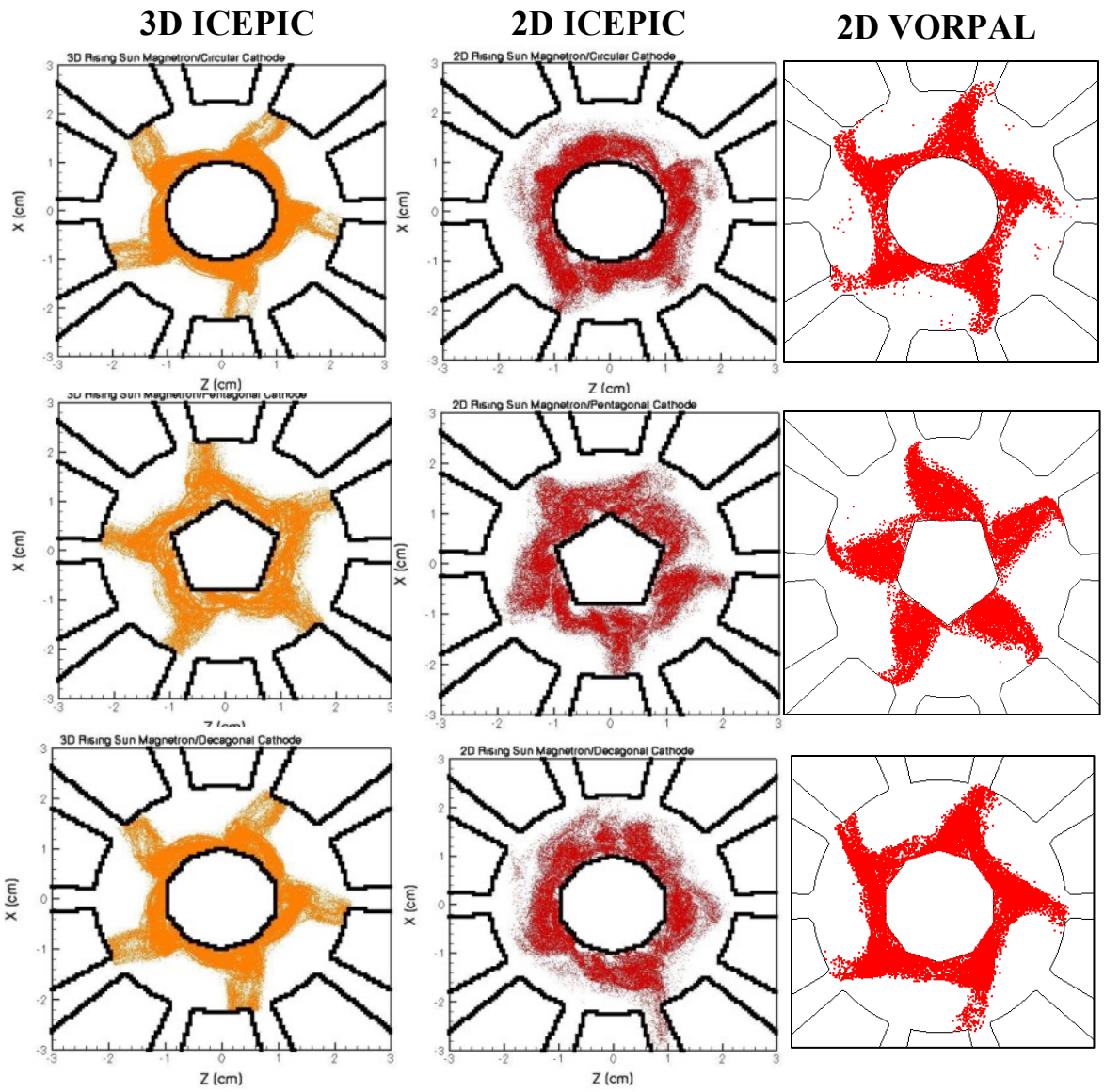

Figure 69: Comparison of ICEPIC model versus VORPAL model. V_{ca} = -22.2 kV, B = 0.09 T, and J'_e = 326 A/m. The top figures show the cylindrical cathode model, the middle figures show the five-sided faceted cathode, and the bottom figures show the ten-sided faceted cathode.

Figure 70 shows the total emitted linear current density versus time for the five-sided faceted cathode. These results were taken with no applied B field, so all the emitted current will be collected at the anode. This was completed to check that the total current

injected to the device was correct. In the figure, it is observed that the current averages to approximately 326 A/m, which matches the current input in the model.

Figure 71 shows the anode linear current density versus time when the device is in operation. It was found that there is an instability in the five-sided cathode oscillations. As it can be observed in Figure 71, this instability results in a current spike to the anode and a subsequent collapse of the spokes. Figure 72 shows the transition of the spokes before the current spike occurs, at the current spike, and after the current spike, when the spokes collapse. For this particular example, the time between 119.8 ns and 143.5 ns was selected. It can be observed that the shape of the spokes changes at the current spike with the electrons forming a more concentrated cloud or clump; then, the clump extends to the anode when the spike occurs. The result is a loss of a large percentage of available electrons. Then, the spokes disconnect and collapse. Following this mechanism, the spokes will form again. As can be seen in Figure 71, this current spike has a periodic behavior. The spike occurs, approximately every 250 ns to 350 ns. This means that every time the current spike occurs the spokes will collapse and reform again. Since the geometry of the cathode consists of five sides, the time that it takes the spokes to go around the cathode is $5\tau_{RF,}$ where 1 τ_{RF} = 1.04 ns corresponds to one facet. Therefore, the periodicity of the instability could be related to a multiple of the RF period. The causes of this instability are mainly attributed to the cathode shape, but further studies are needed to completely understand it. The electron trajectories around the five-sided cathode become distorted and appear to create too many synchronous electrons. These electron clumps give up their energy almost simultaneously, resulting in the current spike. By implementing a ten-sided cathode geometry (increasing the number of facets), this

problem was reduced. Therefore, the remainder of the phase control research work used the ten-sided cathode geometry.

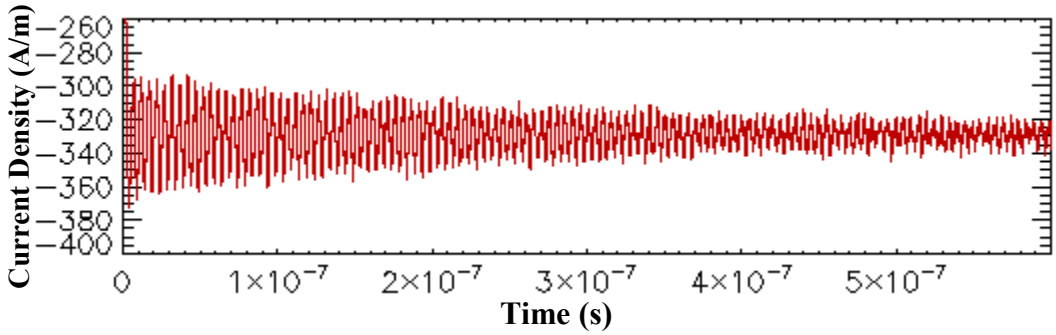

Figure 70: **Five-sided faceted cathode continuous total emitted linear current density versus time with no applied magnetic field (B=0).**

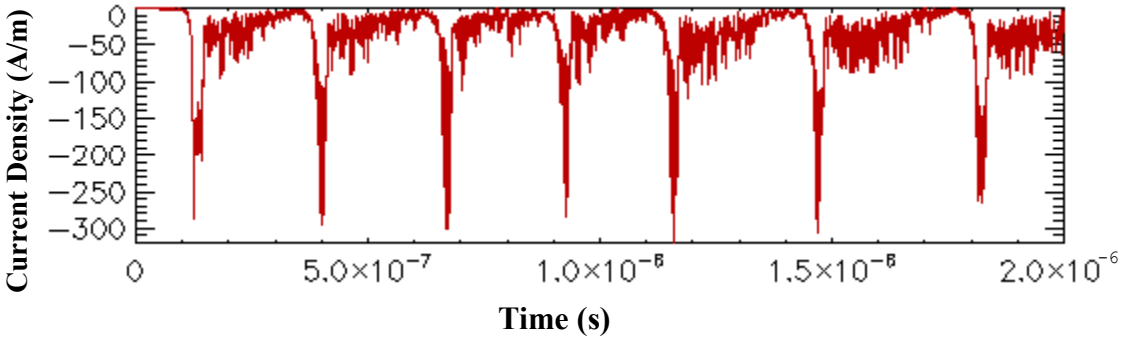

Figure 71: **Five-sided faceted cathode continuous anode linear current density during device operation versus time. The periodic current spikes are followed by spoke collapse.**

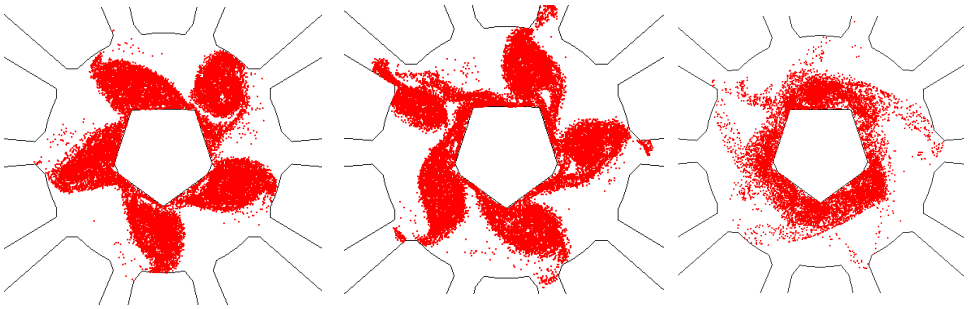

(a) **(b)** **(c)**

Figure 72: **Five-sided faceted cathode showing the transition of the spokes during the current instability. Spokes are shown (a) before current spike at 119.8 ns, (b) at current spike at 121.32 ns, and (c) after spokes collapse at 143.5 ns.**

6.4 Continuous Current Source Model: Ten-Sided Faceted Cathode

The ten-sided faceted cathode geometry was chosen to minimize the current spike problem. Similar analysis was completed for this configuration. The model was simulated at the same reference parameters: V_{ca} = -22.2 kV, B = 0.09 T, and J'_e = 326 A/m. Figure 73 shows the RF B_z field and illustrates the π-mode for the ten-sided faceted cathode. Figure 74 shows the start up time for this device at approximately 110 ns; Figure 75 shows the FFT of the cavity voltage. The plot in Figure 75 indicates the π-mode operation at a frequency of 957 MHz; the 650 MHz peak is still present in this configuration. The linear power density at the loaded cavity was calculated to be 1.2 MW/m, which was the same as for the five-sided cathode.

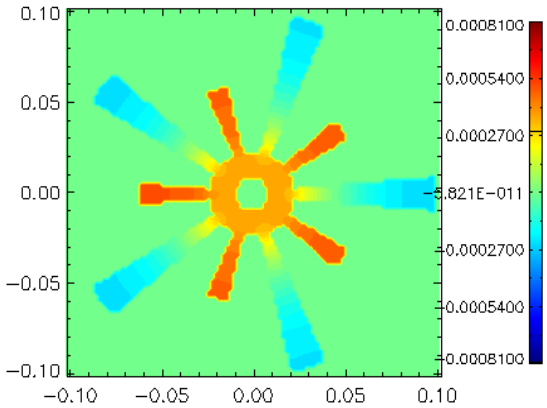

Figure 73: Ten-sided faceted cathode model from VORPAL simulation showing the RF B-field and π-mode. This result corresponds to V_{ca} = -22.2 kV, B = 0.09 T, and J'_e = 326 A/m.

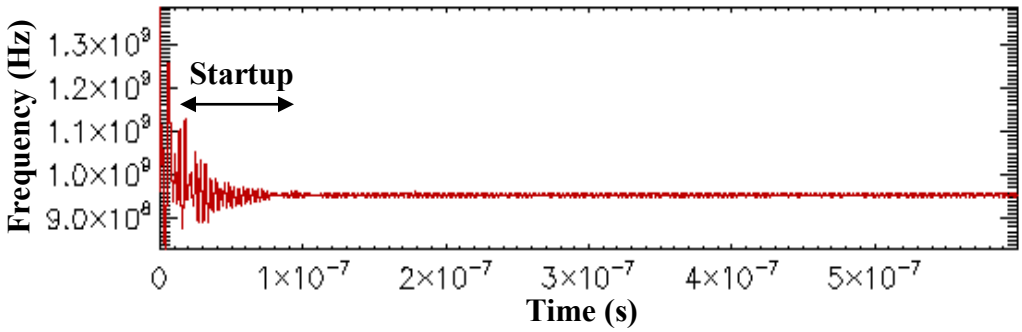

Figure 74: **Ten-sided faceted cathode cavity voltage frequency versus time with moving window, showing the startup time of the device at 110 ns, showing the operating frequency (π-mode) at 957 MHz from VORPAL.**

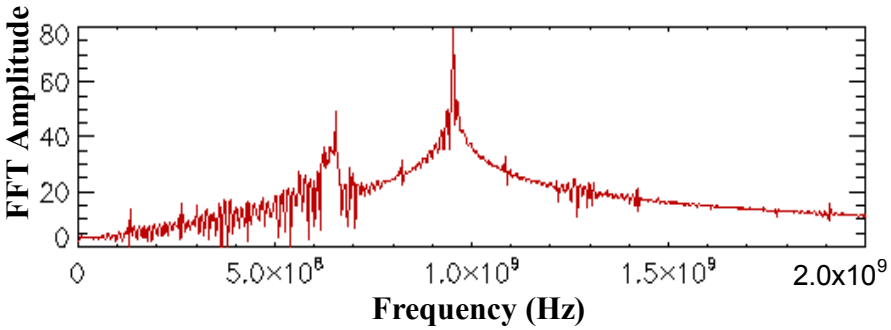

Figure 75: **Ten-sided faceted cathode Fast Fourier Transform (FFT), over entire simulation time, of the loaded cavity voltage from VORPAL simulation. This plot indicates that the π-mode is dominant at the frequency of operation of 957 MHz.**

Figure 76 shows the total emitter linear current density for the ten-sided faceted cathode. This simulation was performed with no applied B field. From the figure, it can be seen that the total emitted current averages to approximately 326 A/m, which matches the input current. Figure 77 shows the anode linear current density when the device is in operation. These results indicate a behavior very similar to the anode current for the cylindrical cathode geometry (see Figure 62), but the large current spikes are not present as in the five-sided cathode model. Instead there is a large spike at ≈ 110 ns, and then the oscillations are more stable. This result indicates that the ten-sided cathode geometry reduced the current instability.

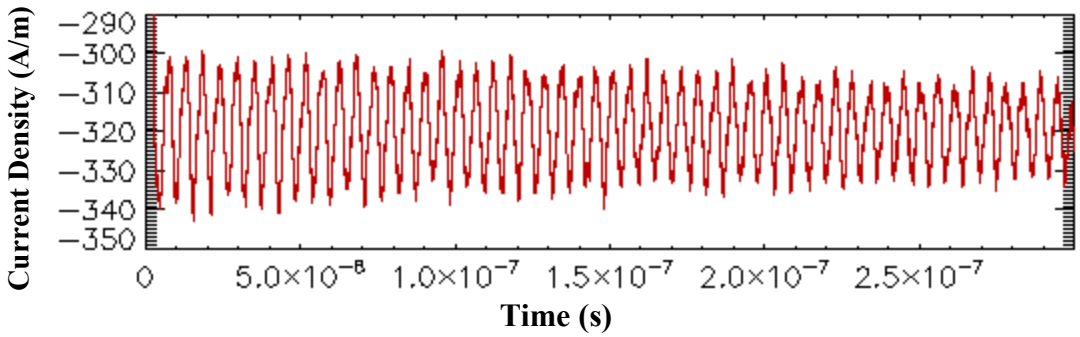

Figure 76: Ten-sided faceted cathode continuous total emitted linear current density versus time with no applied magnetic field (B=0).

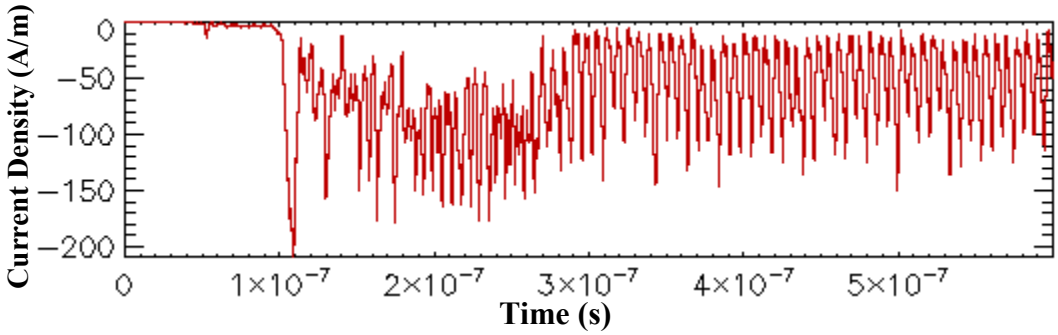

Figure 77: Ten-Sided faceted cathode continuous anode linear current density during device operation versus time.

The simulation for this case was also run for various emitted current densities, and the startup times were determined from the frequency versus time plots in VORPAL. Figure 64 shows the graph of startup time versus total emitted linear current density for various cathode geometries. From this graph, it can be seen that the ten-sided cathode geometry has a startup of 110 ns for the reference parameters. As can be seen, the startup time increases for lower current densities and decreases for higher current densities as expected. From this plot, the three cases: cylindrical, five-sided cathode, and ten-sided show very similar startup times for the reference parameters; however, as the linear current density is decreased (below 326 A/m), the startup times are not so similar depending on cathode shape. It is also noticeable that the cylindrical cathode for the V_{ca} =

-22.2 kV, B = 0.09 T, and J'_e = 326 A/m parameters does not start for current density values below 230 A/m. It was found that for this geometry, there is an increase in mode competition between the 650 MHz mode and the 957 MHz (π-mode); therefore, for values below 230 A/m, the device switches to the lower mode and does not start in π-mode. The nature of this behavior for this particular case needs further study and analysis.

The next step in the simulations is the study of the modulated, addressable, current sources at the operating frequency. This aspect of the work will be discussed in Chapter 7.

6.5 Summary of Results

This chapter studied the continuous current source model for the cylindrical and faceted cathodes. From the results, it is observed that all three models operated at the π-mode with frequencies of 960 MHz and 957MHz, respectively. A current instability was found in the five-sided faceted cathode. This current instability resulted in current spikes, which led to spokes disconnecting and collapsing. The ten-sided faceted cathode reduced this current instability and improved the overall startup time of the device from 200 ns (five-sided cathode) to 110 ns for the reference parameters; however, as the linear current density is decreased (below 326 A/m), the startup times are not so similar depending on cathode shape. Overall, the ten-sided cathode improved stability of the magnetron.

CHAPTER SEVEN: VORPAL SIMULATION RESULTS FOR THE MODULATED, ADDRESSABLE CATHODE

7.1 Overview

This chapter describes the results for the modulated, addressable cathode current source model. Two geometries were studied using this concept: a five-sided faceted cathode and a ten-sided faceted cathode. Work was completed for both cathodes; however, most of the analysis was performed on the ten-sided. Results showing the modulation technique and phase control will be presented in this chapter.

7.2 Modulated Five-Sided Faceted Cathode

Modulated, addressable, discrete current sources were modeled from each facet of the five-sided cathode to study its effect on the magnetron operation. Each facet on the five-sided cathode structure contains 5 emitters that can be addressed spatially and modulated temporally. The discrete current sources allow control in space and time of the current injection. Each ON emitter mimics the location of the electron spoke. The number of emitters can be varied; 5 emitters per side were chosen because it provided a reasonable spoke width; since this technique results in the injection of the electrons all in phase, the width of the spoke is important to allow the device to start. This modulation technique allows control of the startup and location of the spokes. For this simulation, the step size was modified to an integer fraction of the RF period. So for the 957 MHz operating frequency, the time step is set to a multiple of τ_{RF} /N, where τ_{RF} =1.04 ns is an

RF period and N is the number of emitters, which is 5 emitters for this case. Therefore, τ_{RF} /N = 0.208 ns, and the step size was chosen to be 1.0 ps. Figure 78 shows an example of the setup for the discrete current sources, when they are all ON at the same time. Figure 79 shows a diagram of the modulated current sources at the frequency of operation. For demonstration purposes, the B field was turned OFF to show the emitters turning ON in sequence. The diagrams show one RF period. The frequency of modulation is 957 MHz, τ_{rf} = 1.04 ns, and $\Delta t = 1/5\tau_{RF}$.

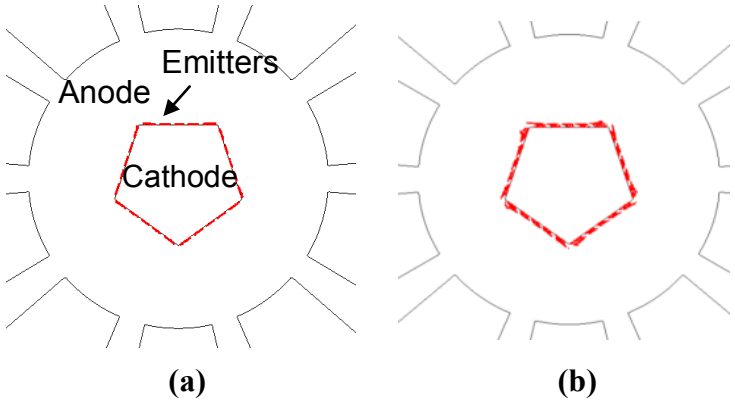

Figure 78: Five-sided faceted cathode showing discrete current sources setup for (a) 0.0987 ns and (b) 0.197 ns. There are five emitters per facet. All emitters are ON at the same time.

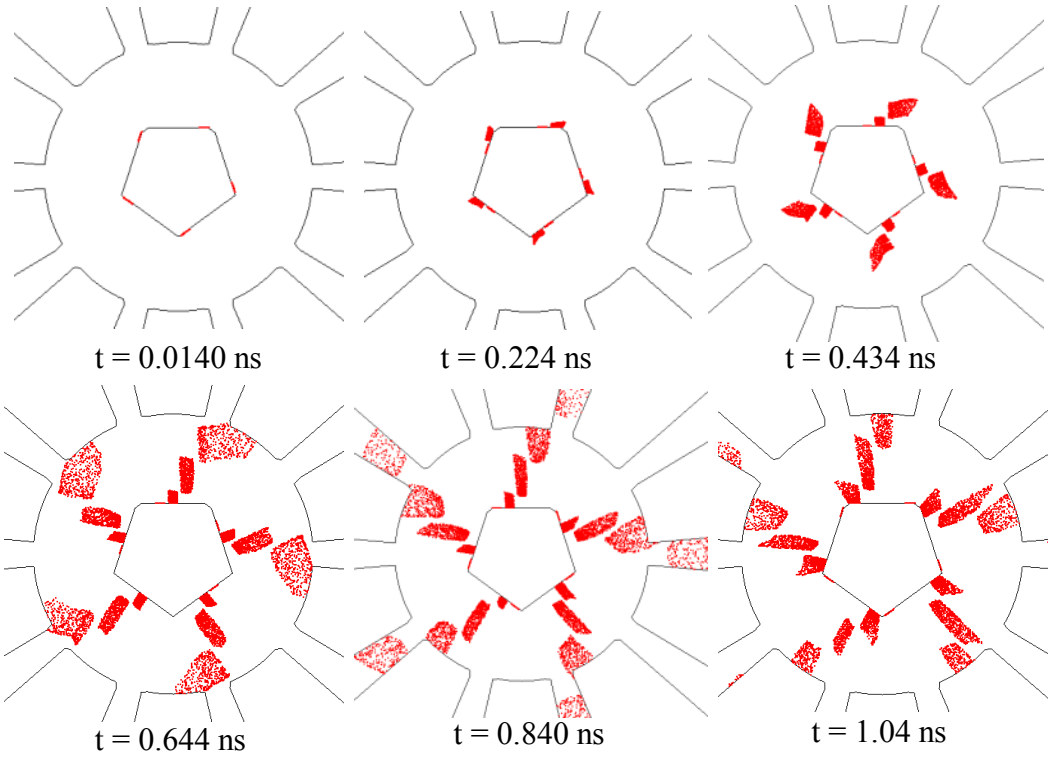

Figure 79: Five-sided faceted cathode with modulated, addressable current sources, with B field turned OFF. This shows the emitters turning ON in sequence. The diagrams show one RF period, τ_{RF}=1.04 ns, Δt = 1/5 τ_{RF}. Frequency of modulation is 957 MHz.

Figure 80 shows the results for the five-sided cathode with modulated, addressable, current sources. From the diagrams, an early start of the spoke formation is observed, however, not fully developed. Before they reach the anode, the spokes collapse, and over time the electrons start forming clumps. However, the device does not reach a stable oscillation. By observing this behavior, various issues were observed with this model: (a) spokes not fully developed, (b) gaps in the spokes, and (c) stability. In order to solve these issues, the current overlap technique and an additional DC hub (see additional simulations in Chapter 5) were proposed to minimize the gaps in the spokes and to test the stability of oscillations.

7.3 Modulated Five-Sided Faceted Cathode with Time Overlap

The time overlap technique discussed in Chapter 5 was implemented in this model. Different percentages of time overlap were tested; only the best and most stable results are shown in Figure 81. The diagrams in Figure 81 show the case with a current overlap of 25%. The frequency of modulation is 957 MHz, $\tau_{RF} = 1.04$ ns, $\Delta t = 1/5\ \tau_{RF}$, where the overlap time corresponds to $\tau_{ov} = 0.0520$ ns. It is observed in the figure that the overlap technique did fix part of the problem; parts of the gaps are covered, and the spokes are clearly formed going from the transition of electron clumps to fully developed spokes. However, the model was still not very stable, and as further study was completed, the same current instability present in the five-sided faceted cathode with a continuous current source was also found with the modulated plus current overlap model approach.

Figure 82 shows the modulated total emitted linear current density. This simulation was completed with no applied B field to check the input current. The current density averages to approximately 326 A/m as expected. Figure 83 shows the anode linear current density during the device operation, and as was mentioned before, the instability is also present in this case at $t \approx 100$ ns. Since this simulation was run for a shorter time, the current spike can be seen in more detail. The spokes were inspected for corresponding times that match the transition before and after the current spike as shown in Figure 84. Figure 85 shows the corresponding Fast Fourier Transform (FFT) of the cavity voltage, which indicates the device is operating at a frequency of 957 MHz. This plot also shows the lower frequency mode of 650 MHz is still present. Also, it can be seen in the figure that the FFT peak is wider compared to the other model cases (cylindrical and faceted with continuous current source); the cause of this spread is

unknown, but it could be attributed to the overlap technique, which is the only change in this case.

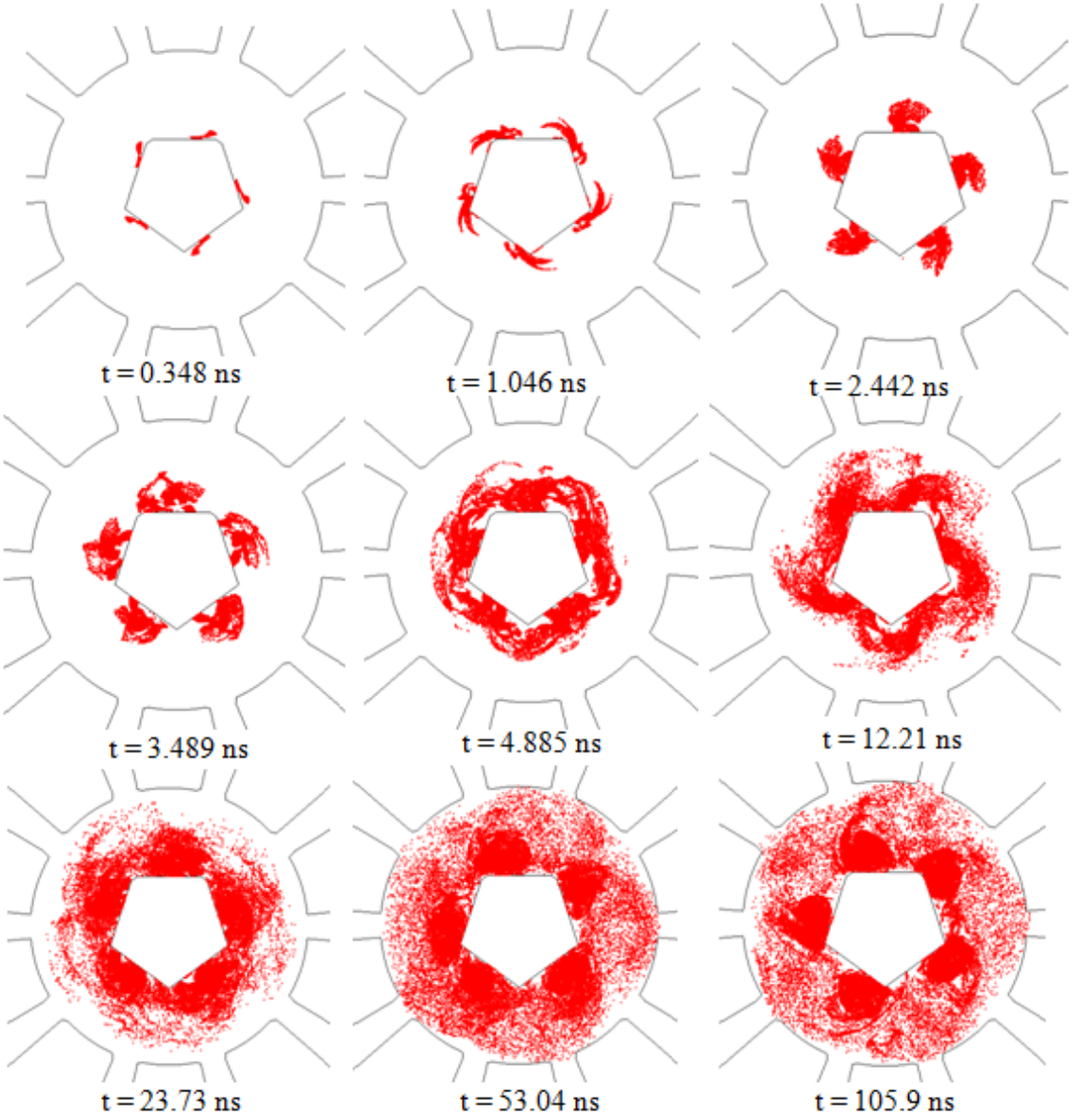

Figure 80: Five-sided faceted cathode with modulated, addressable current sources. The frequency of modulation is 957 MHz, τ_{RF}=1.04 ns, Δt = 1/5 τ_{RF}.

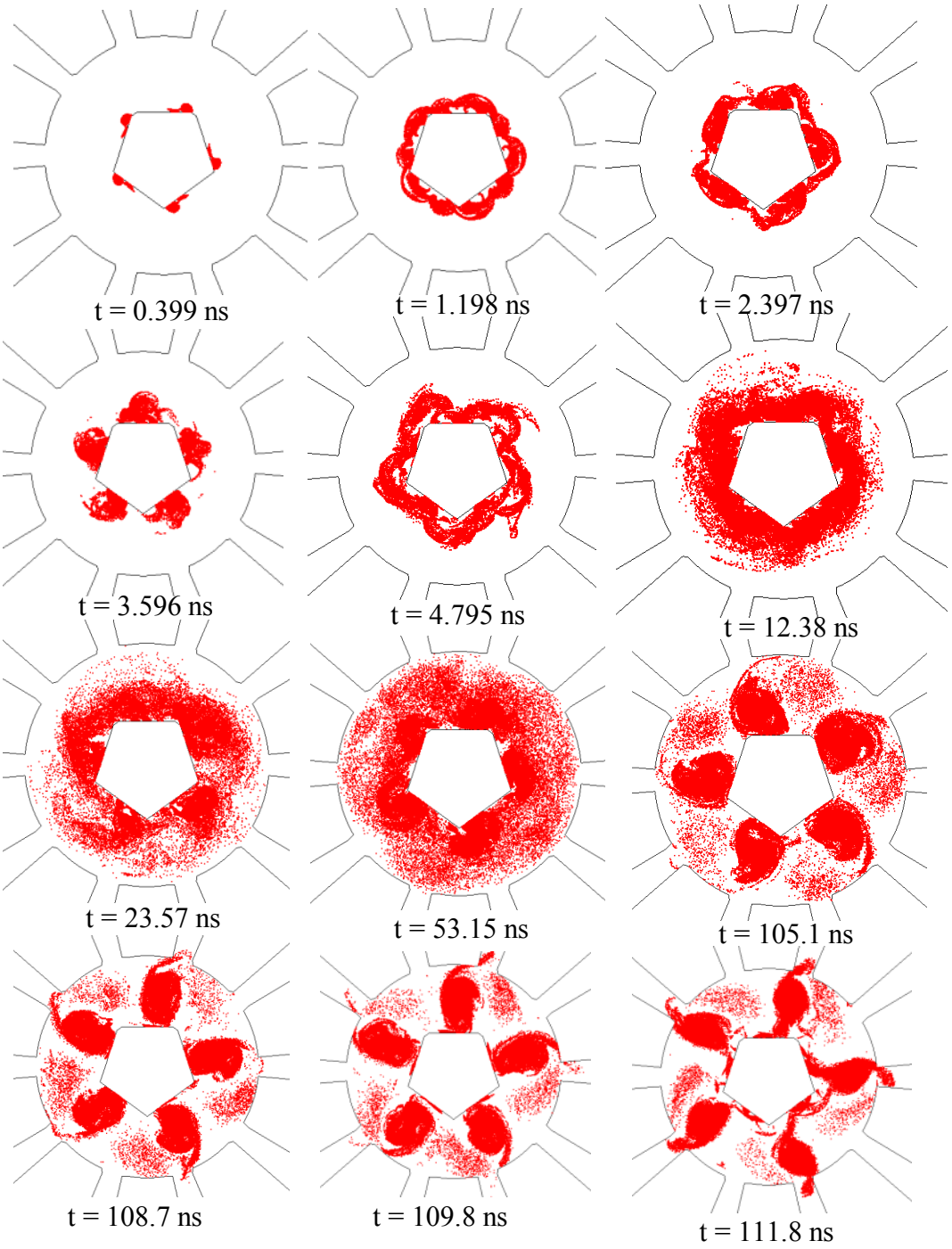

Figure 81: **Five-sided faceted cathode with modulated, addressable current sources plus current overlap. This diagram shows the case for current overlap of 25%. The frequency of modulation is 957 MHz, τ_{RF} = 1.04 ns, $\Delta t = 1/5\ \tau_{RF}$, τ_{ov} = 0.0520 ns.**

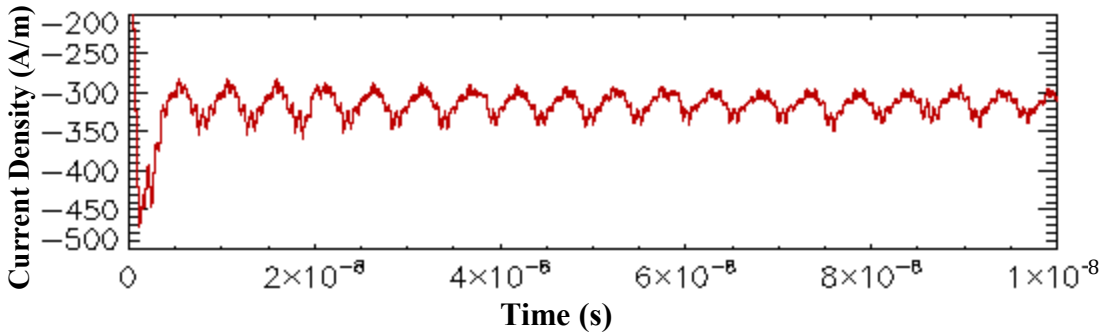

Figure 82: **Modulated total emitted linear current density versus time with no applied magnetic field (B=0) for five-sided faceted cathode with 25% overlap.**

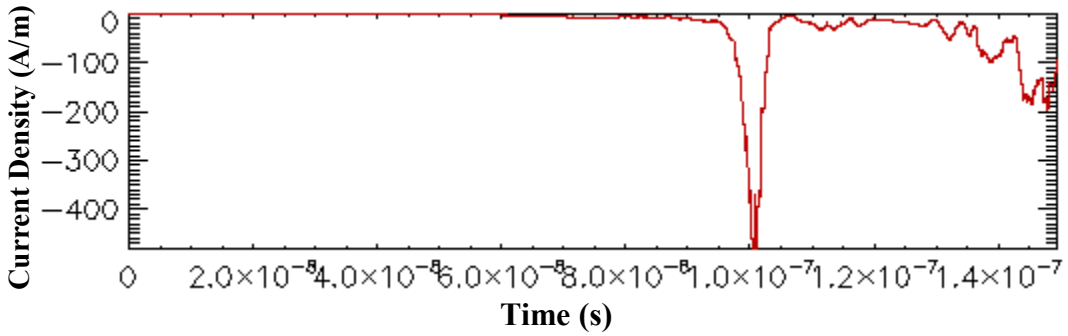

Figure 83: **Modulated anode linear current density versus time during device operation for the five-sided faceted cathode with 25% overlap, showing current spike at around 102 ns.**

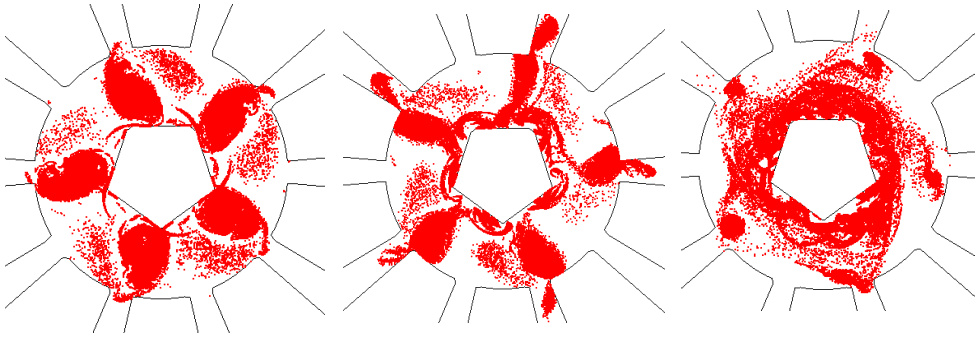

Figure 84: **Transition of the spokes during the current instability for the modulated, addressable current sources for the five-sided faceted cathode with 25% overlap. Spokes are shown (a) before current spike at 110.3 ns, (b) at current spike at 113.1 ns, and (c) after spokes collapse at 116.3 ns.**

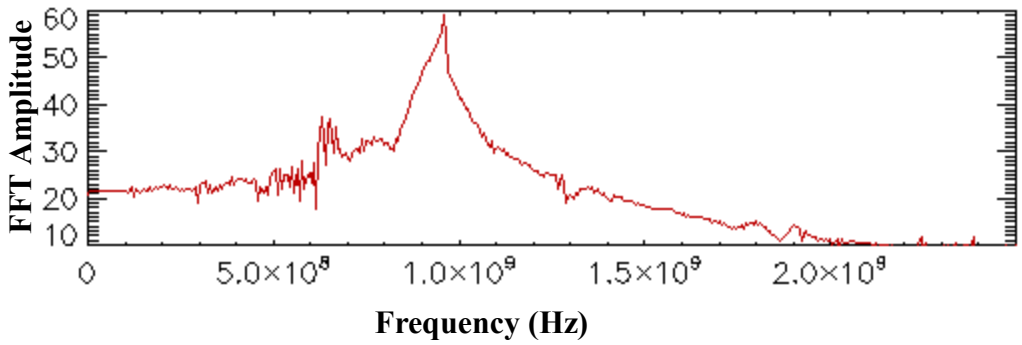

Figure 85: Fast Fourier Transform (FFT) of the loaded cavity voltage from VORPAL Simulation for the modulated, addressable, current source for the five-sided faceted cathode with 25% overlap. This plot indicates that the π-mode is dominant at the frequency of operation of 957 MHz.

Furthermore, it is noticed that for this model with current overlap, the current spike is more pronounced in terms of the spoke shape (thin and long spokes extending inside the anode cavity). The clumps extend towards the anode as the anode current goes very high and then collapse as they try to recover. This effect could be attributed to the modulation technique, because the electrons are controlled and injected synchronous with the RF field, a large fraction of the electrons travel to the anode, and there are not enough asynchronous electrons that go back to the cathode and keep the process going.

7.4 Modulated Five-Sided Cathode with Time Overlap and DC Hub

The DC hub technique was combined with the overlap to fill the gaps and feed electrons to the spokes to maintain stability. Different percentages of current were simulated for the DC hub. Figure 86 shows the best result with a 5% J'_e DC hub. The DC hub is shown with the green electron macroparticles, and the overlap electrons are shown in red. In VORPAL, this is an interchangeable feature; the green electrons were chosen to be on top of the red to demonstrate that the spoke gaps and voids were filled by the

implementation of the DC hub. In Figure 87, an example of the model with modulated overlap case is shown next to the model with only the DC hub electrons shown. Here the different electrons sources can be distinguished. The DC hub was a good solution to the stability and gap problem, as can be seen in Figure 86. The device starts oscillating; the spokes look very well formed, and stability of the model is improved. However, the issues presented with the five-sided, faceted cathode require more study and simulation to develop stable oscillations and to improve startup time. Even though this additional analysis was considered, it was found that a simpler solution to minimize the problems was to use the ten-sided faceted cathode. This model is covered in the next section.

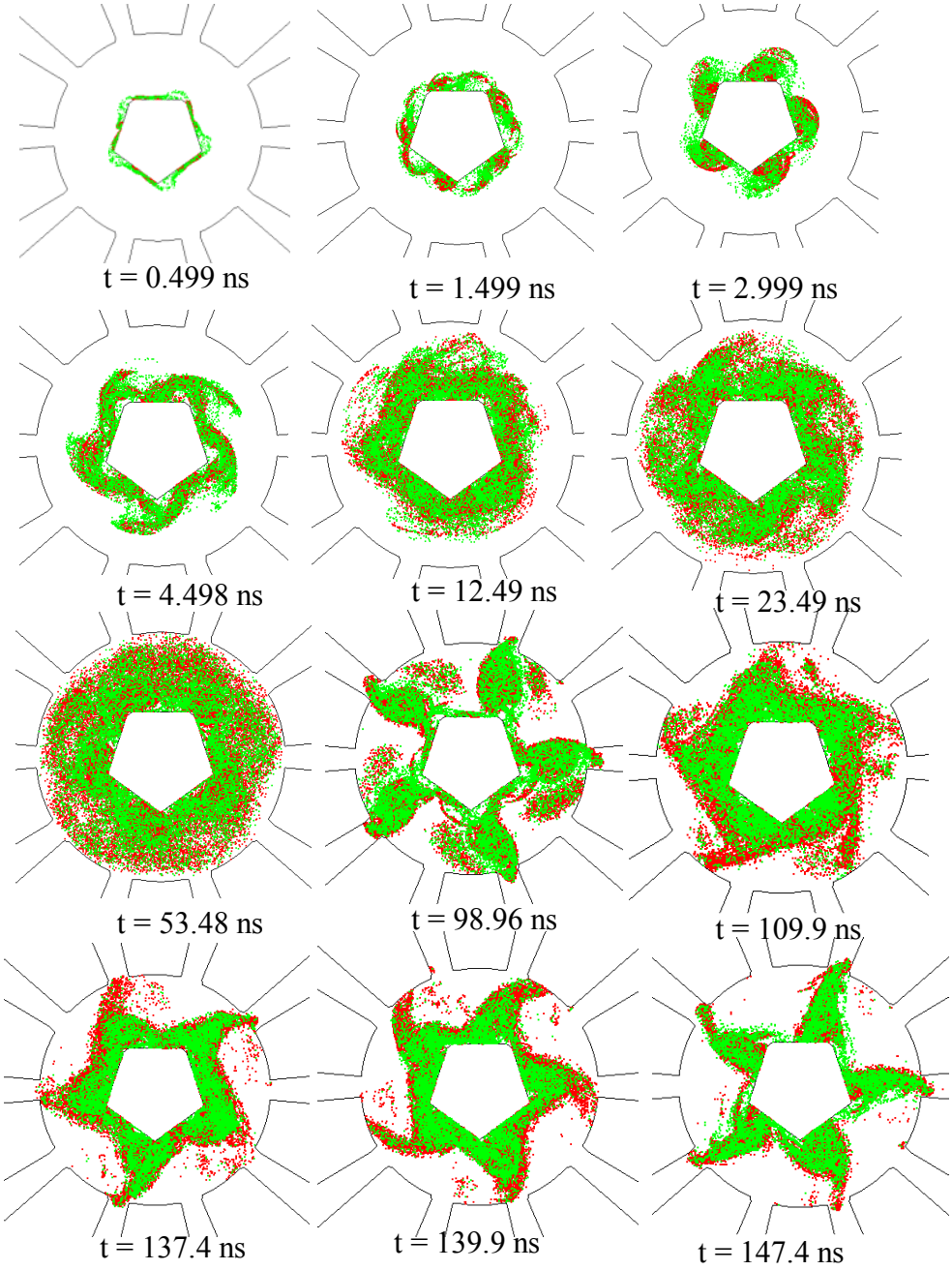

Figure 86: **Five-sided faceted cathode with modulated, addressable current sources with current overlap and DC Hub. This diagram shows a current overlap of 25% (red electrons) and a 5% current DC hub (green electrons). The frequency of modulation is 957 MHz, τ_{RF} = 1.04 ns, $\Delta t = 1/5\ \tau_{RF}$, τ_{ov} = 0.0520 ns. In this figure, green electrons are shown on top of red electrons; this is in an interchangeable feature in VORPAL. Green electrons were chosen to be seen on top to demonstrate the filled up gaps presented with only modulated and overlap technique.**

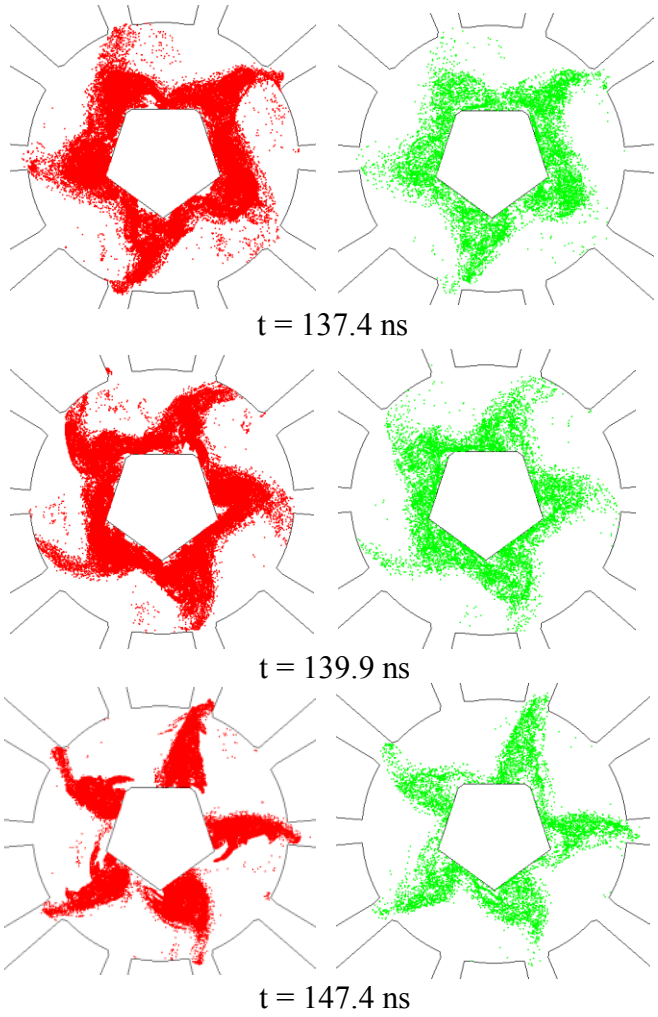

Figure 87: **Five-sided faceted cathode showing: on the left column the modulated plus current overlap (25% overlap) simulation electrons and on the right the DC hub (5% J'_e) electrons. It shows the comparison between the two, and it can be seen that the gaps are filled by the green DC hub electrons.**

7.5 Modulated Ten-Sided Faceted Cathode

The ten-sided, faceted cathode was chosen to reduce the stability issues presented with the five-sided faceted cathode. It was found that this geometry gave a more stable model; therefore, it was used for the remaining studies. The ten-sided cathode contains 3 emitters per facet, which can be turned ON and OFF at any desired time. Since for the rising sun magnetron the π-mode is the primary mode, the 10-cavity device has 5 spokes in π-mode. Therefore, a single spoke rotates past 2 cathode facet plates (6 emitters total) every RF period. For this reason, 5 total emitters were turned ON simultaneously on every other facet at the same facet location at a frequency of 957 MHz with an ON time of $1/6\tau_{RF}$. Figure 88 shows the setup of the discrete current sources on the ten-sided faceted cathode, showing 3 emitters per facet with all of the emitters ON at the same time for demonstration purposes.

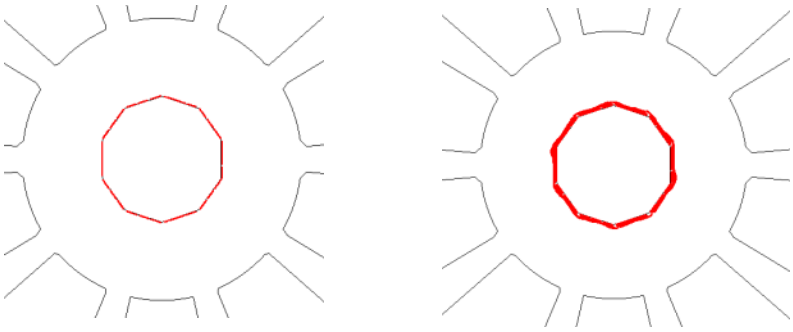

(a) **(b)**

Figure 88: Ten-Sided Faceted cathode showing discrete current sources setup for (a) 0.0163 ns and (b) 0.326 ns. There are three emitters per facet. All emitters are ON at the same time.

Figure 89 shows the diagrams with no applied B field to show the emitters turning ON in sequence. This example shows one RF period of the simulation. It can be seen that 5 emitters are initially turned ON at the same time on every other facet, and then these are followed by the remaining emitters as they complete the first RF period of the simulation.

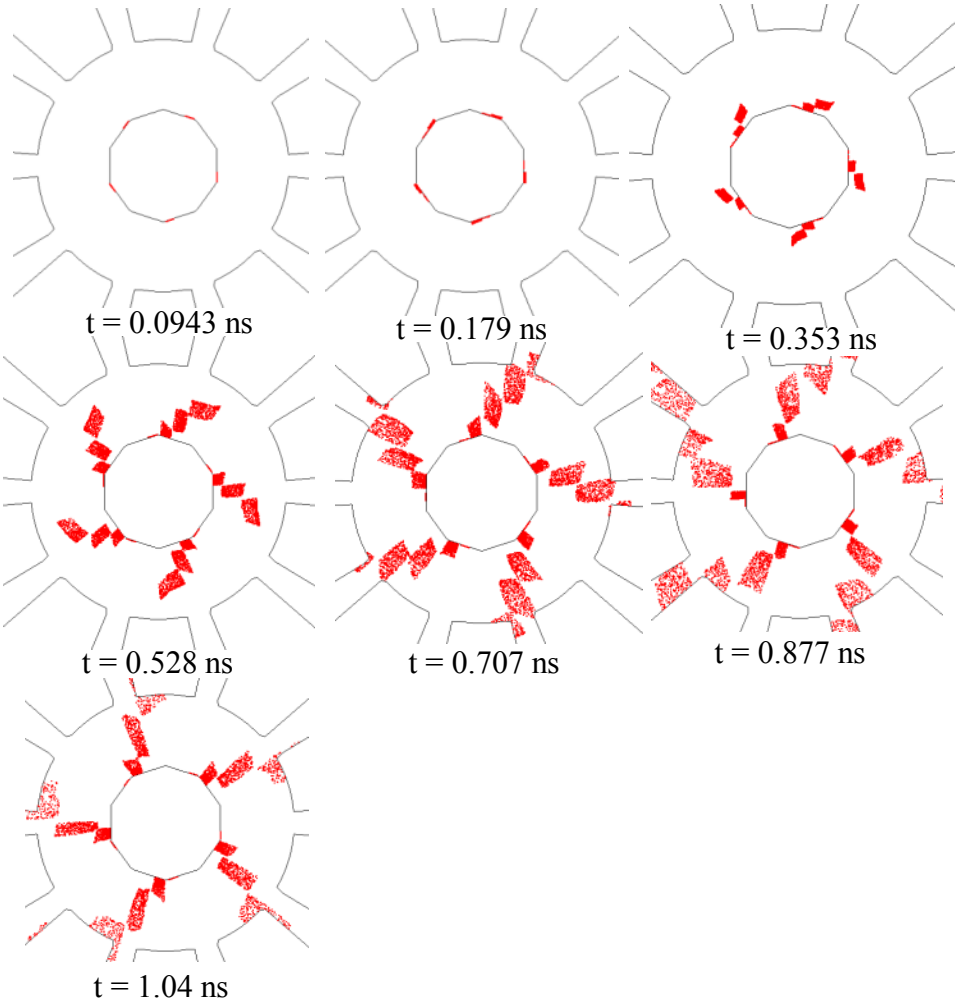

Figure 89: **Ten-sided faceted cathode with modulated, addressable current sources, with B field turned OFF. This shows the emitters turning ON in sequence. The diagrams show one RF period (two facets), τ_{RF}=1.04ns, $\Delta t = 1/6\ \tau_{RF}$. Frequency of modulation is 957 MHz.**

Figure 90 shows the results for the modulated, addressable cathode for the ten-sided geometry. These results demonstrate that the concept to modulate the current injection and control the spokes is viable. As can be seen in the figure, the spokes initially try to form as electron clumps before they develop into complete spokes. These electron clumps were seen in both faceted cathode geometries as an initiation to device spoke formation and oscillation. A similar behavior is observed in the transparent cathode magnetron developed by the University of New Mexico [16]. However, the two mechanisms of operation for the transparent cathode and the modulated, addressable cathode are different; nevertheless, the shape of the spokes as they start forming for both models is very similar. Again, gaps or voids are seen in the electron spokes.

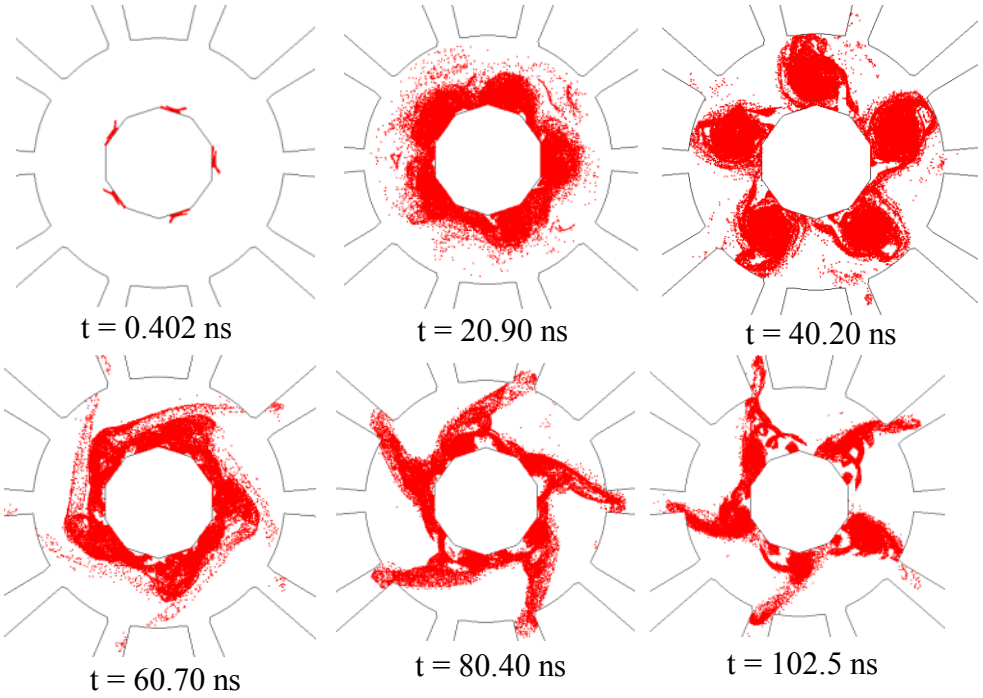

Figure 90: Ten-sided faceted cathode with modulated, addressable current sources. The frequency of modulation is 957 MHz, τ_{RF}=1.04 ns, Δt = 1/6 τ_{RF}.

Figure 91 shows total emitted linear current density versus time. This simulation was run with no applied B field to check injection current. The current averages to 326

A/m as expected. Figure 92 shows the anode linear current density during the device operation. In this case, the current spikes, except for the first spike, are less pronounced and are minimized. The recovery time from the current spike is also minimized. However, one large spike is observed. This single spike was also observed for the continuous model. On the other hand, by inspecting the device oscillations, a more stable model is observed. Figure 93 shows the cavity voltage frequency versus time, showing the startup time of the device at 50 ns, which is much shorter than the 110 ns for the continuous current case. Figure 94 shows the FFT of the cavity voltage. As can be seen in this plot, the frequency of operation for the device is also at 957 MHz. It is also noted that the 650 MHz mode is still present in this case.

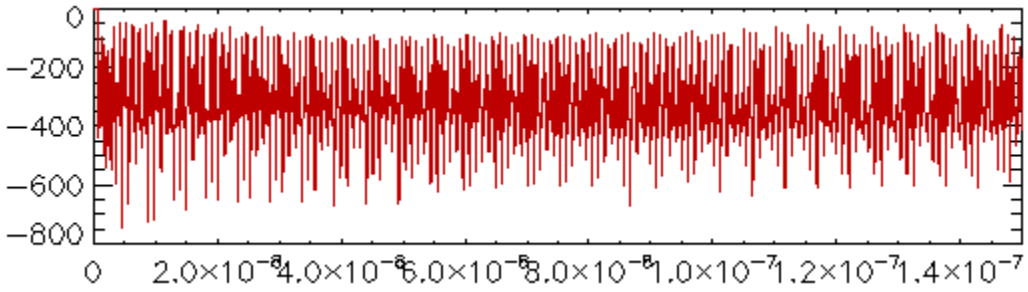

Figure 91: Modulated total emitted linear current density versus time with no applied magnetic field (B=0) for ten-sided faceted cathode.

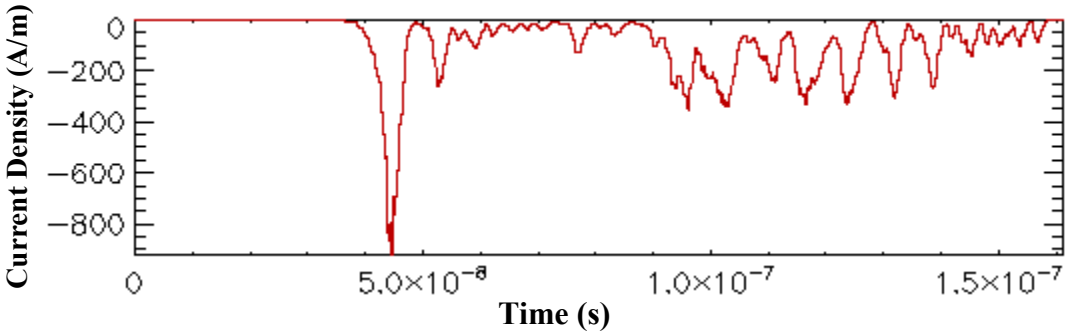

Figure 92: Modulated anode linear current density versus time during device operation for the ten-sided faceted cathode.

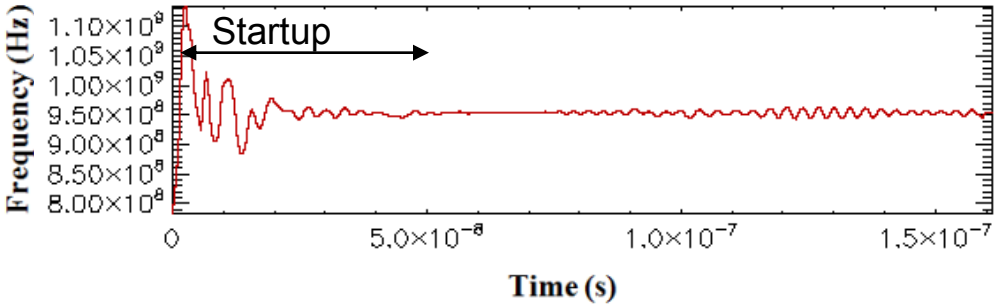

Figure 93: Modulated ten-sided faceted cathode cavity voltage frequency versus time with moving window, showing the startup time of the device at 50 ns showing the operating frequency (π-mode) at 957 MHz from VORPAL.

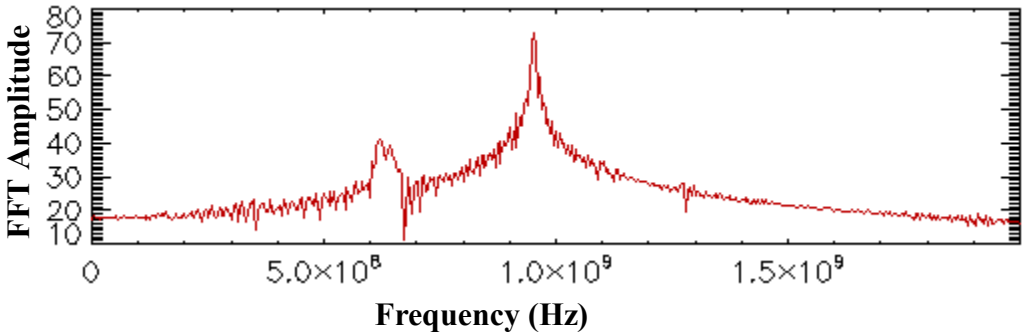

Figure 94: Fast Fourier Transform (FFT), over entire simulation time, of the loaded cavity voltage from VORPAL simulation for the modulated, addressable, current source, ten-sided faceted cathode. This plot indicates that the π-mode is dominant at the frequency of operation of 957 MHz.

7.6 Modulated Ten-Sided Faceted Cathode with DC Hub

For the ten-sided cathode geometry, it was not necessary to implement the current overlap technique because the model showed oscillations just with the modulation of the current only. However, as can be seen in Figure 90, some holes and gaps were observed in the spokes; to fix this problem, a 5% J'_e DC hub was implemented to cover the gaps. This result is shown in Figure 95. The green electrons show the DC hub, and the red electrons are the particles corresponding to the modulated only case. It is observed that

the DC hub successfully fills up the holes in the spokes. Therefore, the DC hub could be used to minimize problems with the spoke formation in the modulated case.

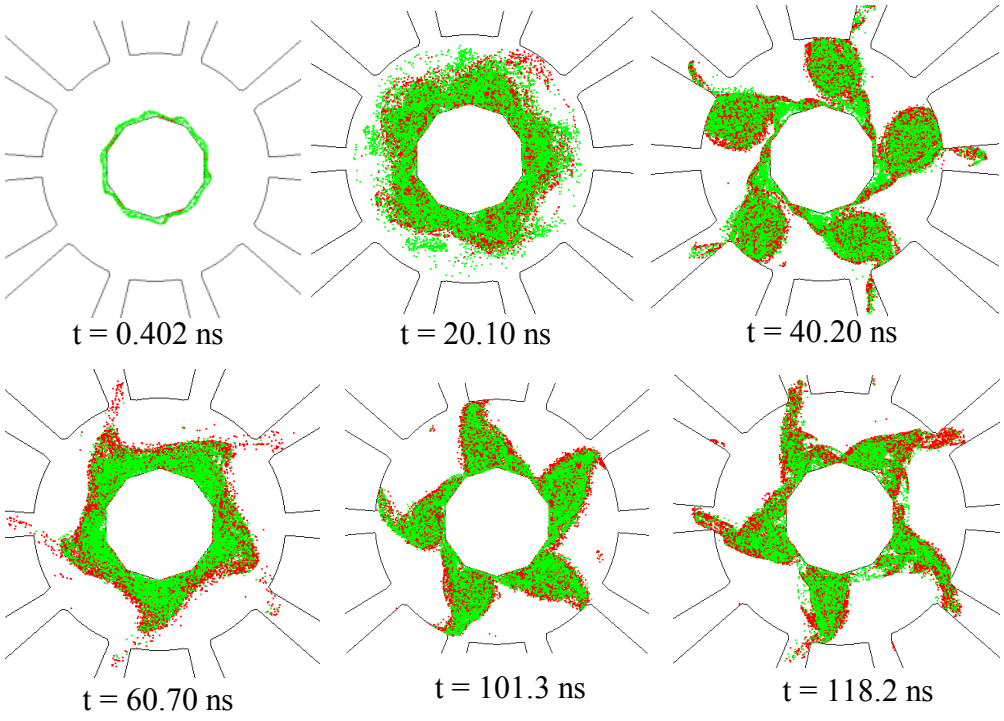

Figure 95: Ten-sided faceted cathode with modulated, addressable current sources with DC Hub. This diagram shows a 5% current DC hub (green electrons). The frequency of modulation is 957 MHz, $\tau_{RF} = 1.04$ ns, $\Delta t = 1/6\ \tau_{RF}$.

The startup time was also studied for this particular geometry; it was found that the ten-sided modulated case has a shorter startup time than all other cases with oscillations starting as soon as 35 ns (see Figure 96). The modulation reduces startup time as was expected. In general, the modulated case cuts the startup time by greater than 50%. As the current density is decreased, the startup time increases, but more slowly than for the continuous current cases. Similarly to the cylindrical cathode model, the

modulated ten-sided faceted cathode does not start for currents below 230 A/m. For currents < 230 A/m, the device switches completely to the lower mode 650 MHz frequency, and it never starts at the π-mode. As mentioned previously, the cause of this behavior needs further study.

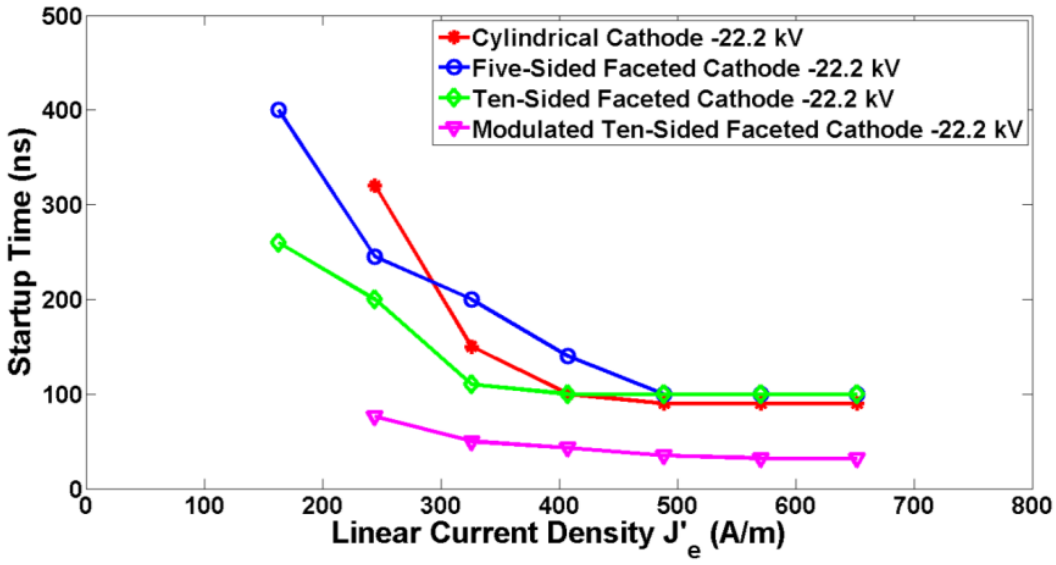

Figure 96: Comparison of startup time versus total emitted linear current density for different cathode geometries: cylindrical and faceted, including continuous current source model and the modulated, addressable current source model for the ten-sided faceted cathode.

Figure 97 shows a plot of the anode current density, J'_a, versus the total emitted linear current density, J'_e, for the ten-sided faceted cathode with continuous current source and with the modulated current source. As can be observed in the curves, the anode current density drawn by the device increases roughly linearly with the total emitted linear current density. It is also observed that the modulated, addressable cathode draws more current than the continuous source model, which means there is an increase in the linear input power density. This result was expected from the modulated,

addressable cathode because electrons are injected in phase. Hence, they will be synchronous and will be more likely to give up energy and transit to the anode.

Table 7.1 shows a summary of results of the linear anode current density, the calculated input power density, the loaded cavity power, and the calculated efficiency for the different cathode geometries at the reference parameters V_{ca} = -22.2 kV, B = 0.09 T, and J'_e = 326 A/m. It is observed that the loaded cavity power is very similar for the three cathode geometries with a continuous current source. The loaded cavity power results also show that the modulation technique increases the output power density and efficiency, as was expected, showing an efficiency of about 95.4%. For the modulated case, the anode current density increases to 100 A/m, and the output power approximately doubles to 2.1 MW/m. Overall, the efficiency increases from 80-85% to 95%. Note, this efficiency should not be taken as absolute value and should only be used for comparison with the continuous current source cases. As was mentioned in Chapter 5, this is a 2D simulation, and there is no real output port; therefore, this power density is not the real coupled output power. However, these results can be used as a relative estimation of the power at the loaded cavity as a demonstration of the modulated cathode increasing the loaded cavity power as was expected.

Figure 98 shows a graph of the loaded cavity power density versus the total emitted linear current density. It is observed that the loaded cavity power density curves present an almost linear increase in power as the emitted current density increases. This behavior is also comparable to the same linear increase in anode current as the total emitted current density increases in the previous figure. As can be seen in the figure, the power density goes up as the emitted current increases; it is clear from the curve that the

modulated current model has a higher loaded cavity power density than the continuous current source model.

Table 7.1: Current densities, power densities, and efficiencies for various cathode geometries: cylindrical, five-sided and ten-sided cathode for the reference parameters V_{ca} = -22.2 kV, B = 0.09 T, and J'_e = 326 A/m.

Cathode	Anode Current Density J'_a (A/m)	Input Power Density (MW/m)	Loaded Cavity Power Density (MW/m)	Efficiency η (%)
Continuous Current Cylindrical	60.81	1.35	1.0	74.3
Continuous Current Five-Sided	69.36	1.54	1.2	77.9
Continuous Current Ten-Sided	67.56	1.5	1.2	80.0
Modulated Current Ten-Sided	100	2.2	2.1	95.4

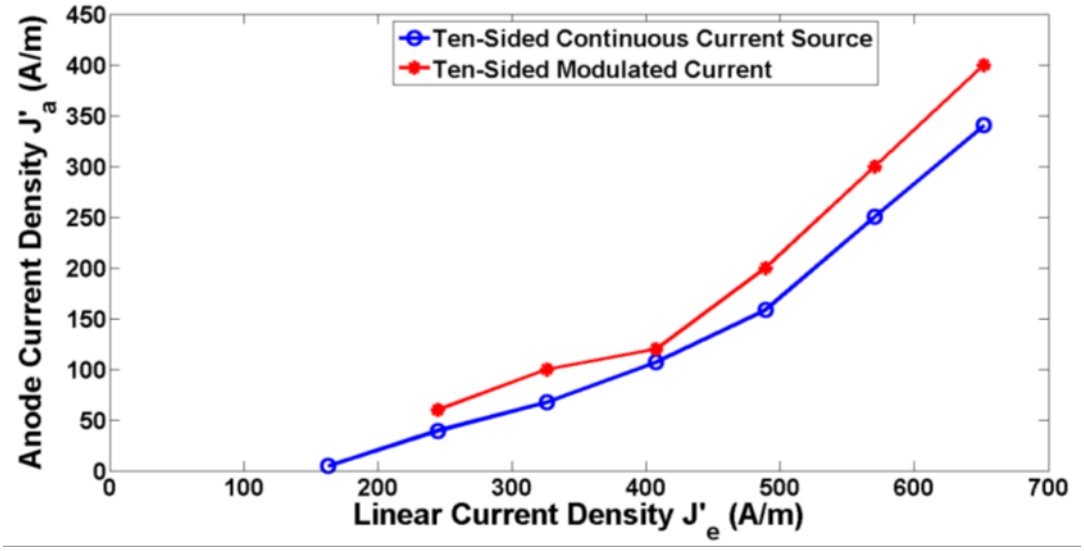

Figure 97: Anode current density versus total emitted linear current density for the ten-sided faceted cathode with continuous current source and modulated current source.

Figure 99 shows the plot of efficiency versus injected current density for both the continuous current source and the modulated current source model for the ten-sided faceted cathode. The modulated current curve shows higher efficiencies until $J'_e \approx$ 500 A/m. It is observed that the maximum efficiency is obtained at the reference parameters V_{ca} = -22.2 kV, B = 0.09 T, and J'_e = 326 A/m in both models. As the current increases, the efficiency decreases, and the efficiency curves for the two cases (continuous and modulated current source) start to merge. At this point, for high current densities ($J'_e >$ 500 A/m), the space charge effects become more significant, and the hub will get closer to the anode. This will result in the electrons having less potential energy to give up, and therefore, the loaded cavity power absorbed will be less. Even though the spokes are formed, they will start to spread out because of the space charge effects; therefore, the peak fields will saturate. This saturation will limit the device efficiency. Therefore, the advantages of using a modulated current source are no longer applicable for this regime.

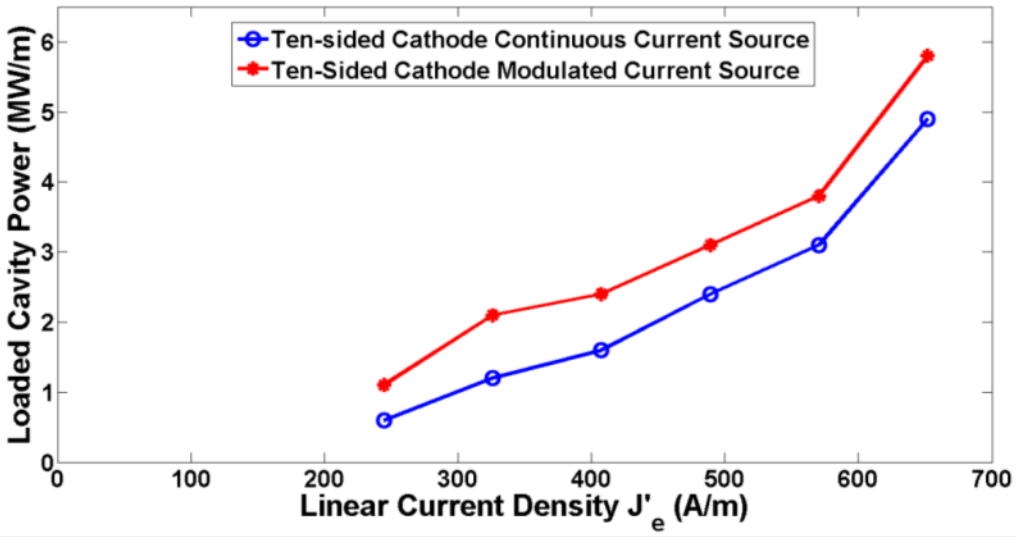

Figure 98: Loaded cavity power versus total emitted linear current density for the ten-sided faceted cathode with continuous current source and modulated current source.

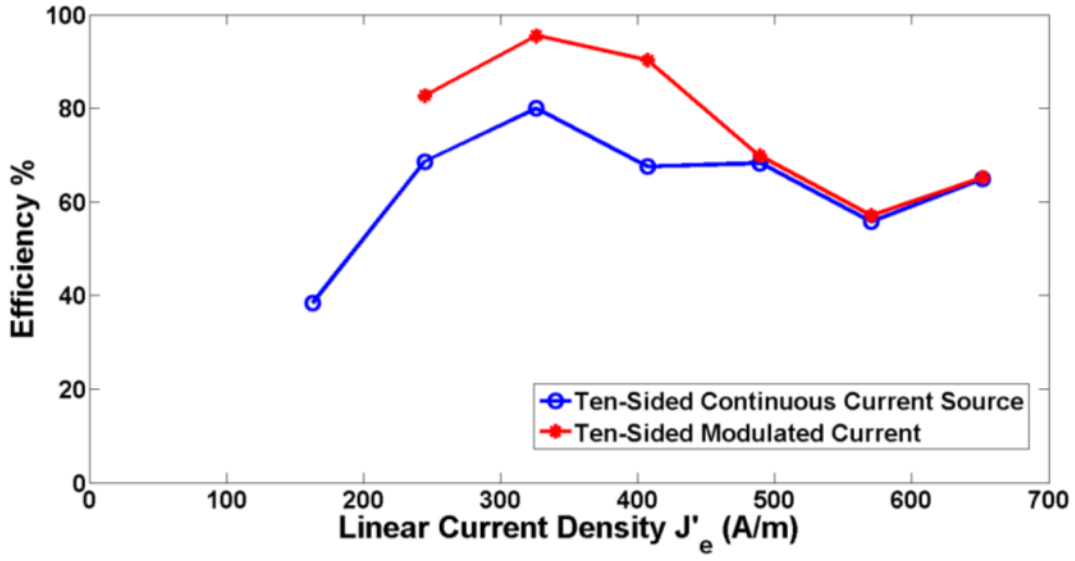

Figure 99: Efficiency versus total emitted linear current density for the ten-sided faceted cathode with continuous current source and modulated current source.

7.7 Modulated Ten-Sided Faceted Cathode with Active Phase Control

After these studies, the simulation of the ten-sided cathode was run three different times for both the modulated and the reference (non-modulated) cases. Figure 100 shows the spokes during oscillation. For the modulated case (Figure 100(a)), the spokes are at the same exact location at the same simulation time (76.38 ns); it can be seen that the spokes remain at the same location because of the modulated current control. Note that while the two bottom spoke simulations are very similar, they are not identical. For the reference case (Figure 100(b)), it shows that the spokes are at three different locations at the same simulation time (322.12 ns) because of the random startup nature of the magnetron. Hence, the modulated, addressable cathode controls the magnetron startup and RF phase.

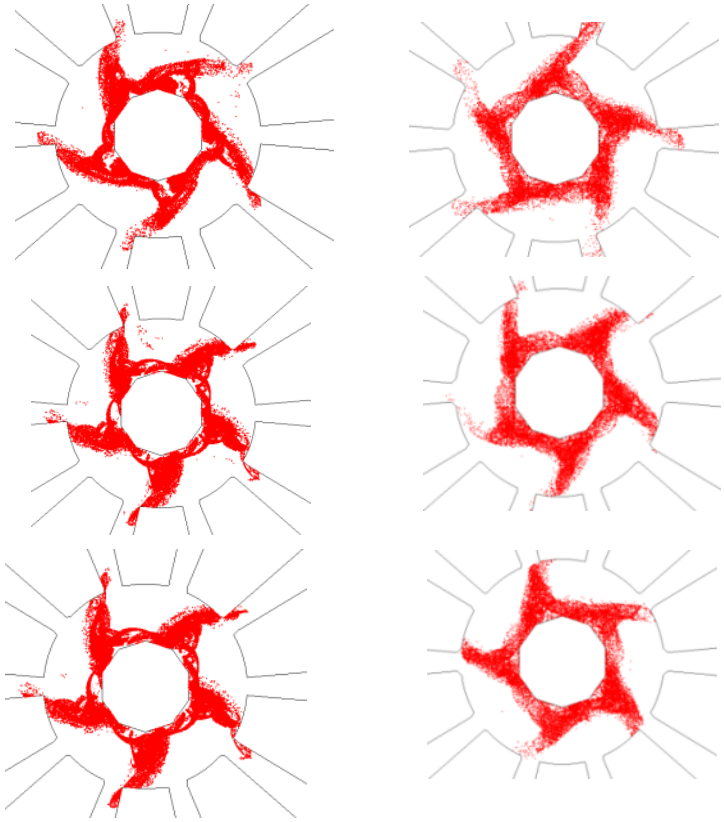

(a) (b)

Figure 100: Ten-sided faceted cathode with (a) Modulated, addressable current sources: Spokes are aligned at the same location in time (76.38 ns) for three different simulation runs, (b) Continuous current source: Spokes are not aligned at the same location in time (322.12 ns) for three different simulation runs.

Using the modulated, addressable, cathode, the phase can also be dynamically controlled. The next results show the case when a phase shift of 180° is driven during oscillation. The phase shift is initiated at 88.4 ns during a reference simulation run, after the device has achieved stable oscillation. As can be seen in Figure 101, the spokes are shown at a time of 82 ns before the 180° shift. Then 14 RF periods later, at a time of 96.8 ns when the spokes have shifted 88.5°, the spokes are shown again in Figure 101(b). The spokes are then shown at two additional times after the phase shift ($17\tau_{RF}$, $35\tau_{RF}$). The

spokes clearly shift location over these times. As can be seen in Figure 101 (d), the spokes have fully shifted location to the adjacent cavities after 35 RF periods, demonstrating the 180° shift as expected. However, these results demonstrate that the modulated, addressable cathode can be used to actively control the RF phase.

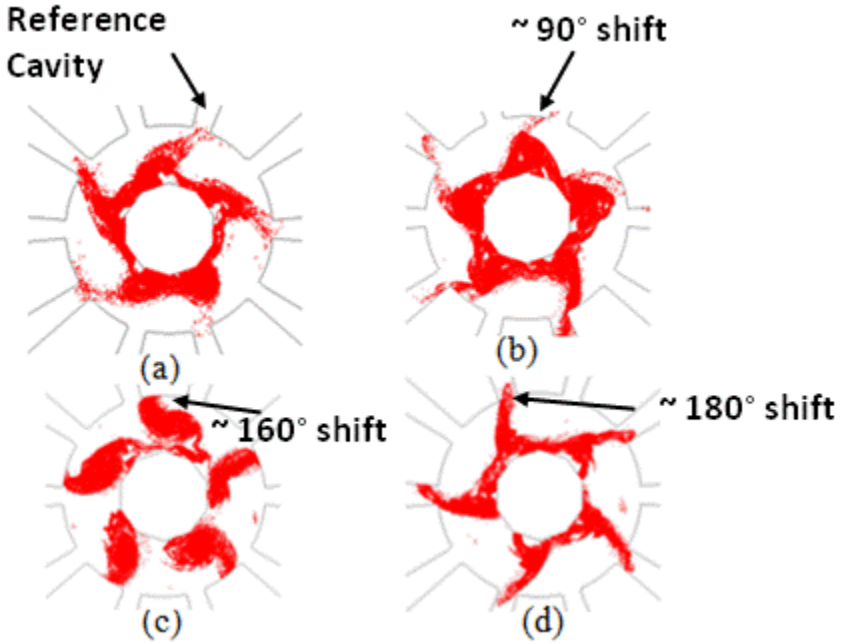

Figure 101: **Ten-sided faceted cathode with modulated addressable current sources, showing transition to a phase shift of 180°. (a) Reference case: Phase = 0° at 82.0 ns, phase shift initiated at 88.40 ns, (b) after 14.5 RF periods (t = 96.8 ns) from the reference, 8 RF periods from the phase shift, (c) after 17 RF periods (t = 100.0 ns), 11 RF periods from the phase shift, (d) after 35 RF periods (t = 118.4 ns), 29 RF periods from the phase shift.**

Figure 102 shows the RF B_z field versus reference time for the ten-sided case with modulated, addressable, current sources. These plots show the transition of the phase shift initiated at 88.40 ns. The RF B_z curves show the shift 14, 17, and 35 RF periods after the reference point. Note that the x-axis is a referenced time with the purpose of showing the phase shift. The real time windows were chosen to cover these ranges: the phase 0° reference at t = 82 ns, phase = 88.5° at t = 96.8 ns, phase = 160.05° at 100 ns, and phase = 178.9° at t = 118.4 ns. These RF B_z curves (Figure 102) also corroborate the results obtained by visually inspecting the spoke phase shift in Figure 101. Figure 103 shows the cavity voltage frequency versus time with the phase shift. In this plot, it can be observed that after the phase is shifted, the model is stable, and the π-mode operation at 957 MHz is maintained.

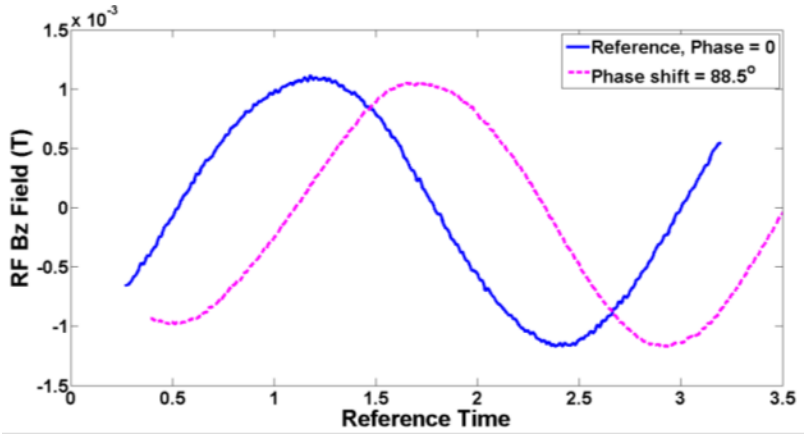

(a)

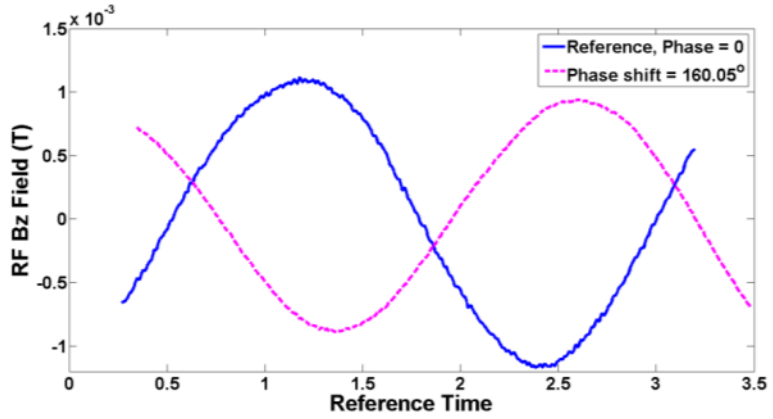

(b)

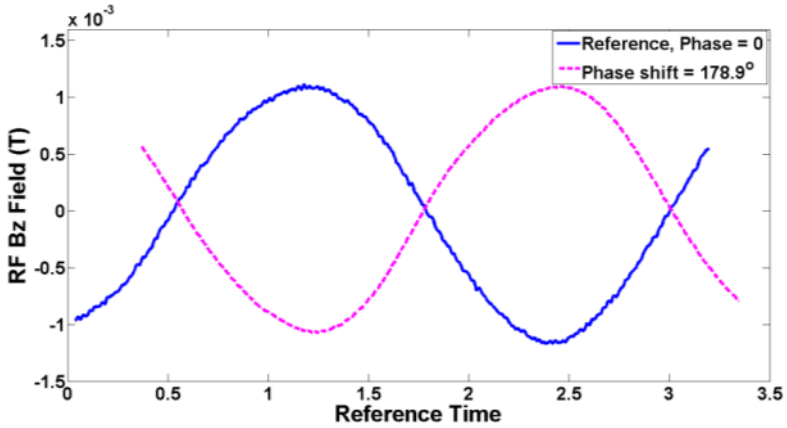

(c)

Figure 102: **RF B_z field vs. reference time; showing transition to a phase shift of 180° initiated at 88.40ns. Reference: Phase=0° (a) After 14.5 RF periods (t=96.8ns) from reference, 8 RF periods from phase shift, (b) after 17 RF Periods (t=100.0ns) from reference, 11 RF periods from phase shift, (c) after 35 RF Periods (t=118.4ns) from reference, 29 RF periods from phase shift.**

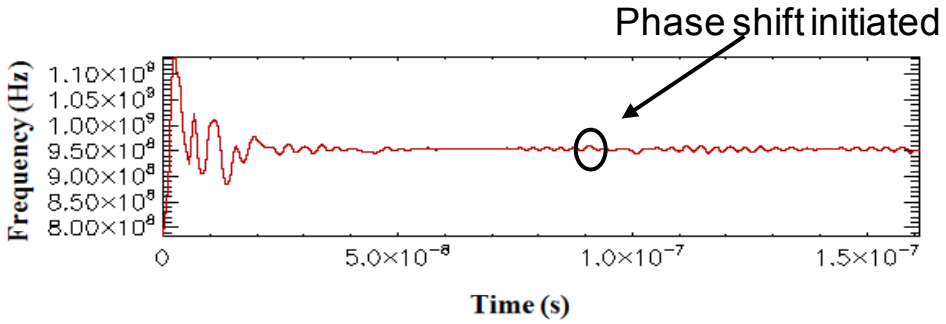

Figure 103: Modulated ten-sided faceted cathode cavity voltage frequency versus time, showing the startup time of the device with phase shift initiated at 88.40 ns. The operating frequency (π-mode) is at 957 MHz from VORPAL.

Finally, in Figure 104, a curve of the phase versus time is graphed. The phase is determined from the RF B_z plots referenced to the phase = 0° case. The graph shows the transition from 0° to 180°. As can be seen in the curve, the phase change occurs slowly until it completely transitions to steady state at 180°. This temporal transition is due to the quality factor, Q, of this magnetron. For higher quality factors, typical for oscillators, it is difficult to have instant changes in phase, as was expected. It can be seen in the results that it takes approximately 25 RF periods after the phase change for the device to fully shift phase to 180°. Therefore, for future work, the study of the phase shift with different values of Q should be considered. It is expected that for a lower quality factor the phase shift (transition from phase 0° to desired phase) will occur more rapidly.

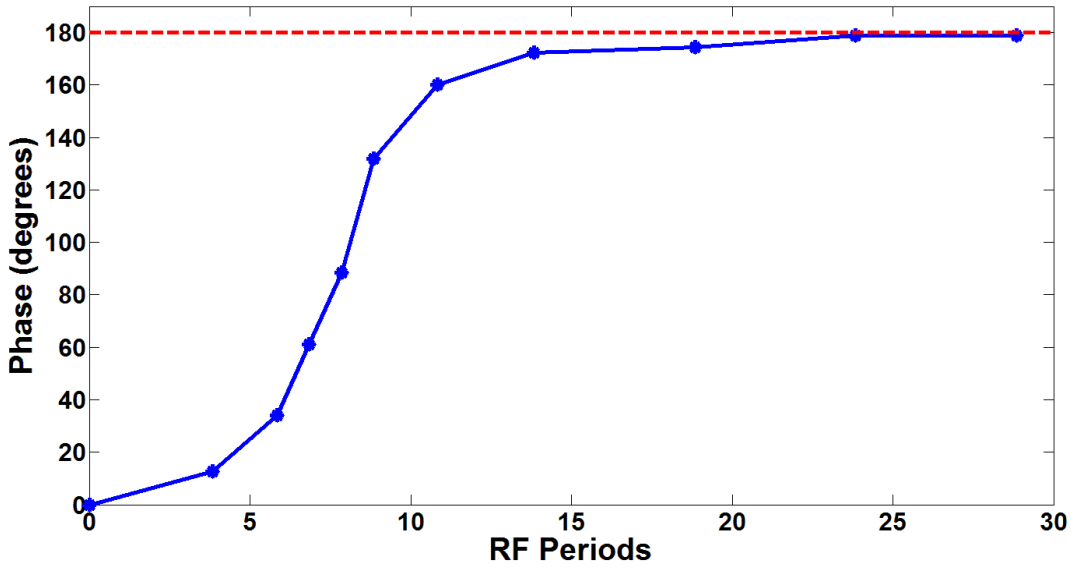

Figure 104: Phase versus RF Periods. Curve for the ten-sided faceted cathode with modulated, addressable current sources. The phase shift is initiated at 88.40 ns. The RF periods for this plot are counted after the phase shift.

7.8 Summary of Results

The ten-sided faceted cathode with modulated current sources improved magnetron operation. It reduced the startup time from 110 ns to 50 ns for the reference case. It gave a higher cavity power density, about 80% increase; therefore, higher efficiency. For the efficiency calculations, the axial losses (2D model) and gated emitter switching power were not included. It was demonstrated that the modulated current sources control the spoke locations and the RF phase; therefore, dynamic phase control was also demonstrated. As shown in Figure 104, the transition from 0° to 180° is observed, showing active phase control. Therefore, the research objective of this dissertation was achieved.

7.9 Discussion of Application of Modulated Addressable Cathode

This research work presented the study of a modulated addressable cathode using discrete current sources modeled in VORPAL. Gated field emitters [94] are proposed for these modulated sources. They present a number of advantages, including a distributed cathode. These emitters can be turned ON and OFF with relatively low (<500 V) gate voltage; they can also be used in arrays, which allows spatial control of the current injection. In order to protect the emitters from ion back bombardment, the proposed concept uses emitters placed below the interaction space in a shielded structure. The spatial and temporal modulation of the gated field emitter arrays is beneficial to control the optimal location of electron injection and the frequency of oscillations. The modeling described in this work is intended for lower frequency (<10 GHz) devices. It has been demonstrated that gated field emitters can be modulated at frequencies up to 10 GHz [95]. In addition, gated field emitters have been used in traveling wave tubes (TWT) [73, 74]. Such results provide the basis for the proposed concept.

The ten-cavity rising magnetron presented in this work operates at ~ 1 GHz, with a cathode radius of 1 cm and an anode radius of 2.24 cm. An actual device would have an axial length of 10 cm [12]. The cathode-anode voltage is set to -22.2 kV with a total injected current of 32.6 A using the 10 cm length. Using the axial power density of 2.1 MW/m from the simulation, this device would generate an output power of about 210 kW. For the five-sided cathode, each facet would emit 1/5 of the total current, 6.52 A. In the case of the ten-sided faceted cathode, each facet would emit 3.26 A. The current density of this device, if emitting from half of the cathode area, is ~ 1 A/cm^2, and it has

been demonstrated that emitter arrays can work at current densities from 100-1000 A/cm^2 [95, 96].

The current injection can also be tuned to optimize the performance of the device. It might also be possible to use only a small amount of modulated injection current (<10%) to control oscillations of the magnetron from startup.

In this model, the slits to protect the emitters were designed for an 8 μm slit exit opening. Since the maximum current possible is extracted from the field emitters, the best approach is to have the smallest slits possible to allow for the highest number of emitters [12]. It is also important to study the emitter capacitance and its relationship to the rise and fall times of the gated emitter pulse. A step function was used for the simulation of the pulse time of the emitters; for a realistic application, it is recommended to design a new circuit model that will allow simulation of the rise and fall time of the elements, which will have a closer approximation to actual emitter operation. Typically, the required RC time for gated field emitters for this application is < 0.2 ns; therefore, the required capacitance per unit area is very small.

Additionally, there is a switching power associated with the emitter gate voltage, and this power can be calculated by using:

$$\boldsymbol{P_s = \frac{1}{2} C_F V_F f} \tag{7.1}$$

where C_F is the emitter capacitance, V_F is the emitter switch gate voltage, and f is the frequency of modulation. For a practical application, using the results from this research work and assuming a switching power of 10% of the power output (21 kW); the required capacitance can be estimated. For example, if emitting from half of the cathode area (~ 31

cm^2), with a typical emitter switching voltage of 100 V, the emitter capacitance must be < 4.2 nF, which results in 134 pF/cm^2. This capacitance value is very small for gated field emitters; therefore, its application will require a much lower emitter voltage value (30-40 V) to allow for a higher capacitance (on the order of nF/cm^2 [96]). If the switching power is considered for the efficiency calculation, using the previous estimates, the efficiency will be of 85%.

CHAPTER EIGHT: SUMMARY AND CONCLUSIONS

The simulation work presented in this dissertation has demonstrated interesting effects in magnetron research. A magnetron configuration implementing gated field emitters as the cathode by placing the emitters in a shielded structure was proposed [12] and simulated using Lorentz2E. In order to implement this structure, a faceted cathode is needed because gated field emitters must be fabricated on a flat surface. Lorentz2E simulations were performed to simulate the electron trajectories and to investigate the sensitivity of the electron injection from the field emitters due to changes in voltage and geometry. It was found that 98% of the rays could exit the slit with a voltage sensitivity (ΔV) between 100-200 V. This is an important result demonstrating that a low sensitivity would be required for the actual fabrication and design of the device with gated field emitters.

The main part of this dissertation was the modeling of this faceted magnetron model using the PIC code VORPAL. The gated field emitters were modeled as modulated, addressable, current sources in VORPAL. The modeling was carried out in two parts: the magnetron model was first simulated using a continuous current source and then with the modulated, addressable current sources. Both models were implemented using a cylindrical cathode and faceted cathodes (five and ten-sided). The continuous current source models were compared with previous results simulated in ICEPIC. The results were very similar and demonstrated the concept of using faceted cathodes. The

three models (cylindrical, five and ten-sided faceted cathodes) oscillated at the π-mode, at a frequency of 960 MHz for the cylindrical cathode and 957 MHz for the faceted cathodes. It was found that a mode of lower frequency at 650 MHz was present in all three models; this was found to be a characteristic of this magnetron geometry.

The five-sided faceted cathode presented various issues; the main issue was an instability present in the anode current. This instability was a result of the cathode shape. It was attributed to the fact that the electron trajectories around the five-sided cathode become distorted and appeared to create too many synchronous electrons. These electrons formed clumps that extended to the anode causing the spokes to disconnect and then collapse. This issue was also present with the modulated, addressable current source model. In addition, gaps in the electron hub and lack of stability were observed in the modulated, addressable current sources for the five-sided faceted cathode. To minimize these issues, a current overlap and the use of a "DC hub" were proposed. Both methods seemed to improve the stability of the device. However, a better solution to minimize these problems, particularly the current instability, was the use of a ten-sided faceted cathode.

The ten-sided cathode approach helped to solve these issues; it minimized the current instability and also improved the overall startup time of the device. Therefore, this geometry was used in the remaining simulations. The simulations with the modulated, addressable cathode showed that the concept of injecting current to control the spokes is viable. The modulated case (using the ten-sided faceted cathode) demonstrated the shortest startup time with oscillations beginning as soon as 35 ns. As expected, the current modulation reduced startup time. Also, although results are 2D with

no output port, the loaded cavity power was higher, thus demonstrating higher efficiency. Although higher efficiency was demonstrated, several points must be considered. Because the simulation was 2D, axial losses are not included. In addition, the modulated cathode requires switch power to turn the emitters ON and OFF. This power could be large and was not included in the efficiency calculation.

The remaining simulations were used to study phase control. It was shown that the modulated cathode controlled the spoke locations and, hence, the RF phase. For normal cathodes, the phase is random. Next, the phase was shifted 180° during oscillation. This change was observed by inspecting the spoke locations compared to a reference case and by plotting the RF B_z field for different points in time compared to the reference. The phase shifted 180° in 25 RF periods. Therefore, active phase control was demonstrated and the research objective of this dissertation was achieved. More simulations are required to determine the details of the phase shift timing.

Based on these results, the modulated, addressable cathode could be used for several applications and studies. An electron source such as gated field emitters or photocathodes is proposed, which could be capable of producing the necessary current and temporal control that is needed for a practical device. This concept could be also implemented in different applications. Future topics for research or analysis would include:

1. The device should be simulated in 3-D with a full power output port to verify the results.
2. A sinusoidal current pulse or a pulse with a variable rise and fall time should be simulated to provide more accurate modeling of a gated emitter pulse.

3. Use Lorentz2E results as input parameters in the VORPAL model.
4. Study of phased controlled magnetrons; multiple devices could be used, where low power magnetrons are combined for higher power output.
5. The device could be used to study noise and active noise generation.
6. It might be possible to use only a small amount of modulated injection current (<10%) to phase control the magnetron from startup.
7. It might be possible to put modulated cathodes into existing magnetrons.
8. The inverted magnetron concept could be used, and it would provide a higher cathode radius, and, hence, larger cathode area. The larger cathode area would reduce current density requirements.
9. The device might also allow both active frequency and active power control. The bandwidth and relationship to the quality factor could be studied.

REFERENCES

[1] G. B. Collins, *Microwave Magnetrons*, New York: McGraw-Hill, 1948.

[2] R. J. Barker, J. H. Booske, N. C. Luhmann, and G. S. Nusinovich, *Modern Microwave and Millimeter-Wave Power Electronics*, pp. 289-334, Piscataway, NJ: John Wiley & Sons, INC., 2005.

[3] D. French, "Investigation of Novel Configurations for High Power Microwave Generation," Nuclear Science, University of Michigan, Ann Arbor, Michigan, 2011.

[4] J. M. Osepchuk, "Microwave power applications," *IEEE Transactions on Microwave Theory and Techniques,* vol. 50, no. 3, pp. 975-985, 2002.

[5] S. Y. Liao, *Microwave Electron-Tube Devices*, pp. 258-301: Prentice-Hall, 1988.

[6] D. M. Pozar, *Microwave Engineering*, 4th ed., pp. 705-707: John Wiley & Sons, 2012.

[7] H. A. H. Boot, and J. T. Randall, "The cavity magnetron," *Journal of the Institution of Electrical Engineers - Part IIIA: Radiolocation,* vol. 93, no. 5, pp. 928-938, 1946.

[8] J. Goerth, "Early magnetron development especially in Germany," *International Conference on the Origins and Evolution of the Cavity Magnetron (CAVMAG)*, pp. 17-22, 2010.

[9] J. M. Osepchuk, "The magnetron and the microwave oven: A unique and lasting relationship," *International Conference on the Origins and Evolution of the Cavity Magnetron (CAVMAG)*, pp. 46-51, 2010.

[10] R. Burman, "Summary of magnetron development," *International Conference on the Origins and Evolution of the Cavity Magnetron (CAVMAG)*, pp. 3-4, 2010.

[11] J. Benford, J. Swegle, and E. Schamiloglu, *High Power Microwaves*, Second ed., pp. 139, 263, New York: Taylor and Francis Group, 2007.

[12] J. Browning, and J. Watrous, "Faceted Magnetron Concept Using Field Emission Cathodes," *Journal of Vacuum Science and Technology B: Microelectronics and Nanometer Structures,* vol. 29, no. 2, pp. 02B109-1 - 02B109-7, 2011.

[13] S. Maurya, V. V. P. Singh, and P. K. Jain, "Study of Output Performance of Partially Dielectric Loaded A6 Relativistic Magnetron," *IEEE Transactions on Plasma Science,* vol. 40, no. 4, pp. 1070-1074, 2012.

[14] M. Franzi, R. Gilgenbach, D. French, B. Hoff, D. Chalenski, D. Simon, and Y. Y. Lau, "Recirculating Planar Magnetron: Simulations and Experiment," *IEEE Transactions on Plasma Science,* vol. 41, no. 4, pp. 639-645, 2013.

[15] D. French, D. Simon, Y. Y. Lau, R. Gilgenbach, B. Hoff, and J. W. Luginsland, "Electron Dynamics and Fast Startup in Inverted Magnetrons," in IEEE International Conference on Plasma Science, Norfolk, VA, 2010, pp. 2.

[16] M. Fuks, and E. Schamiloglu, "Rapid Start of Oscillations in a Magnetron with "Transparent" Cathode," *Physical Review Letters,* vol. 95, no. 20, pp. 205101-1 - 205101-4, 2005.

[17] H. Bosman, M. Fuks, S. Prasad, and E. Schamiloglu, "Improvement of the Output Characteristics of Magnetrons Using the Transparent Cathode," *IEEE Transactions on Plasma Science,* vol. 34, no. 3, pp. 606-619, 2006.

[18] T.-X. Corporation. "Vorpal Reference Manual," http://www.txcorp.com/images/docs/vsim/6.0_docs/reference_manual/VSimReferenceManual.html.

[19] R. T. Rowe, "Geometry and Material Effects on Electron Transport in Hop Funnels," Department of Electrical and Computer Engineering, Boise State University, Boise, 2013.

[20] R. A. Tuck, W. Taylor, M. S. Waite, H. E. Bishop, R. J. Riggs, and J. Browning, "The pFED-a Viable Route to Large Field Emission Displays," in Vacuum Nanoelectronics Conference (IVNC 2005), 2005, pp. 80-81.

[21] "Integrated Engineering Software," www.integratedsoft.com/Products/Lorentz.

[22] "Tech-X Corporation," www.txcorp.com/products/VORPAL/index.php.

[23] N. Faure, and P. Leveque, "2D Particle-In-Cell simulation on rising-sun magnetron," *IEEE/MTT-S International Microwave Symposium*, pp. 899-902, 2007.

[24] K. Hae Jin, S. Jung Uk, and C. Jin Joo, "Particle-in-cell code simulations on a rising-sun magnetron oscillator," *IEEE Transactions on Plasma Science,* vol. 30, no. 3, pp. 956-961, 2002.

[25] E. J. Cruz, "Peer-toPeer Magnetron Locking," Nuclear Engineering and Radiological Sciences, University of Michigan, Ann Arbor, Michigan, 2011.

[26] X. Chen, M. Esterson, and P. A. Lindsay, "Computer modeling of phase locking in magnetrons," *Proc. SPIE Intense Microwave Pulses IV,* vol. 2843, no. 47, pp. 47-56, 1996.

[27] T. A. Treado, P. D. Brown, R. A. Bolton, and T. Hansen, "Long-pulse, high-power, phase-locked magnetron studies," *International Microwave Symposium Digest*, pp. 225-228 vol.1, 1992.

[28] I. M. Rittersdorf, Y. Y. Lau, J. C. Zier, R. M. Gilgenbach, E. J. Cruz, and J. W. Luginsland, "Temporal and spatial locking of nonlinear systems," *Applied Physics Letters,* vol. 97, no. 17, pp. 171502-3, 2010.

[29] S. Maurya, S. Prasad, M. Kumar, P. Chaudhary, N. Shekhawat, and V. V. P. Singh, "Electromagnetic design and analysis of a high power tunable pulsed magnetron using MAGIC-3D," *IEEE International Vacuum Electronics Conference (IVEC)*, pp. 441-442, 2011.

[30] T. P. Fleming, and P. J. Mardahl, "Performance Improvements in the Relativistic Magnetron: The Effect of DC Field Perturbations," *IEEE Transactions on Plasma Science,* vol. 37, no. 11, pp. 2128-2138, 2009.

[31] S. Maurya, V. V. P. Singh, and P. K. Jain, "Performance improvement study of a relativistic magnetron using MAGIC-3D," *IEEE International Vacuum Electronics Conference (IVEC)*, pp. 169-170, 2011.

[32] W. E. Waters, "A theory of magnetron injection guns," *IEEE Transactions on Electron Devices,* vol. 10, no. 4, pp. 226-234, 1963.

[33] E. C. S. Megaw, "The high-power pulsed magnetron: a review of early developments," *Journal of the Institution of Electrical Engineers - Part IIIA: Radiolocation,* vol. 93, no. 1, pp. 194-196, 1946.

[34] A. S. Gilmour, *Microwave Tubes*, pp. 347-379: Artech House, 1986.

[35] S. Maurya, V. V. P. Singh, and P. K. Jain, "Three-Dimensional Particle-in-Cell Simulation of Fast Oscillation Startup and Efficiency Improvement in a Relativistic Magnetron With Electric Priming," *IEEE Transactions on Plasma Science,* vol. 40, no. 10, pp. 2686-2692, 2012.

[36] T. A. Van der Straaten, N. F. Cramer, I. S. Falconer, and B. W. James, "The Cylindrical DC Magnetron Discharge: I. Particle-in-cell Simulation," *J. Phys. D: Appl. Phys.*, no. 31, pp. 177-190, 1998.

[37] C. Xiaodong, M. Esterson, and P. A. Lindsay, "Computer simulation of a high-power magnetron and the possible implications for RF pulse shortening," *IEEE Transactions on Plasma Science,* vol. 26, no. 3, pp. 726-732, 1998.

[38] K. Posthumous, "Oscillations in a Split-Anode Magnetron," *Wireless Engineer*, no. 12, pp. 126-132, 1935.

[39] A. L. Samuel, *Magnetron, Electron Discharge Device, U.S. Patent 2,063,342*, 1934.

[40] N. T. Aleksereff, and D. E. Malearoff, "Generation of High Power Oscillations with a Magnetron in the Centimeter Band," *Journal of Technical Physics USRR,* vol. 10, pp. 1297, 1940.

[41] A. D. Andreev, and K. J. Hendricks, "First multi-cavity magnetrons were built in NII-9, Leningrad, during the spring of 1937 PIC simulations of the first 4-cavity S-band CW magnetron," *International Conference on the Origins and Evolution of the Cavity Magnetron (CAVMAG)*, pp. 71-75, 2010.

[42] W. Arter, and J. Eastwood, "The modelling of relativistic magnetrons," *IEE Seminar Digests,* vol. 1997, no. 374, pp. 3-3, 1997.

[43] N. I. Avtomonov, S. V. Sosnytskiy, and D. M. Vavriv, "Operating Modes of Magnetron Auxiliary Cathode," *The Sixth International Kharkov Symposium on Physics and Engineering of Microwaves, Millimeter and Submillimeter Waves and Workshop on Terahertz Technologies.,* vol. 2, pp. 547-549, 2007.

[44] M. A. Kopot, V. D. Yeryomka, and V. P. Dzyuba, "3-B Simulation of Magnetrons Having a Secondary-Emission Cathode Stimulated by Electrons from a Field Emitter," *IEEE International Vacuum Electronics Conference (IVEC)*, pp. 351-353, 2006.

[45] M. Leconte, "A statistical study of magnetron patents in the early years of electronics between 1920 and 1945; heuristic foucusing around the discovery of the cavity magnetron," *International Conference on the Origins and Evolution of the Cavity Magnetron (CAVMAG)*, pp. 11-16, 2010.

[46] P. A. Redhead, "The Invention of the Cavity Magnetron and its Introduction into Canada and the U.S.A.," *La Physique Au Canada*, novembre/decembre, pp. 321-328, 2001.

[47] J. Zhang, X. Chen, M. Esterson, P. Lindsay, P. Burleigh, and D. Wilson, "3D computer modelling of phase control in a magnetron through the output system," *IEEE International Conference on Plasma Science*, pp. 411-411, 2006.

[48] H. A. H. Boot, and J. T. Randall, "Historical Notes on the Cavity Magnetron," *IEEE Transactions on Electron Devices,* vol. 23, no. 7, pp. 724-729, 1976.

[49] T. J. Davis, "Toward a Viable High-Power Coaxial Microwave Source," School of Electrical Engineering, Cornell University, 1993.

[50] S. Dushman, "Electron emission," *Electrical Engineering,* vol. 53, pp. 1054-1062, 1934.

[51] D. A. Shiffler, M. Ruebush, D. Zagar, M. LaCour, K. Golby, M. Collins, M. Haworth, and R. Umstattd, "Emission Uniformity and Emittance of Explosive Fiel-Emission Cathodes," *IEEE Transactions on Plasma Science,* vol. 30, no. 4, pp. 1592-1596, 2002.

[52] W. M. White, "RF Priming of a Long Pulse Relativistic Magnetron ", Nuclear Engineering and Radiological Sciences, University of Michigan, Ann Arbor, Michigan, 2006.

[53] Y. M. Saveliev, B. A. Kerr, M. I. Harbour, S. C. Douglas, and W. Sibbett, "Operation of a relativistic rising-sun magnetron with cathodes of various diameters," *IEEE Transactions on Plasma Science,* vol. 30, no. 3, pp. 938-946, 2002.

[54] Y. M. Saveliev, S. N. Spark, B. A. Kerr, M. I. Harbour, S. C. Douglas, and W. Sibbett, "New cathodes for a relativistic magnetron," *Proceedings of the 12th International Conference on High-Power Particle Beams,* vol. 2, pp. 861-864 vol.2, 1998.

[55] W. M. White, R. M. Gilgenbach, M. C. Jones, V. B. Neculaes, L. Yue Ying, P. Pengvanich, N. M. C. Jordan, B. W. Hoff, R. Edgar, T. A. Spencer, and D. Price, "Radio frequency priming of a long-pulse relativistic magnetron," *IEEE Transactions on Plasma Science,* vol. 34, no. 3, pp. 627-634, 2006.

[56] W. E. Willshaw, L. Rushforth, A. G. Stainsby, R. Latham, A. W. Balls, and A. H. King, "The high-power pulsed magnetron: development and design for radar

applications," *Journal of the Institution of Electrical Engineers - Part IIIA: Radiolocation,* vol. 93, no. 5, pp. 985, 1946.

[57] V. Bagad, *Microwave Engineering - I*, First ed., Pune, India: Technical Publications Pune, 2009.

[58] L. Ma, "3D Computer Modeling of Magnetrons," Department of Electronic Engineering, Queen Mary, University of London, United Kingdom, 2004.

[59] O. Bunemann, "A Small Amplitude Theory for Magnetrons," *Journal of Electronics and Control*, pp. 1-50, 1957.

[60] W. Knauer, "Diocotron Instability in Plasmas and Gas Discharges," *Journal of Applied Physics,* vol. 37, no. 2, pp. 602-611, 1965.

[61] S. Millman, and A. T. Nordsieck, "The Rising Sun Magnetron," *Journal of Applied Physics,* vol. 19, no. 2, pp. 156-165, 1948.

[62] N. M. Kroll, and J. W. E. Lamb, "The Resonant Modes of the Rising Sun and Other Unstrapped Magnetron Anode Blocks," *Journal of Applied Physics,* vol. 19, no. 2, pp. 166-186, 1948.

[63] A. V. Hollenberg, N. Kroll, and S. Millman, "Rising Sun Magnetrons with Large Numbers of Cavities," *Journal of Applied Physics,* vol. 19, no. 7, pp. 624-635, 1948.

[64] "Ostron Technologies," http://www.ostron.de/.

[65] A. C. Dexter, G. Burt, R. G. Carter, I. Tahir, H. Wang, K. Davis, and R. Rimmer, "First demonstration and performance of an injection locked continuous wave magnetron to phase control a superconducting cavity," *Physical Review Special Topics - Accelerators and Beams,* vol. 14, no. 3, pp. 032001, 2011.

[66] R. Adler, "A Study of Locking Phenomena in Oscillators," *Proceedings of the IRE,* vol. 61, no. 10, pp. 1380-1385, 1946.

[67] E. E. David, "Locking Phenomena in Microwave Oscillators," *Research Laboratory of Electronics*, Massachusetts Institute of Technology, 1948.

[68] E. J. Cruz, B. W. Hoff, P. Pengvanich, Y. Y. Lau, R. M. Gilgenbach, and J. W. Luginsland, "Experiments on peer-to-peer locking of magnetrons," *Applied Physics Letters,* vol. 95, no. 19, pp. 191503-3, 2009.

[69] M. C. Jones, V. B. Neculaes, Y. Y. Lau, R. M. Gilgenbach, and W. M. White, "Cathode priming of a relativistic magnetron," *Applied Physics Letters,* vol. 85, no. 26, pp. 6332-6334, 2004.

[70] V. B. Neculaes, "Magnetron magnetic Priming for Rapid Startup and Noise Reduction," Nuclear Science, University of Michigan, 2005.

[71] C. Mendonca, S. Prasad, E. Schamiloglu, and T. Fleming, "3D ICEPIC simulations of a pulsed relativistic magnetron with transparent cathode: A comparative study," *IEEE Pulsed Power Conference (PPC)*, pp. 823-828, 2011.

[72] D. A. Shiffler, M. Ruebush, M. LaCour, K. Golby, R. Umstattd, M. C. Clark, J. W. Luginsland, D. Zagar, and M. Sena, "Emission Uniformity and Emission Area of Explosive Field Emission Cathodes," *Applied Physics Letters,* vol. 79, no. 18, pp. 2871-2873, 2001.

[73] D. Whaley, R. Duggal, and C. Armstrong, "100 W Operation of a Cold Cathode TWT," *IEEE Transactions on Electron Devices,* vol. 56, no. 5, pp. 896-905, 2009.

[74] D. Whaley, B. Gannon, V. Heinen, K. Kreischer, C. Holland, and C. Spindt, "Experimental Demonstration of an Emission-Gated Traveling-Wave Tube Amplifier," *IEEE Transactions on Plasma Science,* vol. 30, no. 3, 2002.

[75] C. K. Birdsall, and A. B. Langdon, *Plasma Physics Via Computer Simulation*: McGraw-Hill, 1985.

[76] C. Nieter, and J. R. Cary, "VORPAL: a versatile plasma simulation code," *Journal of Computational Physics,* vol. 196, no. 2, pp. 448-473, 2004.

[77] M. C. Lin, C. Nieter, P. H. Stoltz, and D. Smithe, "Accurately and Efficiently Studying the RF Structures Using a Conformal Finite-Difference Time-Domain Particle-in-Cell Method," *The Open Plasma Physics Journal,* vol. 3, pp. 48-52, 2010.

[78] R. W. Lemke, "3D PIC simulation study of the relativistic magnetron," *IEEE International Conference on Plasma Science*, pp. 206, 1998.

[79] B. W. Hoff, M. Franzi, R. M. Gilgenbach, and Y. Y. Lau, "Three-Dimensional Simulations of Magnetic Priming of a Relativistic Magnetron," *IEEE Transactions on Plasma Science,* vol. 38, no. 6, pp. 1292-1301, 2010.

[80] X. Chen, M. Esterson, and P. A. Lindsay, "3D simulation of microwave magnetrons," *IEE Colloquium on High Frequency Simulation: Part Two*, pp. 1/1-1/4, 1997.

[81] J. W. Eastwood, and W. Arter, "3D PIC simulation of relativistic magnetrons," *International Vacuum Electronics Conference*, pp. 1-2, 2000.

[82] C. Nieter, J. R. Cary, D. Smithe, P. H. Stoltz, and G. R. Werner, "Simulations of Electron Effects in Superconducting Cavities with the Vorpal Code," *10th European Particle Accelerator Conference*, pp. 2269-2271, 2006.

[83] C. Nieter, J. R. Cary, G. R. Werner, D. Smithe, and P. H. Stoltz, "Application of Dey-Mittra Conformal Boundary Algorithm to 3D Electromagnetic Modeling," *Journal of Computational Physics*, no. 228, pp. 7902-7916, 2009.

[84] K. S. Yee, "Numerical Solution of Initial Boundary Value Problems Involving Maxwell's Equations in Isotropic Media," *IEEE Transactions on Antennas and Propagation,* vol. AP-14, no. 3, pp. 302-307, 1966.

[85] K. S. Kunz, and R. J. Luebbers, *The Finite Difference Time Domain Method for Electromagnetics*, pp. 429: CRC Press, 2000.

[86] D. M. Sullivan, *Electromagnetic Simulation Using the FDTD Method*, pp. 336, 2000.

[87] R. Courant, K. Friedrichs, and H. Lewy, "On the Partial Difference Equations of Mathematical Physics," *IBM Journal*, March, 1967.

[88] A. C. Cangellaris, and D. B. Wright, "Analysis of the Numerical Error Caused by the Stair-stepped Approximation of a Conducting Boundary in FDTD Simulations of Electromagnetic Phenomena," *IEEE Transactions on Antennas and Propagation,* vol. 39, pp. 1518-1525, 1991.

[89] S. Dey, and R. Mittra, "A Locally Conformal Finite-Difference Time-Domain (FDTD) Algorithm for Modeling Three-Dimensional Perfectly Conducting Objects," *IEEE Microwave and Guided Wave Letters,* vol. 7, no. 9, pp. 273-275, 1997.

[90] R. Schuhmann, T. Weiland, and I. A. Zagorodnov, "A Uniformaly Stable Conformal FDTD-method in Cartesian Grids," *International Journal of Numerical Modeling,* vol. 16, pp. 127, 2003.

[91] C. S. Technology. "3D EM Simulations: Methods for Loaded Q Calculations," www.cst-world.com.

[92] A. Wolski, "Cavities and Waveguides," *Physical Review Special Topics*, 2007.

[93] M. C. Lin, P. H. Stoltz, D. Smithe, H. Song, H. Jong, J. J. Choi, S. J. Kim, and S. H. Jang, "Design and Modeling of Multistate Depressed Collectors by Using,"

Journal of the Korean Physical Society, vol. 60, no. 5, pp. 731-738, March 2012, 2012.

[94] S. G. Bandy, C. Spindt, M. A. Hollis, W. D. Palmer, B. Goplen, and E. G. Wintucky, "Application of Gated Field Emitter Arrays in Microwave Amplifier Tubes," in Vacuum Microelectronics Conference, 1998, pp. 132-133.

[95] C. Spindt, C. Holland, and I. Schwoebel, "Field-Emitter-Array Development for Microwave Applications," in Electron Devices Meeting, IEDM '95, Washington, DC, 1995, pp. 389-392.

[96] D. Whaley, B. Gannon, C. R. Smith, C. Armstrong, and C. Spindt, "Application of Field Emitter Arrays to Microwave Power Amplifiers," *IEEE Transactions on Plasma Science,* vol. 28, no. 3, pp. 727-746, 2000.

APPENDIX A

Lorentz2E Simulations

Complete Results of the Sensitivity Simulations

All the results shown in this section are for a total of 200 electron rays (100 rays per side). The results shown here do not include ray space charge simultaneously with the hub charge. The total charge in the volume was estimated to be -1.35×10^{-8} C. To be conservative, a total volume charge of -1.5×10^{-8} C was then used in the simulation to represent the charge hub [12]. The results are summarized in three parts: (a) variation of the pusher electrode voltage, (b) variation of the emitter voltage, and (c) variation of the geometry (dimensions) of the pusher electrode.

(a) Varying Pusher Electrode Voltage

The pusher electrode voltage was set as the major parameter and held constant for each simulation. The emitter voltage was then varied using the parametric feature. The pusher voltage was varied from -22.20 kV to -22.37 kV for six cases, including the standard case [12]. The emitter voltage range was varied from -22.20 kV to -25.0 kV using 20 steps. Figure A.1 shows four examples of the ray trajectories for different emitter voltages. As can be seen, the rays begin to strike the sole electrode walls and be lost or are turned back to the cathode depending upon the voltage. The simulations are repeated for four additional pusher electrode voltages as shown in Figures A.2-A.4.

(a.1) Pusher electrode at -22.20 kV

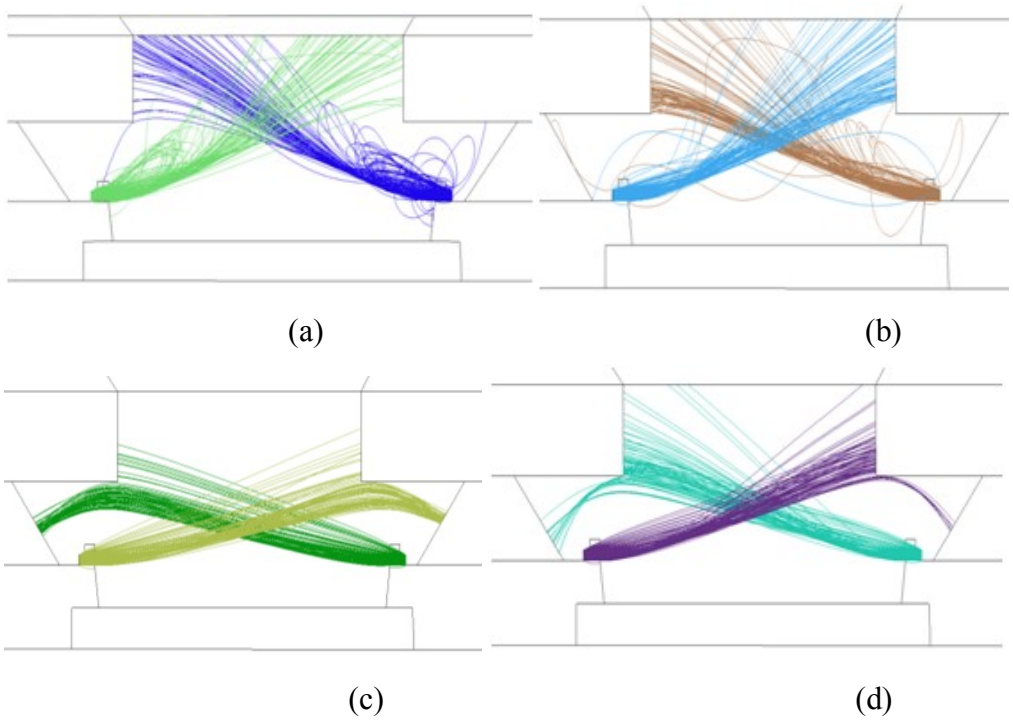

(a) (b)

(c) (d)

Figure A.1: Pusher Electrode Voltage at -22.20 kV. Emitter Voltage at (a) -22.20kV, (b) -22.26 kV, (c) -22.34 kV, and (d) -22.5 kV.

(a.2) Pusher electrode at -22.26 kV

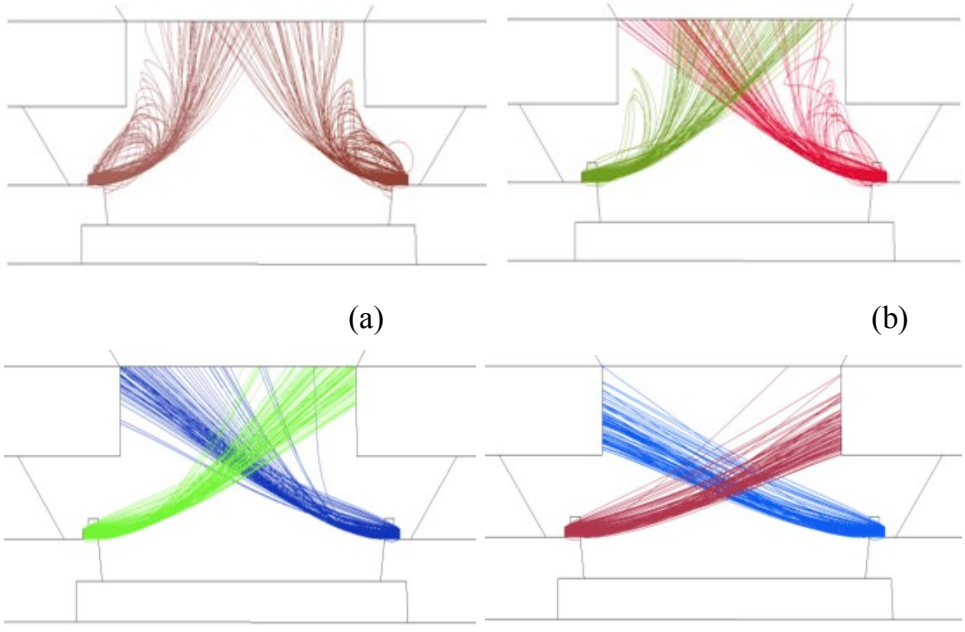

(a) (b)

(c) (d)

Figure A.2: Pusher Electrode Voltage at -22.26 kV. Emitter Voltage at (a) -22.20kV, (b) -22.26 kV, (c) -22.34 kV, and (d) -22.5 kV.

(a.3) Pusher electrode at -22.30 kV

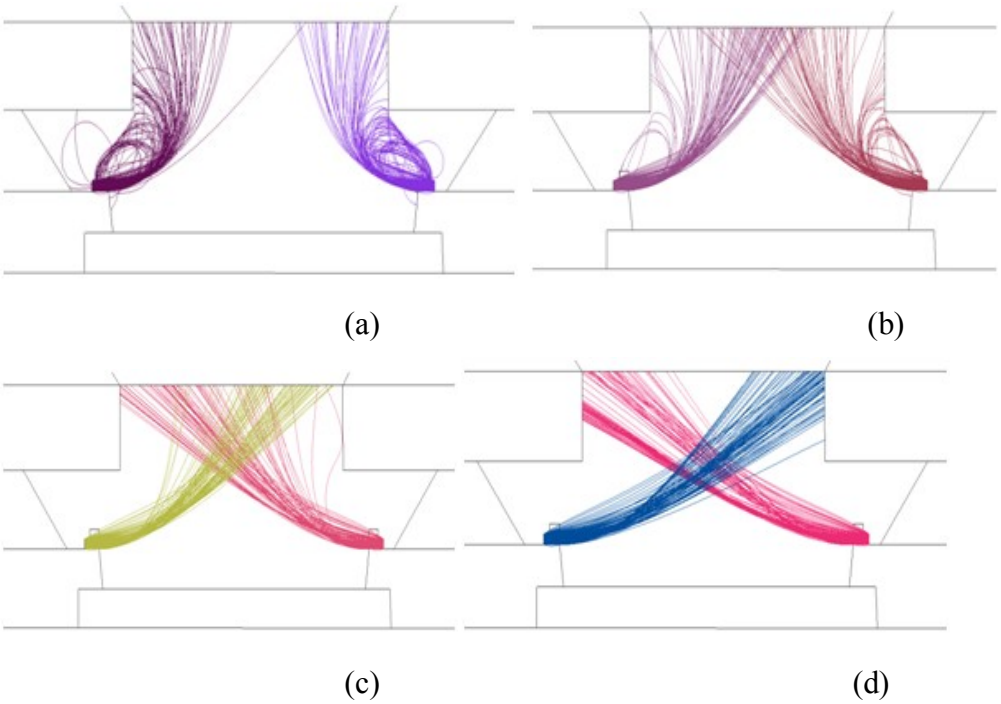

Figure A.3: Pusher Electrode Voltage at -22.30 kV. Emitter Voltage at (a) -22.20kV, (b) -22.26 kV, (c) -22.34 kV, and (d) -22.5 kV.

(a.4) Pusher electrode at -22.37 kV

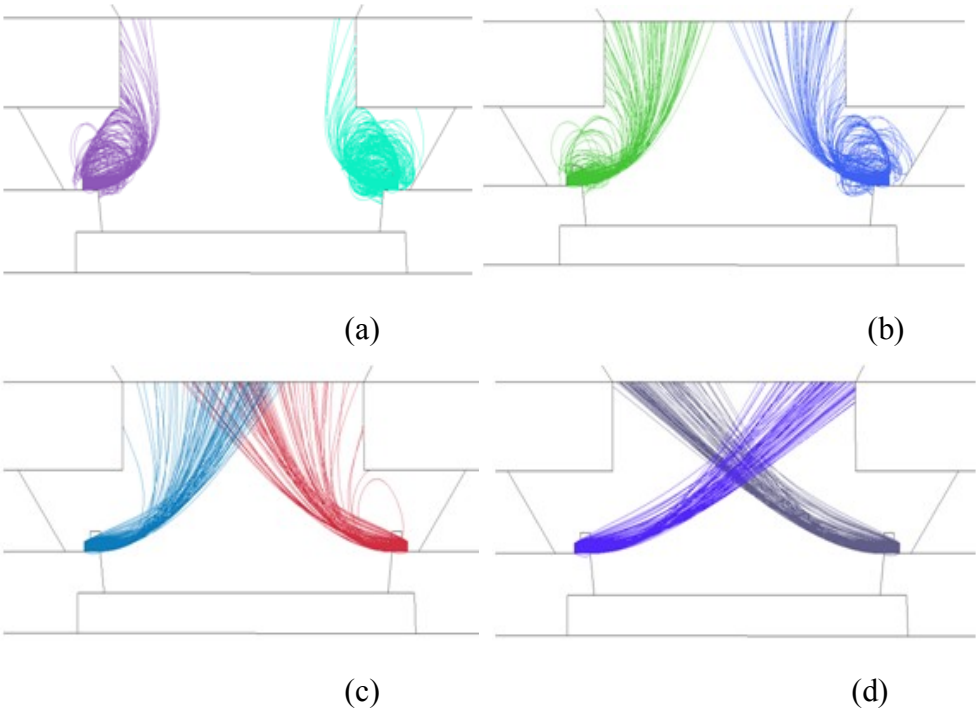

Figure A.4: Pusher Electrode Voltage at -22.37 kV. Emitter Voltage at (a) -22.20 kV, (b) -22.26 kV (c), -22.34 kV, and (d) -22.5 kV.

(a.5) Collector Current Analysis

A diagnostic was placed at the collector to measure the current (number of rays), which exit the slit and strike the collector. In Figure A.5, a plot of the ratio of I_{out}/I_{in} vs. emitter voltage is graphed for the five pusher electrode cases. I_{out} and I_{in} are the collector current and emitter current, respectively. The threshold for the maximum current out was set equal or greater to 90% (this threshold was taken into account for the following cases). The threshold value was determined considering that there are a small percentage of rays that do not come out. This amount of rays was calculated to be approximately between 10-20 rays in total. This amount of emitter current loss (injected emitter current) was calculated and subtracted from the original injected emitter current. The voltage sensitivity (ΔV) was calculated for this threshold value. These results are shown in Table 4.1A.1. This means that the resulting ΔV calculated for each case shows how sensitive the emitters are to the parameter changes. A large ΔV indicates low sensitivity to voltage variation, which is desirable for device operation.

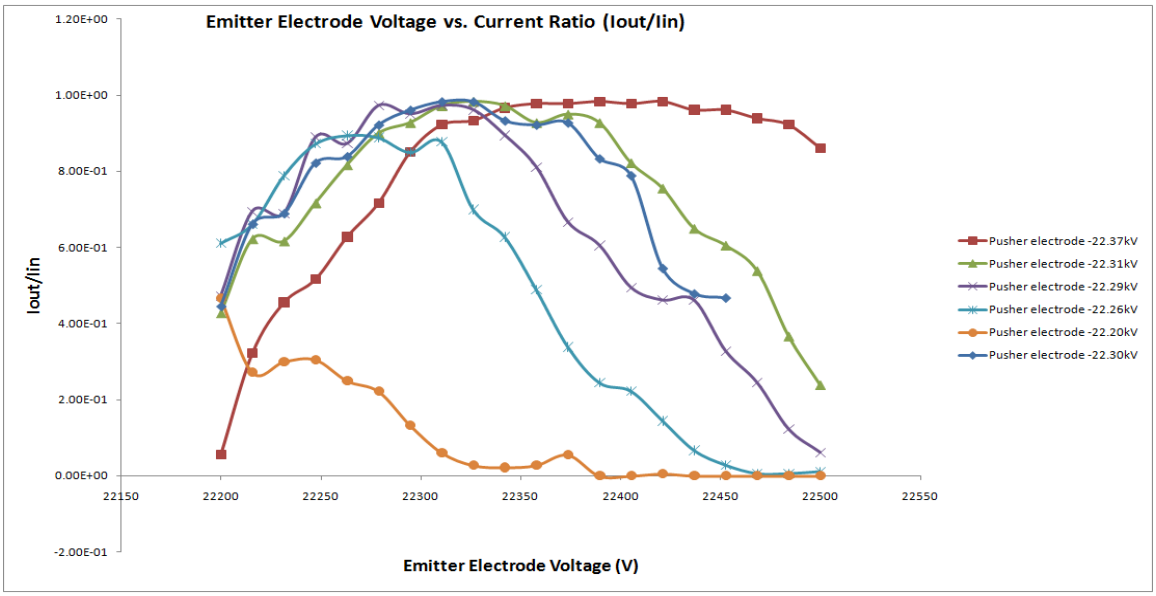

Figure A.5: Emitter voltage versus current ratio.

Table A.1: Voltage sensitivity analysis results for variations in the pusher electrode voltage.

Pusher electrode voltage (kV)	Maximum current out (%)	ΔV (V)
-22.29	97.2%	78.95
-22.30	98.3%	110.5
-22.31	98.3%	102.3
-22.37	98.3%	189.5

(b) Varying Emitter Voltage

The emitter voltage was set as a major parameter with the pusher electrode voltage varied by the parametric function. The emitter voltage was varied from -22.20 kV to -22.37 kV in six cases, including the standard case [12]. The pusher electrode voltage was varied from -22.20 kV to -25.0 kV using 20 steps. Figures A.5-A.8 show the results of the ray trajectories at different pusher electrode voltages with a fixed emitter voltage.

(b.1) Emitter voltage at -22.20 kV

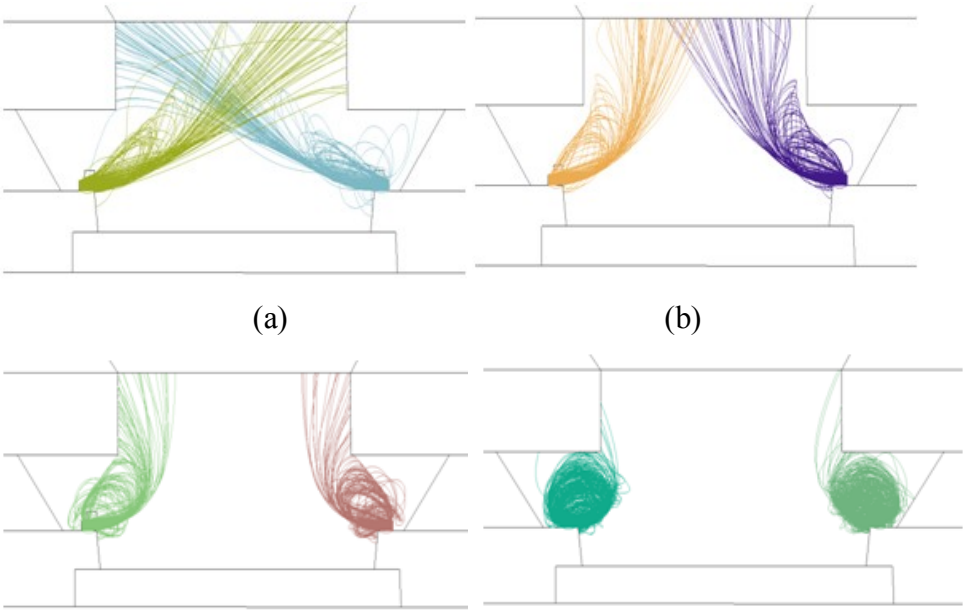

(a) (b)

(c) (d)

Figure A.5: Emitter Voltage at -22.20 kV. Pusher Electrode Voltage at (a) -22.20 kV, (b) -22.26 kV, (c) -22.34 kV, and (d) -22.5 kV.

(b.2) Emitter voltage at -22.26 kV

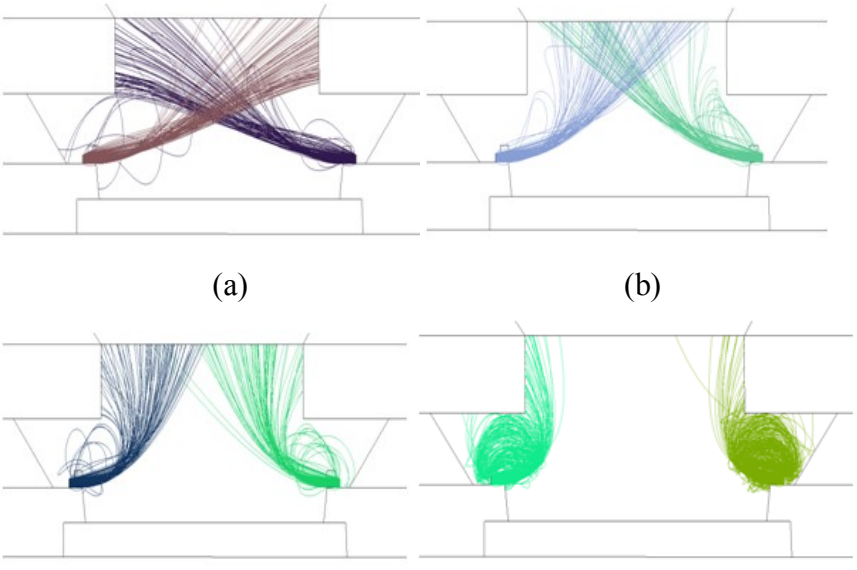

(a) (b)

(c) (d)

Figure A.6: Emitter Voltage at -22.26 kV. Pusher Electrode Voltage at (a) -22.20 kV, (b) -22.26 kV, (c) -22.34 kV, and (d) -22.5 kV.

(b.3) Emitter voltage at -22.30 kV

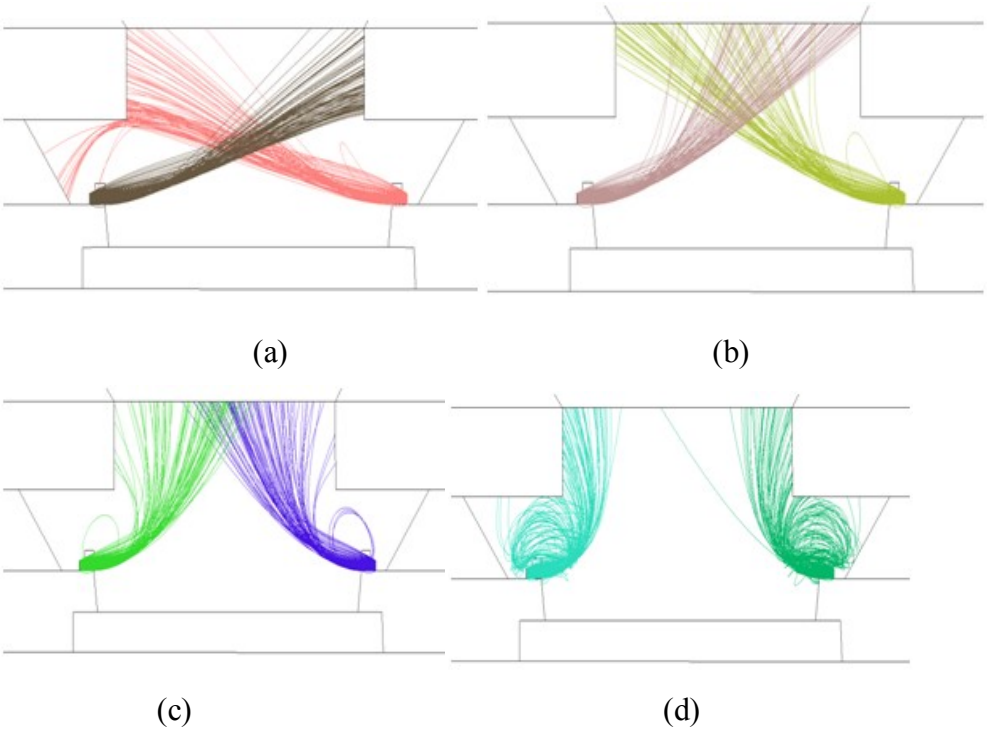

(a) (b)

(c) (d)

Figure A.7: Emitter Voltage at -22.30 kV. Pusher Electrode Voltage at (a) -22.20 kV, (b) -22.26 kV, (c) -22.34 kV, and (d) -22.5 kV.

(b.4) Emitter voltage at -22.37 kV

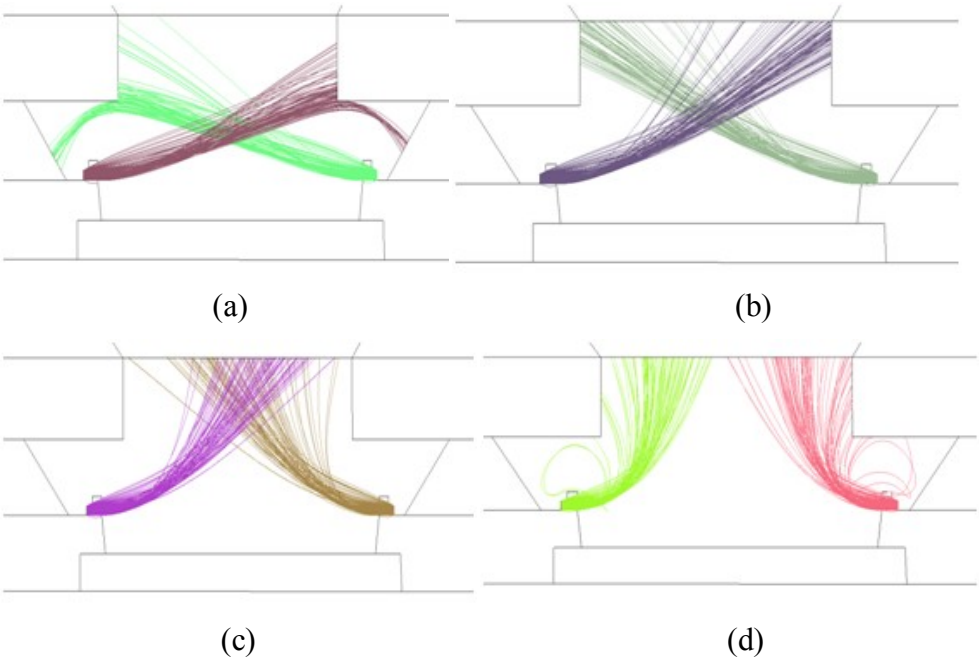

(a) (b)

(c) (d)

Figure A.8: Emitter Voltage at -22.37 kV. Pusher Electrode Voltage at (a) -22.20 kV, (b) -22.26 kV, (c) -22.34 kV, and (d) -22.5 kV.

(b.5) Collector current analysis

A diagnostic was placed at the collector to measure the current at which the rays will hit the collector. In Figure A.9, a plot of the pusher electrode voltage vs. the rate of I_{out}/I_{in} at the different emitter voltages studied in the previous section is presented. The voltage sensitivity (ΔV) was calculated and is presented in Table A.2.

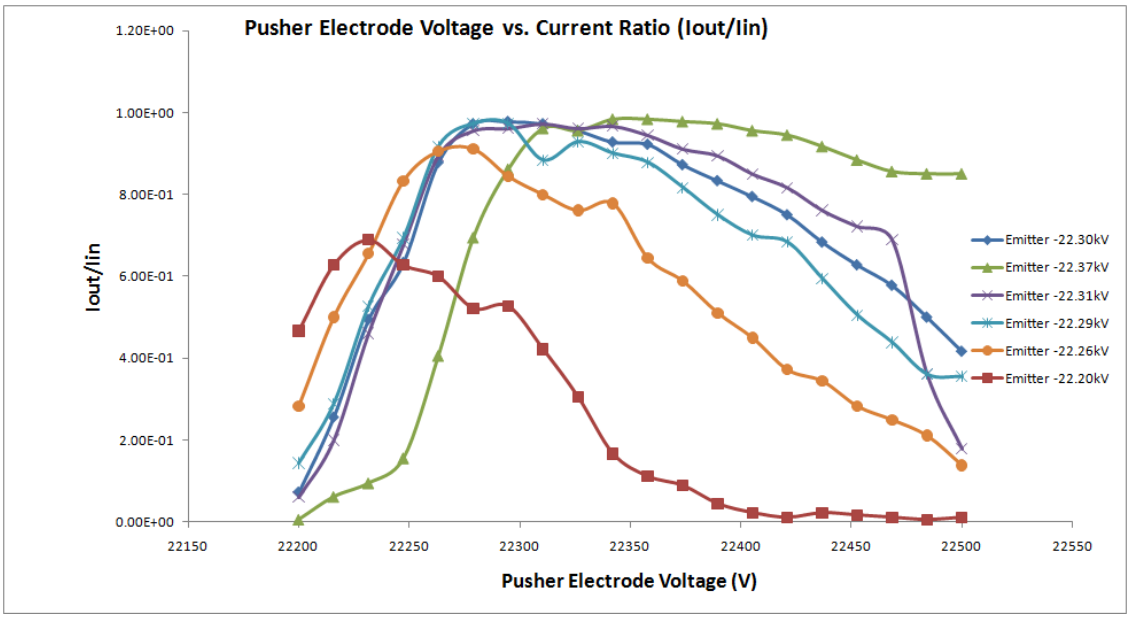

Figure A.9: Pusher Electrode Voltage vs. Current Ratio.

Table A.2: Voltage sensitivity analysis results for variations in the emitter voltage.

Emitter voltage (kV)	Maximum current out (%)	ΔV (V)
-22.26	91.1%	63.15
-22.29	97.2%	78.95
-22.30	97.8%	94.74
-22.31	97.2%	126.3
-22.37	98.3%	157.9

(c) Varying the geometry

In this section, the simulation results are from the variation of the geometry of the pusher electrode; the simulations shown in section (a) and (b) were repeated for each geometry. The pusher electrode has a thickness of 0.9795 µm from the reference model studied in [12]. This thickness was modified to its maximum and minimum to study the device sensitivity due to changing the geometry. The simulations are performed for two different pusher electrode thicknesses: geometry (1) corresponds to a thickness of 1.70 µm and geometry (2) corresponds to a thickness of 0.4475 µm. These results are presented in Figures A.10-A.19 for the 1.70 um case and in Figures A.20-A.28 for the 0.4475 um case. These results clearly show an improvement in the extracted current by moving the pusher electrode closer (vertically) to the emitter.

(c.1) Geometry (1) 1.70 µm thick, varying pusher electrode voltage

(c.1.1) Pusher electrode voltage at -22.20 kV

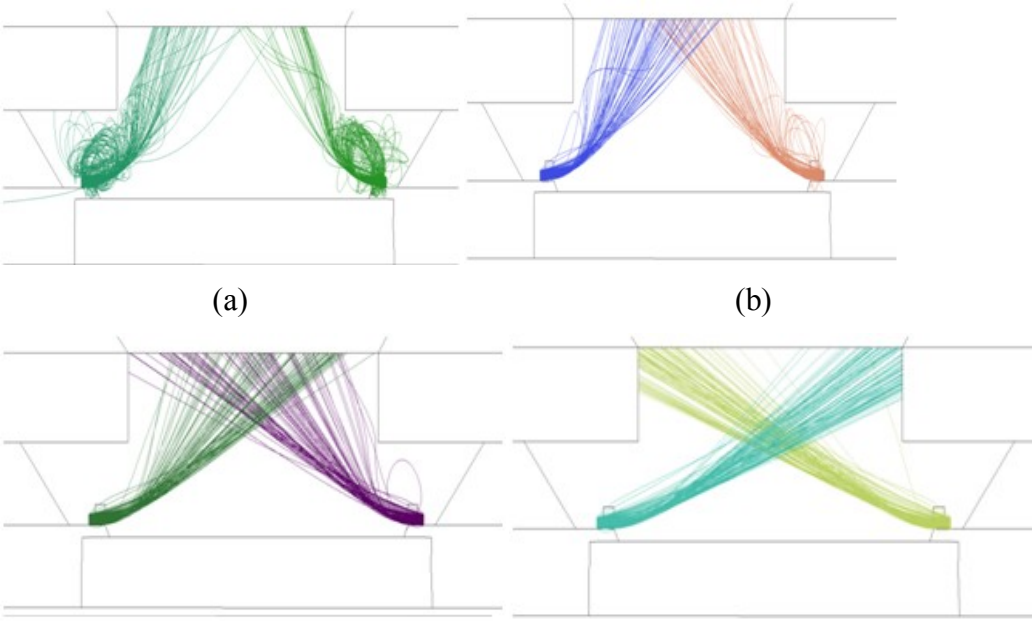

Figure A.10: Pusher Electrode Voltage at -22.20 kV. Emitter Voltage at (a) -22.20 kV, (b) -22.26 kV, (c) -22.34 kV, and (d) -22.5 kV.

(c.1.2) Pusher electrode voltage at -22.26 kV

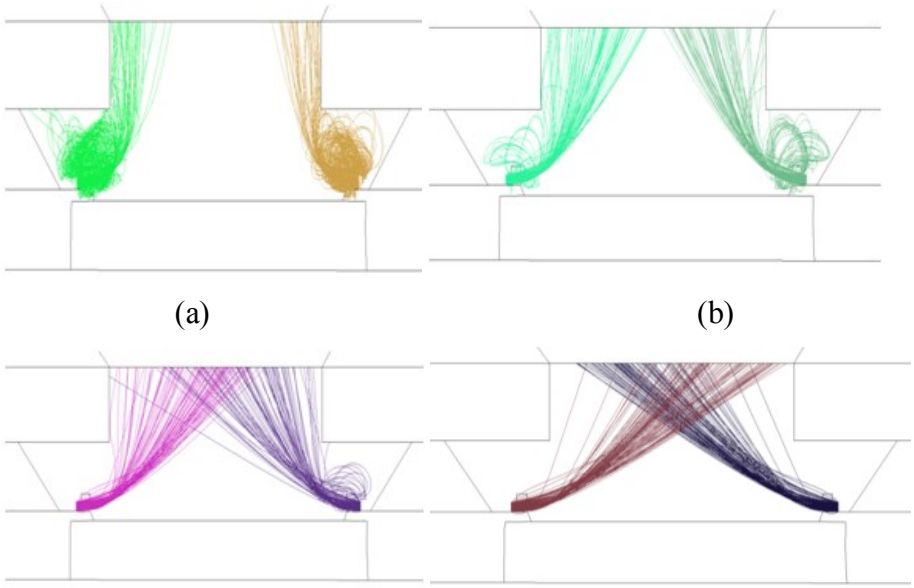

(a) (b)

(c) (d)

Figure A.11: Pusher Electrode Voltage at -22.26 kV. Emitter Voltage at (a) -22.20 kV, (b) -22.26 kV, (c) -22.34 kV, and (d) -22.5 kV.

(c.1.3) Pusher electrode voltage at -22.30 kV

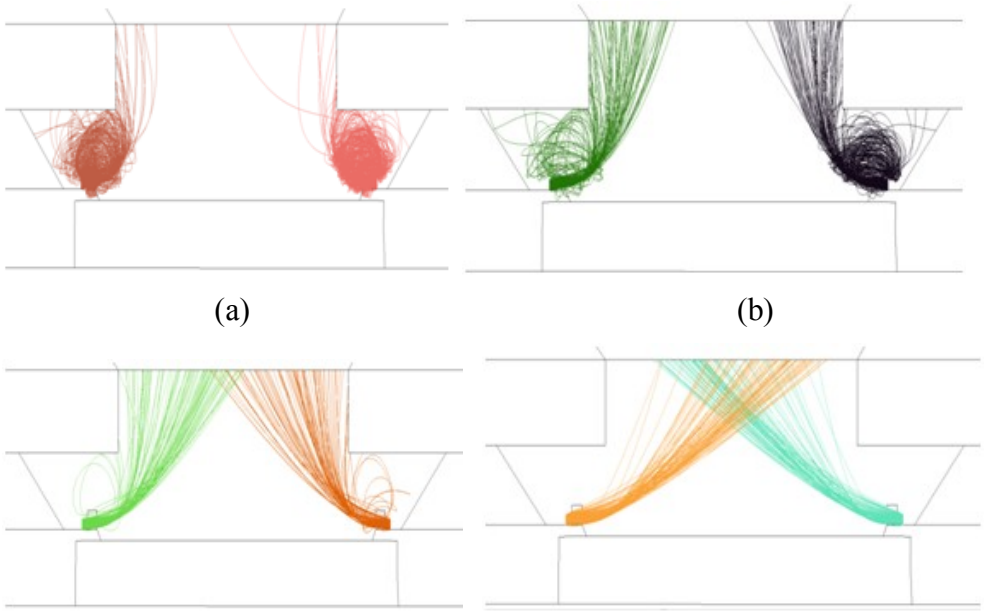

(a) (b)

(c) (d)

Figure A.12: Pusher Electrode Voltage at -22.30 kV. Emitter Voltage at (a) -22.20 kV, (b) -22.26 kV, (c) -22.34 kV, and (d) -22.5 kV.

(c.1.4) Pusher electrode voltage at -22.37 kV

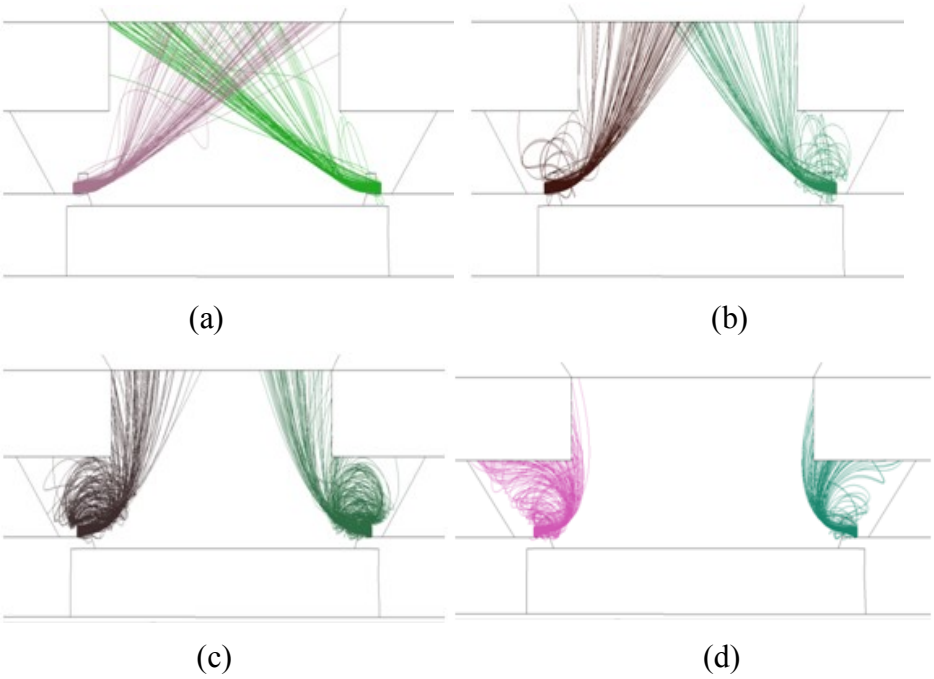

Figure A.13: Pusher Electrode Voltage at -22.37 kV. Emitter Voltage at (a) -22.20 kV, (b) -22.26 kV, (c) -22.34 kV, and (d) -22.5 kV.

(c.1.5) Collector current analysis

Results are shown in Table A.3. Comparing these results with the standard case from [12] discussed in Chapter Three, it can be observed that by moving the pusher electrode higher there is an improvement in the amount of current exit the slit.

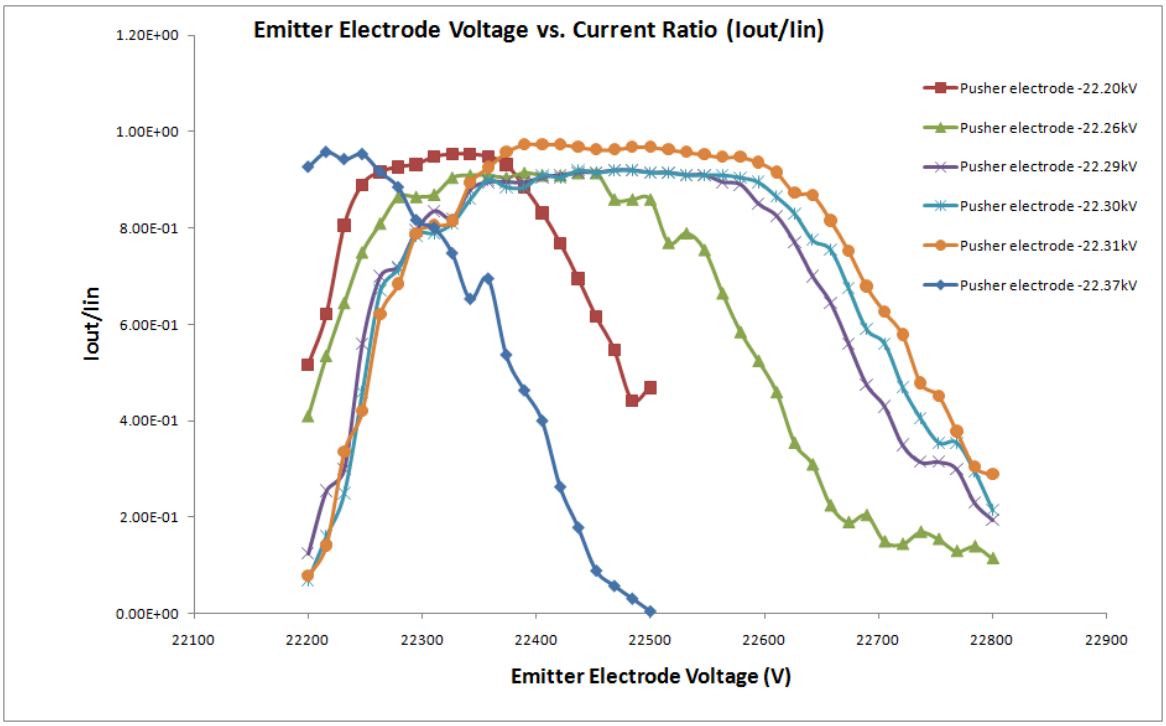

Figure A.14: Emitter Voltage vs. Current Ratio at Different Pusher Electrode Voltages.

Table A.3: Voltage sensitivity analysis results for variations in the pusher electrode voltage.

Pusher electrode voltage (kV)	Maximum current out (%)	ΔV (V)
-22.20	95.3%	79
-22.26	96.3%	126
-22.29	96.8%	189
-22.30	96.8%	222
-22.31	97.4%	173
-22.37	95.7%	190

(c.2) Geometry (1) 1.70 µm thick, varying emitter voltage

(c.2.1) Emitter voltage at -22.20 kV

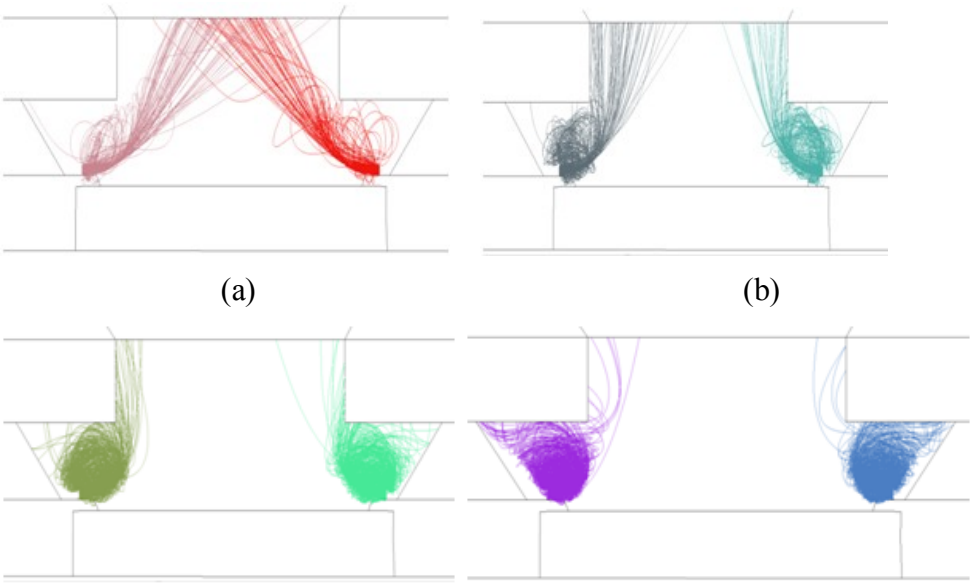

Figure A.15: Emitter Voltage at -22.20 kV. Pusher Electrode Voltage at (a) -22.20 kV, (b) -22.26 kV, (c) -22.34 kV, and (d) -22.5 kV.

(c.2.2) Emitter voltage at -22.26 kV

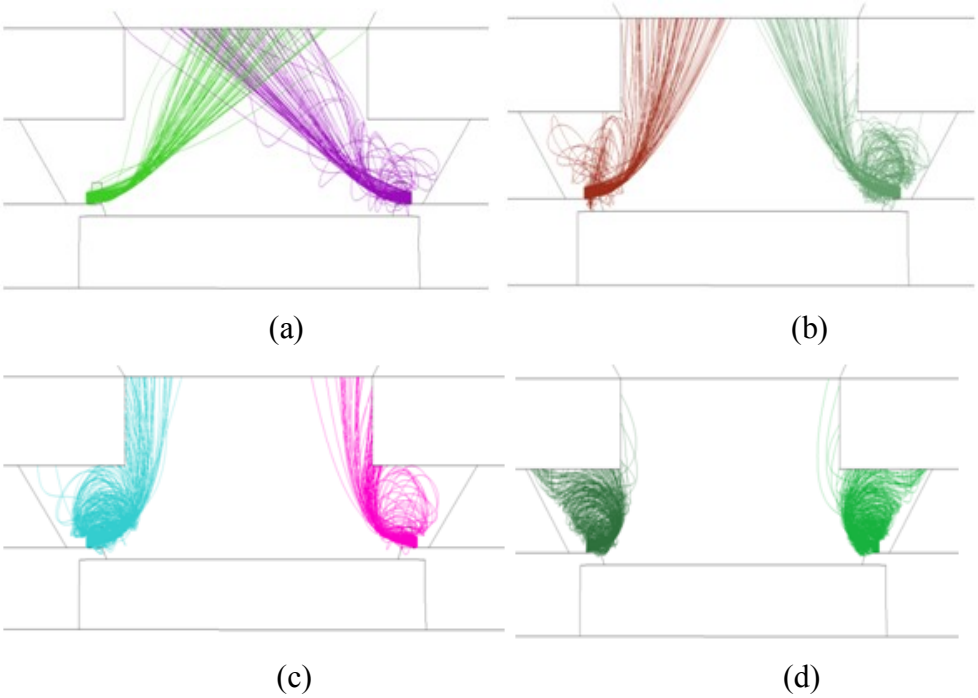

Figure A.16: Emitter Voltage at -22.26 kV. Pusher Electrode Voltage at (a) -22.20 kV, (b) -22.26 kV, (c) -22.34 kV, and (d) -22.5 kV.

(c.2.3) Emitter voltage at -22.30 kV

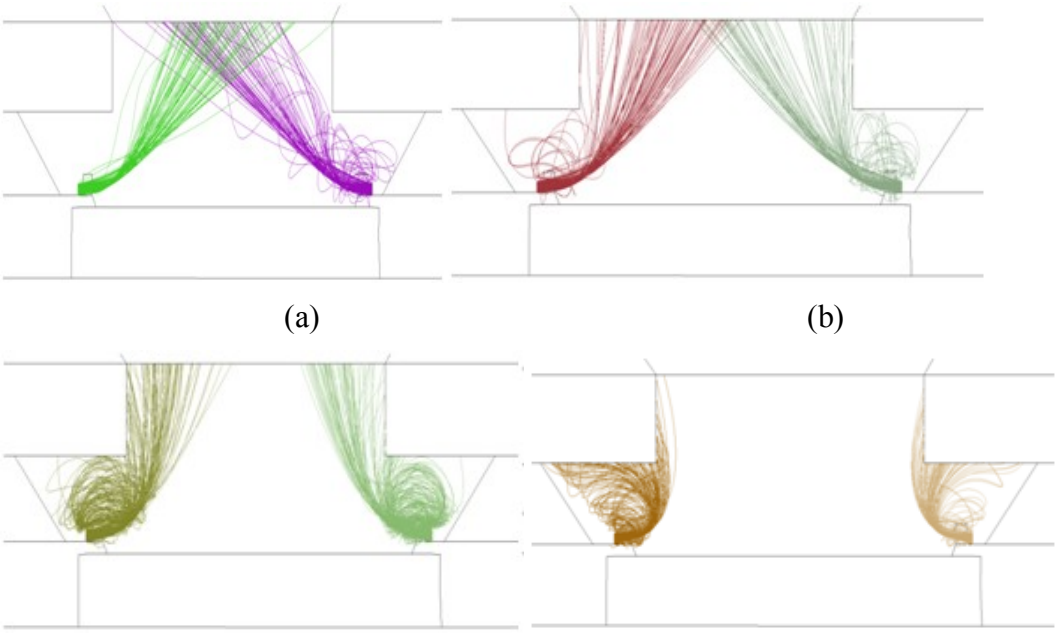

Figure A.17: Emitter Voltage at -22.30 kV. Pusher Electrode Voltage at (a) -22.20 kV, (b) -22.26 kV, (c) -22.34 kV, and (d) -22.5 kV.

(c.2.4) Emitter voltage at -22.37 kV

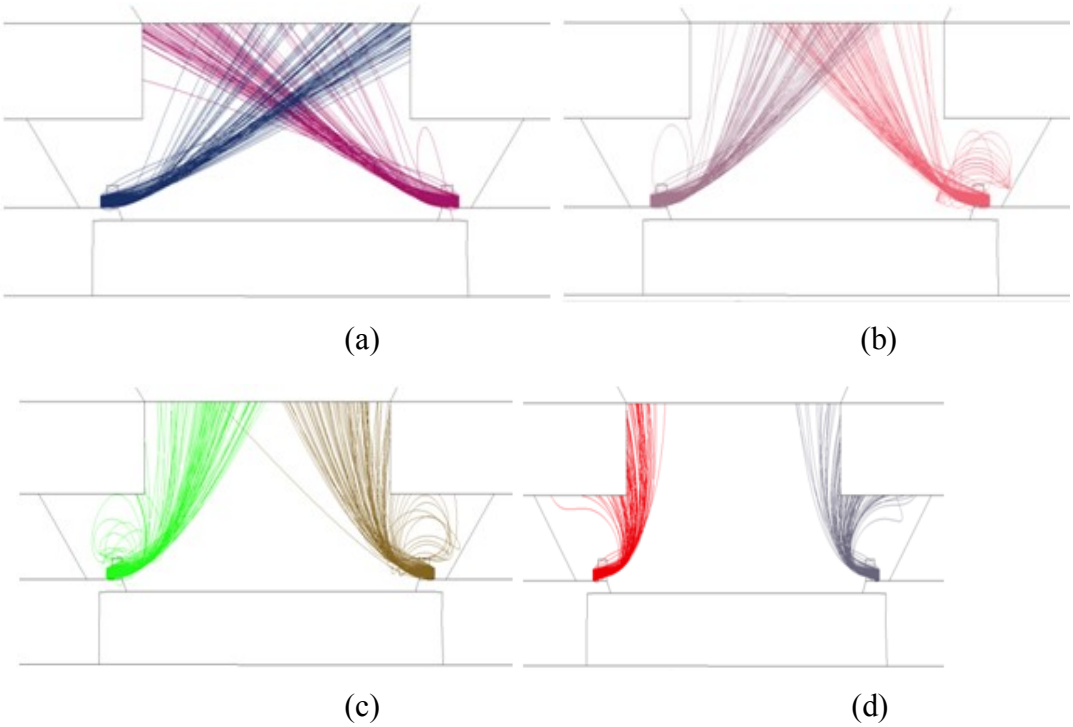

Figure A.18: Emitter Voltage at -22.37 kV. Pusher Electrode Voltage at (a) -22.20 kV, (b) -22.26 kV, (c) -22.34 kV, and (d) -22.5 kV.

(c.2.5) Collector current analysis

Results are shown in Table A.4. Comparing these results with the standard case from [12] discussed in Chapter Three, it can be observed that by moving the pusher electrode higher the amount of current out the slit is improved.

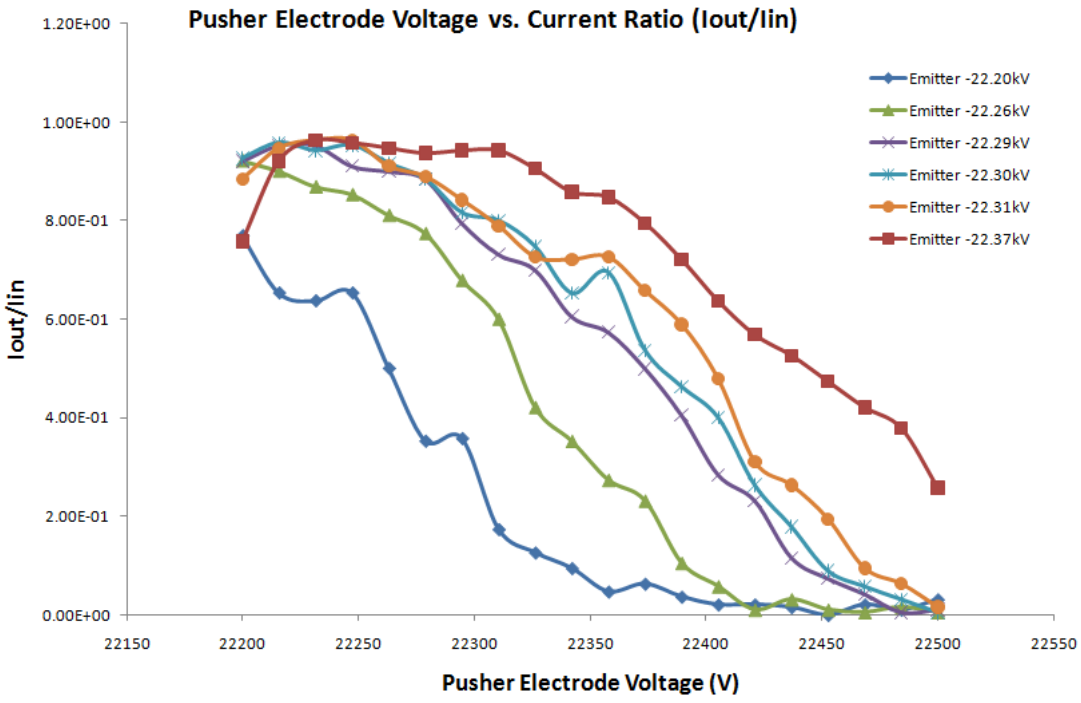

Figure A.19: Pusher Electrode Voltage vs. Current Ratio at Different Emitter Voltages.

Table A.4: Voltage sensitivity analysis results for variations in the emitter voltage.

Emitter voltage (kV)	Maximum current out (%)	ΔV (V)
-22.26	92.1%	113
-22.29	95.3%	90
-22.30	95.8%	90
-22.31	96.3%	90
-22.37	96.3%	110.5

(c.3) Geometry (2) 0.4475 µm thick, varying pusher electrode voltage

(c.3.1) Pusher electrode voltage at -22.20 kV

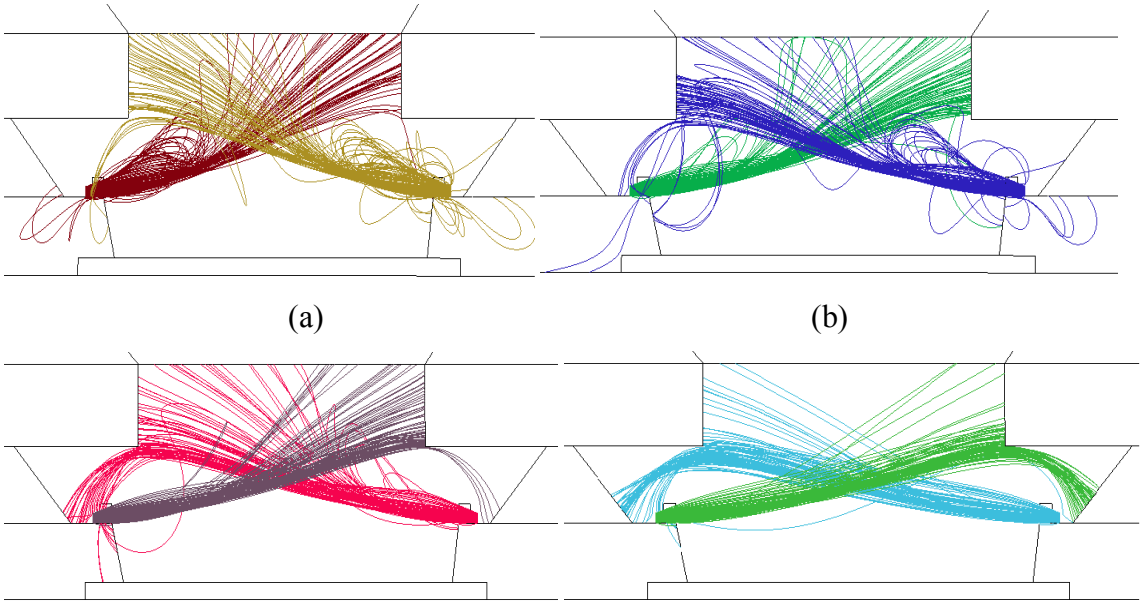

(a) (b)

(c) (d)

Figure A.20: Pusher Electrode Voltage at -22.20 kV. Emitter Voltage at (a) -22.20 kV, (b) -22.26 kV, (c) -22.34 kV, and (d) -22.5 kV.

(c.3.2) Pusher electrode voltage at -22.26 kV

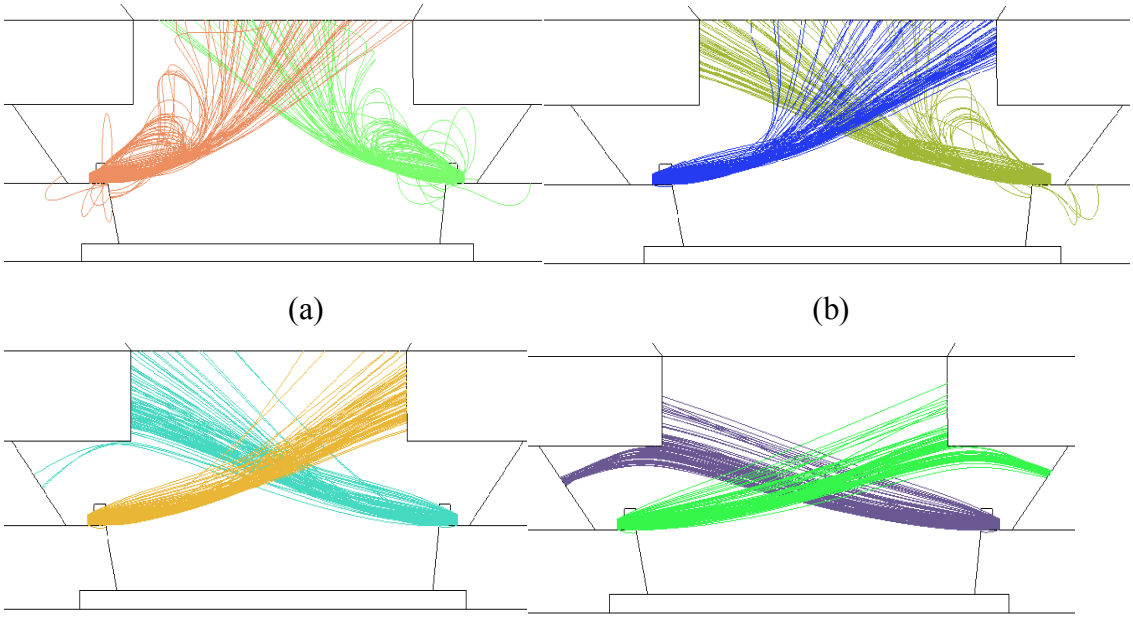

(a) (b)

(c) (d)

Figure A.21: Pusher Electrode Voltage at -22.26 kV. Emitter Voltage at (a) -22.20 kV, (b) -22.26 kV, (c) -22.34 kV, and (d) -22.5 kV.

(c.3.3) Pusher electrode voltage at -22.30 kV

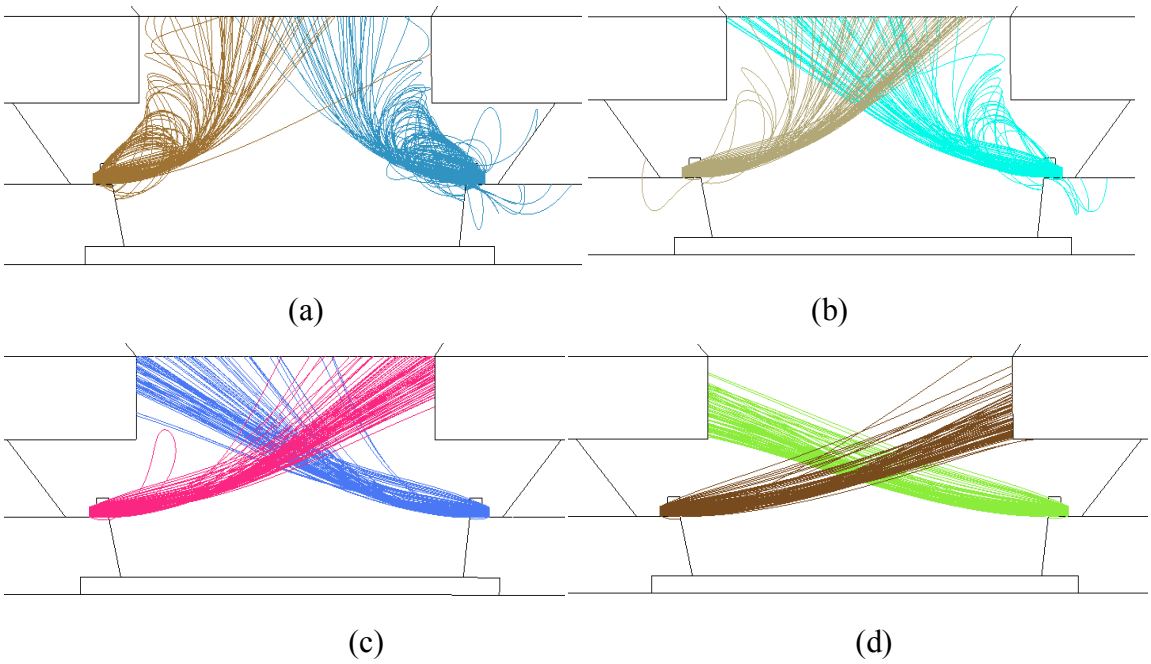

Figure A.22: Pusher Electrode Voltage at -22.30 kV. Emitter Voltage at (a) -22.20 kV, (b) -22.26 kV, (c) -22.34 kV, and (d) -22.5 kV.

(c.3.4) Pusher electrode voltage at -22.37 kV

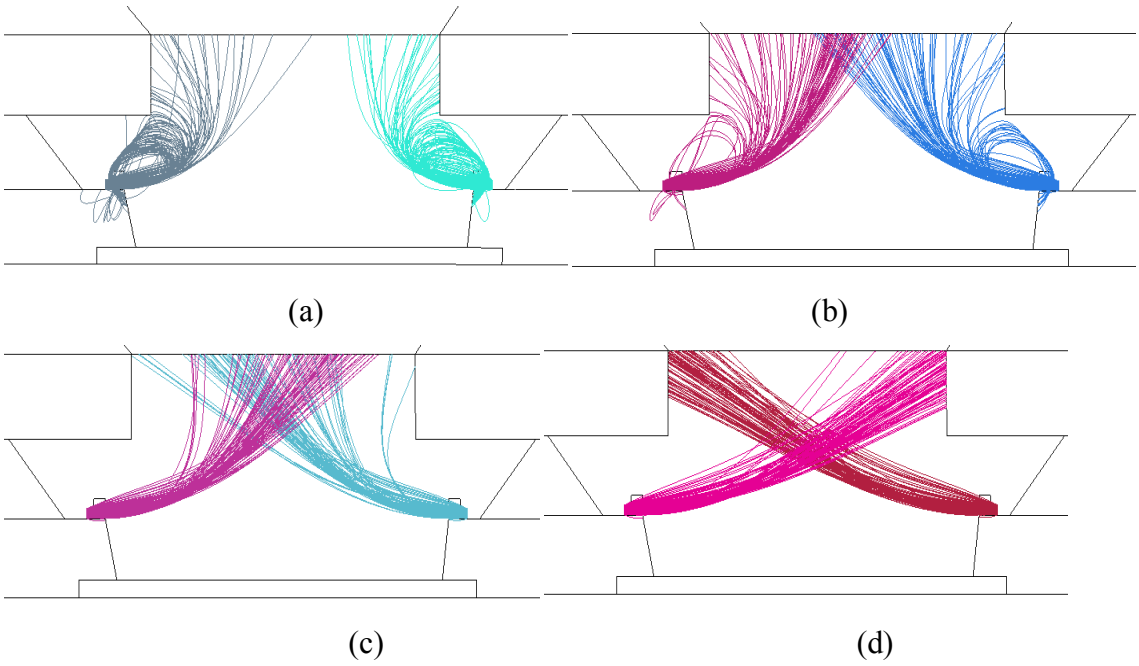

Figure A.23: Pusher Electrode Voltage at -22.37 kV. Emitter Voltage at (a) -22.20 kV, (b) -22.26 kV, (c) -22.34 kV, and (d) -22.5 kV.

(c.3.5) Collector current analysis

The results for ΔV are presented in Table A.5. Comparing these results with the standard case from [12] discussed in Chapter Three, it can be observed that by lowering the pusher electrode the amount of current out is improved just for few cases.

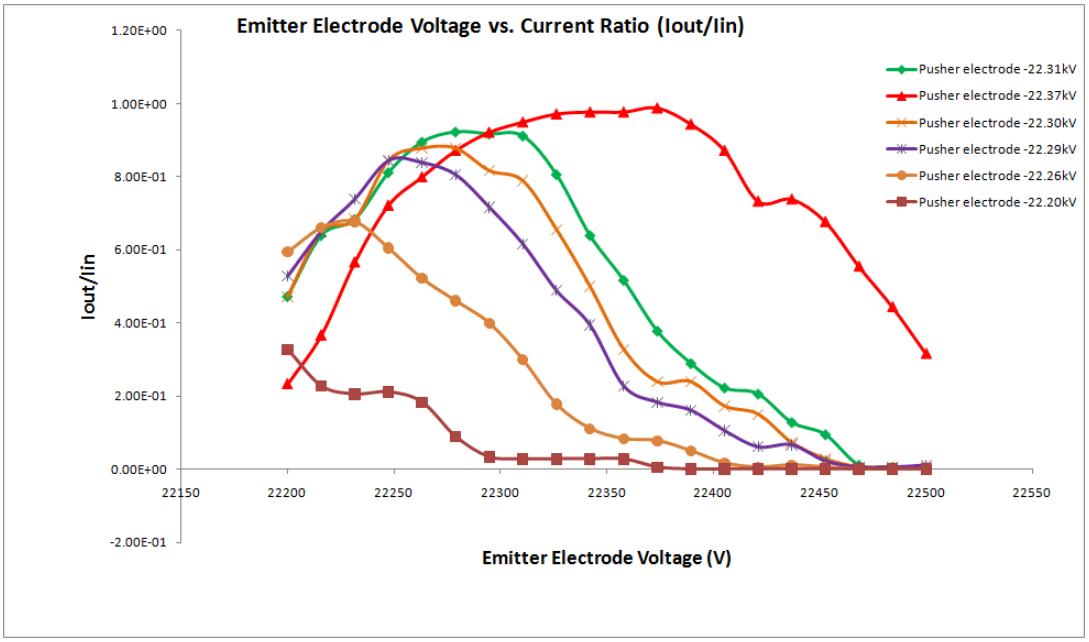

Figure A.24: Emitter Voltage vs. Current Ratio at Different Pusher Electrode Voltages.

Table A.5: Voltage sensitivity analysis results for variations in the pusher electrode voltage.

Pusher electrode voltage (kV)	Maximum current out (%)	ΔV (V)
-22.31	92.2%	80
-22.37	98.9%	95

(c.4) Geometry (2) 0.4475 µm thick, varying emitter voltage

(c.4.1) Emitter voltage at -22.20 kV

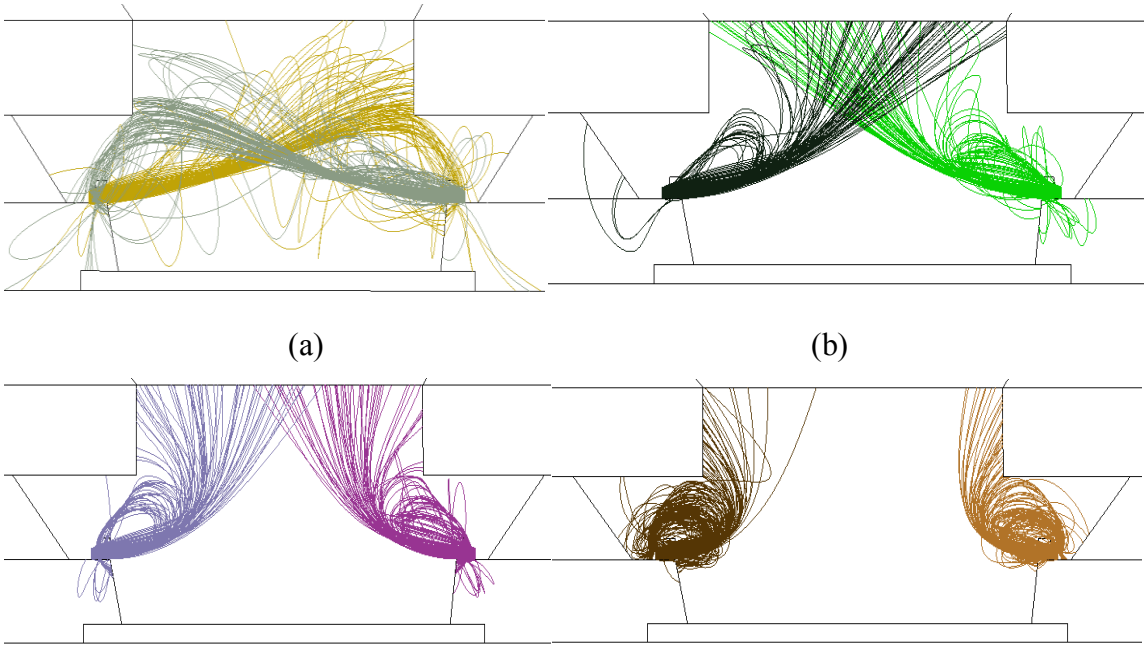

(a) (b)

(c) (d)

Figure A.25: Emitter Voltage at -22.20 kV. Pusher Electrode Voltage at (a) -22.20 kV, (b) -22.26 kV, (c) -22.34 kV, and (d) -22.5 kV.

(c.4.2) Emitter voltage at -22.26 kV

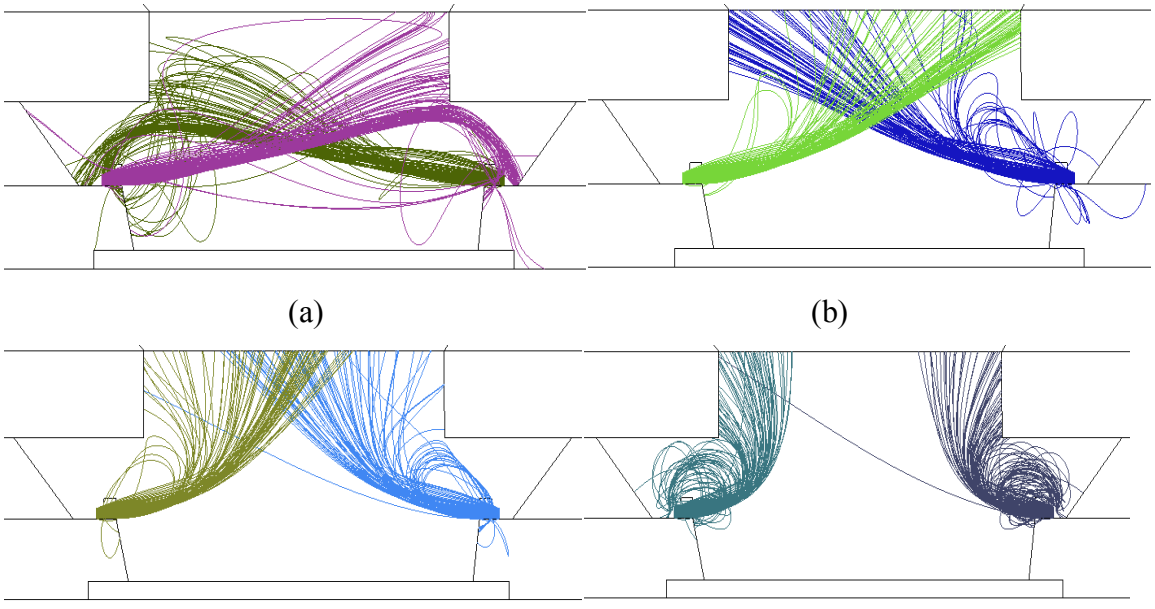

(a) (b)

(c) (d)

Figure A.26: Emitter Voltage at -22.26 kV. Pusher Electrode Voltage at (a) -22.20 kV, (b) -22.26 kV, (c) -22.34 kV, and (d) -22.5 kV.

(c.4.3) Emitter voltage at -22.30 kV

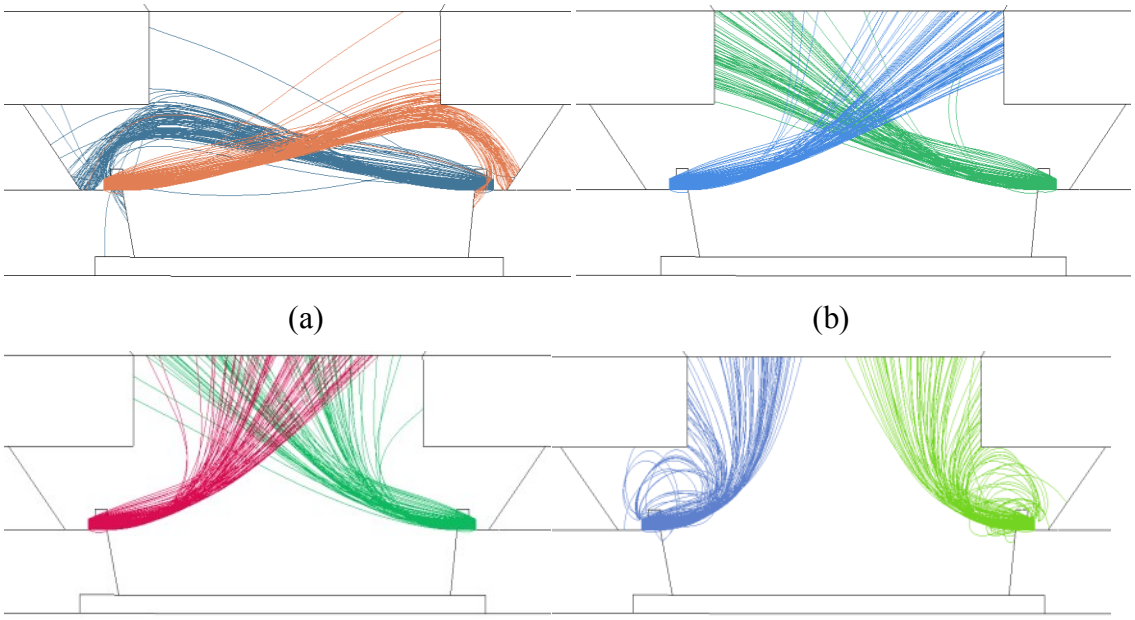

(a) (b)

(c) (d)

Figure A.27: Emitter Voltage at -22.30 kV. Pusher Electrode Voltage at (a) -22.20 kV, (b) -22.26 kV, (c) -22.34 kV, and (d) -22.5 kV.

(c.4.4) Emitter voltage at -22.37 kV

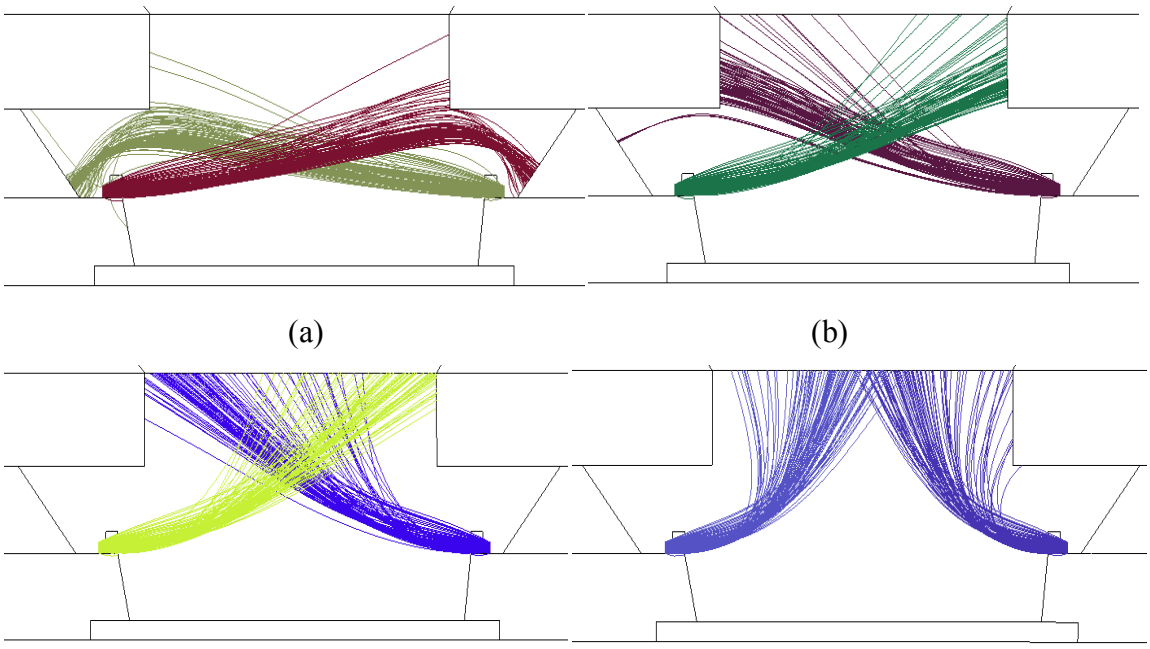

(a) (b)

(c) (d)

Figure A.28: Emitter Voltage at -22.37 kV. Pusher Electrode Voltage at (a) -22.20 kV, (b) -22.26 kV, (c) -22.34 kV, and (d) -22.5 kV.

(c.4.5) Collector current analysis

The results for ΔV are presented in Table A.6. Comparing these results with the standard case from [12] discussed in Chapter Three, it can be observed that by lowering the pusher electrode the amount of current out is improved just for few cases.

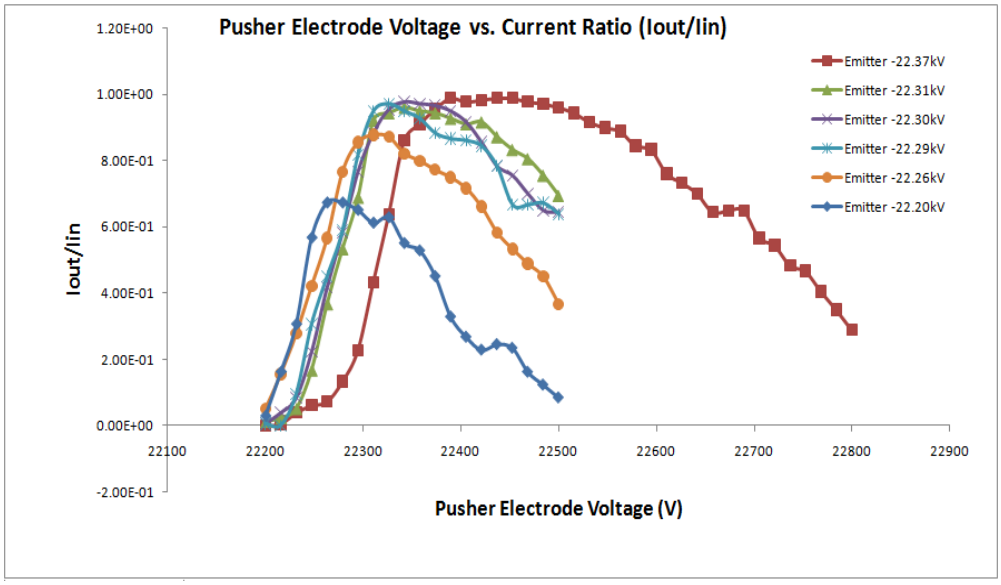

Figure A.29: Pusher Electrode Voltage vs. Current Ratio at Different Emitter Voltages.

Table A.6: Voltage sensitivity analysis results for variations in the emitter voltage.

Emitter voltage (kV)	Maximum current out (%)	ΔV (V)
-22.29	97.2%	95
-22.30	97.8%	110.5
-22.31	96.1%	130
-22.37	98.9%	200

APPENDIX B

VORPAL Simulation Input Decks

Continuous Current Source Model

```
$ import mathphys.mac
$ import geometry.mac
$ import mal.mac
# units
$ CM = 1.0e-2
$ NANOSECONDS = 1.0e-9
$ GIGAHERTZ = 1.0e9
$ METER = 1.0
$ SECONDS = 1.0
$ VOLTS = 1.0
$ AMPS = 1.0
$ TESLA = 1.0
$ DEGREES = PI/180.0
# - - - - - - - - - - - - - - - - - - - - - - - - - - - - - - - - - - - - - - - - - - - - - - - - - - - - - - - - - - - -
# - - - - - - - - - - - - - - - - - - - - - - - - - - - - - - - - - - - - - - - - - - - - - - - - - - - - - - - - - - - -
#
# ___ TYPICAL TYPES OF RUNS ___
# 1) to determine the mode spectrum, set: IMPULSE_EXCITATION=1,
PI_MODE_PRIMING=0, INCLUDE_DC_VOLTAGE=0, INCLUDE_PARTICLES=0
# 2) to calibrate the pi-mode frequency and Q, set: IMPULSE_EXCITATION=0,
PI_MODE_PRIMING=1, INCLUDE_DC_VOLTAGE=0, INCLUDE_PARTICLES=0
# 3) to calibrate DC voltage, set: IMPULSE_EXCITATION=0,
PI_MODE_PRIMING=0, INCLUDE_DC_VOLTAGE=1, INCLUDE_PARTICLES=0
# 4) to perform an actual run, set: IMPULSE_EXCITATION=0,
PI_MODE_PRIMING=0, INCLUDE_DC_VOLTAGE=1, INCLUDE_PARTICLES=1
#
# You may also include IMPULSE_EXCITATION or PI_MODE_PRIMING in an actual
run, to try to get a faster turnon.
#
# - - - - - - - - - - - - - - - - - - - - - - - - - - - - - - - - - - - - - - - - - - - - - - - - - - - - - - - - - - - -
- - - - - - -
# IMPULSE EXCITATION CONTROL
$ IMPULSE_EXCITATION = 0
# PI MODE PRIMING CONTROL
```

```
$ PI_MODE_PRIMING = 0
# DC VOLTAGE CONTROL
$ INCLUDE_DC_VOLTAGE = 1
# PARTICLES CONTROL
$ INCLUDE_PARTICLES = 1
# SIMULATION RUN TIME CONTROL
$ RISETIME = 1.0*NANOSECONDS
$ RUNTIME = 600.0*NANOSECONDS
$ NUMBER_OF_DUMPS = 50
# - - - - - - - - - - - - - - - - - - - - - - - - - - - - - - - - - - - - - - - - - - - - - - - - - - - - - - - - -
# 2D Rising Sun Magnetron geometry parameters
# ... the first-of-the-NCAVITY CAVITY1's is centered on the positive X axis
$ PENTAGON_CATHODE = 0
$ RCATHODE = 1.000*CM
$ RANODE = 2.242*CM
$ RCAVITY1 = 10.000*CM
$ RCAVITY2 = 6.000*CM
$ ANGLECAVITY1 = 10.0*DEGREES
$ ANGLECAVITY2 = 10.0*DEGREES
$ NCAVITY = 5
# Magnetron cavity loading parameter, controls Q, which goes as 1/NU_LOADING
$ NU_LOADING = 200.0e6/SECONDS
# Magnetron operating parameters
$ VOLTAGE_DC = 26.0e3*VOLTS
$ EMITTED_CURRENT = 500.0*AMPS/METER
$ BSTATIC = 0.12*TESLA
# - - - - - - - - - - - - - - - - - - - - - - - - - - - - - - - - - - - - - - - - - - - - - - - - - - - - - - - - -
# WORKSHEET
# In a magnetron, the DC_VOLTAGE must be above the Hartree voltage, which is given
by
$ HARTREE_MODE_FREQ = 0.96*GIGAHERTZ
$ HARTREE_MODE_PHIDOT = TWOPI*HARTREE_MODE_FREQ/NCAVITY
$ HARTREE_VDRIFT_SPOKE =
0.5*(RANODE+RCATHODE)*HARTREE_MODE_PHIDOT
$ HARTREE_VDRIFT_ANODE = RANODE*HARTREE_MODE_PHIDOT
$ HARTREE_VOLTAGE = BSTATIC*(RANODE-
RCATHODE)*HARTREE_VDRIFT_SPOKE -
0.5*ELECMASS*HARTREE_VDRIFT_ANODE**2/ELEMCHARGE
# uncomment this line to print out HARTREE_VOLTAGE
# - - - - - - - - - - - - - - - - - - - - - - - - - - - - - - - - - - - - - - - - - - - - - - - - - - - - - - - - -
- - - - - - -
# Simulation Domain Size, at least a cell larger than any structure
$ LX = 20.4*CM
$ LY = 20.4*CM
$ XBGN = -0.5*LX
$ YBGN = -0.5*LY
```

```
$ XEND = XBGN + LX
$ YEND = YBGN + LY
# Grid
$ NX = 102
$ NY = 102
$ NZ = 1
$ DX = LX/NX
$ DY = LY/NY
# Time parameters, apply Dey-Mittra Courant condition
$ DM_FRAC = 0.5
$ DT = 0.98*DM_FRAC/LIGHTSPEED/math.sqrt(1.0/(DX*DX)+1.0/(DY*DY))
$ TIMESTEPS = int(RUNTIME/DT)
$ NSTEPSPERDUMP = int(TIMESTEPS/NUMBER_OF_DUMPS)
# anode geometry function
<function solid_anode(x,y)>
H(RANODE^2-x^2-y^2)-0.4
</function>
$ DPHI = TWOPI/NCAVITY
<function wrapped_angle1(x,y)>
mod(atan2(y,x)+TWOPI+0.5*DPHI,DPHI)-0.5*DPHI
</function>
<function wrapped_angle2(x,y)>
mod(atan2(y,x)+TWOPI+1.0*DPHI,DPHI)-0.5*DPHI
</function>
<function cavities1(x,y)>
H(0.5*ANGLECAVITY1-abs(wrapped_angle1(x,y)))*H(x^2+y^2-
RANODE^2)*H(RCAVITY1^2-x^2-y^2)-0.4
</function>
<function cavities2(x,y)>
H(0.5*ANGLECAVITY2-abs(wrapped_angle2(x,y)))*H(x^2+y^2-
RANODE^2)*H(RCAVITY2^2-x^2-y^2)-0.4
</function>
<function anode(x,y)>
max(max(solid_anode(x,y),cavities1(x,y)),cavities2(x,y))
</function>
<GridBoundary theAnode>
kind = rgnGridBndry
dmFrac = DM_FRAC
calculateVolume = true
<STRgn region>
kind = stFuncRgn
<STFunc function>
kind = expression
expression = anode(x,y)
</STFunc>
</STRgn>
```

```
</GridBoundary>
# cathode geometry function, five-sided
$ if PENTAGON_CATHODE == 1
# the first vertex is at radius RCATHODE, and polar angle VERTEX_ANGLE
$ TWOPIFIFTHS = TWOPI/5.0
$ VERTEX_ANGLE = 0.0*TWOPIFIFTHS
$ xa = RCATHODE*cos(VERTEX_ANGLE+0.0*TWOPIFIFTHS)
$ ya = RCATHODE*sin(VERTEX_ANGLE+0.0*TWOPIFIFTHS)
$ xb = RCATHODE*cos(VERTEX_ANGLE+1.0*TWOPIFIFTHS)
$ yb = RCATHODE*sin(VERTEX_ANGLE+1.0*TWOPIFIFTHS)
$ xc = RCATHODE*cos(VERTEX_ANGLE+2.0*TWOPIFIFTHS)
$ yc = RCATHODE*sin(VERTEX_ANGLE+2.0*TWOPIFIFTHS)
$ xd = RCATHODE*cos(VERTEX_ANGLE+3.0*TWOPIFIFTHS)
$ yd = RCATHODE*sin(VERTEX_ANGLE+3.0*TWOPIFIFTHS)
$ xe = RCATHODE*cos(VERTEX_ANGLE+4.0*TWOPIFIFTHS)
$ ye = RCATHODE*sin(VERTEX_ANGLE+4.0*TWOPIFIFTHS)
<function cathode(x,y)>
1.0-geoPentagon(x,y,xa,ya,xb,yb,xc,yc,xd,yd,xe,ye)-0.4
</function>
$ else
# circular cathode
<function cathode(x,y)>
H(x^2+y^2-RCATHODE^2)-0.4
</function>
$ endif
<GridBoundary theCathode>
kind = rgnGridBndry
dmFrac = DM_FRAC
calculateVolume = true
<STRgn region>
kind = stFuncRgn
<STFunc function>
kind = expression
expression = cathode(x,y)
</STFunc>
</STRgn>
</GridBoundary>

# ___Decagon___ten-sided . If decagon used comment pentagon function and use this
# points must be sequenced in counter-clockwise order around decagon (right-hand-rule)
# cathode geometry function
$ if DECAGON_CATHODE == 1
# the first vertex is at radius RCATHODE, and polar angle VERTEX_ANGLE
$ TWOPITENTHS = TWOPI/10.0
$ VERTEX_ANGLE = 3.5*TWOPI/2
$ xa = RCATHODE*cos(VERTEX_ANGLE+0.0*TWOPITENTHS)
```

```
$ ya = RCATHODE*sin(VERTEX_ANGLE+0.0*TWOPITENTHS)
$ xb = RCATHODE*cos(VERTEX_ANGLE+1.0*TWOPITENTHS)
$ yb = RCATHODE*sin(VERTEX_ANGLE+1.0*TWOPITENTHS)
$ xc = RCATHODE*cos(VERTEX_ANGLE+2.0*TWOPITENTHS)
$ yc = RCATHODE*sin(VERTEX_ANGLE+2.0*TWOPITENTHS)
$ xd = RCATHODE*cos(VERTEX_ANGLE+3.0*TWOPITENTHS)
$ yd = RCATHODE*sin(VERTEX_ANGLE+3.0*TWOPITENTHS)
$ xe = RCATHODE*cos(VERTEX_ANGLE+4.0*TWOPITENTHS)
$ ye = RCATHODE*sin(VERTEX_ANGLE+4.0*TWOPITENTHS)
$ xf = RCATHODE*cos(VERTEX_ANGLE+5.0*TWOPITENTHS)
$ yf = RCATHODE*sin(VERTEX_ANGLE+5.0*TWOPITENTHS)
$ xg = RCATHODE*cos(VERTEX_ANGLE+6.0*TWOPITENTHS)
$ yg = RCATHODE*sin(VERTEX_ANGLE+6.0*TWOPITENTHS)
$ xh = RCATHODE*cos(VERTEX_ANGLE+7.0*TWOPITENTHS)
$ yh = RCATHODE*sin(VERTEX_ANGLE+7.0*TWOPITENTHS)
$ xi = RCATHODE*cos(VERTEX_ANGLE+8.0*TWOPITENTHS)
$ yi = RCATHODE*sin(VERTEX_ANGLE+8.0*TWOPITENTHS)
$ xj = RCATHODE*cos(VERTEX_ANGLE+9.0*TWOPITENTHS)
$ yj = RCATHODE*sin(VERTEX_ANGLE+9.0*TWOPITENTHS)
<function cathode(x,y)>
1.0-geoDecagon(x,y,xa,ya,xb,yb,xc,yc,xd,yd,xe,ye,xf,yf,xg,yg,xh,yh,xi,yi,xj,yj)-0.4
</function>
$ else
# circular cathode
<function cathode(x,y)>
H(x^2+y^2-RCATHODE^2)-0.4
</function>
$ endif
<GridBoundary theCathode>
kind = rgnGridBndry
dmFrac = DM_FRAC
calculateVolume = true
<STRgn region>
kind = stFuncRgn
<STFunc function>
kind = expression
expression = cathode(x,y)
</STFunc>
</STRgn>
</GridBoundary>

# assembled geometry function
<function magnetron2D(x,y)>
min(cathode(x,y),anode(x,y))
</function>
<GridBoundary theMagnetron>
```

```
kind = funcGridBndry
dmFrac = DM_FRAC
calculateVolume = true
<STFunc function>
kind = expression
expression = magnetron2D(x,y)
</STFunc>
</GridBoundary>
# cavity loading parameters
# ... only the first CAVITY1 along the positive X axis is loaded
$ RBGN_LOADING = 0.5*(RANODE+RCAVITY1)
$ LY_LOADING = RCAVITY1*ANGLECAVITY1+2.0*DY
$ IXBGN_LOADING = int((RBGN_LOADING-XBGN)/DX+0.5)
$ IYBGN_LOADING = int((-0.5*LY_LOADING -YBGN)/DY)
$ IYEND_LOADING = int(( 0.5*LY_LOADING -YBGN)/DY)+1
$ LOADING_FACTOR = sqrt((1.0-
0.5*DT*NU_LOADING)/(1.0+0.5*DT*NU_LOADING))
dimension = 2
floattype = double
<Grid globalGrid>
numPhysCells = [NX NY NZ]
lengths = [LX LY LZ]
startPositions = [XBGN YBGN ZSTART]
</Grid>
dt = DT
dumpPeriodicity = NSTEPSPERDUMP
nsteps = TIMESTEPS
<Decomp decomp>
decompType = regular
periodicDirs = [2]
</Decomp>
$ if INCLUDE_DC_VOLTAGE==1
# Generate electrostatic field between cathode and anode
# using combined source with feedback & drain
# and finite-difference divergence-free 1/r current profile
# normalized to charge equivalent cylindrical capacitior in RISETIME
$ APPROX_CAPACITANCE = TWOPI*EPSILON0/log(RANODE/RCATHODE)
$ CURRENT_DC = APPROX_CAPACITANCE*(VOLTAGE_DC/RISETIME)
<function rHatOverRcomponent1(x1,x2,DX1,DX2)>
(atan2(x1,x2-0.5*DX2)-atan2(x1,x2+0.5*DX2))/DX2
</function>
<function rHatOverRcomponent2(x1,x2,DX1,DX2)>
(atan2(x2,x1-0.5*DX1)-atan2(x2,x1+0.5*DX1))/DX1
</function>
<function rampup(t)>
1.0-exp(-1.0*max(0.0,t)/RISETIME)
```

```
</function>
<SumRhoJ sumRhoJ>
<Source feedbackVoltageSource>
kind = varadd
lowerBounds = [0 0 0]
upperBounds = [NX NY NZ]
components = [1 2]
<STFunc component1>
kind = feedbackSTFunc
feedback = voltageFeedback
expression = (CURRENT_DC/TWOPI)*rHatOverRcomponent1(x,y,DX,DY)
</STFunc>
<STFunc component2>
kind = feedbackSTFunc
feedback = voltageFeedback
expression = (CURRENT_DC/TWOPI)*rHatOverRcomponent2(x,y,DX,DY)
</STFunc>
</Source>
<Source constantVoltageDrain>
kind = varadd
lowerBounds = [0 0 0]
upperBounds = [NX NY NZ]
components = [1 2]
<STFunc component1>
kind = expression
expression = -
1.0*rampup(t)*(CURRENT_DC/TWOPI)*rHatOverRcomponent1(x,y,DX,DY)
</STFunc>
<STFunc component2>
kind = expression
expression = -
1.0*rampup(t)*(CURRENT_DC/TWOPI)*rHatOverRcomponent2(x,y,DX,DY)
</STFunc>
</Source>
</SumRhoJ>
$ endif
# the static magnetic field
<EmField myExternalBField>
kind = funcEmField
<Component Bz>
index = 5
<STFunc component5>
kind = expression
expression = BSTATIC
</STFunc>
</Component>
```

```
</EmField>
# the Maxwell Equations dynamic fields
<EmField YeeEmField>
kind = emMultiField
# - - - - - - - - - - - - - - - -
<Field edgeE>
numComponents = 3
offset = edge
</Field>
<Field faceB>
numComponents = 3
offset = face
</Field>
<Field nodalE>
numComponents = 3
overlap = [1 2]
offset = none
dumpPeriod = 0
</Field>
<Field nodalB>
numComponents = 3
overlap = [1 2]
offset = none
dumpPeriod = 0
</Field>
externalFields = [SumRhoJ]
# - - - - - - - - - - - - - - - -
<FieldMultiUpdater ampere>
gridBoundary = theMagnetron
interiorness = deymittra
kind = yeeAmpereUpdater
components = [0 1 2]
contractFromBottomInNonComponentDir = 1
lowerBounds = [0 0 0]
upperBounds = [NX NY NZ]
readFields = [faceB SumRhoJ]
writeFields = [edgeE]
</FieldMultiUpdater>
<FieldMultiUpdater faraday>
gridBoundary = theMagnetron
interiorness = deymittra
kind = yeeFaradayUpdater
components = [0 1 2]
expandToTopInComponentDir=1
lowerBounds = [0 0 0]
upperBounds = [NX NY NZ]
```

```
readFields = [edgeE]
writeFields = [faceB]
</FieldMultiUpdater>
<FieldUpdater deyMittraFaraday>
gridBoundary = theMagnetron
interiorness = deymittra
kind = deyMittraUpdater
lowerBounds = [0 0 0]
upperBounds = [NX NY NZ]
readFields = [edgeE]
writeFields = [faceB]
</FieldUpdater>
<FieldUpdater loadB>
kind = STFuncUpdater
operation = multiply
lowerBounds = [IXBGN_LOADING IYBGN_LOADING 0 ]
upperBounds = [$NX+1$ $IYEND_LOADING+1$ $NZ+1$]
component = 2
writeComponents = [2]
writeFields = [faceB]
<STFunc loadingFunction>
kind = expression
expression = LOADING_FACTOR
</STFunc>
</FieldUpdater>
<FieldUpdater computeNodalB>
kind = faceToNodeVec
lowerBounds = [0 0 0]
upperBounds = [NX NY NZ]
readFields = [faceB]
writeFields = [nodalB]
</FieldUpdater>
<FieldUpdater computeNodalE>
kind = edgeToNodeVec
lowerBounds = [0 0 0]
upperBounds = [NX NY NZ]
readFields = [edgeE]
writeFields = [nodalE]
</FieldUpdater>
$ if IMPULSE_EXCITATION==1
# want cavity1Voltage to be roughly 0.1*VOLTAGE_DC
$ BNORMALIZATION =
(0.1*VOLTAGE_DC/(ANGLECAVITY1*RANODE)/LIGHTSPEED)*(0.05*DT/DT)
<function excitationPulse(t)>
BNORMALIZATION*sin(PI*max(0.0,min(1.0,0.05*t/DT)))^2
</function>
```

```
<function singleCavityProfile(x,y,z)>
H(x^2+y^2-RANODE^2)*H(cavities1(x,y))*H(0.5*PI/NCAVITY-
abs(atan2(y,x)))*cos(0.5*PI*(RCAVITY1-sqrt(x^2+y^2))/(RCAVITY1-RANODE))^2
</function>
<FieldUpdater impluseBz>
kind = STFuncUpdater
operation = add
lowerBounds = [0 0 0]
upperBounds = [NX NY NZ]
component = 2
writeComponents = [2]
writeFields = [faceB]
<STFunc loadingFunction>
kind = expression
expression = excitationPulse(t)*singleCavityProfile(x,y,z)
</STFunc>
</FieldUpdater>
$ endif
$ if PI_MODE_PRIMING==1
# want cavity1Voltage to be roughly 0.1*VOLTAGE_DC
$ BNORMALIZATION =
(0.1*VOLTAGE_DC/(ANGLECAVITY1*RANODE)/LIGHTSPEED)*(4.0*DT/RISETI
ME)
<function primePulse(t)>
BNORMALIZATION*sin(PI*max(0.0,min(1.0,4.0*t/RISETIME)))^2
</function>
# The approximate BzProfile should try to have the null lines roughly in the correct
location
# ... Rising Sun Mode has node partway up the long cavity arm, had to work hard for
that!
$ RNULL = RANODE*(1.0-0.5*PI/NCAVITY) + 0.5*abs(RCAVITY1-RCAVITY2)
$ KCAVITY = 0.5*PI/(max(RCAVITY1,RCAVITY2)-RNULL)
$ FCAV1 = cos(KCAVITY*(RCAVITY1-RANODE))
$ FCAV2 = -1.0*cos(KCAVITY*(RCAVITY2-RANODE))
$ FCAVA = 0.5*(FCAV1+FCAV2)
$ FCAVD = 0.5*(FCAV1-FCAV2)
<function approximateBzProfile(x,y,z)>
H(x^2+y^2-
RANODE^2)*H(cavities1(x,y))*abs(cos(NCAVITY*atan2(y,x)))*cos(KCAVITY*(RCA
VITY1-sqrt(x^2+y^2))) - \
H(x^2+y^2-
RANODE^2)*H(cavities2(x,y))*abs(cos(NCAVITY*atan2(y,x)))*cos(KCAVITY*(RCA
VITY2-sqrt(x^2+y^2))) + \
H(RANODE^2-x^2-y^2)*H(cathode(x,y))
*abs(cos(NCAVITY*atan2(y,x)))*FCAVD*((sqrt(x^2+y^2)-RCATHODE)/(RANODE-
RCATHODE))^2*(-1.0+2.0*H(cos(NCAVITY*atan2(y,x)))) + \
```

```
H(RANODE^2-x^2-y^2)*H(cathode(x,y))*FCAVA
</function>
<FieldUpdater primeBz>
kind = STFuncUpdater
operation = add
lowerBounds = [0 0 0]
upperBounds = [NX NY NZ]
component = 2
writeComponents = [2]
writeFields = [faceB]
<STFunc loadingFunction>
kind = expression
expression = primePulse(t)*approximateBzProfile(x,y,z)
</STFunc>
</FieldUpdater>
$ endif
# - - - - - - - - - - - - - - - -
<InitialUpdateStep init_step1>
alsoAfterRestore = 1
toDtFrac = 0.
updaters = [computeNodalE]
messageFields = [nodalE]
</InitialUpdateStep>
<InitialUpdateStep init_step2>
alsoAfterRestore = 1
toDtFrac = 0.
messageFields = [nodalB]
updaters = [computeNodalB]
</InitialUpdateStep>
<UpdateStep step1>
toDtFrac = 0.5
updaters = [loadB faraday deyMittraFaraday]
messageFields = [faceB]
</UpdateStep>
<UpdateStep step2>
toDtFrac = 1.0
updaters = [ampere]
messageFields = [edgeE]
</UpdateStep>
<UpdateStep step3>
toDtFrac = 1.0
$ if (IMPULSE_EXCITATION==1) and (PI_MODE_PRIMING==1)
updaters = [faraday deyMittraFaraday loadB impluseBz primeBz]
$ endif
$ if (IMPULSE_EXCITATION==1) and (PI_MODE_PRIMING==0)
updaters = [faraday deyMittraFaraday loadB impluseBz]
```

```
$ endif
$ if (IMPULSE_EXCITATION==0) and (PI_MODE_PRIMING==1)
updaters = [faraday deyMittraFaraday loadB primeBz]
$ endif
$ if (IMPULSE_EXCITATION==0) and (PI_MODE_PRIMING==0)
updaters = [faraday deyMittraFaraday loadB]
$ endif
messageFields = [faceB]
</UpdateStep>
<UpdateStep step4>
toDtFrac = 1.
updaters = [computeNodalE]
messageFields = [nodalE]
</UpdateStep>
<UpdateStep step5>
toDtFrac = 1.
updaters = [computeNodalB]
messageFields = [nodalB]
</UpdateStep>
# - - - - - - - - - - - - - - - -
</EmField>
# diagnostics
$ IX_AXIS = int((0.0-XBGN)/DX+0.5)
$ IY_AXIS = int((0.0-YBGN)/DY+0.5)
<History cathodeAnodeVoltage>
kind = pseudoPotential
field = YeeEmField.edgeE
referencePoint = [IX_AXIS IY_AXIS]
measurePoint = [NX IY_AXIS]
</History>
$ RBGN_LOADING = 0.5*(RANODE+RCAVITY1)
$ IX_CAVITY1_LINE = int((RANODE -XBGN)/DX)+2
$ IX_CAVITY1_POINT = int((RCAVITY1-XBGN)/DX)-1
$ LY_CAVITY_LINE = RANODE*ANGLECAVITY1+2.0*DY
$ IYBGN_CAVITY_LINE = int((-0.5*LY_CAVITY_LINE-YBGN)/DY)
$ IYEND_CAVITY_LINE = int(( 0.5*LY_CAVITY_LINE-YBGN)/DY)+1
<History cavity1Voltage>
kind = pseudoPotential
field = YeeEmField.edgeE
referencePoint = [IX_CAVITY1_LINE IYBGN_CAVITY_LINE]
measurePoint = [IX_CAVITY1_LINE IYEND_CAVITY_LINE]
</History>
<History cavity1Bfield_Tesla>
kind = fieldAtIndices
point = [IX_CAVITY1_POINT IY_AXIS]
field = YeeEmField.faceB
```

```
components = [2]
</History>
<History cavity1Loading_Watts>
kind = fieldPoyn
lowerBounds = [$IXBGN_LOADING-1$ IYBGN_LOADING 0 ]
upperBounds = [$IXBGN_LOADING-1$ $IYEND_LOADING+1$ $NZ+1$]
fields = [YeeEmField.edgeE YeeEmField.faceB]
</History>
<History fieldEnergy_Joules>
kind = EMfieldEnergy
fields = [YeeEmField.edgeE YeeEmField.faceB]
</History>
# special diagnostic for DC voltage feedback
$ if INCLUDE_DC_VOLTAGE==1
<History voltageFeedback>
kind=feedback
feedbackHist=cathodeAnodeVoltage
timeConstant=RISETIME
<STFunc desiredHistory>
kind=expression
expression = VOLTAGE_DC*rampup(t)
</STFunc>
</History>
$ endif
$ if INCLUDE_PARTICLES == 1
# the fields used for the Lorentz force
<ComboEmField myComboEmField>
kind = comboEmField
emField1 = YeeEmField
emField2 = myExternalBField
dumpField = 0
</ComboEmField>
# emission algorithm parameters
$ PARTPERCELLPERSTEP = 10
$ AREA_EMIT = 2.0*PI*RCATHODE
$ APPROXNUMEMITCELLS = AREA_EMIT/sqrt(DY*DX)
$ JDENS_EMIT = EMITTED_CURRENT/AREA_EMIT
$ NOM_DEN =
EMITTED_CURRENT*DT/(ELEMCHARGE*APPROXNUMEMITCELLS*PARTPE
RCELLPERSTEP)
$ FOREVER = 1.0*SECONDS
$ VTHERMAL = 1.5e5 # meters/second
<Species electrons>
verbosity = 0
kind=relBorisVW
charge = ELECCHARGE
```

```
mass = ELECMASS
emField = myComboEmField
nominalDensity = NOM_DEN
nomPtclsPerCell = PARTPERCELLPERSTEP
numPtclsInMacro = 1.0e5
<ParticleSource cutCellEmitter>
kind = xvLoaderEmitter
positionFunction = random
useCornerMove = true
emitBasedOnLocalForce = true
loadOnShift = false
loadAfterInit = false
applyTimes = [RISETIME FOREVER]
<PositionGenerator thisGen>
kind = cutCellPosGen
numMacroPtclsPerStep = PARTPERCELLPERSTEP
emitterBoundary = theCathode
emissionOffset = 0.1
</PositionGenerator>
<VelocityGenerator emitVelGen>
kind = funcVelGen
velocityIsLocal = true
<STFunc component0>
kind = expression
expression = -1.0*VTHERMAL
</STFunc>
</VelocityGenerator>
<STFunc currentDensityFunc>
kind = expression
expression = JDENS_EMIT
</STFunc>
</ParticleSource>
<ParticleSink cathodeElectronSink>
kind = absSavCutCell
gridBoundary = theCathode
lowerBounds = [ -1 -1 -1 ]
upperBounds = [$NX+1$ $NY+1$ $NZ+1$]
</ParticleSink>
<ParticleSink anodeElectronSink>
kind = absSavCutCell
gridBoundary = theAnode
lowerBounds = [ -1 -1 -1 ]
upperBounds = [$NX+1$ $NY+1$ $NZ+1$]
</ParticleSink>
</Species>
<History anodeCurrent_Amps>
```

```
kind = speciesCurrAbs
species = electrons
ptclAbsorber = anodeElectronSink
</History>
<History cathodeReturnCurrent_Amps>
kind = speciesCurrAbs
species = electrons
ptclAbsorber = cathodeElectronSink
</History>
<History anodeElectronHeat_Watts_timesDT>
kind = speciesEngyAbs
species = electrons
ptclAbsorber = anodeElectronSink
</History>
<History cathodeElectronHeat_Watts_timesDT>
kind = speciesEngyAbs
species = electrons
ptclAbsorber = cathodeElectronSink
</History>
<History numMacroParticles>
kind = speciesNumberOf
species = electrons
</History>
$ endif
```

Modulated, Addressable Cathode

```
##Current density model changes from previous code.
# emission algorithm parameters
$ MASK_FACTOR = min(NUMBER_OF_EMITTERS*(PHIEND_EMIT-
PHIBGN_EMIT)/TWOPI,1.0)
$ PARTPERCELLPERSTEP = int(3.0/MASK_FACTOR+0.5)
$ AREA_EMIT = 2.0*PI*RCATHODE*MASK_FACTOR
$ APPROXNUMEMITCELLS = AREA_EMIT/sqrt(DY*DX)
$ JDENS_EMIT = EMITTED_CURRENT/AREA_EMIT
$ NOM_DEN =
EMITTED_CURRENT*DT/(ELEMCHARGE*APPROXNUMEMITCELLS*PARTPE
RCELLPERSTEP)
$ FOREVER = 1.0*SECONDS
$ VTHERMAL = 1.5e5 # meters/second
$ DPHI_EMIT = TWOPI/NUMBER_OF_EMITTERS
<function emissionAngle(x,y)>
mod(atan2(y,x)+TWOPI+0.5*DPHI_EMIT,DPHI_EMIT)-0.5*DPHI_EMIT
</function>
<function emissionMask(x,y)>
H(PHIEND_EMIT-emissionAngle(x,y))*H(emissionAngle(x,y)-PHIBGN_EMIT)
</function>
<Species electrons>
verbosity = 0
kind=relBorisVW
charge = ELECCHARGE
mass = ELECMASS
emField = myComboEmField
nominalDensity = NOM_DEN
nomPtclsPerCell = PARTPERCELLPERSTEP
numPtclsInMacro = 1.0e5
#Macro for particle source (multiple emitters)
<macro ParticleSourceat(source_name,phibgn,phiend,tbegin,tend)>
<ParticleSource source_name>
kind = xvLoaderEmitter
positionFunction = random
useCornerMove = true
emitBasedOnLocalForce = true
loadOnShift = false
loadAfterInit = false
applyTimes = [tbegin tend]
<PositionGenerator thisGen>
kind = cutCellPosGen
```

```
numMacroPtclsPerStep = PARTPERCELLPERSTEP
emitterBoundary = theCathode
emissionOffset = 0.1
<STFunc mask>
kind = expression
expression = H((phiend)-atan2(y,x))*H(atan2(y,x)-(phibgn))
</STFunc>
</PositionGenerator>
<VelocityGenerator emitVelGen>
kind = funcVelGen
velocityIsLocal = true
<STFunc component0>
kind = expression
expression = -1.0*VTHERMAL
</STFunc>
</VelocityGenerator>
<STFunc currentDensityFunc>
kind = expression
expression = JDENS_EMIT*emissionMask(x,y)
</STFunc>
</ParticleSource>
</macro>
<function fix_angle(angle)>
mod(angle+PI,TWOPI)-PI
</function>

###Location of each current source. This corresponds to the ten-sided cathode.
###PHIBGN – start location of the current source.
###PHIEND – end location of the current source.
##########################################################################
########################1/5
$PHIBGN1=fix_angle(VERTEX_ANGLE+0.1699*TWOPITENTHS+0.1699*TWOPIT
ENTHS/NUMBER_OF_EMITTERS)-5.0*DEGREES
$PHIEND1=fix_angle(VERTEX_ANGLE+0.1699*TWOPITENTHS+0.1699*TWOPIT
ENTHS/NUMBER_OF_EMITTERS)+5.0*DEGREES
$PHIBGN2=fix_angle(VERTEX_ANGLE+0.40*TWOPITENTHS+0.40*TWOPITENT
HS/NUMBER_OF_EMITTERS)-5.0*DEGREES
$PHIEND2=fix_angle(VERTEX_ANGLE+0.40*TWOPITENTHS+0.40*TWOPITENT
HS/NUMBER_OF_EMITTERS)+5.0*DEGREES
$PHIBGN3=fix_angle(VERTEX_ANGLE+0.65*TWOPITENTHS+0.65*TWOPITENT
HS/NUMBER_OF_EMITTERS)-5.0*DEGREES
$PHIEND3=fix_angle(VERTEX_ANGLE+0.65*TWOPITENTHS+0.65*TWOPITENT
HS/NUMBER_OF_EMITTERS)+5.0*DEGREES
$PHIBGN4=fix_angle(VERTEX_ANGLE+0.99*TWOPITENTHS+0.99*TWOPITENT
HS/NUMBER_OF_EMITTERS)-5.0*DEGREES
```

```
$PHIEND4=fix_angle(VERTEX_ANGLE+0.99*TWOPITENTHS+0.99*TWOPITENT
HS/NUMBER_OF_EMITTERS)+5.0*DEGREES
$PHIBGN5=fix_angle(VERTEX_ANGLE+1.26*TWOPITENTHS+1.26*TWOPITENT
HS/NUMBER_OF_EMITTERS)-5.0*DEGREES
$PHIEND5=fix_angle(VERTEX_ANGLE+1.26*TWOPITENTHS+1.26*TWOPITENT
HS/NUMBER_OF_EMITTERS)+5.0*DEGREES
$PHIBGN6=fix_angle(VERTEX_ANGLE+1.54*TWOPITENTHS+1.54*TWOPITENT
HS/NUMBER_OF_EMITTERS)-5.0*DEGREES
$PHIEND6=fix_angle(VERTEX_ANGLE+1.54*TWOPITENTHS+1.54*TWOPITENT
HS/NUMBER_OF_EMITTERS)+5.0*DEGREES
$PHIBGN7=fix_angle(VERTEX_ANGLE+1.80*TWOPITENTHS+1.80*TWOPITENT
HS/NUMBER_OF_EMITTERS)-5.0*DEGREES
$PHIEND7=fix_angle(VERTEX_ANGLE+1.80*TWOPITENTHS+1.80*TWOPITENT
HS/NUMBER_OF_EMITTERS)+5.0*DEGREES
$PHIBGN8=fix_angle(VERTEX_ANGLE+2.09*TWOPITENTHS+2.09*TWOPITENT
HS/NUMBER_OF_EMITTERS)-5.0*DEGREES
$PHIEND8=fix_angle(VERTEX_ANGLE+2.09*TWOPITENTHS+2.09*TWOPITENT
HS/NUMBER_OF_EMITTERS)+5.0*DEGREES
$PHIBGN9=fix_angle(VERTEX_ANGLE+2.36*TWOPITENTHS+2.36*TWOPITENT
HS/NUMBER_OF_EMITTERS)-5.0*DEGREES
$PHIEND9=fix_angle(VERTEX_ANGLE+2.36*TWOPITENTHS+2.36*TWOPITENT
HS/NUMBER_OF_EMITTERS)+5.0*DEGREES
$PHIBGN10=fix_angle(VERTEX_ANGLE+2.65*TWOPITENTHS+2.65*TWOPITEN
THS/NUMBER_OF_EMITTERS)-5.0*DEGREES
$PHIEND10=fix_angle(VERTEX_ANGLE+2.65*TWOPITENTHS+2.65*TWOPITEN
THS/NUMBER_OF_EMITTERS)+5.0*DEGREES
$PHIBGN11=fix_angle(VERTEX_ANGLE+2.92*TWOPITENTHS+2.92*TWOPITEN
THS/NUMBER_OF_EMITTERS)-5.0*DEGREES
$PHIEND11=fix_angle(VERTEX_ANGLE+2.92*TWOPITENTHS+2.92*TWOPITEN
THS/NUMBER_OF_EMITTERS)+5.0*DEGREES
$PHIBGN12=fix_angle(VERTEX_ANGLE+3.20*TWOPITENTHS+3.20*TWOPITEN
THS/NUMBER_OF_EMITTERS)-5.0*DEGREES
$PHIEND12=fix_angle(VERTEX_ANGLE+3.20*TWOPITENTHS+3.20*TWOPITEN
THS/NUMBER_OF_EMITTERS)+5.0*DEGREES
$PHIBGN13=fix_angle(VERTEX_ANGLE+3.50*TWOPITENTHS+3.50*TWOPITEN
THS/NUMBER_OF_EMITTERS)-5.0*DEGREES
$PHIEND13=fix_angle(VERTEX_ANGLE+3.50*TWOPITENTHS+3.50*TWOPITEN
THS/NUMBER_OF_EMITTERS)+5.0*DEGREES
$PHIBGN14=fix_angle(VERTEX_ANGLE+3.75*TWOPITENTHS+3.75*TWOPITEN
THS/NUMBER_OF_EMITTERS)-5.0*DEGREES
$PHIEND14=fix_angle(VERTEX_ANGLE+3.75*TWOPITENTHS+3.75*TWOPITEN
THS/NUMBER_OF_EMITTERS)+5.0*DEGREES
$PHIBGN15=fix_angle(VERTEX_ANGLE+4.00*TWOPITENTHS+4.00*TWOPITEN
THS/NUMBER_OF_EMITTERS)-5.0*DEGREES
$PHIEND15=fix_angle(VERTEX_ANGLE+4.00*TWOPITENTHS+4.00*TWOPITEN
THS/NUMBER_OF_EMITTERS)+5.0*DEGREES
```

```
$PHIBGN16=fix_angle(VERTEX_ANGLE+4.30*TWOPITENTHS+4.30*TWOPITEN
THS/NUMBER_OF_EMITTERS)-5.0*DEGREES
$PHIEND16=fix_angle(VERTEX_ANGLE+4.30*TWOPITENTHS+4.30*TWOPITEN
THS/NUMBER_OF_EMITTERS)+5.0*DEGREES
$PHIBGN17=fix_angle(VERTEX_ANGLE+4.60*TWOPITENTHS+4.55*TWOPITEN
THS/NUMBER_OF_EMITTERS)-5.0*DEGREES
$PHIEND17=fix_angle(VERTEX_ANGLE+4.60*TWOPITENTHS+4.55*TWOPITEN
THS/NUMBER_OF_EMITTERS)+5.0*DEGREES
$PHIBGN18=fix_angle(VERTEX_ANGLE+4.85*TWOPITENTHS+4.85*TWOPITEN
THS/NUMBER_OF_EMITTERS)-5.0*DEGREES
$PHIEND18=fix_angle(VERTEX_ANGLE+4.85*TWOPITENTHS+4.85*TWOPITEN
THS/NUMBER_OF_EMITTERS)+5.0*DEGREES
$PHIBGN19=fix_angle(VERTEX_ANGLE+5.15*TWOPITENTHS+5.15*TWOPITEN
THS/NUMBER_OF_EMITTERS)-5.0*DEGREES
$PHIEND19=fix_angle(VERTEX_ANGLE+5.15*TWOPITENTHS+5.15*TWOPITEN
THS/NUMBER_OF_EMITTERS)+5.0*DEGREES
$PHIBGN20=fix_angle(VERTEX_ANGLE+5.43*TWOPITENTHS+5.43*TWOPITEN
THS/NUMBER_OF_EMITTERS)-5.0*DEGREES
$PHIEND20=fix_angle(VERTEX_ANGLE+5.43*TWOPITENTHS+5.43*TWOPITEN
THS/NUMBER_OF_EMITTERS)+5.0*DEGREES
$PHIBGN21=fix_angle(VERTEX_ANGLE+5.71*TWOPITENTHS+5.71*TWOPITEN
THS/NUMBER_OF_EMITTERS)-5.0*DEGREES
$PHIEND21=fix_angle(VERTEX_ANGLE+5.71*TWOPITENTHS+5.71*TWOPITEN
THS/NUMBER_OF_EMITTERS)+5.0*DEGREES
$PHIBGN22=fix_angle(VERTEX_ANGLE+5.98*TWOPITENTHS+5.98*TWOPITEN
THS/NUMBER_OF_EMITTERS)-6.5*DEGREES
$PHIEND22=fix_angle(VERTEX_ANGLE+5.98*TWOPITENTHS+5.98*TWOPITEN
THS/NUMBER_OF_EMITTERS)+6.5*DEGREES
$PHIBGN23=fix_angle(VERTEX_ANGLE+6.3*TWOPITENTHS+6.28*TWOPITENT
HS/NUMBER_OF_EMITTERS)-5.7*DEGREES
$PHIEND23=fix_angle(VERTEX_ANGLE+6.3*TWOPITENTHS+6.28*TWOPITENT
HS/NUMBER_OF_EMITTERS)+5.7*DEGREES
$PHIBGN31=fix_angle(VERTEX_ANGLE+6.3*TWOPITENTHS+6.28*TWOPITENT
HS/NUMBER_OF_EMITTERS)-5.7*DEGREES+TWOPI
$PHIEND31=fix_angle(VERTEX_ANGLE+6.3*TWOPITENTHS+6.28*TWOPITENT
HS/NUMBER_OF_EMITTERS)+5.7*DEGREES+TWOPI
$PHIBGN24=fix_angle(VERTEX_ANGLE+6.50*TWOPITENTHS+6.50*TWOPITEN
THS/NUMBER_OF_EMITTERS)-5.0*DEGREES
$PHIEND24=fix_angle(VERTEX_ANGLE+6.50*TWOPITENTHS+6.50*TWOPITEN
THS/NUMBER_OF_EMITTERS)+5.0*DEGREES
$PHIBGN25=fix_angle(VERTEX_ANGLE+6.80*TWOPITENTHS+6.80*TWOPITEN
THS/NUMBER_OF_EMITTERS)-5.0*DEGREES
$PHIEND25=fix_angle(VERTEX_ANGLE+6.80*TWOPITENTHS+6.80*TWOPITEN
THS/NUMBER_OF_EMITTERS)+5.0*DEGREES
$PHIBGN26=fix_angle(VERTEX_ANGLE+7.09*TWOPITENTHS+7.09*TWOPITEN
THS/NUMBER_OF_EMITTERS)-5.0*DEGREES
```

```
$PHIEND26=fix_angle(VERTEX_ANGLE+7.09*TWOPITENTHS+7.09*TWOPITEN
THS/NUMBER_OF_EMITTERS)+5.0*DEGREES
$PHIBGN27=fix_angle(VERTEX_ANGLE+7.35*TWOPITENTHS+7.35*TWOPITEN
THS/NUMBER_OF_EMITTERS)-5.0*DEGREES
$PHIEND27=fix_angle(VERTEX_ANGLE+7.35*TWOPITENTHS+7.35*TWOPITEN
THS/NUMBER_OF_EMITTERS)+5.0*DEGREES
$PHIBGN28=fix_angle(VERTEX_ANGLE+7.65*TWOPITENTHS+7.65*TWOPITEN
THS/NUMBER_OF_EMITTERS)-5.0*DEGREES
$PHIEND28=fix_angle(VERTEX_ANGLE+7.65*TWOPITENTHS+7.65*TWOPITEN
THS/NUMBER_OF_EMITTERS)+5.0*DEGREES
$PHIBGN29=fix_angle(VERTEX_ANGLE+7.92*TWOPITENTHS+7.92*TWOPITEN
THS/NUMBER_OF_EMITTERS)-5.0*DEGREES
$PHIEND29=fix_angle(VERTEX_ANGLE+7.92*TWOPITENTHS+7.92*TWOPITEN
THS/NUMBER_OF_EMITTERS)+5.0*DEGREES
$PHIBGN30=fix_angle(VERTEX_ANGLE+8.20*TWOPITENTHS+8.20*TWOPITEN
THS/NUMBER_OF_EMITTERS)-5.0*DEGREES
$PHIEND30=fix_angle(VERTEX_ANGLE+8.20*TWOPITENTHS+8.20*TWOPITEN
THS/NUMBER_OF_EMITTERS)+5.0*DEGREES
##########################################################################
##########################
##########This portion of the code show 5 periods of the modulated current sources
###1/5
#############################################################1/5
ParticleSourceat(mysource1,PHIBGN1,PHIEND1,0.00e-10,1.73e-10)
ParticleSourceat(mysource2,PHIBGN2,PHIEND2,1.73e-10,3.47e-10)
ParticleSourceat(mysource3,PHIBGN3,PHIEND3,3.47e-10,5.20e-10)
ParticleSourceat(mysource4,PHIBGN4,PHIEND4,5.20e-10,6.93e-10)
ParticleSourceat(mysource5,PHIBGN5,PHIEND5,6.93e-10,8.67e-10)
ParticleSourceat(mysource6,PHIBGN6,PHIEND6,8.67e-10,1.04e-09)
ParticleSourceat(mysource7,PHIBGN7,PHIEND7,0.00e-10,1.73e-10)
ParticleSourceat(mysource8,PHIBGN8,PHIEND8,1.73e-10,3.47e-10)
ParticleSourceat(mysource9,PHIBGN9,PHIEND9,3.47e-10,5.20e-10)
ParticleSourceat(mysource10,PHIBGN10,PHIEND10,5.20e-10,6.93e-10)
ParticleSourceat(mysource11,PHIBGN11,PHIEND11,6.93e-10,8.67e-10)
ParticleSourceat(mysource12,PHIBGN12,PHIEND12,8.67e-10,1.04e-09)
ParticleSourceat(mysource13,PHIBGN13,PHIEND13,0.00e-10,1.73e-10)
ParticleSourceat(mysource14,PHIBGN14,PHIEND14,1.73e-10,3.47e-10)
ParticleSourceat(mysource15,PHIBGN15,PHIEND15,3.47e-10,5.20e-10)
ParticleSourceat(mysource16,PHIBGN16,PHIEND16,5.20e-10,6.93e-10)
ParticleSourceat(mysource17,PHIBGN17,PHIEND17,6.93e-10,8.67e-10)
ParticleSourceat(mysource18,PHIBGN18,PHIEND18,8.67e-10,1.04e-09)
ParticleSourceat(mysource19,PHIBGN19,PHIEND19,0.00e-10,1.73e-10)
ParticleSourceat(mysource20,PHIBGN20,PHIEND20,1.73e-10,3.47e-10)
ParticleSourceat(mysource21,PHIBGN21,PHIEND21,3.47e-10,5.20e-10)
ParticleSourceat(mysource22,PHIBGN22,PHIEND22,5.20e-10,6.93e-10)
ParticleSourceat(mysource23,PHIBGN23,PHIEND23,6.93e-10,8.67e-10)
```

```
ParticleSourceat(mysource31,PHIBGN31,PHIEND31,6.93e-10,8.67e-10)
ParticleSourceat(mysource24,PHIBGN24,PHIEND24,8.67e-10,1.04e-09)
ParticleSourceat(mysource25,PHIBGN25,PHIEND25,0.00e-10,1.73e-10)
ParticleSourceat(mysource26,PHIBGN26,PHIEND26,1.73e-10,3.47e-10)
ParticleSourceat(mysource27,PHIBGN27,PHIEND27,3.47e-10,5.20e-10)
ParticleSourceat(mysource28,PHIBGN28,PHIEND28,5.20e-10,6.93e-10)
ParticleSourceat(mysource29,PHIBGN29,PHIEND29,6.93e-10,8.67e-10)
ParticleSourceat(mysource30,PHIBGN30,PHIEND30,8.67e-10,1.04e-09)
#####################################################################
###2/5
############################################################2/5
ParticleSourceat(mysource31,PHIBGN1,PHIEND1,1.04e-09,1.21e-09)
ParticleSourceat(mysource32,PHIBGN2,PHIEND2,1.21e-09,1.39e-09)
ParticleSourceat(mysource33,PHIBGN3,PHIEND3,1.39e-09,1.56e-09)
ParticleSourceat(mysource34,PHIBGN4,PHIEND4,1.56e-09,1.73e-09)
ParticleSourceat(mysource35,PHIBGN5,PHIEND5,1.73e-09,1.91e-09)
ParticleSourceat(mysource36,PHIBGN6,PHIEND6,1.91e-09,2.08e-09)
ParticleSourceat(mysource37,PHIBGN7,PHIEND7,1.04e-09,1.21e-09)
ParticleSourceat(mysource38,PHIBGN8,PHIEND8,1.21e-09,1.39e-09)
ParticleSourceat(mysource39,PHIBGN9,PHIEND9,1.39e-09,1.56e-09)
ParticleSourceat(mysource40,PHIBGN10,PHIEND10,1.56e-09,1.73e-09)
ParticleSourceat(mysource41,PHIBGN11,PHIEND11,1.73e-09,1.91e-09)
ParticleSourceat(mysource42,PHIBGN12,PHIEND12,1.91e-09,2.08e-09)
ParticleSourceat(mysource43,PHIBGN13,PHIEND13,1.04e-09,1.21e-09)
ParticleSourceat(mysource44,PHIBGN14,PHIEND14,1.21e-09,1.39e-09)
ParticleSourceat(mysource45,PHIBGN15,PHIEND15,1.39e-09,1.56e-09)
ParticleSourceat(mysource46,PHIBGN16,PHIEND16,1.56e-09,1.73e-09)
ParticleSourceat(mysource47,PHIBGN17,PHIEND17,1.73e-09,1.91e-09)
ParticleSourceat(mysource48,PHIBGN18,PHIEND18,1.91e-09,2.08e-09)
ParticleSourceat(mysource49,PHIBGN19,PHIEND19,1.04e-09,1.21e-09)
ParticleSourceat(mysource50,PHIBGN20,PHIEND20,1.21e-09,1.39e-09)
ParticleSourceat(mysource51,PHIBGN21,PHIEND21,1.39e-09,1.56e-09)
ParticleSourceat(mysource52,PHIBGN22,PHIEND22,1.56e-09,1.73e-09)
ParticleSourceat(mysource53,PHIBGN23,PHIEND23,1.73e-09,1.91e-09)
ParticleSourceat(mysource54,PHIBGN31,PHIEND31,1.73e-09,1.91e-09)
ParticleSourceat(mysource55,PHIBGN24,PHIEND24,1.91e-09,2.08e-09)
ParticleSourceat(mysource56,PHIBGN25,PHIEND25,1.04e-09,1.21e-09)
ParticleSourceat(mysource57,PHIBGN26,PHIEND26,1.21e-09,1.39e-09)
ParticleSourceat(mysource58,PHIBGN27,PHIEND27,1.39e-09,1.56e-09)
ParticleSourceat(mysource59,PHIBGN28,PHIEND28,1.56e-09,1.73e-09)
ParticleSourceat(mysource60,PHIBGN29,PHIEND29,1.73e-09,1.91e-09)
ParticleSourceat(mysource61,PHIBGN30,PHIEND30,1.91e-09,2.08e-09)
#####################################################################
###3/5
############################################################3/5
ParticleSourceat(mysource71,PHIBGN1,PHIEND1,2.08e-09,2.25e-09)
```

ParticleSourceat(mysource72,PHIBGN2,PHIEND2,2.25e-09,2.43e-09)
ParticleSourceat(mysource73,PHIBGN3,PHIEND3,2.43e-09,2.60e-09)
ParticleSourceat(mysource74,PHIBGN4,PHIEND4,2.60e-09,2.77e-09)
ParticleSourceat(mysource75,PHIBGN5,PHIEND5,2.77e-09,2.95e-09)
ParticleSourceat(mysource76,PHIBGN6,PHIEND6,2.95e-09,3.12e-09)
ParticleSourceat(mysource77,PHIBGN7,PHIEND7,2.08e-09,2.25e-09)
ParticleSourceat(mysource78,PHIBGN8,PHIEND8,2.25e-09,2.43e-09)
ParticleSourceat(mysource79,PHIBGN9,PHIEND9,2.43e-09,2.60e-09)
ParticleSourceat(mysource80,PHIBGN10,PHIEND10,2.60e-09,2.77e-09)
ParticleSourceat(mysource81,PHIBGN11,PHIEND11,2.77e-09,2.95e-09)
ParticleSourceat(mysource82,PHIBGN12,PHIEND12,2.95e-09,3.12e-09)
ParticleSourceat(mysource83,PHIBGN13,PHIEND13,2.08e-09,2.25e-09)
ParticleSourceat(mysource84,PHIBGN14,PHIEND14,2.25e-09,2.43e-09)
ParticleSourceat(mysource85,PHIBGN15,PHIEND15,2.43e-09,2.60e-09)
ParticleSourceat(mysource86,PHIBGN16,PHIEND16,2.60e-09,2.77e-09)
ParticleSourceat(mysource87,PHIBGN17,PHIEND17,2.77e-09,2.95e-09)
ParticleSourceat(mysource88,PHIBGN18,PHIEND18,2.95e-09,3.12e-09)
ParticleSourceat(mysource89,PHIBGN19,PHIEND19,2.08e-09,2.25e-09)
ParticleSourceat(mysource90,PHIBGN20,PHIEND20,2.25e-09,2.43e-09)
ParticleSourceat(mysource91,PHIBGN21,PHIEND21,2.43e-09,2.60e-09)
ParticleSourceat(mysource92,PHIBGN22,PHIEND22,2.60e-09,2.77e-09)
ParticleSourceat(mysource93,PHIBGN23,PHIEND23,2.77e-09,2.95e-09)
ParticleSourceat(mysource94,PHIBGN31,PHIEND31,2.77e-09,2.95e-09)
ParticleSourceat(mysource95,PHIBGN24,PHIEND24,2.95e-09,3.12e-09)
ParticleSourceat(mysource96,PHIBGN25,PHIEND25,2.08e-09,2.25e-09)
ParticleSourceat(mysource97,PHIBGN26,PHIEND26,2.25e-09,2.43e-09)
ParticleSourceat(mysource98,PHIBGN27,PHIEND27,2.43e-09,2.60e-09)
ParticleSourceat(mysource99,PHIBGN28,PHIEND28,2.60e-09,2.77e-09)
ParticleSourceat(mysource100,PHIBGN29,PHIEND29,2.77e-09,2.95e-09)
ParticleSourceat(mysource101,PHIBGN30,PHIEND30,2.95e-09,3.12e-09)
##
###4/5
##4/5
ParticleSourceat(mysource101,PHIBGN1,PHIEND1,3.12e-09,3.29e-09)
ParticleSourceat(mysource102,PHIBGN2,PHIEND2,3.29e-09,3.47e-09)
ParticleSourceat(mysource103,PHIBGN3,PHIEND3,3.47e-09,3.64e-09)
ParticleSourceat(mysource104,PHIBGN4,PHIEND4,3.64e-09,3.81e-09)
ParticleSourceat(mysource105,PHIBGN5,PHIEND5,3.81e-09,3.99e-09)
ParticleSourceat(mysource106,PHIBGN6,PHIEND6,3.99e-09,4.16e-09)
ParticleSourceat(mysource107,PHIBGN7,PHIEND7,3.12e-09,3.29e-09)
ParticleSourceat(mysource108,PHIBGN8,PHIEND8,3.29e-09,3.47e-09)
ParticleSourceat(mysource109,PHIBGN9,PHIEND9,3.47e-09,3.64e-09)
ParticleSourceat(mysource110,PHIBGN10,PHIEND10,3.64e-09,3.81e-09)
ParticleSourceat(mysource111,PHIBGN11,PHIEND11,3.81e-09,3.99e-09)
ParticleSourceat(mysource112,PHIBGN12,PHIEND12,3.99e-09,4.16e-09)
ParticleSourceat(mysource113,PHIBGN13,PHIEND13,3.12e-09,3.29e-09)

ParticleSourceat(mysource114,PHIBGN14,PHIEND14,3.29e-09,3.47e-09)
ParticleSourceat(mysource115,PHIBGN15,PHIEND15,3.47e-09,3.64e-09)
ParticleSourceat(mysource116,PHIBGN16,PHIEND16,3.64e-09,3.81e-09)
ParticleSourceat(mysource117,PHIBGN17,PHIEND17,3.81e-09,3.99e-09)
ParticleSourceat(mysource118,PHIBGN18,PHIEND18,3.99e-09,4.16e-09)
ParticleSourceat(mysource119,PHIBGN19,PHIEND19,3.12e-09,3.29e-09)
ParticleSourceat(mysource120,PHIBGN20,PHIEND20,3.29e-09,3.47e-09)
ParticleSourceat(mysource121,PHIBGN21,PHIEND21,3.47e-09,3.64e-09)
ParticleSourceat(mysource122,PHIBGN22,PHIEND22,3.64e-09,3.81e-09)
ParticleSourceat(mysource123,PHIBGN23,PHIEND23,3.81e-09,3.99e-09)
ParticleSourceat(mysource124,PHIBGN31,PHIEND31,3.81e-09,3.99e-09)
ParticleSourceat(mysource125,PHIBGN24,PHIEND24,3.99e-09,4.16e-09)
ParticleSourceat(mysource126,PHIBGN25,PHIEND25,3.12e-09,3.29e-09)
ParticleSourceat(mysource127,PHIBGN26,PHIEND26,3.29e-09,3.47e-09)
ParticleSourceat(mysource128,PHIBGN27,PHIEND27,3.47e-09,3.64e-09)
ParticleSourceat(mysource129,PHIBGN28,PHIEND28,3.64e-09,3.81e-09)
ParticleSourceat(mysource130,PHIBGN29,PHIEND29,3.81e-09,3.99e-09)
ParticleSourceat(mysource131,PHIBGN30,PHIEND30,3.99e-09,4.16e-09)
##
###5/5
##4/5
ParticleSourceat(mysource131b,PHIBGN1,PHIEND1,4.16e-09,4.33e-09)
ParticleSourceat(mysource132,PHIBGN2,PHIEND2,4.33e-09,4.51e-09)
ParticleSourceat(mysource133,PHIBGN3,PHIEND3,4.51e-09,4.68e-09)
ParticleSourceat(mysource134,PHIBGN4,PHIEND4,4.68e-09,4.85e-09)
ParticleSourceat(mysource135,PHIBGN5,PHIEND5,4.85e-09,5.03e-09)
ParticleSourceat(mysource136,PHIBGN6,PHIEND6,5.03e-09,5.20e-09)
ParticleSourceat(mysource137,PHIBGN7,PHIEND7,4.16e-09,4.33e-09)
ParticleSourceat(mysource138,PHIBGN8,PHIEND8,4.33e-09,4.51e-09)
ParticleSourceat(mysource139,PHIBGN9,PHIEND9,4.51e-09,4.68e-09)
ParticleSourceat(mysource140,PHIBGN10,PHIEND10,4.68e-09,4.85e-09)
ParticleSourceat(mysource141,PHIBGN11,PHIEND11,4.85e-09,5.03e-09)
ParticleSourceat(mysource142,PHIBGN12,PHIEND12,5.03e-09,5.20e-09)
ParticleSourceat(mysource143,PHIBGN13,PHIEND13,4.16e-09,4.33e-09)
ParticleSourceat(mysource144,PHIBGN14,PHIEND14,4.33e-09,4.51e-09)
ParticleSourceat(mysource145,PHIBGN15,PHIEND15,4.51e-09,4.68e-09)
ParticleSourceat(mysource146,PHIBGN16,PHIEND16,4.68e-09,4.85e-09)
ParticleSourceat(mysource147,PHIBGN17,PHIEND17,4.85e-09,5.03e-09)
ParticleSourceat(mysource148,PHIBGN18,PHIEND18,5.03e-09,5.20e-09)
ParticleSourceat(mysource149,PHIBGN19,PHIEND19,4.16e-09,4.33e-09)
ParticleSourceat(mysource150,PHIBGN20,PHIEND20,4.33e-09,4.51e-09)
ParticleSourceat(mysource151,PHIBGN21,PHIEND21,4.51e-09,4.68e-09)
ParticleSourceat(mysource152,PHIBGN22,PHIEND22,4.68e-09,4.85e-09)
ParticleSourceat(mysource153,PHIBGN23,PHIEND23,4.85e-09,5.03e-09)
ParticleSourceat(mysource154,PHIBGN31,PHIEND31,4.85e-09,5.03e-09)
ParticleSourceat(mysource155,PHIBGN24,PHIEND24,5.03e-09,5.20e-09)

```
ParticleSourceat(mysource156,PHIBGN25,PHIEND25,4.16e-09,4.33e-09)
ParticleSourceat(mysource157,PHIBGN26,PHIEND26,4.33e-09,4.51e-09)
ParticleSourceat(mysource158,PHIBGN27,PHIEND27,4.51e-09,4.68e-09)
ParticleSourceat(mysource159,PHIBGN28,PHIEND28,4.68e-09,4.85e-09)
ParticleSourceat(mysource160,PHIBGN29,PHIEND29,4.85e-09,5.03e-09)
ParticleSourceat(mysource161,PHIBGN30,PHIEND30,5.03e-09,5.20e-09)
#####################################################################

###And so on. Each particle source represents a current source and is individually timed.

###Many particle sources were generated up to 150 ns of total simulation run.

###This can also be change to a modulus function with a single pulse s(t)

### s(mod(t,T)) and the current density function can be modified to expression =
###JDENS_EMIT*emissionMask(x,y) *H(mod(t,T)-tbegin)*H(tend-mod(t,T)) and
###making applyTimes=[0 1] instead.


<ParticleSink cathodeElectronSink>
kind = absSavCutCell
gridBoundary = theCathode
lowerBounds = [ -1 -1 -1 ]
upperBounds = [$NX+1$ $NY+1$ $NZ+1$]
</ParticleSink>
<ParticleSink anodeElectronSink>
kind = absSavCutCell
gridBoundary = theAnode
lowerBounds = [ -1 -1 -1 ]
upperBounds = [$NX+1$ $NY+1$ $NZ+1$]
</ParticleSink>
</Species>
<History anodeCurrent_Amps>
kind = speciesCurrAbs
species = electrons
ptclAbsorber = anodeElectronSink
</History>
<History cathodeReturnCurrent_Amps>
kind = speciesCurrAbs
species = electrons
ptclAbsorber = cathodeElectronSink
</History>
<History anodeElectronHeat_Watts_timesDT>
kind = speciesEngyAbs
species = electrons
ptclAbsorber = anodeElectronSink
</History>
<History cathodeElectronHeat_Watts_timesDT>
```

```
kind = speciesEngyAbs
species = electrons
ptclAbsorber = cathodeElectronSink
</History>
<History numMacroParticles>
kind = speciesNumberOf
species = electrons
</History>
$ endif


####If DC Hub is desired. It is defined as another particle source, using a continuous
current source.
########################HUB PARAMETERS##############################
$ JDENS_EMIT_Hub = EMITTED_CURRENT_Hub/AREA_EMIT
$ NOM_DEN_Hub =
EMITTED_CURRENT_Hub*DT/(ELEMCHARGE*APPROXNUMEMITCELLS*PAR
TPERCELLPERSTEP)
<Species hubelectrons>
verbosity = 0
kind=relBorisVW
charge = ELECCHARGE
mass = ELECMASS
emField = myComboEmField
nominalDensity = NOM_DEN_Hub
nomPtclsPerCell = PARTPERCELLPERSTEP
numPtclsInMacro = 1.0e5
<macro ParticleSourceat(source_name,phibgn,phiend,tbegin,tend)>
<ParticleSource source_name>
kind = xvLoaderEmitter
positionFunction = random
useCornerMove = true
emitBasedOnLocalForce = true
loadOnShift = false
loadAfterInit = false
applyTimes = [tbegin tend]
<PositionGenerator thisGen>
kind = cutCellPosGen
numMacroPtclsPerStep = PARTPERCELLPERSTEP
emitterBoundary = theCathode
emissionOffset = 0.1
<STFunc mask>
kind = expression
expression = H((phiend)-atan2(y,x))*H(atan2(y,x)-(phibgn))
</STFunc>
</PositionGenerator>
<VelocityGenerator emitVelGen>
```

```
kind = funcVelGen
velocityIsLocal = true
<STFunc component0>
kind = expression
expression = -1.0*VTHERMAL
</STFunc>
</VelocityGenerator>
<STFunc currentDensityFunc>
kind = expression
expression = JDENS_EMIT_Hub*emissionMask(x,y)
</STFunc>
</ParticleSource>
</macro>
<function fix_angle(angle)>
mod(angle+PI,TWOPI)-PI
</function>
$PHIBGN0=-1.0*PI
$PHIEND0=1.0*PI
ParticleSourceat(mysource0,PHIBGN0,PHIEND0,0.0,150.0e-09)
<ParticleSink cathodeElectronSink>
kind = absSavCutCell
gridBoundary = theCathode
lowerBounds = [ -1 -1 -1 ]
upperBounds = [$NX+1$ $NY+1$ $NZ+1$]
</ParticleSink>
<ParticleSink anodeElectronSink>
kind = absSavCutCell
gridBoundary = theAnode
lowerBounds = [ -1 -1 -1 ]
upperBounds = [$NX+1$ $NY+1$ $NZ+1$]
</ParticleSink>
</Species>
```